

LEE SURFACE FLOW PHENOMENA OVER SPACE SHUTTLE
AT LARGE ANGLES OF ATTACK AT $M_\infty = 6$

By V. Zakkay, M. Miyazawa, and C. R. Wang

(NASA-CR-132501) LEE SURFACE FLOW
PHENOMENA OVER SPACE SHUTTLE AT LARGE
ANGLES OF ATTACK AT M SUB INFINITY EQUAL
6 (New York Univ.) 180 p HC \$5.50

N74-33437

Unclas

CSCL 20D G3/01 50134



Prepared under Grant No. NGR 33-016-179 by
NEW YORK UNIVERSITY
New York, NY

for

NATIONAL AERONAUTICS AND SPACE ADMINISTRATION

CONTENTS

	PAGE
SUMMARY	1
INTRODUCTION	2
SYMBOLS	6
TESTING TECHNIQUE AND INSTRUMENTATION	8
Space Shuttle Model and Cone Model	8
Surface Heat Transfer and Pressure Measurements	9
Space Shuttle Flow Field Surveys	10
Oil Flow Studies	10
RESULTS AND DISCUSSIONS OF THE SPACE SHUTTLE ORBITER EXPERIMENTS	11
Distribution of Surface Pressure and Heat Transfer Rate on Lee Surface	12
Oil Flow Studies and Separation Patterns	16
Flow Field Surveys	18
Windward and Circumferential Flow Phenomena	20
THEORETICAL PREDICTION OF THE LEEWARD CENTERLINE HEAT TRANSFER	22
Assumptions	22
Comparison Between Theory and Experiments	23
ANALYSIS OF FLOW FIELD OVER SPACE SHUTTLE MODEL CONFIGURATION	24
Physical Model	24
Flow Field Computation Scheme	24
Boundary Layer Computation Scheme	24
Determination of the Effective Body Shape	25
Numerical Example	25
Comparison Between Theory and Experiments	25
CONCLUSIONS	26
APPENDIX - SEPARATION PATTERNS ON YAWED CONES	30
REFERENCES	43

LEE-SURFACE FLOW PHENOMENA OVER SPACE-SHUTTLE

AT LARGE ANGLES OF ATTACK AT $M_{\infty} = 6$

by V. Zakkay, M. Miyazawa, and C.R. Wang

New York University

SUMMARY

Surface pressure and heat transfer, flow separation, flow field, and oil flow patterns on the leeward side of a space shuttle orbiter model are investigated at a free stream Mach number of 6. The free stream Reynolds numbers are between 1.64×10^7 and 1.31×10^8 per meter, and the angle of attack is varied between 0° and 40° for the present experiments. The stagnation temperatures for the tests are approximately 500°K and the wall temperature is maintained at 290°K . Existing numerical methods of three-dimensional inviscid supersonic flow theory and compressible boundary layer theory are used to predict the present experimental measurements. Results of the present tests indicate two distinct types of flow separation and surface peak heating depending on the angle of attack; the free vortex layer type separation characterized by one pair of separation lines and peak heating attributed to boundary layer transition for $\alpha = 10^\circ, 20^\circ$; the bubble type separation characterized by two pairs of separation lines and peak heating attributed to vortex interaction in the separation region for $\alpha = 30^\circ$ and 40° . Large axial components of velocity are also measured in the separated flow field. Laminar boundary layer theory predicts the leeward center line surface heat transfer rates satisfactory for zero angle of attack. Turbulent boundary layer theory with a separation shape factor of 1.9 agrees with the heat transfer measurements for angle of attack. Inviscid supersonic flow

theory over an equivalent body geometry also agrees approximately with the profile measurements of the flow field on the leeward plane of symmetry. Oil flow studies indicate similarity of leeward surface flow patterns between the space shuttle orbiter model and yawed cone. Separation criteria obtained on conical bodies could be extrapolated to predict the separation which occurs on the portion of leeward surface after the expansion shoulder of the space shuttle.

INTRODUCTION

A complete description of the leeward surface heating of a space shuttle orbiter requires an understanding of three-dimensional flow separation, vortices lifting off the surface, and effect of the free stream conditions on the flow field. Recent studies of heat transfer over a space shuttle orbiter at angle of attack in hypersonic flow indicate the existence of localized high heating associated with vortex interaction in the separated flow region over the leeward surface. Flow separation due to various body shapes and shock boundary layer interaction has been a recent major research topic of many investigators. Results of heat transfer in separated flow and flow separation phenomena, covering a wide range of flow speeds, can be found in Ref. 1. Systematic experiments of heat transfer associated with laminar, transitional, and turbulent separation on a flat plate at Mach 6 has been conducted by Holloway, et al., Ref. 2.

Initial research on lee-surface heating and flow separation over several configurations has been done in Refs. 3 to 10: Experiments of flowfields over high swept data wings in a Mach 6 free stream, Ref. 3, have shown that coiled vortex sheets exist on the lee-surface of a wing and that high heat transfer

rates are induced by the vortex sheet. The circulatory motion of the vortices induces a downward flow toward the centerline of high energy air which then turns outward drawing low energy fluid from the center area. The localized high heating in the center region is characterized by the feather like trace (reattachment region) in oil flow patterns.

Further experimental work, over a wide range of Reynolds number, Ref. 4, confirmed the above observations and revealed two heating peaks, the higher peak occurs due to the existence of vortex system and the second peak is attributed to the boundary layer transition of the reattachment flow. More comprehensive analyses of the leeward flow phenomena on delta wing, blunt cone, and conceptual space shuttle orbiter have been performed by Whitehead, et al., Ref. 7 and flowfield models which account for the interaction of the vortex and the boundary layer on the leeward surface, have been proposed for these configurations. Experimental results of heat transfer, surface pressure distributions, and oil flow patterns on conceptual space shuttle configurations in Mach 6 and Mach 19 free streams, Refs. 7, 8, and 9 show that a) the vortex-induced peak heating is significantly influenced by Reynolds number at Mach 6; the location is affected by the angle of attack and is insensitive to Reynolds number, b) there exists a threshold Reynolds number below which peak heating decreases abruptly with decreasing Reynolds number, c) due to Reynolds number effect, relative low leeward surface heating without peak phenomena, was observed in tests of Mach 19, d) the effect of surface pressure on the peak heating is insignificant, the peak heating phenomena is not caused by an abrupt increase in pressure, e) variations in leeward surface geometry significantly influence vortex-induced peak heating and modification of upper surface geometry to introduce vortex lift-off can reduce

the vortex induced heating. Similar behavior of the leeward flow phenomena over a blunt cone has also been found.

Experimental results, Ref. 11, on an orbiter model have shown lower leeward surface heating levels at Mach 5. No significant peak heating was observed and satisfactory correlation of the lee-surface heating was not found either.

Significant progress in three-dimensional separation flow analysis has been achieved by Maskell, etc., Refs. 12, 13, and 14. Starting from the general concept of flow separation that the line of separation must be an envelope of the limiting streamlines, Maskell, Ref. 14, studied the significance of three-dimensional flow separation without using the boundary layer concept. He has shown that a) three-dimensional separated flow consists of two basic types: a bubble type and a free vortex type, each of which is characterized by a particular form of surface flow pattern, b) the bubble type separation requires the existence of a singular point, and the surface of separation encloses fluid which is not part of the main stream but is carried along with the body, c) separation line for a free vortex layer has only regular points, and the space outside the body on either side of the surface of separation is filled by the mainstream fluid, d) a combination of these two types of flow patterns is the general result of flow separation. Bubble type separation, free vortex type separation, and combination of both types can be found on a body of revolution at an angle of attack. Maskell concluded that flow separation can be inferred from a study of the surface flow pattern if it does indicate the nature of limiting streamlines and that surface flow visualization techniques are crucial in analyzing separated flow. His analysis is also applicable to any type of boundary layer flow.

Experiments of flow separation over yawed cone at hypersonic speed have been done by Tracy, etc., Refs. 15-21. Their results show that Maskell's separation flow patterns exist on the surface of cones. Previous theoretical and numerical analyses of the flow field over a circular cone apply to small angle of attack. Recently, Kutler, et al., Refs. 22, 23, and 24 developed a numerical method capable of determining multiple shocked, three-dimensional supersonic flow field. Some numerical results were in good agreement with experiments, including the case of a space shuttle configuration at an angle of attack of 15.3° .

Based on the results of incompressible laminar boundary layer analysis and experiments, Wang, Ref. 13, has shown that, for a spheroid with moderate thickness ratio, a bubble type separation prevails at low incidence ($\alpha = 3^\circ$), a free vortex type separation dominates at high incidence ($\alpha = 12^\circ$) and the separation reverts to a closed bubble type as the incidence continues to increase. He concluded that common features of free vortex type are: a) it is a cross flow separation due to the reversal of cross flow velocity, b) the separation line does not necessarily originate or terminate at singular points, c) the limiting streamlines of separated and unseparated regions may originate from the same sources. The separation phenomena for inclined bodies of revolution were also explored. He also concluded that basic features of the surface flow patterns is similar in high speed flow and in low speed flow, particularly for a simple shaped body like a blunt cone.

Because of the sparsity of experimental results on the space shuttle and the concern on heating of the leeward side, further research is required to verify the possibility of using existing results of flow field over similar body geometry to analyze space shuttle flow phenomena. In the present

investigation, theory and experiment have been undertaken to examine the following problems:

- a) the surface heat transfer on the leeward side of the space shuttle with different free stream Reynolds numbers and angles of attack.
- b) the peak heating due to boundary layer transition and flow separation and comparison of the correlations of surface peak heating over different space shuttle configurations.
- c) the leeward flowfield in the vortex flow region and the method of constructing an equivalent model for leeward flowfield analysis.
- d) criteria for vortex generation on the leeward flow and the effect of transition on vortex generation.
- e) the similarity between the flowfields over conical body and space shuttle and validity of interpreting the space shuttle leeward flowfield by extrapolating the flow properties over simple body geometry.

SYMBOLS

- a speed of sound
- C_p pressure coefficient
- c specific heat of wall material
- d wall thickness
- h heat transfer coefficient, $q_w / (T_{\infty} - T_w)$
- L body length of a model
- M Mach number

p pressure
q heat transfer rate
r radius
 R_{∞} free stream unit Reynolds number, per meter
 $R_{\infty,L}$ free stream Reynolds number based on model length
s distance along the body surface from the nose
T temperature
t time
V flow velocity
x,y,z body axes
 α angle of attack
 θ_c cone half-angle
 μ viscosity
 ρ density

Subscripts

b body surface
B model base
N model nose
p conditions at peak heating
s separation
s1 primary separation
s2 secondary separation
t local stagnation conditions
t2 local stagnation conditions behind a normal shock
w conditions at the wall
wo laminar stagnation conditions

- ∞ free stream conditions
- ∞ free stream stagnation conditions

TESTING TECHNIQUES AND INSTRUMENTATION

Present experiments were performed in a Mach 6 blowdown type axisymmetric wind tunnel, Fig. 1, at the New York University Aerospace Laboratory. The test section of the tunnel is 30.5 cm in diameter. For all the tests of present experiments, stagnation temperatures were nominally 500°K and the stagnation pressure is varied from 1.38×10^6 to 1.38×10^7 Newton/m². The resulting free stream Reynolds numbers were in the range of 1.64×10^7 to 1.31×10^8 per meter.

Space Shuttle Model and Cone Model

Based on NASA shuttle design, two space shuttle models with identical configurations were made for the tests. The basic body of these models was made of brass and the necessary segments for instrumentation along the body surface were replaced by stainless steel or shimstock. Schematics of these models are shown in Figs. 2 and 3, and their photographs are shown in Figs. 4 and 5. Details of the model have been described in Ref. 25.

The model, used for surface heat transfer measurements, was instrumented with chromel-alumel thermocouples welded to the inside surface of the model. Thickness of the wall (stainless steel) on the nose part varies from 0.053 cm to 0.081 cm. Stainless steel shimstock of 0.025 cm thickness, were used for the other parts of the model. Locations of the thermocouples are given in Figs. 6 and 7.

The other model, used for surface pressure measurements, was equipped with pressure taps of 0.16 cm diameter orifice. Scanivalves and transducers,

calibrated for very small pressure range, were used to sense pressure through the orifice. Locations of the pressure taps are shown in Figs. 8 and 9. Pressure and temperature data were recorded on a multi-channel visicorder through galvanometers with response time less than 0.01 sec.

A special support for the space shuttle model was constructed. As shown in Fig. 10, it consists of two semi-circular struts to avoid interactions which would affect the base pressure, and the leeward flowfield. All leads of thermocouples and pressure taps were taken through a groove inside the strut. Figure 11 shows a front view of the space shuttle model on its support.

A conical model was used only for oil flow studies. The model has a cone half-angle of 7.5° and three different noses, Figs. 12 and 13, one sharp nose and two blunt noses (bluntness: $r_n/r_B = 0.12$ and 0.24).

Surface Heat Transfer and Pressure Measurements

Transient thin wall technique was used to calculate the local heat transfer rate from the slope of the temperature-time record. This technique can be expressed as:

$$q_w = (\rho c d)_w \left(\frac{dT}{dt} \right)_{t=0}$$

where ρ , c , and d are the properties of the wall material (stainless steel). In this technique, a sharp slope at zero time is necessary. For this purpose the whole nozzle section was evacuated well below the expected free stream static pressure before each test. Heat transfer data obtained were reduced to a dimensionless form q_w/q_{w0} , with q_{w0} being the laminar stagnation heat transfer rate on a sphere of 0.38 cm in radius calculated from Lees' theory, Ref. 27. Local surface pressure measured over the space shuttle model was normalized

with respect to the free stream static pressure and is presented as p/p_∞ in this paper.

Space Shuttle Flow Field Surveys

Profiles of total pressure, static pressure, and total temperature of the flow field along the leeward plane of symmetry were measured with three different boundary layer probes; static pressure, total pressure, and total temperature probes. A schematic of the probe is shown in Fig. 14. These measurements were performed by traversing the probes perpendicular to the body axis from the leeward top surface with an automatic mechanism. In order to minimize the error introduced by the shock boundary layer interaction due to the presence of the probe in the supersonic region, streamline shaped probes were used. The static probe has a conical tip faired into a 0.10 cm hypodermic needle. Lateral orifices located 10 to 15 probe diameters downstream were drilled in the probe. The total pressure probe consists of a hypodermic needle 0.1 cm diameter flattened at the tip with a thickness of 0.015 cm and an opening of 0.005 cm. The total temperature probe was made of an unshield, open-tip chromel-alumel thermocouple. Near the wall, the flow field is characterized by the sublayer. It is desirable to have the tip of each probe much less than the thickness of the sublayer. The error of the measurements can be reduced by making the probe tip as small as possible.

Oil Flow Studies

Oil flow techniques were employed to determine the surface (limiting) streamlines, and separation patterns on the surface of the space shuttle orbiter. Before each test, a mixture of Dow Corning 200 silicon oil (50-100 centistokes) and carbon black powder was sprayed over the entire model surface.

After each test, the model was taken out of the tunnel and photographed. In the oil flow studies, it was important to choose the correct viscosity for each test conditions. For the present tests, oil with viscosity between 70 to 100 centistokes was found to produce the best results when properly mixed with black carbon. Similar techniques were used in the oil flow studies over the cone models and details of this part of experiments are presented in the appendix.

RESULTS AND DISCUSSIONS OF THE SPACE SHUTTLE ORBITER EXPERIMENTS

The experimental results of surface pressure and heat transfer measurements, Leeward flowfield surveys, and oil flow studies on the space shuttle orbiter model are summarized and presented in this section. The effects of free stream Reynolds number and angle of attack to the surface measurements, peak heating phenomena, separation patterns are also discussed in this section. Details of the experimental data can be found in Ref. 25. However, the test conditions are shown in the following table:

MEASUREMENTS	α	$R_{\infty,L} \times 10^{-7}$
Surface Heat Transfer	$0^{\circ} \rightarrow 40^{\circ}$	0.32 \rightarrow 2.57
Surface Pressure	$0^{\circ} \rightarrow 40^{\circ}$	0.50 \rightarrow 2.42
Flowfield Survey	$20^{\circ} \rightarrow 30^{\circ}$	0.61 \rightarrow 2.31
Oil Flow	$10^{\circ} \rightarrow 40^{\circ}$	0.92 \rightarrow 2.39

with

$$M_{\infty} = 5.93$$

$$P_{O\infty} = 1.38 \times 10^6 - 1.38 \times 10^7 \text{ Newton/m}^2$$

$$T_{O\infty} = 450 - 500^{\circ}\text{K}$$

$$T_w/T_{O\infty} = 0.6 \sim 0.7$$

Distributions of Surface Pressure and Heat Transfer Rate on Lee-Surface

Surface pressure distributions along the leeward centerline at different angles of attack are given in Figs. 15-19. At zero angle of attack, Fig. 15, shows that the surface pressure distribution is not influenced by the changes in the free stream Reynolds number. For comparison, surface pressure on a sharp cone having the same cone half-angle, Ref. 28, is also shown in the figure. The cone values agree with present experimental results over the nose region of the model. As the angle of attack increases, Reynolds number effect on the surface pressure appears in the region after the expansion corner, lower pressure level is found with a higher free stream Reynolds number, Figs. 16-19. Thus, the viscous interaction is significant in that region. Similar results have been found in Ref. 15. The strongest viscous interaction effect is found at $\alpha = 30^{\circ}$ in the present experiments, particularly in the region after the expansion corner.

Measurements of the heat transfer rates are shown in Figs. 20 to 38. All the heat transfer data presented here were nondimensionalized by the theoretical laminar stagnation point heat transfer rate, q_{w0} , on a sphere ($r = 0.38$ cm) having the same nose radius of the model at the same test conditions. There are several methods to estimate q_{w0} ; Lees, Fay and Ridell, and Eckert and Tewfik, Refs. 27, 29, and 30. However, sample calculations have shown that

these methods yield approximately the same results. In the present investigation, theoretical values obtained from Lees' method was used. Present experimental results of stagnation heat transfer coefficient h_{w0} is plotted in terms of Reynolds number $R_{\infty,L}$ in Fig. 39. They are in good agreement with theoretical results.

In order to assess the results of the heat transfer data, and compare it with a reference point, some estimates have been made based on the measured surface pressure distribution and two-dimensional or axisymmetric boundary layer assumptions, neglecting the cross flow effects. Two extreme entropy relations were used to determine the local external flow conditions; the local inviscid stagnation pressure was assumed constant at the value behind the normal shock and the conical shock, due to a sharp cone with $\theta_c = 19.3^\circ$ at zero angle of attack. The modified Lees method, Ref. 30, was used for laminar calculation. Turbulent heat transfer rates were calculated by using the Reshotko-Tucker method, Ref. 31, and the Flat Plate Reference Enthalpy Method, Ref. 32. Results of the theoretical heat transfer calculations are compared in Fig. 40. For the present test conditions, there is no significant difference in turbulent heat transfer between two-dimensional and axisymmetric flows. Thus, the Reshotko-Tucker method with conical entropy and FPPE method with both entropy relations were used to estimate the turbulent heat transfer rates for $\alpha > 0^\circ$. This estimate was based on the measured surface pressure distributions corresponding to each heat transfer test and the assumption that attached boundary layer flow exists on the lee-surface. Results are compared with experimental measurements in Figs. 20-34.

The effect of Reynolds number on lee-surface heat transfer rates at a specified angle of attack, are shown in Figs. 30-34. Separation points

determined from oil flow studies are shown.

At $\alpha = 0^\circ$ (Fig. 30) and from comparison with theory: laminar boundary layer flow is found to exist over the major portion of the lee-surface. Although the space shuttle orbiter is a three-dimensional body and the laminar estimate, Ref. 30, assumes a highly cooled wall with the negligible effect of local pressure gradient, the laminar axisymmetric calculation agrees with measurements in the front portion before the shoulder. After the shoulder, scattering experimental data are found. The cross flow effect in the leeward plane of symmetry can be neglected for $\alpha = 0^\circ$.

At $\alpha = 10^\circ$ (Fig. 31), the maximum heat transfer rate in the nose region is approximately the value given by the two-dimensional turbulent boundary layer theory for the case of $R_{\infty,L} = 2.42 \times 10^7$. For other cases, experiments are in good agreement with laminar boundary layer theory. Boundary layer transition occurs in that region as the free stream Reynolds number increases. This tendency becomes more pronounced at an angle of attack of 20° , Fig. 32 and turbulent boundary layer is believed to exist over the nose portion at $R_{\infty,L} = 2.42 \times 10^7$. Peak heating also appears in the nose region for $\alpha = 10^\circ$ and 20° . This suggested that peak heating is due to boundary layer transition for the case of small angle of attack. At $\alpha = 20^\circ$, another peak heating appears in the region after the expansion shoulder. This is due to the flow separation and will be discussed later.

For high angles of attack ($\alpha = 30^\circ, 40^\circ$), peak heating phenomena associated with flow separation, termed the vortex-induced peak heating, are observed (Figs. 33, 34). In both cases, the maximum heating values are found to be nearly the same order of magnitude as the local turbulent heat transfer rates calculated from attached boundary layer analyses. Vortex shear layer

exists over the body surface after the shoulder. Measurements of the heat transfer rate indicate that transition of the vortex shear layer occurs for the cases of $\alpha = 30^\circ$ and the vortex shear layer becomes turbulent for $\alpha = 40^\circ$.

Lee-surface heat transfer results are plotted for different values of Reynolds number with the angle of attack as a parameter in Figs. 35 through 39, to study the effect of angle of attack on the lee-surface heating phenomena. For all the Reynolds numbers covered in the present tests, heat transfer rates obtained at angles of attack were not high enough to exceed those of $\alpha = 0^\circ$ in front of the shoulder. After the expansion over the shoulder section, however, heat transfer rates increase rapidly, indicating the flow in this region is similar to the boundary layer flow transition from laminar to turbulent. At relatively low angles of attack ($\alpha = 10^\circ, 20^\circ$), laminar boundary layer exists over the lee-surface of the nose section before the shoulder at low Reynolds number. As the Reynolds number increases, the transition point moves forward, resulting in higher heating value (peak heating) before the flow undergoes an abrupt expansion over the shoulder section (Figs. 31,32). Since there is no significant Reynolds number effect on the pressure field before the shoulder, flow starts to expand at almost the same position for all Reynolds numbers where the boundary layer is still transitional or has just become turbulent.

Maximum and secondary peak heat transfer rates obtained for various Reynolds numbers and angles of attack are shown in Figs. 41 and 42. In Fig. 41, the peak heating is plotted as a function of Reynolds number $R_{\infty,L}$, where a distinction is made between the peak heating within a separated flow region and that due to boundary layer transition as determined with the aid of oil flow studies. The same data are plotted against the local Reynolds number $R_{\infty,L}$ in Fig. 42. Both figures show that peak heating values due to

transition are strong functions of Reynolds number and increase with $R_{\infty,L}$ or $R_{\infty,x}$ rapidly over the range of Reynolds numbers of present tests. Correlation of the boundary layer transitional peak heating in terms of Reynolds number shows similar behavior as that of Ref. 10. However, peak heating within the separated region does not consistently correlate with Reynolds number, and seems to increase for some angles of attack and decreases for some angles of attack as may be observed from Figure 41. For the most critical angle of attack where the highest peak heating exists ($\alpha = 30^\circ$), the heating rates are practically independent of Reynolds number.

The peak heating due to vortex-surface interactions, vortex-induced peak heating, is observed at high angles of attack ($\alpha = 20^\circ, 30^\circ, 40^\circ$). This type of peak heating is caused by the thinning of the viscous shear layer as a result of outflow induced by the vortices. The phenomena which occurs here is conclusively not a result of the pressure distribution. This may be observed clearly from Figs. 16 to 19, and especially from Fig. 18 for $\alpha = 30^\circ$. The trend is that lower pressures are obtained as the Reynolds number increases. Therefore, it can be concluded that peak heating rates within a vortex region is not caused by abrupt changes in the surface pressure distribution.

Relation between the location of peak heating and free stream Reynolds number of the present experiments is shown in Fig. 43. The location is found independent of free stream Reynolds number. Similar results have been found in Ref. 10.

Oil Flow Studies and Separation Patterns

A selected number of oil flow photographs are presented in Figs. 44-51. The nose portion of Fig. 49 is magnified in Fig. 52 to show an example of the bubble type separation. Circumferential locations of separation lines are

determined from the oil flow pictures and given in Figs. 53-56. Some experimental results of sharp cones are included in these figures.

Separation lines, limiting streamlines, separated flow regions, and feather-like high shear (heating) regions are found in Figs. 44-51. At relatively low angles of attack ($\alpha = 10^\circ, 20^\circ$; Figs. 44-47), the separation type is a "free vortex layer" type in terms of Maskell's separation models in three-dimensional flow. On the other hand, the separation type on the front part is considered to be a bubble type at high angles of attack ($\alpha = 30^\circ, 40^\circ$; Figs. 48-51).

The nose part of Fig. 49 is magnified and presented in Fig. 52 to show an example of the bubble type separation which starts at a singular point. In this figure, the feather-like high shear (heating) region near the leeward centerline is clearly observed following the separated flow region immediately behind the singular point (starting point of separation). This high shear region, a kind of reattachment flow region, is created by a vortex-surface interaction and it is here that the vortex-induced peak heating phenomenon is observed in heat transfer measurements. It is also seen that this high shear region is followed by another separated flow region corresponding to a low heat transfer region as confirmed by heat transfer data.

Two pairs of separation lines were obtained for all the cases tested here with the angle of attack ranging from 10° to 40° . At $\alpha = 10^\circ$ (Fig. 53), the inner separation line ($\varphi = 150^\circ$) seems to be the primary line, although it is difficult to judge in this case. Stetson's sharp cone result, Refs. 16 and 17 is in good agreement with the inner separation line. Primary and secondary separation lines are distinguished clearly at $\alpha = 20^\circ$ as shown in Fig. 54 along with a sharp cone result by Feldhuhn et al., Ref. 20. In this case the effect of Reynolds number is found to be rather significant compared to the

other cases. The same pattern of separation lines (primary and secondary) is also observed at $\alpha = 30^\circ$ and 40° (Figs. 55 and 56). In these cases, the locations of secondary separation lines change along the body axis direction, but the primary separation lines are found to be stable over a large portion of the body from the nose part. The locations of both primary and secondary separation lines agree very well with the results of a sharp cone, Ref. 20. It is concluded that the separation pattern over the space shuttle configuration at $\alpha = 30^\circ$ and 40° is similar to that over a cone except for a certain distance where streamwise pressure gradient effects persist. From the above results of separated flow patterns and the boundary layer phenomena at different angles of attack, possible patterns of separated flow in a cross section of the space shuttle orbiter at different ranges of angles of attack is shown in Fig. 57. This pattern is deduced from the flow field data and the oil flow pictures.

Flow Field Surveys

Total pressure, static pressure, and total temperature profiles in the leeward meridian plane, with the model at 20° and 30° angles of attack, are shown in Figs. 58-67. Velocity profiles, calculated from these measured profiles, are also given in Figs. 68-70. The flow field surveys have been done within the separated flow region. Locations of the external shocks determined from schlieren photographs, Figs. 71-72 are included in these figures.

As may be observed from Fig. 58 through Fig. 65 that there is a large variation in both the static pressure and pitot pressure normal to the surface of the body. The variation of the pressure as a function of Reynolds number is quite large close to the nose region as may be observed from Fig. 58. This is

due to the proximity of the measurements to the location of the shoulder, and therefore to the location of separated region. From the observations of the oil flow picture of Fig. 46 which is for low Reynolds number and that of Fig. 47 which is for high Reynolds number, it can clearly be seen that the flow pattern in this region is quite different, and therefore affects the normal pressure distribution. Further back on the body, there seems to be only a slight variation with Reynolds number as may be observed from Figs. 59 through 65. In all the measurements there seems to be a region of constant pressure normal to the surface of the body followed by a large increase. It may imply that this region of constant pressure could be characterized as the height of the vortex, which seems to increase with Reynolds number. Figs. 66 and 67 present the stagnation temperature profiles normal to the surface. As may be observed there is a distinct variation of the total temperature within the vortex, which gives an indication of the height of the vortex. The stagnation temperature seems to be quite high even in the proximity of the surface, confirming the fact that there is a large inflow of hot external air towards the leeward side of the body which gives rise to the high peak heating rates.

The velocity profiles shown in Figs. 68 through to 70 have been calculated from the static pressure, pitot pressure, and stagnation temperature profiles. These profiles which are the first to be deduced within the vortex region are quite unique and important since they indicate that the axial velocity within the vortex is quite large and must not be considered as a dead air region as usually is indicated within a separated region. In order to compare the present results with that of Ref. 33, the present results are plotted in the form of C_p , pitot and are presented in Figs. 73, 74, and 75.

As may be observed the present results agree very well with the results of Ref. 33 when plotted in this manner, and show little variations of C_p , pitot as a function of the normal distance from the body. Profiles of static pressure have not been measured in Ref. 33 and no conclusions could be made for the type of velocity that can be obtained within the vortex region. Therefore it is concluded here that in order to deduce the velocity distribution within the vortex, stagnation temperature, static pressure, and total pressure measurements have to be performed.

Windward and Circumferential Flow Phenomena

Distributions of surface pressure and heat transfer rates along the windward centerline are shown in Figs. 76-78. Circumferential distributions of surface pressures are given in Figs. 79-83, in which the locations of separation lines obtained from oil flow studies are also indicated. However, not enough pressure taps were installed to detect precise circumferential pressure distributions.

a) Windward Flow Phenomena

Pressure distributions along the windward centerline are shown in Fig. 76. There is no significant change in pressure for different Reynolds numbers at angles of attack from 0° to 40° , indicating negligible viscous interactions on the windward surface.

Heat transfer distributions along the windward centerline are shown in Figs. 77 and 78. Analytical estimates of heat transfer rates, based on the measured surface pressure distributions and the Flat Plate Reference Enthalpy Method (FPREM) by Eckert, Ref. 32, are included in these figures. The normal shock entropy relation was used throughout to determine the local flow conditions since it is assumed that swallowing has not been completed. At

$\alpha = 0^\circ$, 10° , and 20° experimental results for low Reynolds numbers agree fairly well with laminar estimates, suggesting that laminar boundary layer exists on the windward surface. As the Reynolds number increases, transition of boundary layer from laminar to turbulent occurs. At large angles of attack ($\alpha = 30^\circ$, 40°), the greater part of the windward surface boundary layer is found to be turbulent.

b) Circumferential Flow Phenomena

When there is no separation in the cross-flow plan at small angles of attack, the circumferential pressure distribution shows smooth expansion or compression. When the adverse pressure gradient, Figs. 79-83, becomes significant on the leeward side of the cross section, separation takes place as expected. Reynolds number effects become significant only in separated flow regions at large angles of attack ($\alpha = 30^\circ$, 40°), consistent with the surface pressure measurements along the leeward centerline.

Large differences in the circumferential distributions of heat transfer rates, as shown in Figs. 84-93, are observed at $\alpha = 0^\circ$, 10° , and 20° , in the windward side of each cross section, with a general tendency toward higher heating values for high Reynolds numbers. This is due to the change of boundary layer flow from laminar to turbulent. At $\alpha = 30^\circ$ and 40° , the entire flow over the body is turbulent for the Reynolds number range covered in the present tests, with little scattering in heat transfer measurements. The general trend of heat transfer within a separated flow region is that the minimum heat transfer is not obtained at the location of separation lines. For large angles of attack (Figs. 90-93), the position of the minimum heat transfer is located between the two separation lines. This is in agreement with the recent result on a yawed cone by Marcillat and Roux, Ref. 18.

THEORETICAL ANALYSIS OF THE LEEWARD CENTERLINE HEAT TRANSFER

In the previous section of results and discussions, theory of attached boundary layer has been used to estimate approximately the leeward centerline heat transfer rates. The effect of flow separation at various angles of attack has not been considered. In this section, results of an existing turbulent boundary layer theory, taking into account the separation effect, is presented. Momentum integral equation of compressible turbulent boundary layer is solved numerically. The expression of local skin friction in terms of reference properties and boundary layer shape factor, Ref. 31, is used. Local heat transfer rate is obtained from the Reynolds analogy.

Assumptions

Theory and numerical method in solving a turbulent compressible boundary layer with pressure gradients and cross flow has been developed by Zakkay et al., Ref. 34. This method is used to predict the present leeward surface centerline heat transfer measurements. The following assumptions were made:

- a) The shape factors of the boundary are $1.8 \approx 1.9$
- b) An axisymmetric body, with local radius the same as the distance from the leeward centerline of the model to its body axis, was used
- c) The cross flow effect is neglected
- d) The pressure gradient normal to the leeward surface is neglected
- e) Two extreme stagnation pressures were used to determine the local external flow conditions, i.e., the local inviscid stagnation pressure was assumed

constant at the values behind the normal shock and the conical shock due to a cone of 19.3° half angle in Mach 5.93 free stream

Comparisons Between Theory and Experiments

In order to ensure the existence of turbulent boundary layer over the leeward surface, the experimental results with the largest free stream Reynolds number of 2.40×10^7 , are considered only. Theoretical results are compared with experiments in Figs. 94-98.

At $\alpha = 0^\circ$, theory predicts higher heat transfer rates than the measurements. Results of laminar boundary layer theory, Ref. 27, is in better agreement with experiments.

At an angle of attack, present numerical results agree with measurements especially for the cases of large angle of attack. This also indicates that transition of laminar to turbulent occurs when the model is at small angle of attack, $\alpha = 10^\circ$.

Relation between the boundary layer thickness and the shape factor for turbulent boundary layer with pressure gradient has been found by Truckenbrodt, Ref. 35. The boundary layer separates at $H = 1.8 \sim 1.9$. These values were used in the present computation to account for the separation effect. The variation of the shape factor, as a function of the local momentum thickness, has not been considered. An initial momentum thickness must be given to carry out the numerical integration step by step and it was estimated by the method of Ref. 31 for the present studies. Further improvement of the numerical results can be made if detailed circumferential pressure measurements are available to estimate the cross flow effect.

ANALYSIS OF FLOW FIELD OVER SPACE SHUTTLE MODEL CONFIGURATION

Results of this experimental investigation, the previous discussion, and the discussion in the appendix, provide some necessary ingredients in order to analyze the flow field over the space shuttle orbiter and the interaction between the flow field and the vortices.

The method proposed here is a semi-empirical procedure which utilizes an equivalent body shape to develop the flow field. (An example can be found in the numerical analysis section of the Appendix). The equivalent body is derived from a combination of viscous turbulent boundary layer up to the point of separation, and a correlation of flow field data within the separated region. From the equivalent body, the flow field is calculated using an inviscid program modified to analyze the flow over the complicated geometry. The method of approach involves the following steps:

Physical Model

The physical model which is employed incorporates the concept of an "effective" body to represent the region of high shear adjacent to the geometric body. This shear layer, including both the boundary layer and the vortices, was considered to be enclosed by a streamline or stream surface which divided the region of high shear from the outer inviscid shock layer.

Flow Field Computation Scheme

Once the effective body shape has been determined, Kutler's method of analyzing the flow field over three-dimensional configurations at high angle of attack can be used to determine the inviscid flow field over the effective body surface.

Boundary Layer Computation Scheme

In order to characterize the effective body shape in the separated region and to define the surface conditions, boundary layer computation

scheme is required. The boundary layer theory, including streamline tracing concept with small cross flow assumption, can be utilized for this purpose because it provides the three-dimensional capability which is an essential feature of the viscous flow phenomena in this study.

Determination of the Effective Body Shape

The effective body will be established by an iteration procedure wherein different body shapes are prescribed as input to a computer program until a satisfactory match of the calculated surface pressure variation with the measurements was obtained. A sample calculation is given in the Numerical Analysis section of the Appendix. Correlation of the surface pressure measurements, Fig. 99, shall be used to generalize the nominal body shape in order to account for the effects of Mach number and angle of attack, Ref. 37.

Numerical Example

In order to evaluate the procedure in determining the flow field, a simplified analysis was performed for the present configuration. An axially symmetric body was chosen having the body profiles of the leeward plane of symmetry of the space shuttle. An equivalent body was constructed based on the data obtained from the sharp cones. The numerical results of the pressure distributions in the leeward plane of symmetry are shown in Figs. 100-101.

Comparisons Between Theory and Experiments

The flow field profile measurements are reproduced in Figs. 100-101 for comparisons. These figures indicate that:

- a) The inviscid flow theory over a yawed cone predicts the experimental pressure measurements satisfactory for relatively small angle of attack of 20°

b) In contrast to the results of Figs. 119-122, larger surface pressures are obtained from the theory.

c) Numerical results predict the location of the external shock for the space shuttle at an angle of attack of 20° .

Present profile data were measured in the separated region after the expansion over the shoulder on the leeward surface. Effects of the flow separation and expansion over the shoulder induce the differences between theory and experiments. The complicated geometry of the space shuttle model has not been properly considered in the present computation. Considering the assumptions made for this analysis, it is very rewarding to see that the trends are the same as obtained from the experimental results.

CONCLUSIONS

Experimental and analytical investigations of heat-transfer and flow-separation phenomena associated with a space shuttle orbiter at small and large angles of attack have been performed. In view of the impact of high lee-side heating rates upon thermal protection system weight, the main efforts have been directed toward the understanding of the leeward flow phenomena associated with separation. Experiments have been carried out with an orbiter model at Mach 6, at Reynolds numbers from 1.64 to 13.1×10^7 per meter and angles of attack from 0° to 40° . In addition, a conical flow analysis related to orbiter applications has been investigated numerically. From the present studies, the following conclusions have been reached.

- 1) A large Reynolds number effect occurred on the pressure distribution on the lee side of the orbiter with

pressure decreasing for an increasing Reynolds number.

The largest variation was observed at $\alpha = 30^\circ$ (Fig. 18).

- 2) At $\alpha = 0^\circ$, laminar boundary layer flow existed over major portions of the lee surface with axisymmetric-type flow in the nose section and two-dimensional type flow behind the shoulder. For $\alpha = 0^\circ$, the boundary layer was not separated, and the overall lee-surface heating level could be predicted approximately with laminar boundary layer theory. At large angles of attack turbulent boundary layer theory, with a shape factor of 1.8 - 1.9, predicted the heat transfer rates satisfactorily, especially for the case with high Reynolds number.
- 3) At $\alpha = 10^\circ$ and 20° , the boundary layer over the nose section varied from laminar to transitional then to turbulent as the Reynolds number increased. Separation of a free-vortex-layer type occurred after the shoulder on the leeward side. At larger angles of attack ($\alpha = 30^\circ, 40^\circ$), bubble-type separation, starting at a singular point, existed near the nose region and was immediately followed by a feather-like high heating region resulting from a reattachment created by vortex-surface interaction.
- 4) There were two distinct types of high heating rates on the lee-surface of the orbiter: peak heating due to boundary layer transition and peak heating associated with vortex interactions within a separated flow

region. The former appeared at relatively low angles of attack ($\alpha = 10^\circ, 20^\circ$), and the latter was observed at relatively large angles of attack ($\alpha = 20^\circ, 30^\circ, 40^\circ$). At $\alpha = 20^\circ$ both types of heating peaks appeared.

- 5) The peak heating due to boundary layer transition correlated with the free stream Reynolds number; the heating value increased rapidly with the Reynolds number. The maximum peak heating due to vortex-surface interactions (vortex-induced peak heating) occurred at $\alpha = 30^\circ$. The results showed no distinct variation with Reynolds number (Figs. 41, 42). This peak heating is lower than has been observed previously by other investigations.
- 6) A large axial component of velocity was measured in the separated flow region over the orbiter leeward surface. These results were obtained from measurements of static pressure, total pressure, and stagnation temperature. Pitot pressure measurements alone were not sufficient to deduce velocity profiles, since large pressure and temperature gradients exist normal to the surface.
- 7) Different flow fields over yawed cones were found at different ranges of angles of attack, each characterized by distinct and typical flow phenomena present on the leeward side. Two types of separation were found.

Free-vortex-layer separation with one pair of separation lines appeared at moderate angle of attack, and two pairs of separation lines (primary and secondary), with two vortex flow regions between separation lines, appeared at large angle of attack.

- 8) Flow field over a yawed blunt cone became conical after a length of $S/R \approx 20$. In the conical flow region, the separation patterns were similar to those of a sharp cone. Different flow phenomena, depending on the angle of attack, existed in the front part of a moderate blunt cone; free-vortex-type separation was found over the entire body surface at moderate angles of attack and bubble-type separation, which was not found by previous investigations, seemed to occur at high angle of attack.
- 9) A unique numerical analysis capable of capturing internal shocks, developed by Kutler et al., was modified and applied successfully to calculate the inviscid flow field over highly yawed circular cones. The pressure fields obtained by this method agreed very well with experimental results in the attached flow region up to the primary separation point with a small displacement effect of viscosity, while large discrepancies were present in the separated flow region of the leeward side.
- 10) Surface flow patterns on the rear portion of the orbiter configuration were found to be similar to those of a cone. This suggests that some of the

characteristics of orbiter leeward flow can be inferred from conical flow analysis. It was shown that the effect of vortex interaction on the pressure field of the orbiter can be evaluated by an inviscid analysis performed over an appropriate fictitious "equivalent body" surface which accounts for viscous effects. This equivalent body was obtained from pressure correlations and separation criteria obtained from previous experimental results. The height of the separation region is dictated by the leeward pressure obtained from the correlation curve of Fig. 100. Preliminary calculated results using this type of model for analyzing the flow field seemed to agree with the flow field measurements.

APPENDIX-SEPARATION PATTERNS OVER YAWED CONES

In order to clarify the phenomena associated with the separation pattern on the leeward side of the space shuttle, a simplified axially symmetric cone was tested, and oil flow patterns were taken for the same Mach number. The separation patterns on conical configurations have been studied recently by Wang, Ref. 13, and Maskell, Ref. 14. The separation patterns that are deduced from the following tests will be discussed in terms of the above references, and will be used as a first step in order to analyze the separation flow pattern over the space shuttle configuration. The tests were carried out in the same wind tunnel and for the same range of Reynolds number as the tests for the space shuttle.

Experiment

a) Models and Testing Conditions

Three models used in the experiments are shown in Figs. 12 and 13. These models consist of a common conical body, cone half angle of 7.5° , and three noses of different bluntness. Test conditions are tabulated in the following table:

MODEL	MEASUREMENTS	α	R_∞ (1/meter)
Sharp Cone	Oil Flow	$7.5^\circ \sim 22.5^\circ$	$(1.61 \sim 12.71) \times 10^7$
Blunt Cones $r_N/r_B = 0.12, 0.24$	Oil Flow	$7.5^\circ \sim 22.5^\circ$	$(11.51 \sim 13.05) \times 10^7$

with

$$M_\infty = 5.93$$

$$P_{O_\infty} = 1.38 \times 10^6 \sim 1.38 \times 10^7 \text{ Newton/m}^2$$

$$T_{O_\infty} = 450 - 500^\circ\text{K}$$

$$T_w/t_{O_\infty} = 0.6 \sim 0.7$$

Similar oil flow techniques used in the space shuttle experiments were employed again. Photographs of the oil flow patterns are given in Figs. 102-109. Peripheral locations of the separation lines, obtained from these experiments, are given in Figs. 110-116.

Discussions of the Oil Flow Patterns

a) Sharp Cone

At small angles of attack, $\alpha/\theta_c \leq 1.0$, Figs. 102 (a,b) and 103 (a), free vortex type separation occurs in the narrow region near the leeward

center line and its boundary is not clearly defined. Effect of free stream Reynolds number on leeward separation patterns is found insignificant. With large angle of attack, $\alpha/\theta_c = 1.33$, Fig. 103(b), the separation region becomes broader and one pair of symmetric separation lines appear. A vortex flow, with a reattachment line coincides with the centerline, exists between these two separation lines. The peripheral locations of the separation lines vary from 150° to 160° off the windward centerline. These separation patterns agree with existing typical separation patterns for a sharp cone at moderate angle of attack in a hypersonic flow.

As the angle of attack increases further, completely different separation patterns with two pairs of separation lines occur. The primary separation line is always located at $\varphi = 135^\circ$ and the secondary line is at $\varphi = 165^\circ$. Between these two pairs of separation lines, there exists two vortex flow regions with reattachment lines: one at the leeward centerline and the other two located between the primary and secondary separation lines. Examples are shown in Figs. 104 and 105. Figures 102-105 also show that surface flow over a sharp circular cone is conical except for a tiny region near the tip.

Present results of the peripheral locations of the separation lines are compared with existing results in Figs. 110-111. For small angle of attack, $\alpha/\theta_c \leq 1.5$, present results follow the trend of Stetson's results, Ref. 16 and 17. For large angle of attack, $\alpha/\theta_c > 1.5$, present results agree with those of Feldhuhn's and Rainbird's investigations, Refs. 19 and 20, despite the fact that tests were conducted with different free stream conditions.

b) Blunt Nose Cones

As shown in Figs. 106-108, surface flow becomes conical after a certain distance from the nose where three-dimensional effect of the bluntness is predominant. The separation patterns are similar to that of a sharp cone in the conical flow region. One pair of separation lines occur at moderate angle of attack, $\alpha/\theta_c < 1.33$. At large angle of attack, two pairs of separation lines appear. For both cases, reattachment lines exist between the separation lines. The separation pattern in this conical flow region is a free vortex layer type.

In the front part of the body where three-dimensional effects prevail, different features exist, depending on the angle of attack. For $\alpha/\theta_c < 1.5$, in Fig. 106, singular point does not exist and free vortex layer type separation appears over the entire body surface. When the angle of attack increases, surface flow pattern starts to change from a free vortex layer type to a bubble type separation with two pairs of separation lines. At even higher angles of attack, $\alpha/\theta_c \geq 2.0$, complete separation region is enlarged and may easily be observed showing a singular point at the beginning of separation region, Figs. 107(b)-108. This surface flow pattern is magnified and is presented in Fig. 109.

In Figs. 112-116, results of the blunt nosed cone are compared with those of sharp cone experiments. They agree well with the exception to a certain length from the nose tip where conical flow does not exist. The distance, necessary for establishing for a conical flow, depends on the bluntness, angle of attack, and free stream conditions. This distance is shorter for larger angle of attack, α/θ_c . From present results, flow becomes conical

after 20 to 30 nose radii for $\alpha/\theta_c \geq 2$, and 40 to 50 nose radii for $\alpha/\theta_c < 2$. Stetson, Refs. 16 and 17, measured surface pressure over sharp and blunt nose cones with cone half angle of 5.6° and obtained the distance to return to an equivalent sharp cone pressure distribution varying from 88 nose radii at $\alpha/\theta_c = 0.9$ to 35 nose radii at $\alpha/\theta_c = 3.0$ for laminar flow conditions.

Flow Field Models

Based on the present experiments, two basic flow field models over yawed cones, depending on the angle of attack, have been determined. At moderate angle of attack, $\alpha/\theta_c < 1.5$, separation occurs and one pair of separation lines appears at $\varphi = 150^\circ - 165^\circ$. An example is given in Fig. 117. At large angle of attack, $\alpha/\theta_c \geq 1.5$, two pairs of separation lines appear. The peripheral locations of these separation lines are stable and independent of the free stream Reynolds number. An example is shown in Fig. 118.

The criterion of transition from moderate to large angle of attack is determined by an internal shock which appears when the cross flow becomes supersonic. The relative incidence of transition, in terms of α/θ_c , is approximately 1.5 from the present experiment. An inviscid flow calculation, described later, shows that the cross flow Mach number becomes larger than 1.0 at $\alpha/\theta_c = 1.1 \sim 1.3$ for a cone in a hypersonic flow. This condition corresponds to the appearance of a very weak shock, strong enough to produce a primary separation. This is found to be in good agreement with experiment. Based on the above discussion and the present experiments, the flow field over a yawed cone can be divided into three main categories, each characterized by distinct flow phenomena present on the leeward surface. These and possible methods of predicting the fluid flow properties in each region are

presented in the following:

a) Small Angle of Attack, $0 \leq \alpha/\theta_c \leq 1.0$

There is no separation throughout the flow field and the inviscid flow theory predicts the pressure distribution accurately. Boundary layer approximation can be used to analyze the flow field along the leeward surface with the aid of inviscid theory to provide the boundary conditions.

b) Moderate Angle of Attack, $1.0 \leq \alpha/\theta_c \leq 1.5$

Vortex layer type separation, with one pair of separation lines, appears on the leeward surface. Due to the absence of the internal shock and relative small vortex region on the leeward surface, inviscid flow theory predicts the pressure distributions satisfactorily. Boundary layer approximation is valid up to the point of separation.

c) High Angle of Attack, $\alpha/\theta_c > 1.5$

An internal shock occurs in the flow field. The primary separation is caused by this internal shock and two pairs of separation lines appear. The vortex region, associated with separation on the leeward surface, is large and the inviscid flow theory fails to predict the actual flow field. However, the pressure field of the vortex region near the leeward surface can be evaluated by an inviscid theory if an equivalent body accounts properly for the separated region.

Comparison of Present Results of Separation with Other Work

Based on present experiments, two flow field models over a yawed cone have been found from the separation patterns due to different angles of attack. Marciilat and Roux, Ref. 18, showed theoretically that separation starts at a relative incidence of $\alpha/\theta_c = 0.87$. Tracy, Ref. 19, observed

large effects of Reynolds numbers on the development of flow field at $\alpha/\theta_c \geq 0.8$. Stetson, Refs. 16 and 17, found the incipient separation occurs at $\alpha/\theta_c = 0.7$. Rainbird, Ref. 19, chose a value of $\alpha/\theta_c \leq 0.7$ as the criterion of small incidence. Present experiments show that a single pair of separation lines appears on the leeward surface at $\alpha/\theta_c = 1.0$. These results have been obtained from different flow conditions. Therefore, the present results of Fig. 117 can be applied to a cone at moderate angle of attack, $0.7 \leq \alpha/\theta_c \leq 1.5$.

For the present test conditions, the relative incidence of transition from the single separation line to the double separation pattern was found approximately at $\alpha/\theta_c = 1.5$ and agrees with the results obtained by Marcillat and Roux, Ref. 18. At $\alpha/\theta_c = 1.2 \sim 1.5$, an internal shock occurs and produce a primary separation line at $\phi = 125^\circ$. Marcillat and Roux, Ref. 18, also found that inviscid flow theory fails to predict the actual flowfield under this condition. According to Jones, Ref. 36, failure of the calculation by an inviscid theory occurs when the entropy singularity lifts off the leeward surface. The appearance of the internal shock might be related to the lift off of the vortex from the surface. It is also interesting to note that the two-proposed models, Figs. 117-118, are compatible with Maskell's models.

Comparisons of oil flow studies on yawed cones, Figs. 102-105 and Figs. 110-112 with those on a space-shuttle model, Figs. 44-56, show that the surface flow patterns are similar at large angle of attack. This suggests that the general trend of leeward flow field on a space-shuttle type body can be inferred from conical flow analysis far back on the body.

Numerical Analysis

Previous analyses on circular cones are applicable to cones at small and moderate angles of attack. At large angle of attack, the inviscid flow theory fails to describe the actual flow phenomena due to the appearance of an internal shock followed by a region of large separated flow.

Recently Kutler et al., Ref. 22, developed a quite unique numerical method which is capable of determining multi-shocked, three-dimensional supersonic flowfields. The restriction of this method is that the local flow along the body axis (x) extending downstream has to be supersonic, which is satisfied for hypersonic vehicles such as a space shuttle at most flight conditions of current interest. Starting from given initial values over a blunt nose, the governing equations in conservation-law form are solved by a finite difference method of a second-order noncentered algorithm between the body surface and the external shock wave. The external shock, which bounds the disturbed region, is treated as a discontinuity, whereas the secondary shocks within the disturbed region, if any, are captured automatically. Numerical calculations of this method were in good agreement with experimental results. Examples include a space shuttle configuration (the inclination angle of the leeward nose part is about 20°) at $\alpha = 15.3^\circ$ and a sharp cone ($\theta_c = 15^\circ$) in hypersonic flows, Ref. 22. The flowfield either over a space shuttle orbiter or over a sharp cone at large angles of attack has never been analyzed by utilizing this method.

In the present analysis, the authors decoded and modified the original program for the flowfield calculation of highly yawed cones. The initial value or starting solution could be anything since the final steady state solution is obtained asymptotically as the calculation marches along the

body axis (x). In the present calculations, the cone solution at zero angle of attack has been chosen as the initial value. The circumferential angle between $\varphi = 0^\circ$ and $\varphi = 180^\circ$ was divided into 18 or 36 intervals, whereas 5 or 10 divisions were used in the radial direction between the body surface and the external shock. Calculation steps to ensure the convergence to the final solution depends on the mesh size chosen and flow conditions (M_∞ , α , θ_c), but typical steps were about 100 to 400 with reasonably short computer time. Two examples for which experimental data are available are compared with present numerical results.

a) Examples

The first example is the experiment by Tracy, Ref. 15, on a circular cone of 10° cone half-angle at Mach 7.87. Circumferential pressure distributions obtained by the present numerical analysis for $\alpha = 10^\circ$, 16° , 20° , and 24° , are shown in Figs. 119-122 and are compared with experiments. As can be seen in these figures, the inviscid surface pressure is lower than the measured value due to the displacement effect of viscosity. The magnitude of this effect appears to be relatively small up to $\varphi \approx 120^\circ$, beyond which it becomes larger, indicating a large viscous or vortex region present on the leeward surface. It is noted here that the boundary layer flow over the cone surface before the separation is laminar for these test conditions. All the cases calculated here ($\alpha/\theta_c = 1.0 - 2.4$) show that the general trend of inviscid surface pressure distribution is quite similar to that of actual flow.

Figure 123 shows inviscid cross-flow Mach number distributions. From this figure it is observed that the cross flow becomes supersonic for $\alpha > 10^\circ$,

thereby producing an internal shock at $\varphi \approx 160^\circ$. The inviscid external shock locations are presented and compared with experimental results in Fig. 124. These results are in good agreement.

The second example corresponds to experiments by McElderry, Ref. 21, on a circular cone with $\theta_c = 6^\circ$ and $M_\infty = 6$. For their test conditions, Reynolds numbers were high enough to keep the entire boundary layer flow over the surface turbulent (before separation). Circumferential pressure distributions obtained from numerical methods are shown in Figs. 125-127 and compared with experimental results. At $\alpha = 6^\circ$ ($\alpha/\theta_c = 1.0$), the inviscid analysis agrees with experiments, Fig. 125. Displacement effect due to viscosity is smaller than the previous example (Tracy's laminar case). For large angles of attack ($\alpha = 9^\circ, 12^\circ$; $\alpha/\theta_c = 1.5, 2.0$), the discrepancies between the present inviscid flow analysis and experimental results become significant in the separated flow region ($\varphi > 125^\circ$) where strong vortex-surface interactions exist.

The inviscid cross-flow Mach number distributions are shown in Fig. 128. An internal shock occurs for $\alpha/\theta_c \geq 1.5$, but its location is different from the location inferred from the surface pressure of the experimental result. Locations of the external shock obtained from the numerical method are given in Fig. 129.

The feasibility of applying the numerical method developed by Kutler et al. to the inviscid flow calculation over highly yawed cones and finally to the space shuttle has been shown, thereby handling internal shocks successfully. On the other hand, large discrepancies between actual flow phenomenon and inviscid analysis have been recognized in the separated flow region where the strong vortex interactions exist. If this effect due

to viscosity or vortex interactions near the leeward surface is properly accounted for, this numerical method will be capable of analyzing a complicated leeward flowfield over highly yawed cones in hypersonic flows.

b) Corrections for Viscous Displacement Effects

It was shown in the previous section that there is a viscous displacement effect for a highly yawed cone in hypersonic flows. This effect is relatively small for small angle of attack which can account for large discrepancies in the surface pressure distributions between theory and experiment. However, for large angle of attack, the separated flow region on the leeward surface becomes significant due to vortex interactions. Therefore, the inviscid flow analysis cannot be applied to this region directly unless some corrections for this viscous effect on the pressure field are made.

According to Rainbird, Ref. 19, it is appropriate to use the "near" surface (rather than the isentropic surface) values of the inviscid flow solutions as the external conditions for boundary layer calculations. The above suggestion by Rainbird, applied to the attached boundary layer flow, is extended here to determine the "near" surface conditions in a separated flow region. For simplicity, the "near" surface is defined as the fictitious surface which will give the same pressure distribution as the experiments. This corresponds to finding the viscous displacement effect in a separated flow region.

To examine the above idea, a sample calculation has been carried out in Ref. 37, on a yawed circular cone corresponding to one of the McElderry's experiments ($M_\infty = 6$, $\theta_c = 6^\circ$, $\alpha = 9^\circ$; Ref. 21). The above mentioned numerical analysis of inviscid flow was applied to find the best possible, but simple surface contour which produces the experimental surface pressure distribution.

After several trial-and-error calculations a circular-elliptical cone connected at $\varphi = 127^\circ$ was found to give practically the desired pressure distribution, where the major axis of the ellipse is 1.14 compared to the radius of circle of 1.0. The calculated pressure distribution is presented in Fig. 130, along with the numerical solution for a circular cone and experimental data. The change in pressure due to this small modification of the surface contour is seen to be significant; the surface pressure distribution calculated over the modified cone is in good agreement with the experimental pressure distribution on the original circular cone. Figure 131 shows the cross-flow Mach number distributions for circular and modified cones as well as the change of the body radius in the circumferential direction, $\partial r_B / \partial \varphi$. Due to the abrupt change in the surface inclination in the φ direction ($\partial r_B / \partial \varphi$), the internal shock occurs at $\varphi = 125^\circ$, corresponding to the location of the primary separation obtained in experiments on the circular cone. Therefore, the inviscid surface flow over the present modified cone is found to represent fairly well the actual surface flow involving separation on the circular cone. However, a small pressure change at the secondary separation point ($\varphi \approx 165^\circ$) for the actual circular cone flow was not realized by this modified cone.

From the above sample calculation, it is found that the effect of vortex interactions on the pressure field in a separated flow region over a highly yawed cone can be evaluated by an inviscid flow analysis if an appropriate fictitious surface (near surface) is found corresponding to the actual surface pressure distribution on the circular cone. The surface flow calculated by an inviscid flow analysis over this fictitious cone described fairly well the actual surface flow phenomena on the original circular cone.

Therefore, it is concluded that a good inviscid flow analysis (as the one employed here), corrected for the viscous displacement effect, offers a powerful means in calculating conical flow involving separation. Such a method has been presented by the senior author in detail in Ref. 37 for a sharp conical body.

REFERENCES

1. Chang, P.K., "Separation of Flow," Pergamon Press, Inc., 1970.
2. Holloway, P.F., Sterrett, J.R., and Creekmore, H.S., "An Investigation of Heat Transfer Within Regions of Separated Flow at a Mach Number of 6.0," NASA TN D-3074, 1965.
3. Whitehead, A.H., Jr. and Keyes, J.W., "Flow Phenomena and Separation over Delta Wings with Trailing-Edge Flaps at Mach 6," AIAA Journal, Vol. 6, No. 12, Dec. 1968, pp. 2380-2387.
4. Whitehead, A.H., Jr., "Effect of Vortices on Delta Wing Lee-Side Heating at Mach 6," AIAA Journal, Vol. 8, No. 3, March 1970, pp. 599-600.
5. Whitehead, A.H., Jr. and Bertram, M.H., "Alleviation of Vortex-Induced Heating to the Lee Side of Slender Wings in Hypersonic Flow," AIAA Journal, Vol. 9, No. 9, September 1971, pp. 1870-1872.
6. Rao, D.M., "Hypersonic Lee-Surface Heating Alleviation on Delta Wing by Apex-Drooping," AIAA Journal, Vol. 9, Sept. 1971, pp. 1875-1876.
7. Whitehead, A.H., Jr., Hefner, J.N., and Rao, D.M., "Lee-Surface Vortex Effects over Configurations in Hypersonic Flow," AIAA Paper No. 72-77, 1972.
8. Hefner, J.N. and Whitehead, A.H., Jr., "Lee-Side Heating Investigations, Part I - Experimental Lee-Side Heating Studies on a Delta-Wing Orbiter," NASA Space Shuttle Technology Conference, Vol. I, NASA TM X-2272, 1971, pp. 267-287.

9. Hefner, J.N. and Whitehead, A.H., Jr., "Lee-Side Flow Phenomena on Space Shuttle Configurations at Hypersonic Speeds, Part II - Studies of Lee-Surface Heating At Hypersonic Mach Numbers," Space Shuttle Aero-Thermodynamics Technology Conference, Vol. II, NASA TM X-2507, 1972, pp. 451-467.
10. Hefner, J.N., "Lee-Surface Heating and Flow Phenomena on Space Shuttle Orbiters at Large Angles of Attack and Hypersonic Speeds," NASA TN D-7088, 1972.
11. Bertin, J.J. et al., "The Effect of Nose Geometry on the Aerothermodynamic Environment of Shuttle Entry Configurations," Texas University at Austin, Aerospace Engineering Report No. 73001, 1973.
12. Rosenhead, L. (Editor), "Laminar Boundary Layers," Oxford, at the Clarendon Press, 1963.
13. Wang, K.C., "Separation Patterns of Boundary Layer over an Inclined Body of Revolution," AIAA Paper No. 71-130, 1971. (Also, AIAA Journal, Vol. 10, No. 8, August 1972, pp. 1044-1050.)
14. Maskell, E.C., "Flow Separation in Three Dimensions," RAE Report Aero. 2565, 1955.
15. Tracy, R.R., "Hypersonic Flow over a Yawed Circular Cone," GALCIT Hypersonic Research Project Memorandum, No. 69, 1963.
16. Stetson, K.F., "Boundary-Layer Separation on Slender Cones at Angle of Attack," AIAA Journal, Vol. 10, No. 5, May 1972, pp. 642-648.

17. Stetson, K.F., "Experimental Results of Laminar Boundary Layer Separation on a Slender Cone at Angle of Attack at $M_{\infty} = 14.2$," ARL 71-0127, August 1971, Aerospace Research Labs., Wright-Patterson Air Force Base, Ohio.
18. Marcillat, J. and Rous, B., "Experimental and Theoretical Study of Supersonic Viscous Flow over a Yawed Circular Cone," AIAA Journal, Vol. 10, No. 12, December 1972, pp. 1625-1630.
19. Rainbird, W.J., "Turbulent Boundary-Layer Growth and Separation on a Yawed Cone," AIAA Journal, Vol. 6, No. 12, December 1968, pp. 2410-2416.
20. Feldhuhn, R.H., Winkelmann, A.E., and Pasiuk, L., "An Experimental Investigation of the Flow Field Around a Yawed Cone," AIAA Paper No. 70-766, 1970.
21. McElderry, E.D., Unpublished Data, 1972, Aerospace Research Labs., Wright-Patterson Air Force Base, Ohio.
22. Kutler, P., Reinhardt, W.A. and Warming, R.F., "Numerical Computation of Multishocked, Three-Dimensional Supersonic Flow Fields with Real Gas Effects," AIAA Paper No. 72-702, 1972.
23. Kutler, P., Warming, R.F., and Lomax, H., "Computation of Space Shuttle Flowfields Using Noncentered Finite-Difference Schemes," AIAA Journal, Vol. 11, No. 2, February 1973, pp. 196-204.
24. Warming, R.F., Kutler, P., and Lomax, H., "Second-and-Third-Order Noncentered Difference Schemes for Nonlinear Hyperbolic Equations," AIAA Journal, Vol. 11, No. 2, February 1973, pp.189-196.

25. Zakkay, V., Miyazawa, M., and De Simone, G., "Reynolds Number and Mach Number Effect on Space Shuttle Configuration," Final Report of NASA Grant, New York University, September 1972.
26. Love, E.S., "Advanced Technology and the Space Shuttle," The Tenth Von Karman Lecture, Astronautics and Aeronautics, February, 1973, pp. 30-66.
27. Lees, L., "Laminar Heat Transfer over Blunt-Nosed Bodies at Hypersonic Flight Speeds," Jet Propulsion, Vol. 26, No. 4, April 1956, pp. 259-269.
28. Sims, J.L., "Tables for Supersonic Flow Around Right Circular Cones at Zero Angle of Attack," NASA SP-3004, 1964.
29. Fay, J.A. and Riddell, F.R., "Theory of Stagnation Point Heat Transfer in Dissociated Air," Journal of the Aeronautical Sciences, Vol. 25, No. 2, February 1958, pp. 73-85, 121.
30. Eckert, E.R.G. and Tewfik, O.E., "Use of Reference Enthalpy in Specifying the Laminar Heat-Transfer Distribution Around Blunt Bodies in Dissociated Air," Journal of the Aero/Space Sciences, Vol. 27, No. 6, June 1960, pp. 464-466.
31. Reshotko, E. and Tucker, M., "Approximate Calculation of the Compressible Turbulent Boundary Layer with Heat Transfer and Arbitrary Pressure Gradient," NACA TN-4154, 1957.
32. Eckert, E.R.G., "Engineering Relations for Friction and Heat Transfer to Surfaces in High Velocity Flow," Journal of the Aeronautical Sciences, Vol. 22, No. 8, August 1955, pp. 585-587.

33. Cleary, J.W., "Lee-Side Flow Phenomena on Space Shuttle Configuration at Hypersonic Speeds," NASA TM X-2507, 1972.
34. Zakkay, V., Calarese, W., and Wang, C.R., "Hypersonic Turbulent Boundary Layer with Pressure Gradients and Cross Flow," Synoptic, AIAA J., 10, 1972, pp. 1392-1394.
35. Schlichting, H., "Boundary Layer Theory," Fourth Edition, McGraw-Hill Co., pp. 570-571.
36. Jones, D.J., "Numerical Solutions of the Flow Field for Conical Bodies in a Supersonic Stream," Aeronautical Report LR-507, July 1968, National Research Council of Canada, Ottawa, Canada.
37. Zakkay, V., Economos, C., and Alzner, E., "Leeside Flow Field Description over Cones at Large Incidence," AFFDL-TR-74-19, Advanced Technology Laboratories, Inc.

PRECEDING PAGE BLANK NOT FILMED

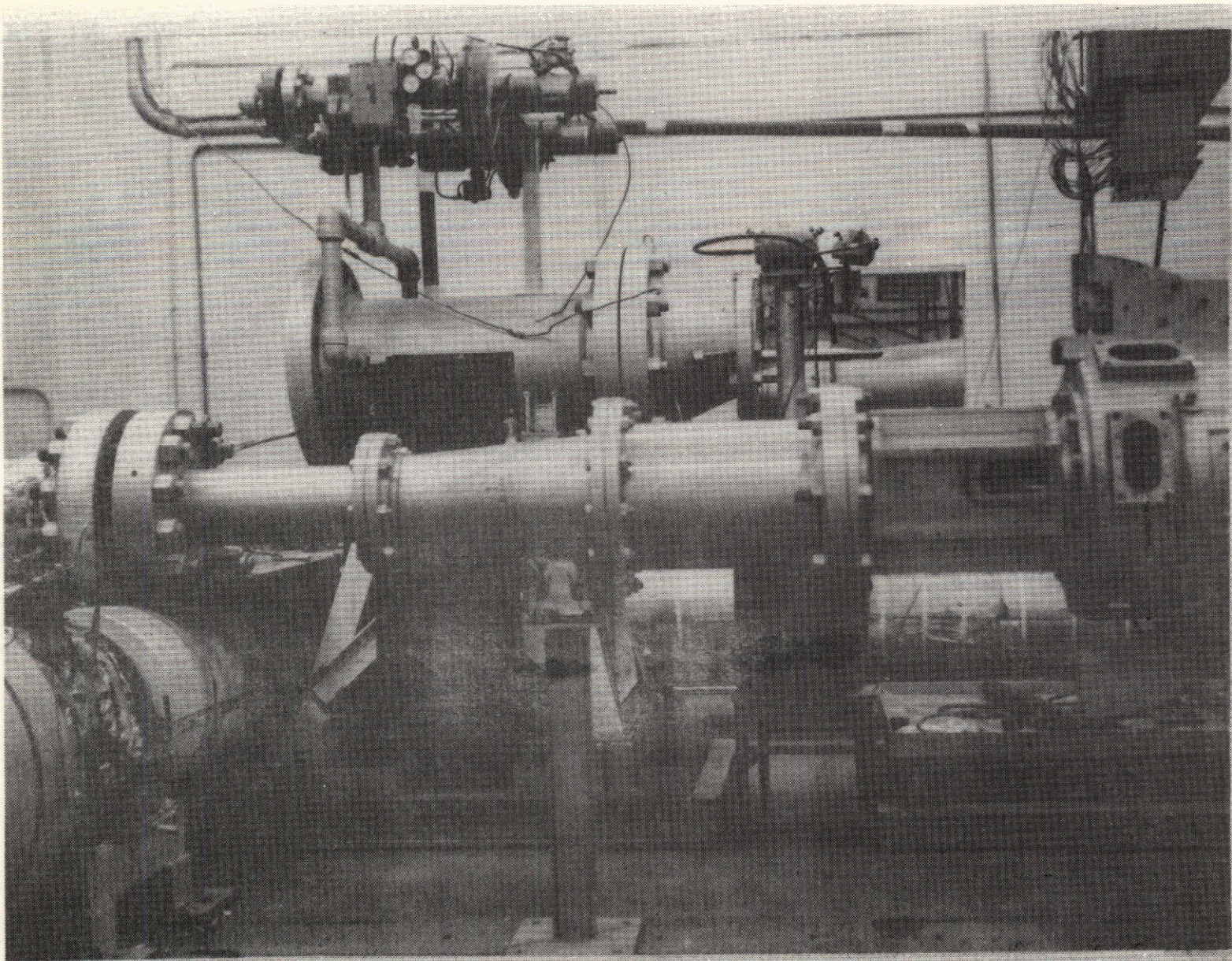
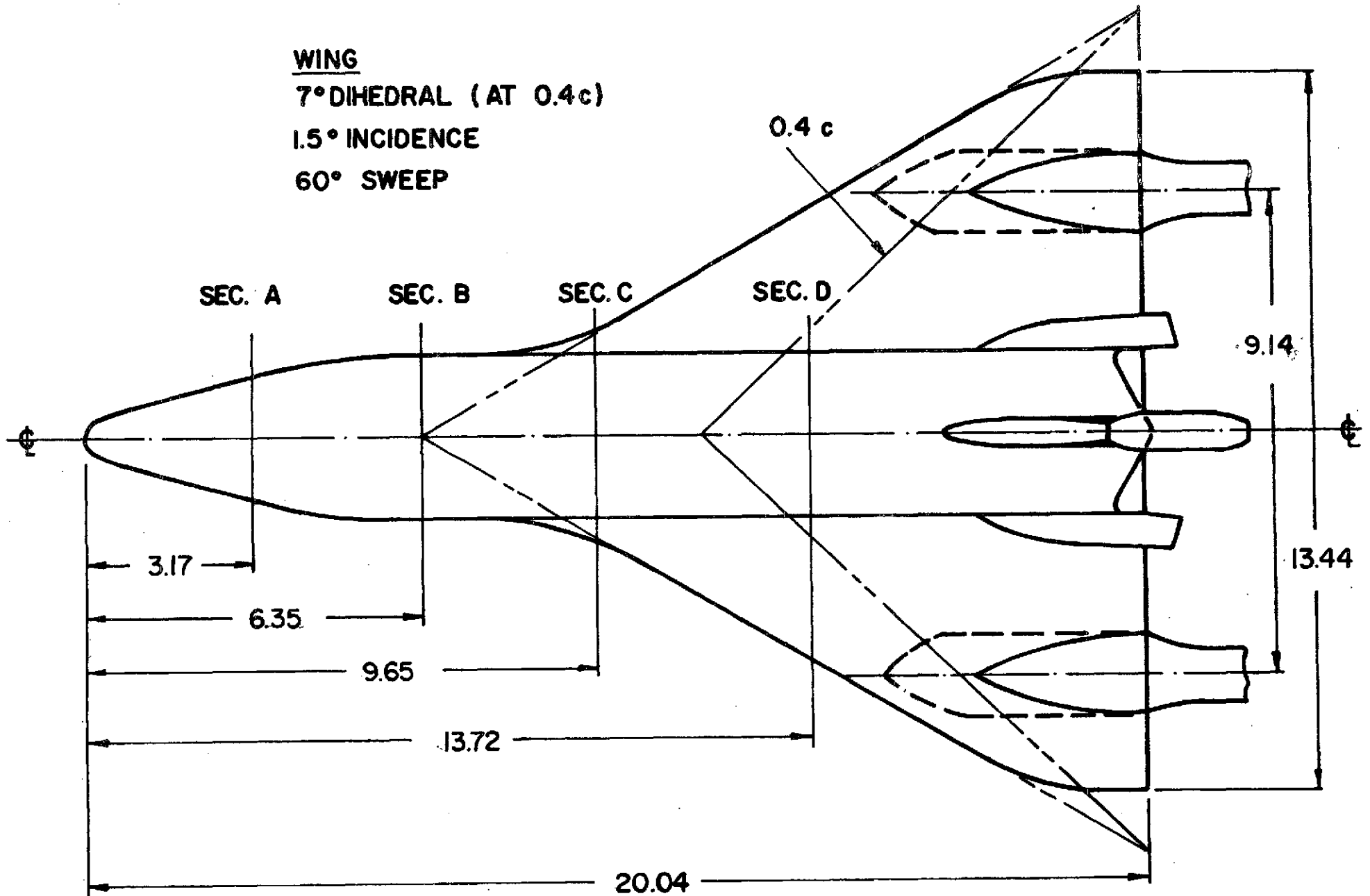


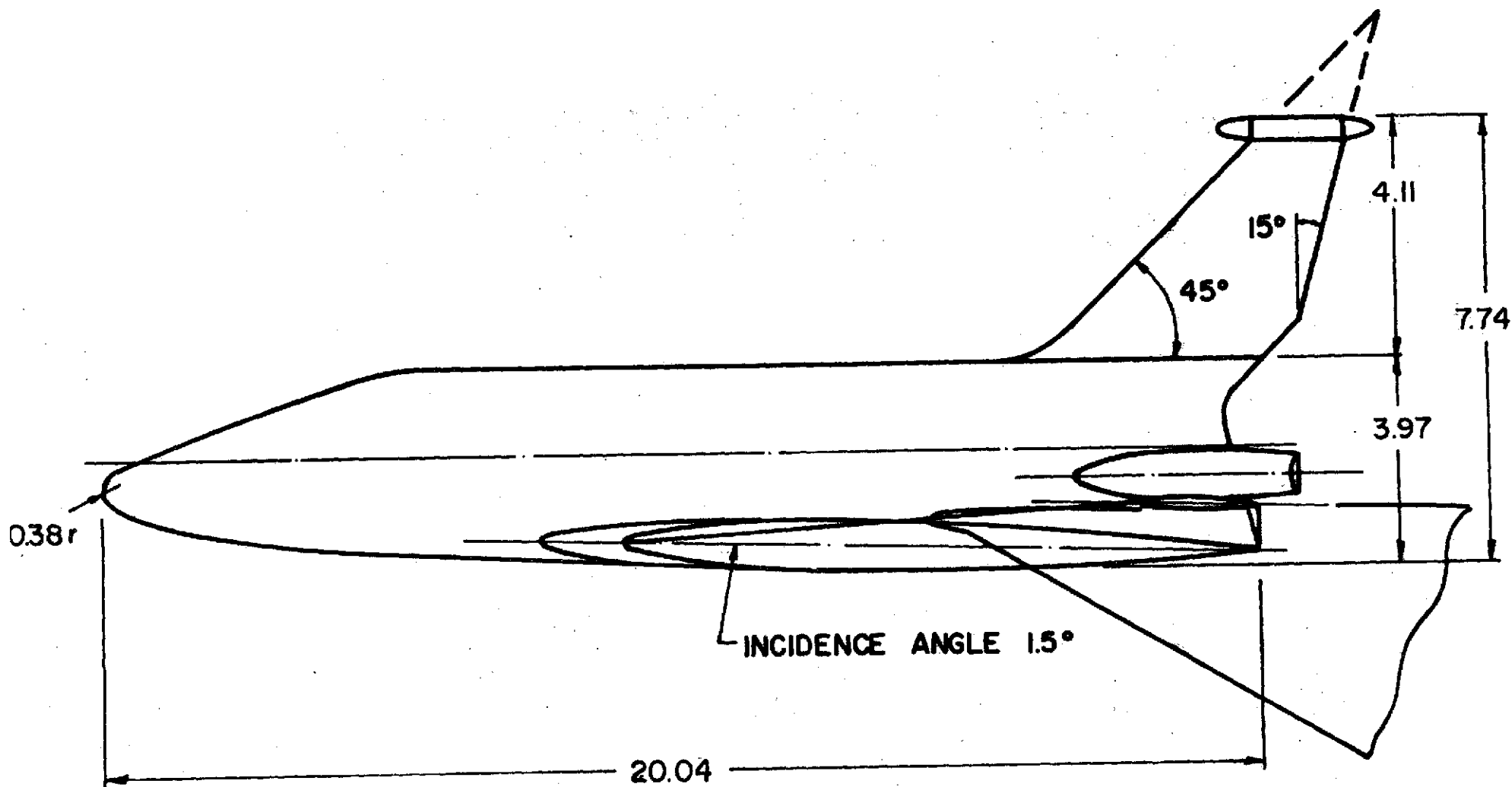
Fig. 1 Photograph of Wind Tunnel

WING
7° DIHEDRAL (AT 0.4c)
1.5° INCIDENCE
60° SWEEP



DIMENSIONS IN CM.

Fig. 2 Space Shuttle Model Configuration (Top View)



DIMENSIONS IN CM.

Fig. 3 Space Shuttle Model Configuration (Side View)

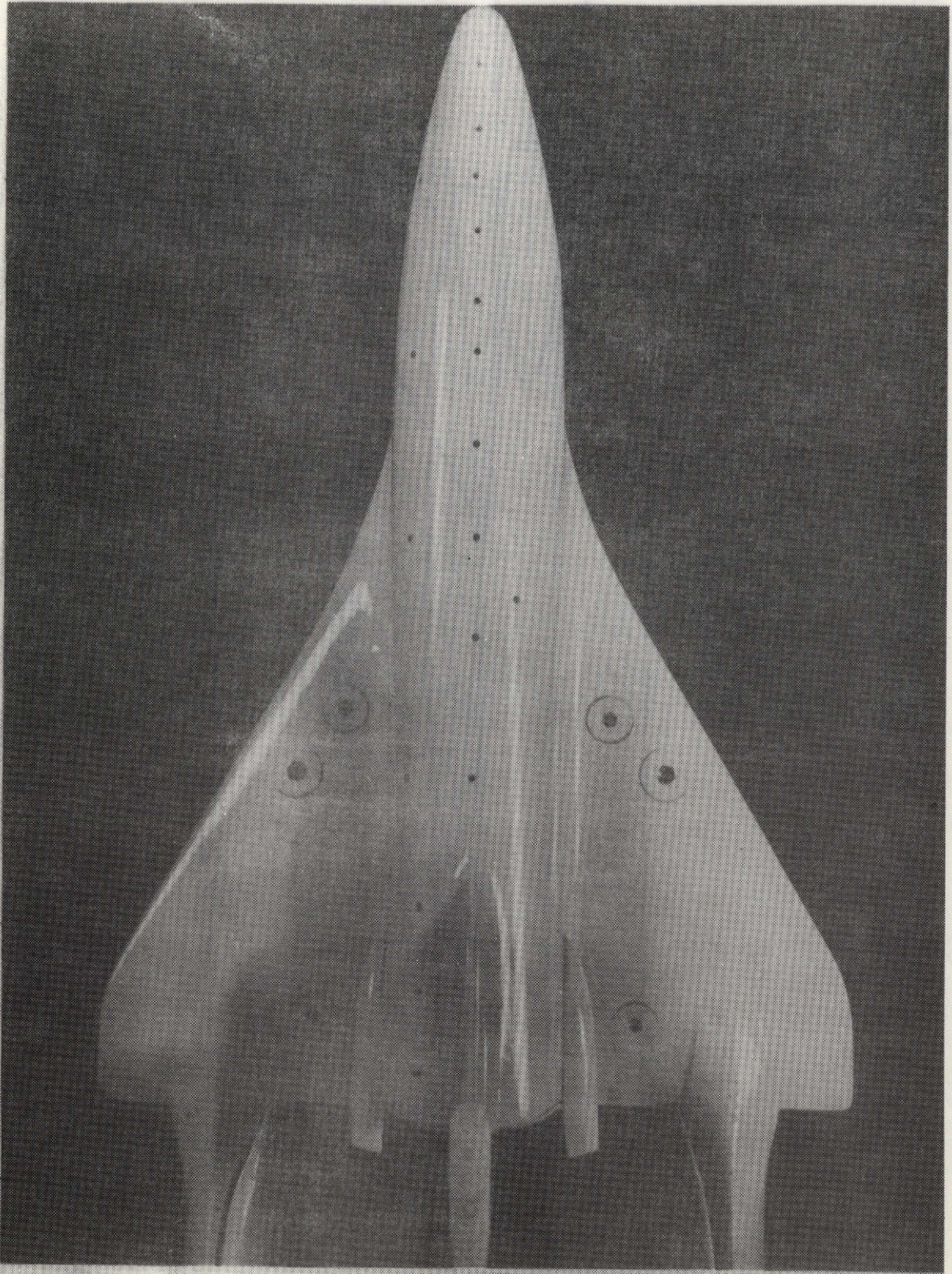


Fig. 4 Photograph of Pressure Model (Top View)

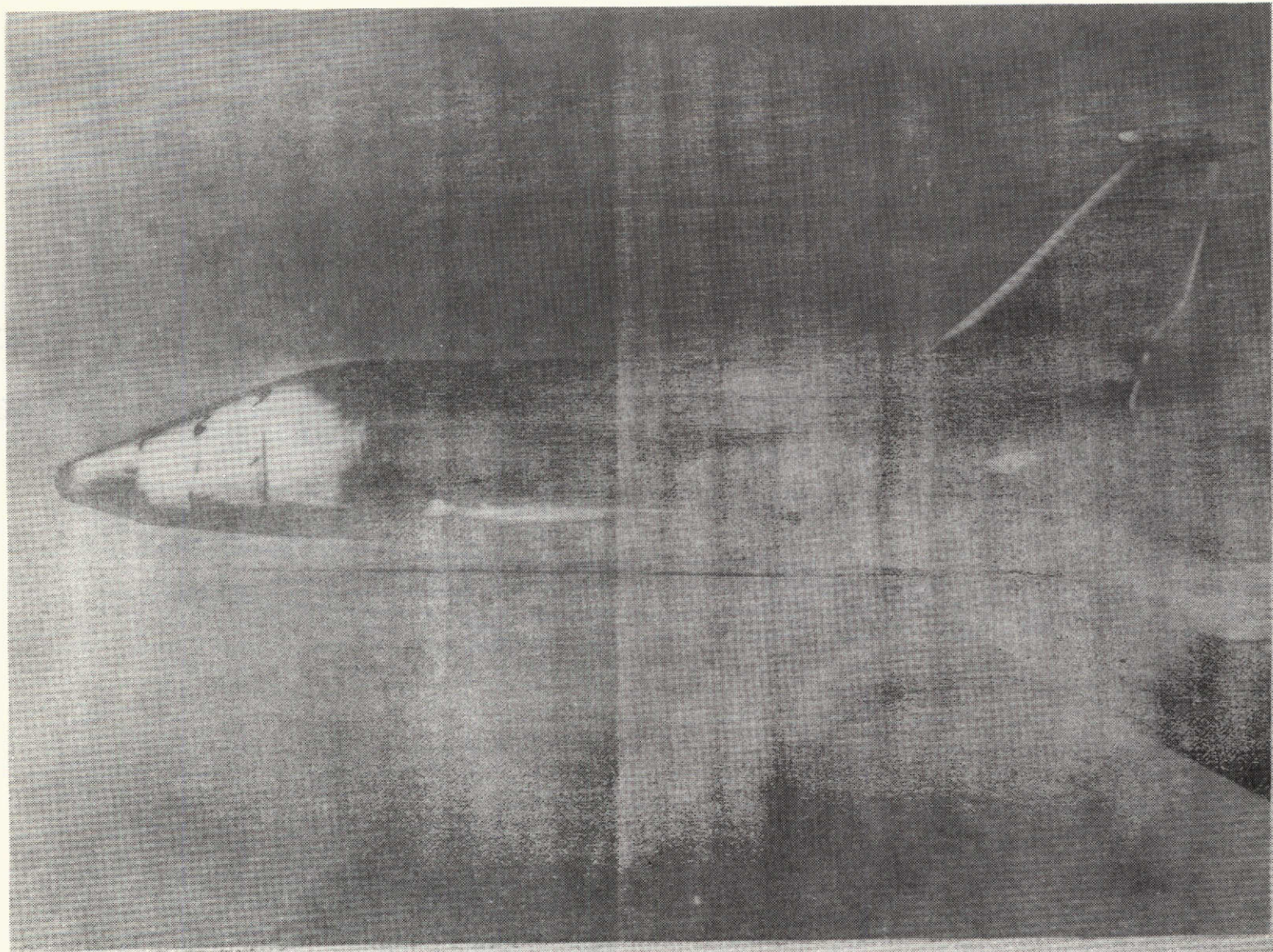
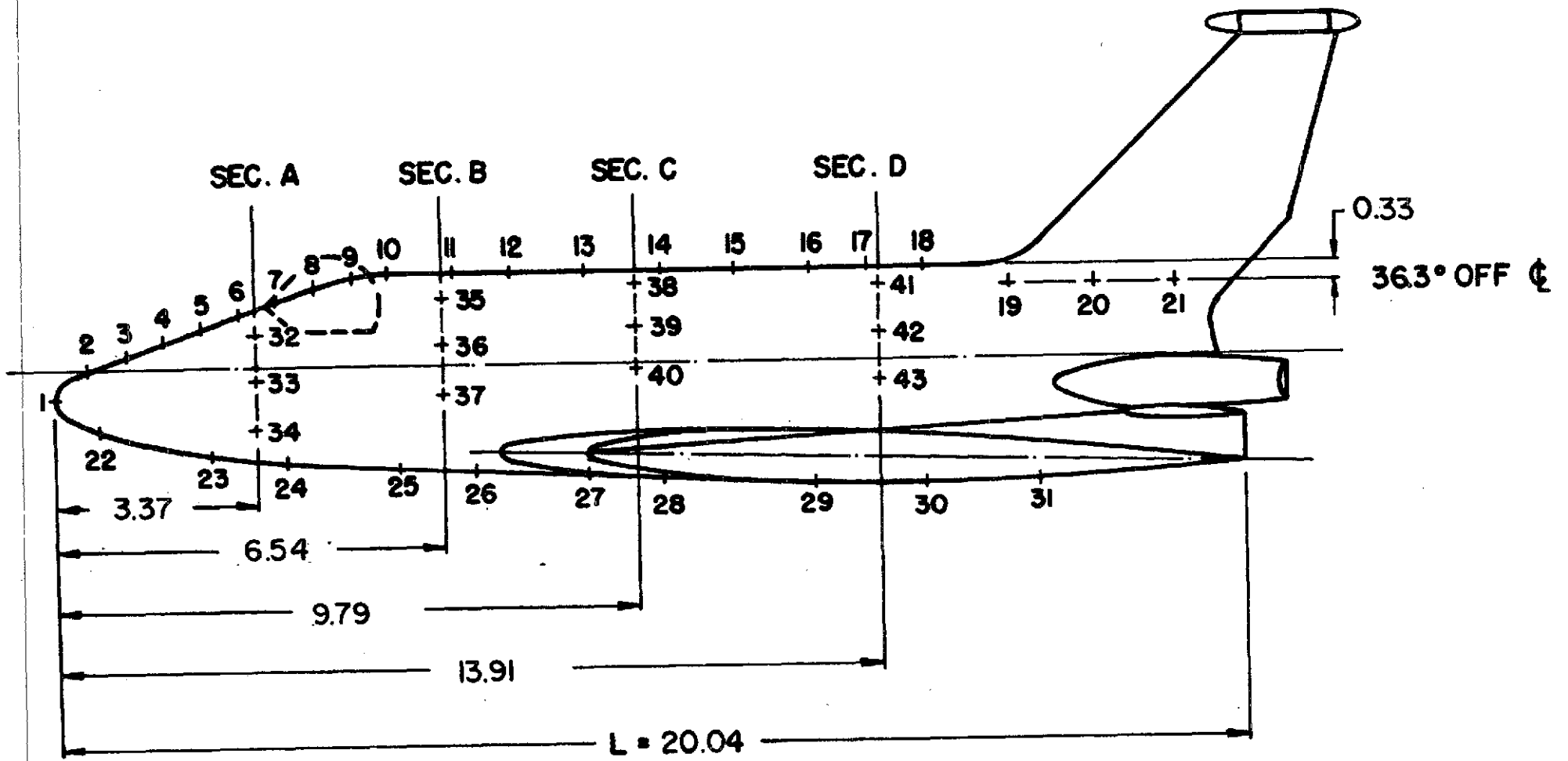


Fig. 5 Photograph of Heat Transfer Model (Side View)



DIMENSIONS IN CM.

Fig. 6 Thermocouple Locations

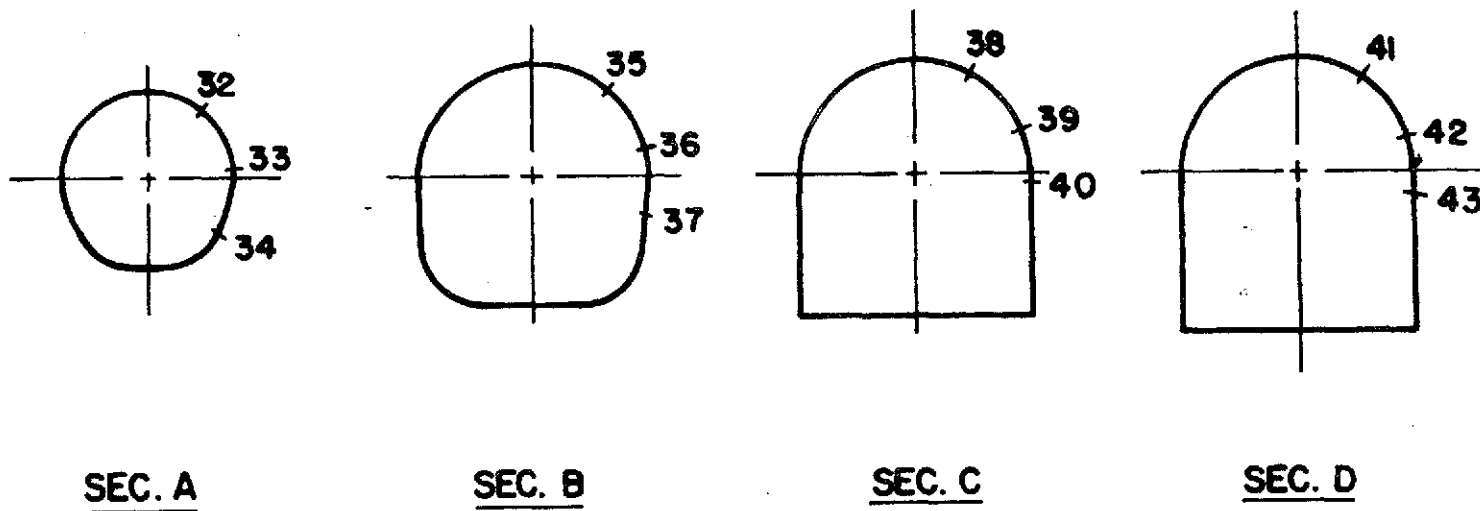


Fig. 7 Circumferential Locations of Thermocouples

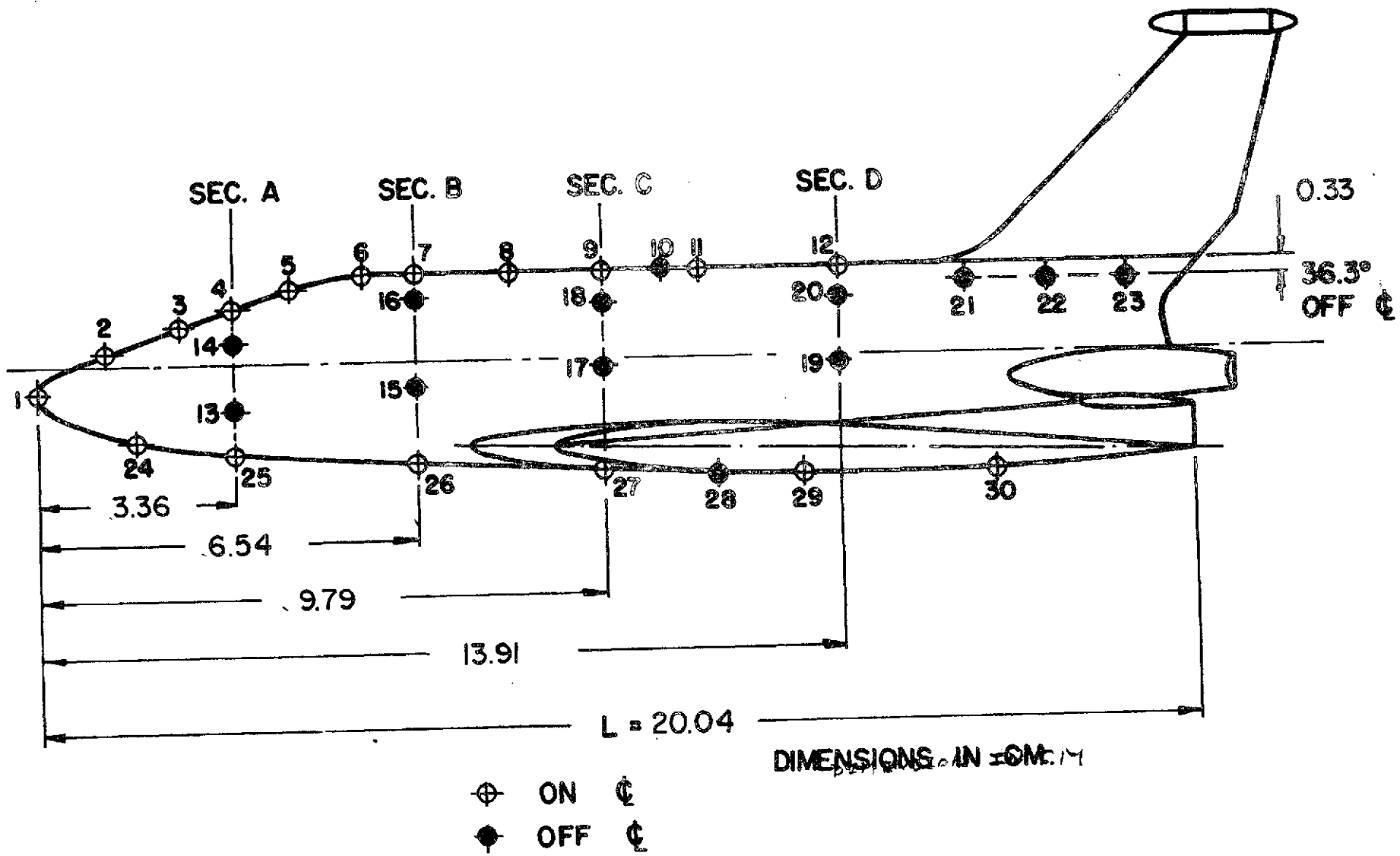


Fig. 8 Pressure Tap Locations

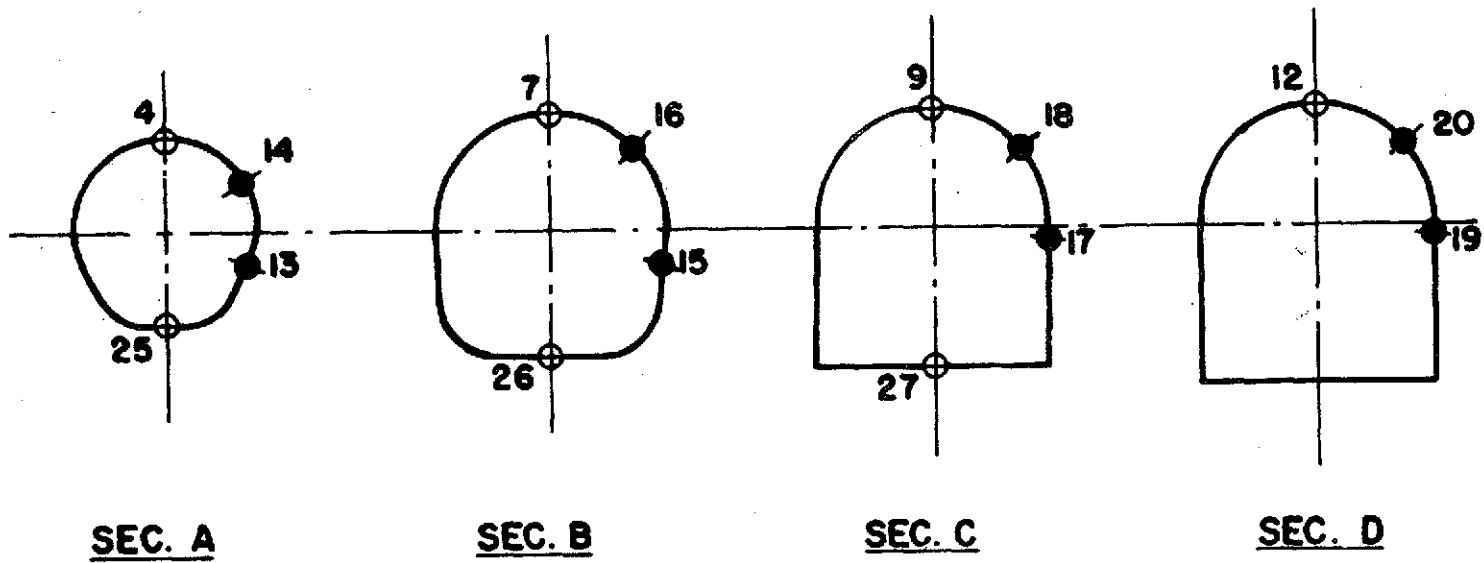
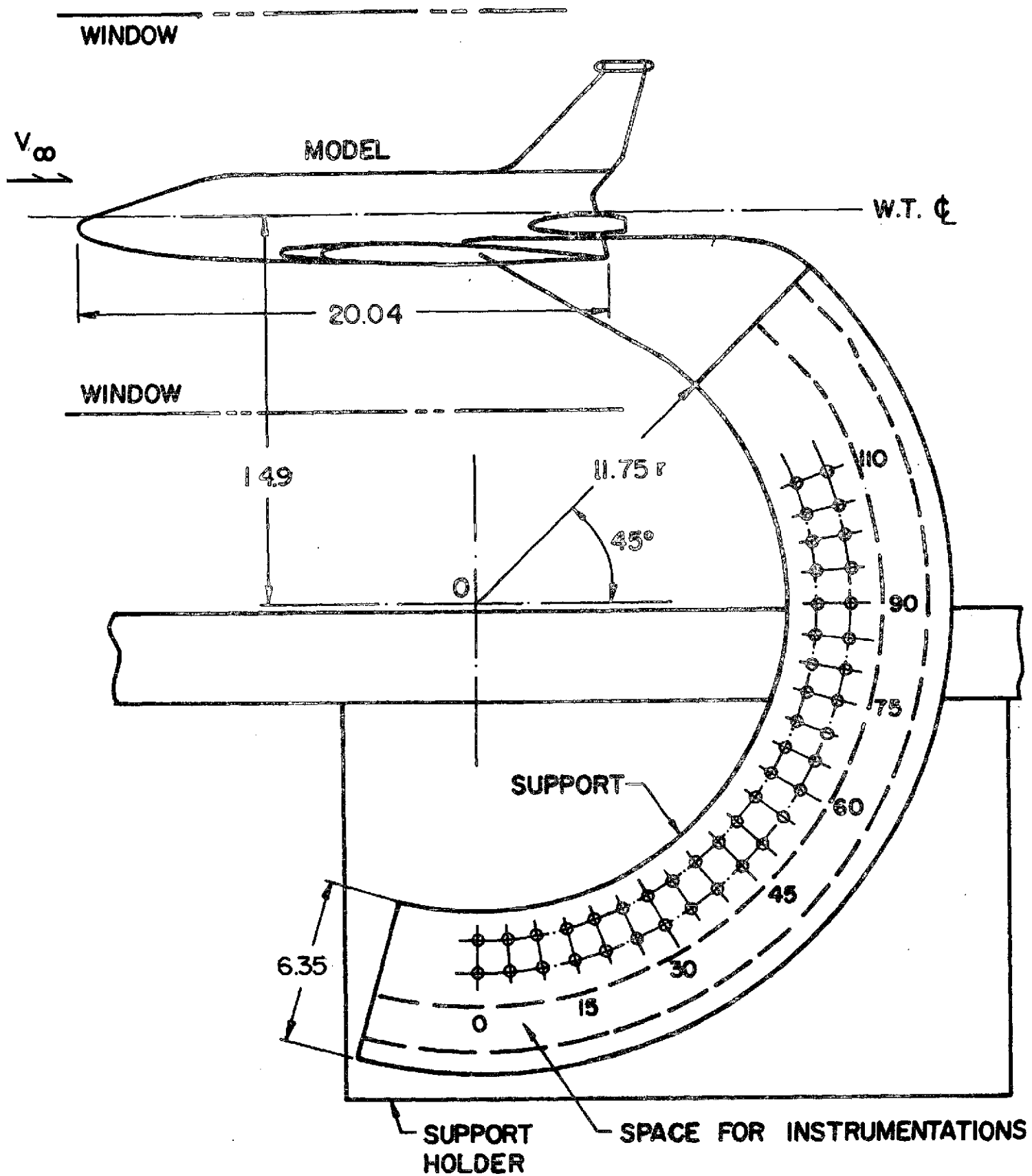


Fig. 9 Circumferential Locations of Pressure Taps



ALL DIMENSIONS IN CM.

Fig. 10 Support Mechanism for Space Shuttle Model

REPRODUCIBILITY OF THE
ORIGINAL PAGE IS POOR

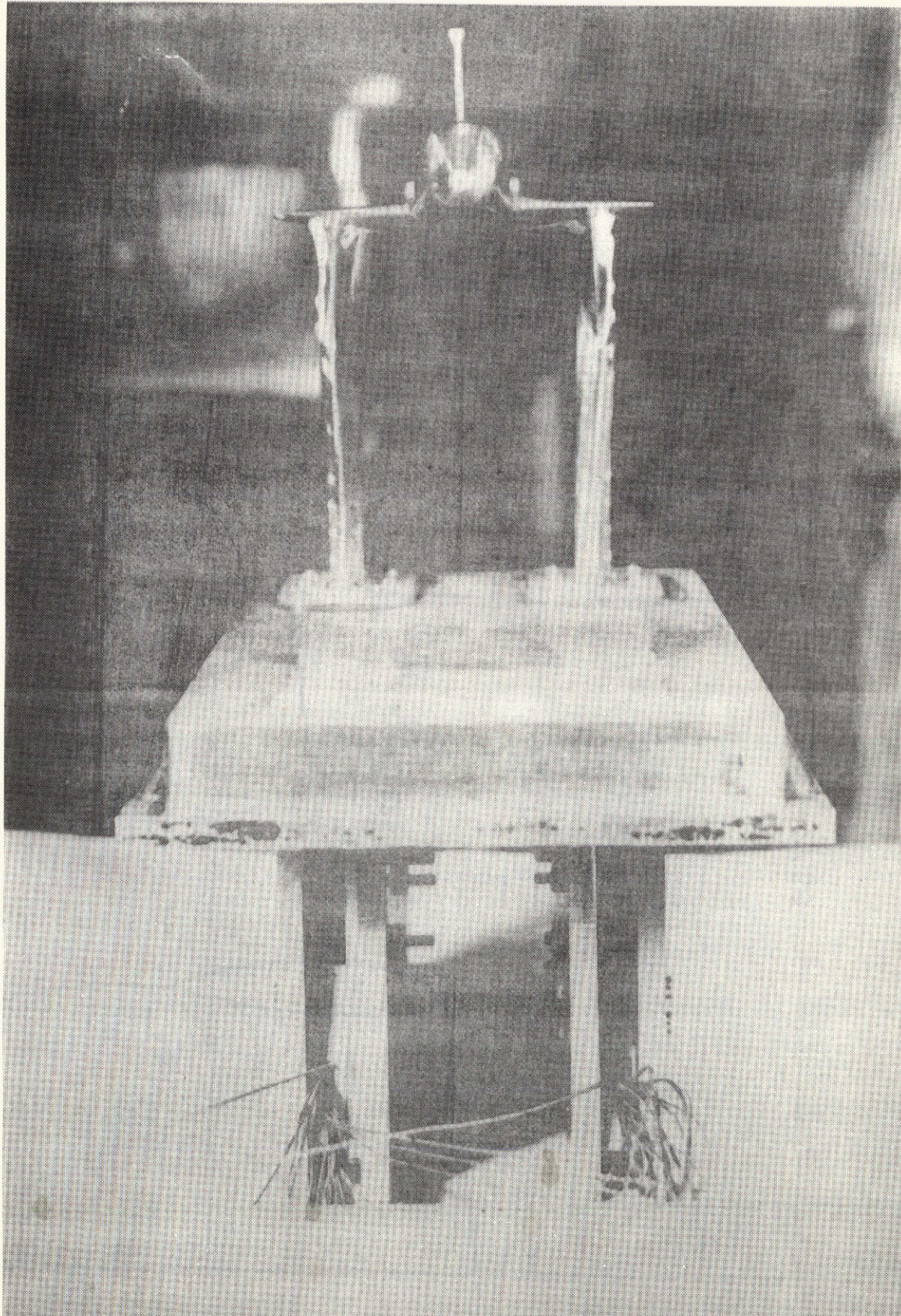
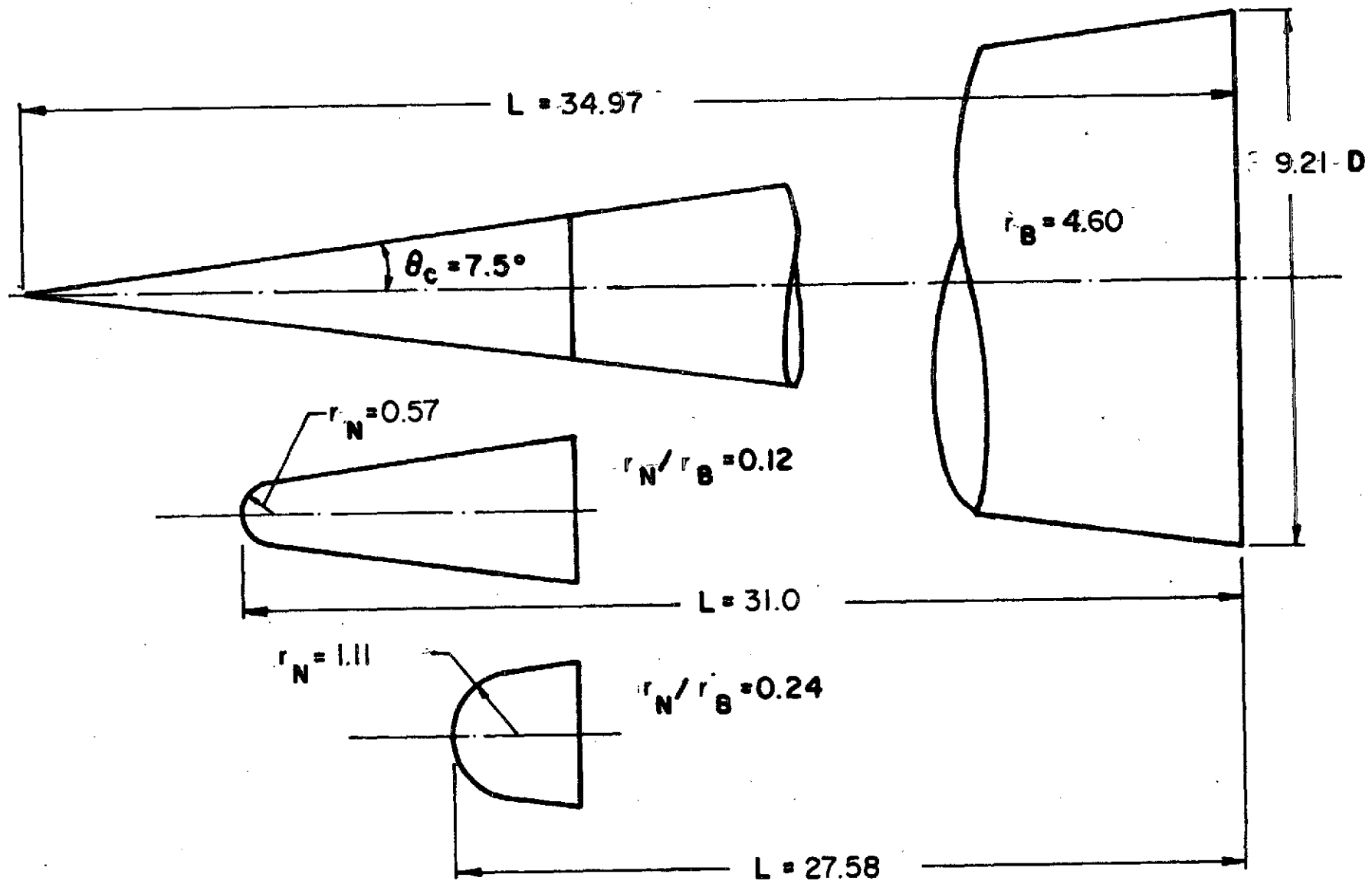


Fig. 11 Photograph of Heat Transfer Model Mounted on the Model Support



DIMENSIONS IN CM.

Fig. 12 Sharp and Blunt Cone Models

REPRODUCIBILITY OF THE
ORIGINAL PAGE IS POOR.

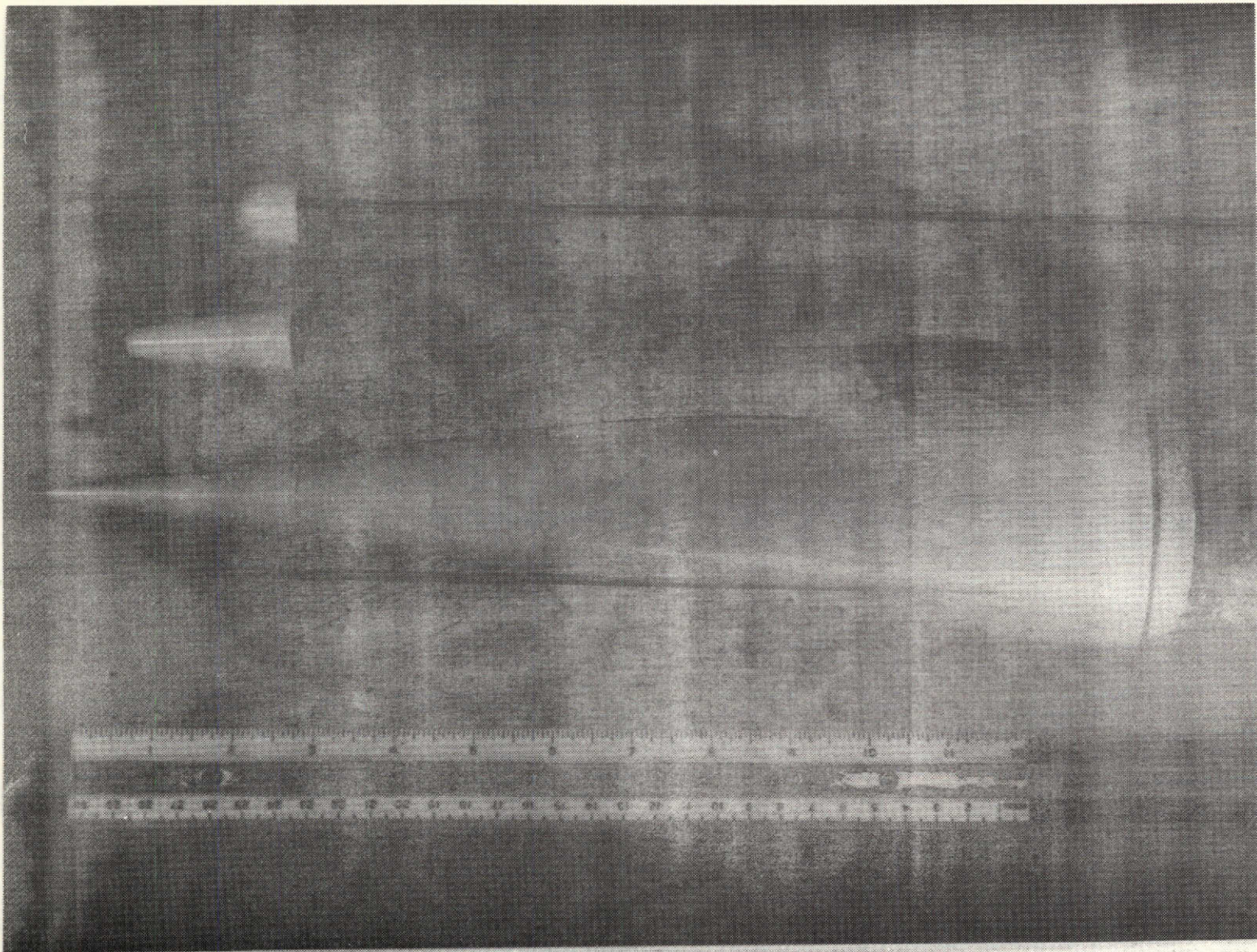


Fig. 13 Photograph of Cone Models

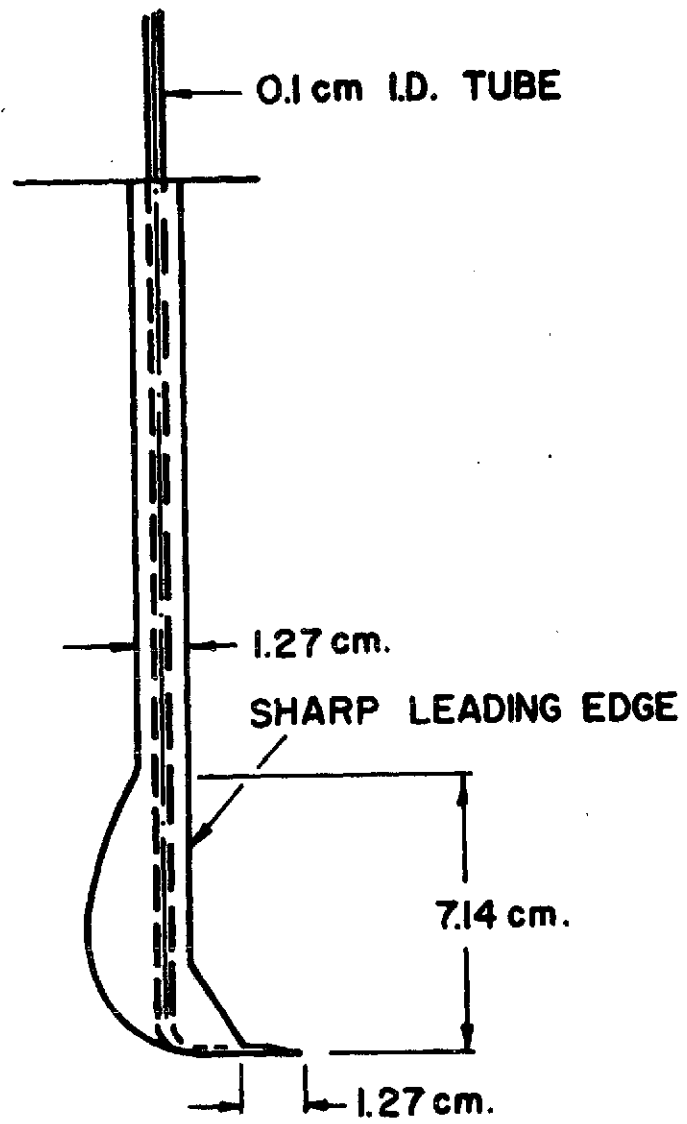


Fig. 14 Boundary Layer Probe

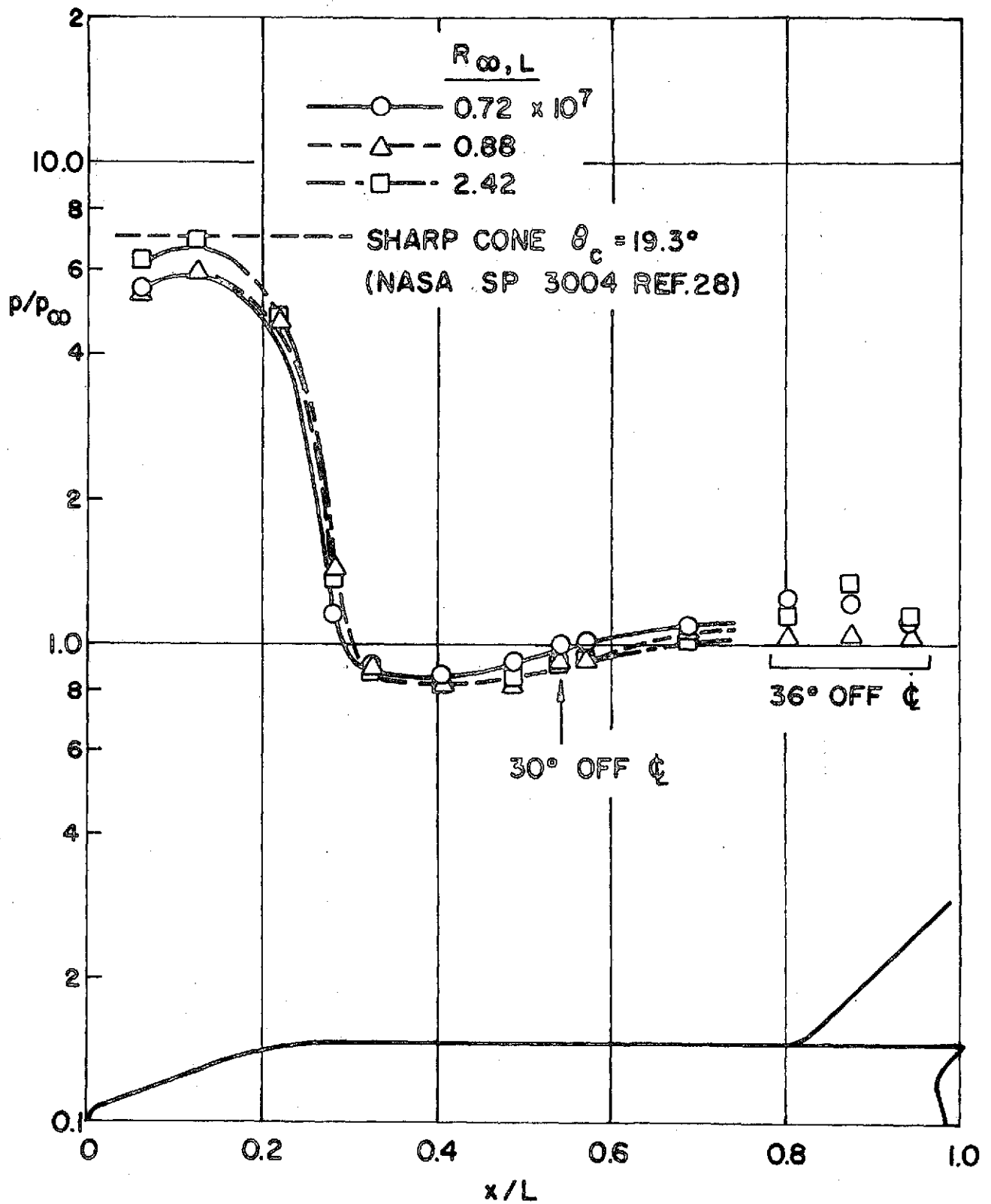


Fig. 15 Surface Pressure Distributions along Leeward Centerline ; $\alpha = 0^\circ$

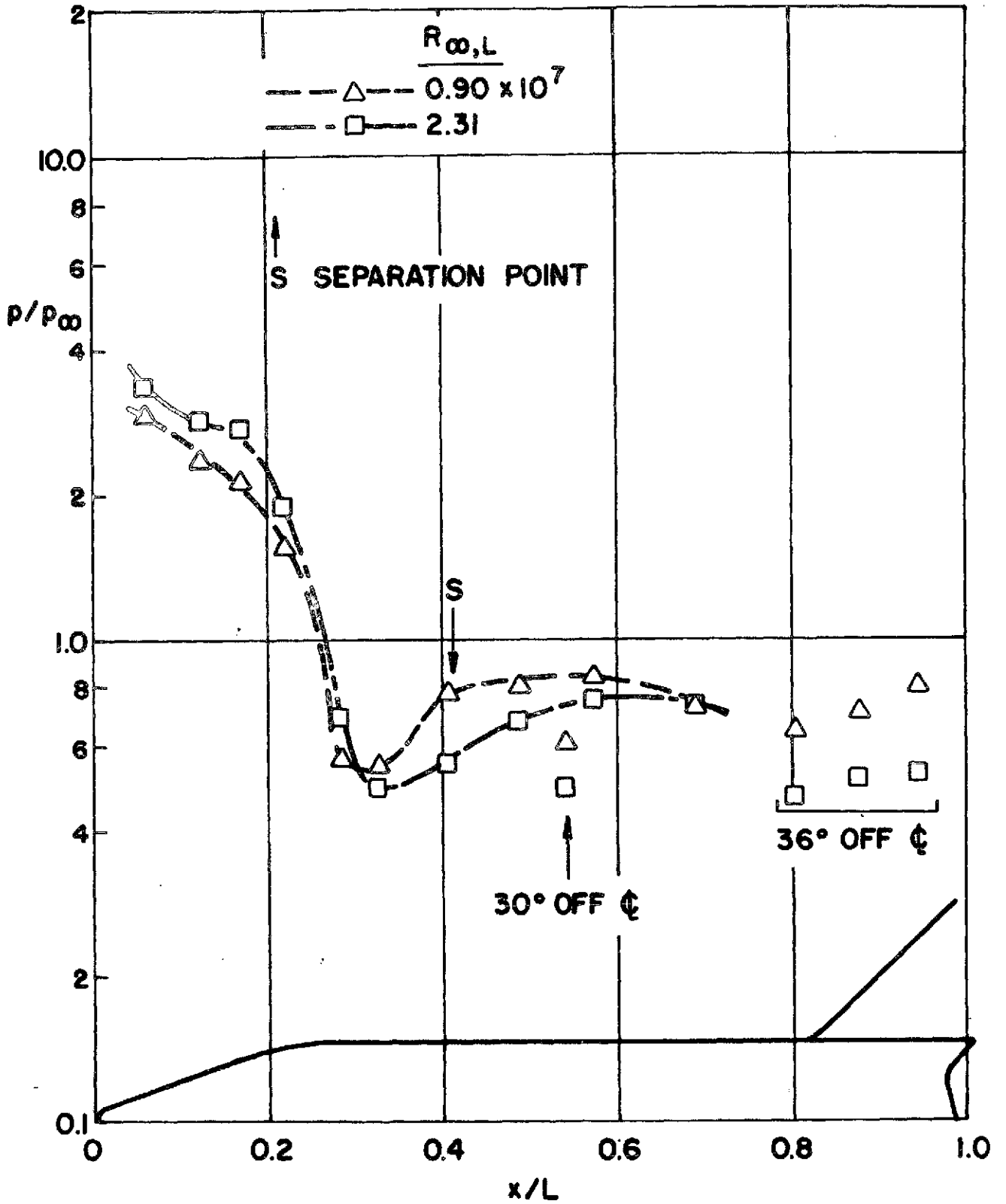


Fig. 16 Surface Pressure Distributions along Leeward Centerline ; $\alpha = 10^\circ$

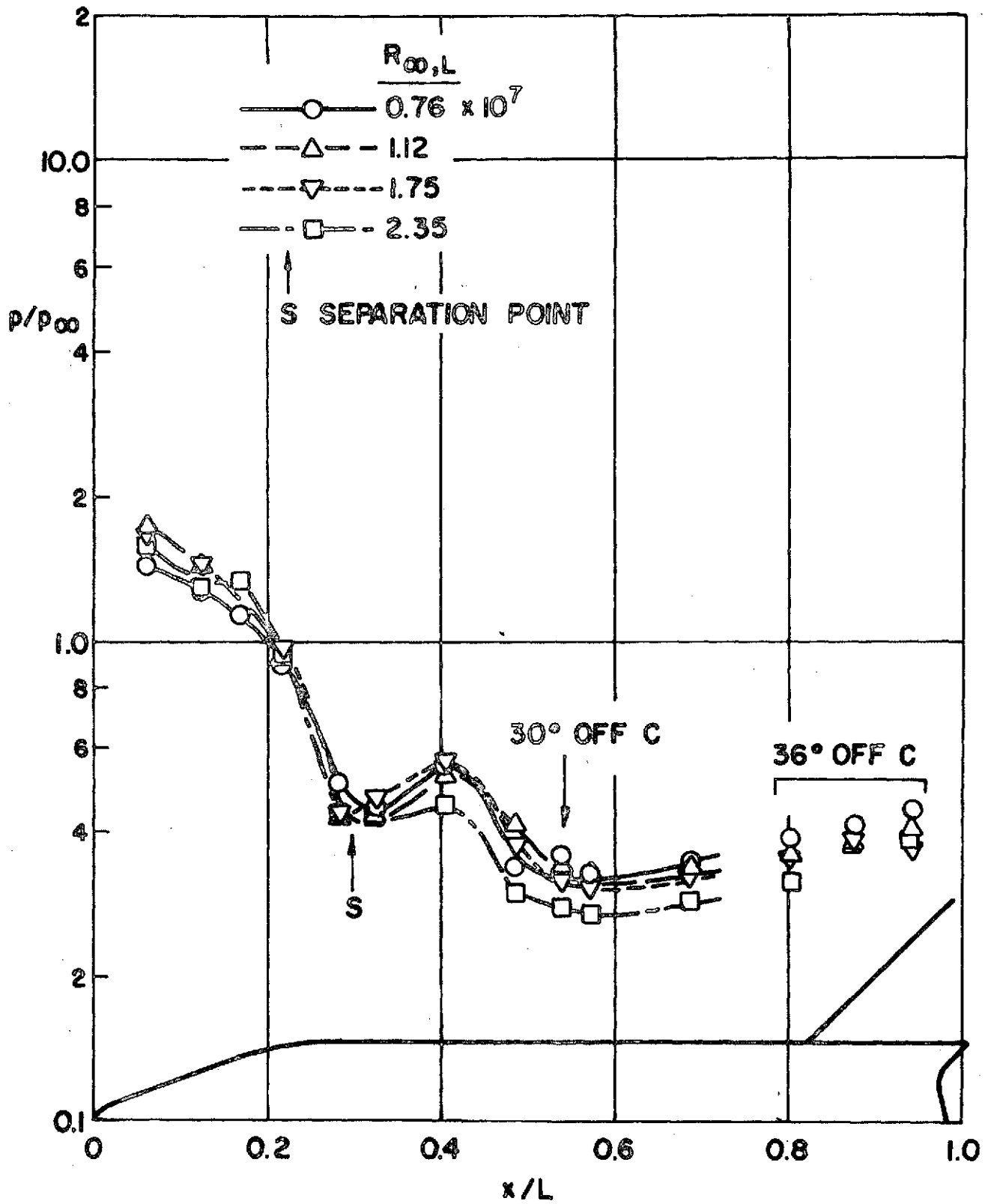


Fig. 17 Surface Pressure Distributions along Leeward Centerline ; $\alpha = 20^\circ$

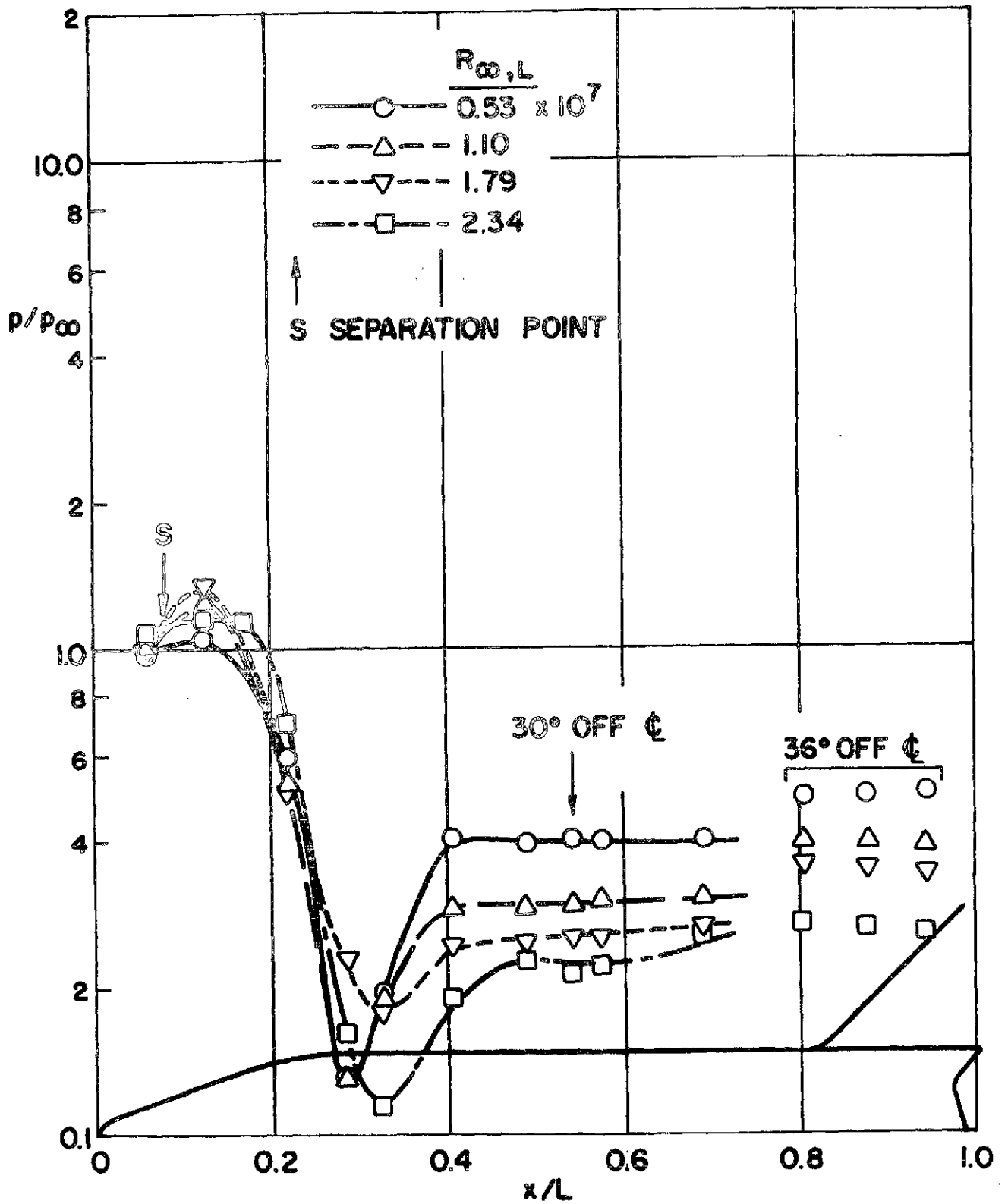


Fig. 18 Surface Pressure Distributions along Leeward Centerline ; $\alpha = 30^\circ$

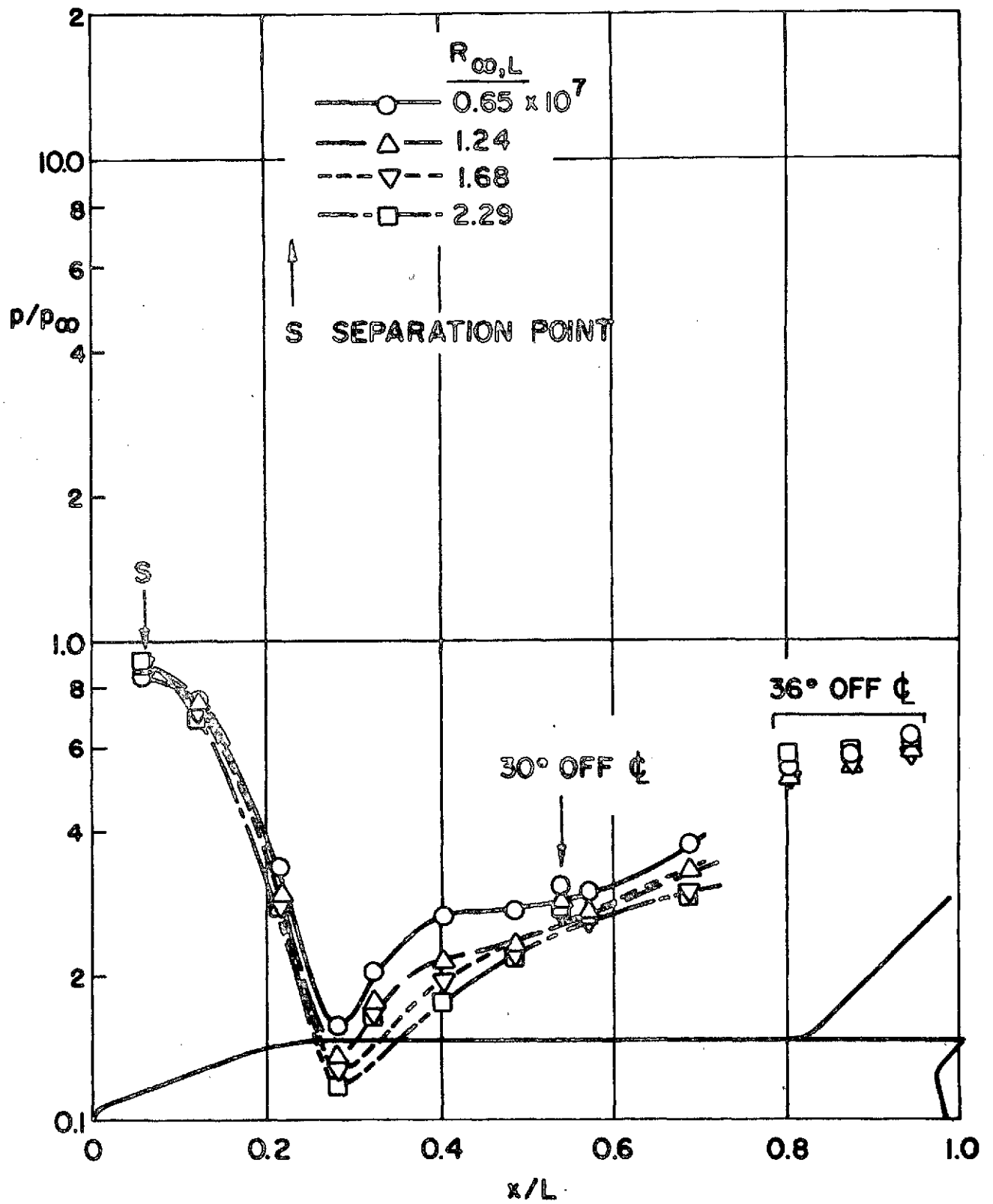


Fig. 19 Surface Pressure Distributions along Leeward Centerline ; $\alpha = 40^\circ$

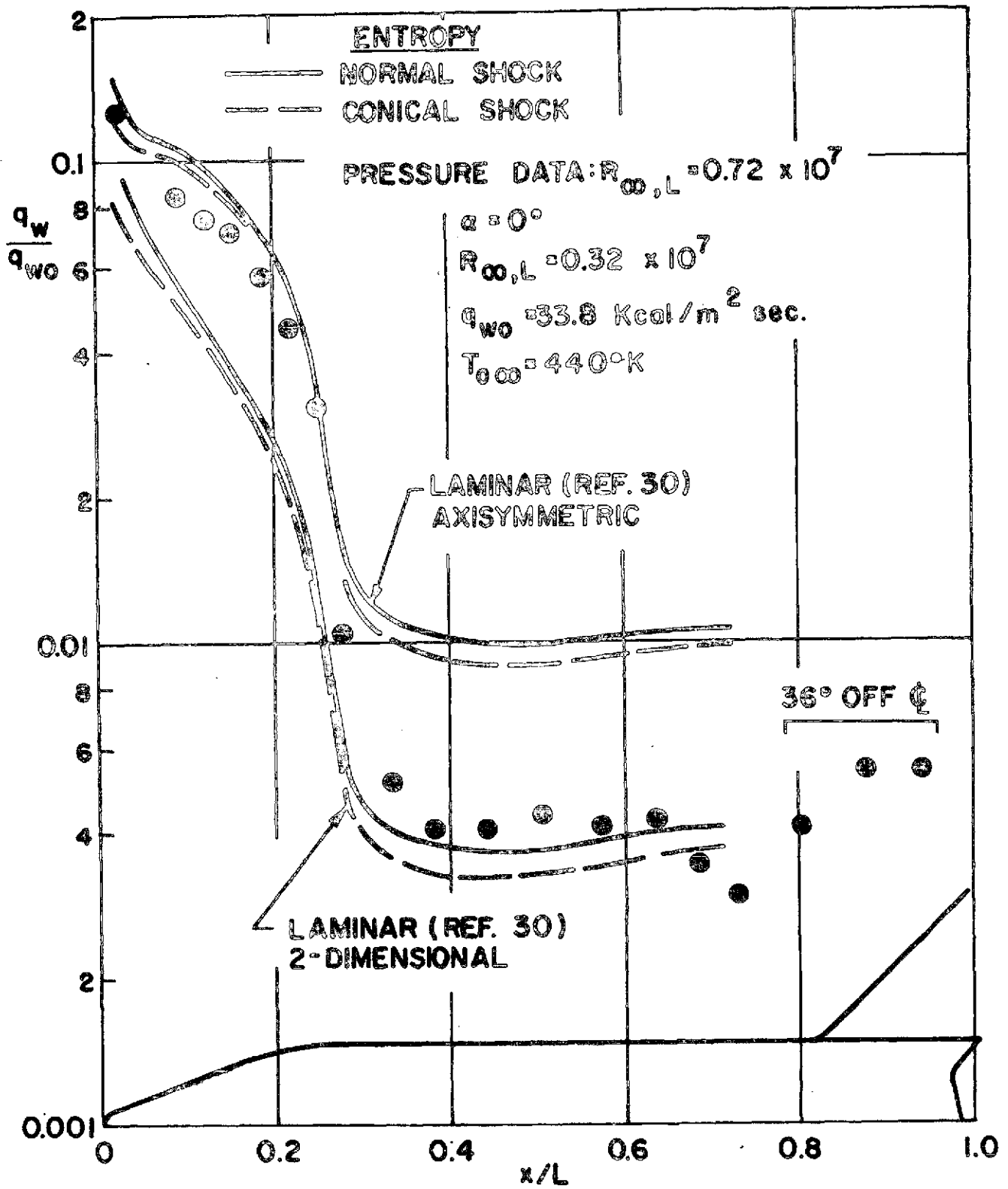


Fig. 20 Heat Transfer Distribution along Leeward Centerline ;
 $\alpha = 0^\circ, R_{\infty,L} = 0.32 \times 10^7$

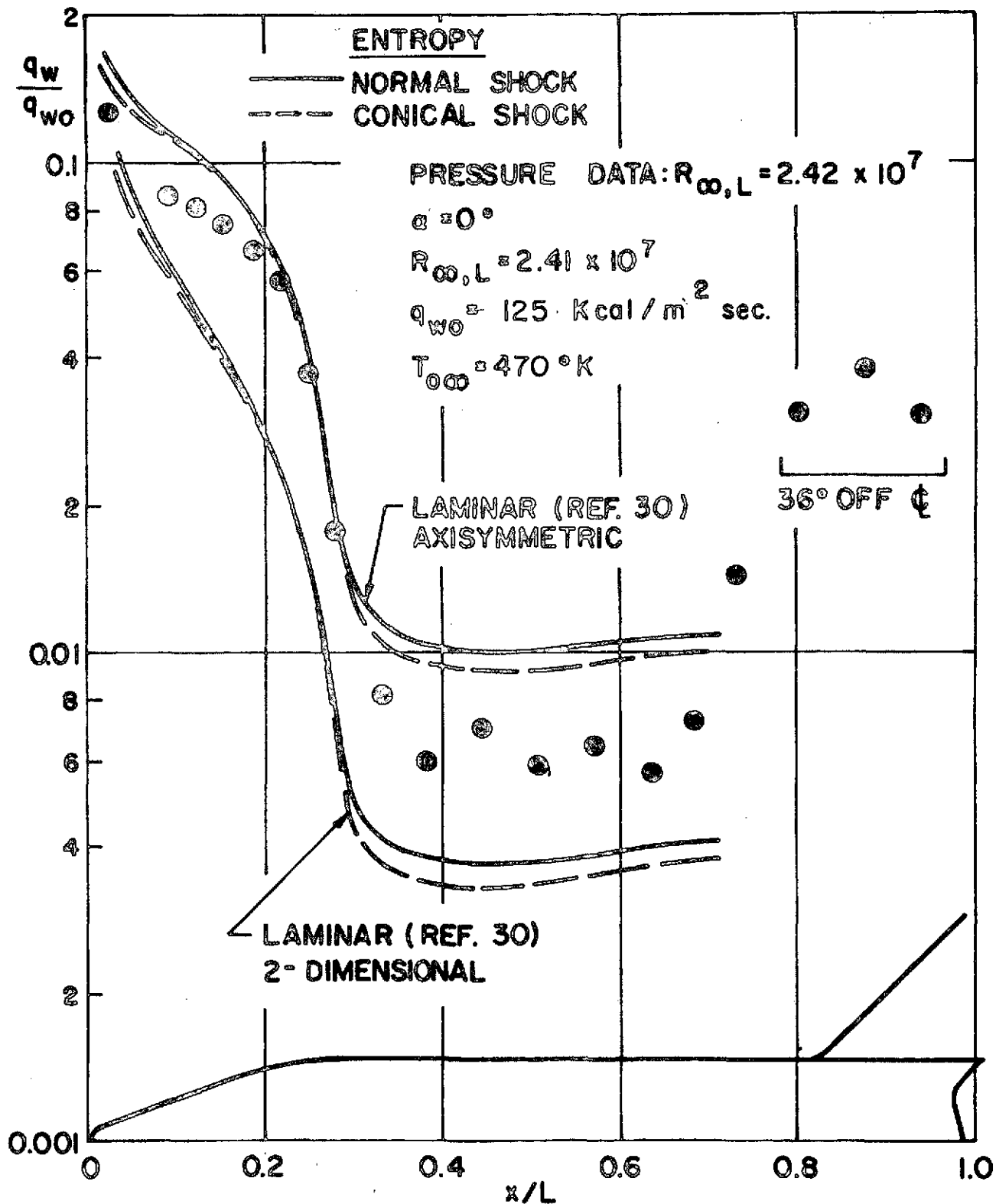


Fig. 24 Heat Transfer Distribution along Leeward Centerline ;
 $\alpha = 0^\circ, R_{\infty,L} = 2.41 \times 10^7$

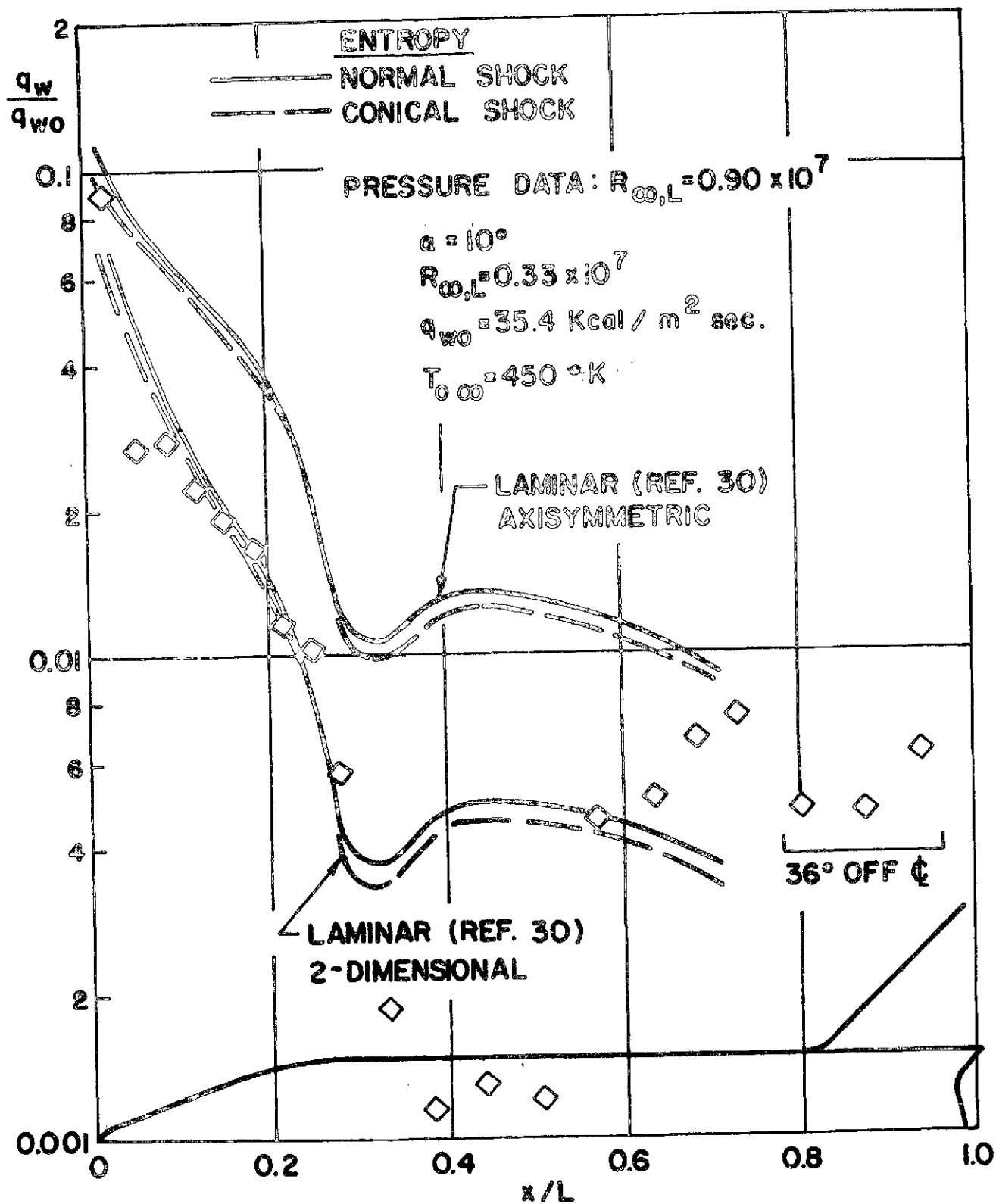


Fig. 22 Heat Transfer Distribution along Leeward Centerline ;
 $\alpha = 10^\circ$, $R_{\infty,L} = 0.33 \times 10^7$

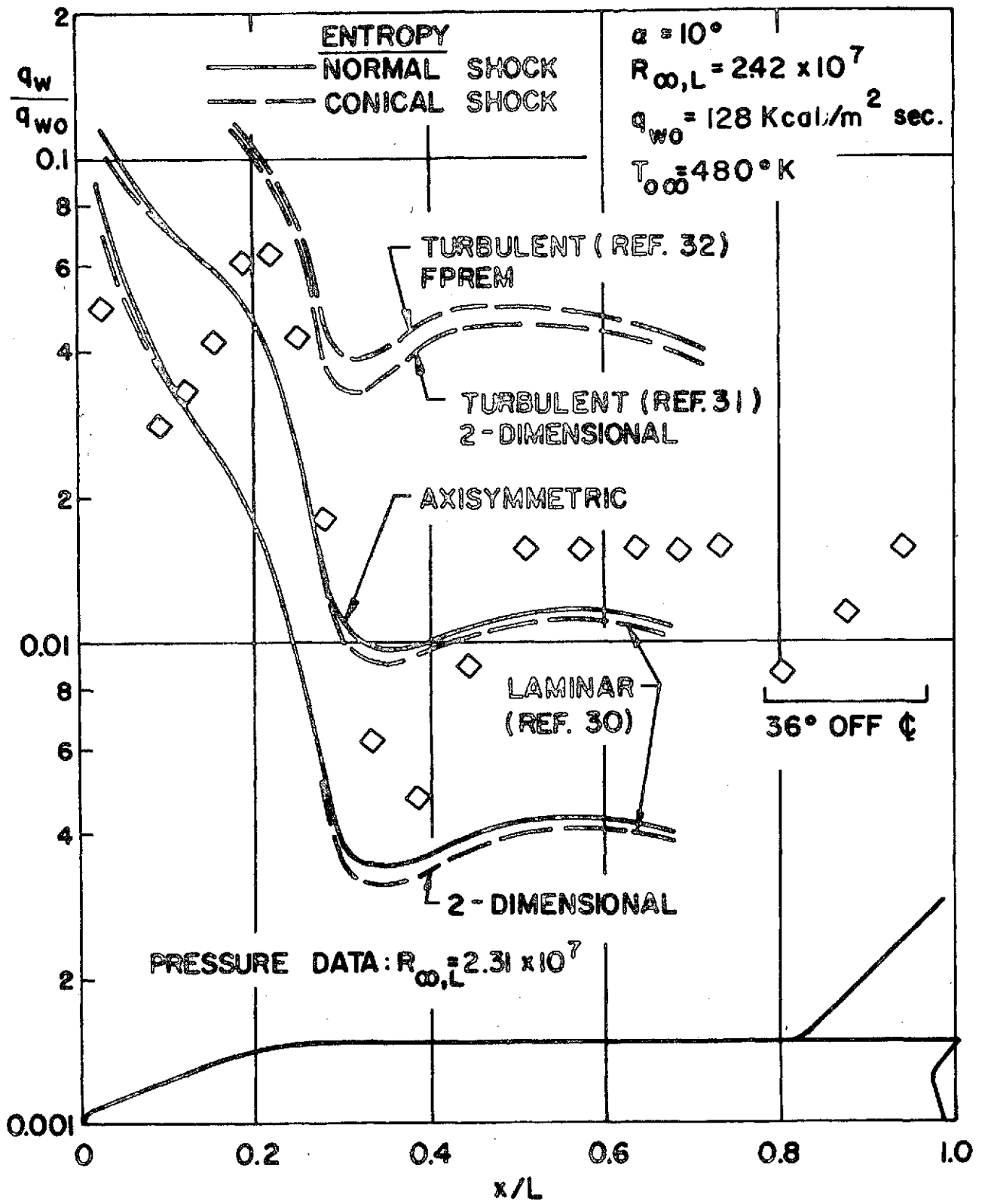


Fig. 23 Heat Transfer Distribution along Leeward Centerline ;
 $\alpha = 10^\circ, R_{\infty,L} = 2.42 \times 10^7$

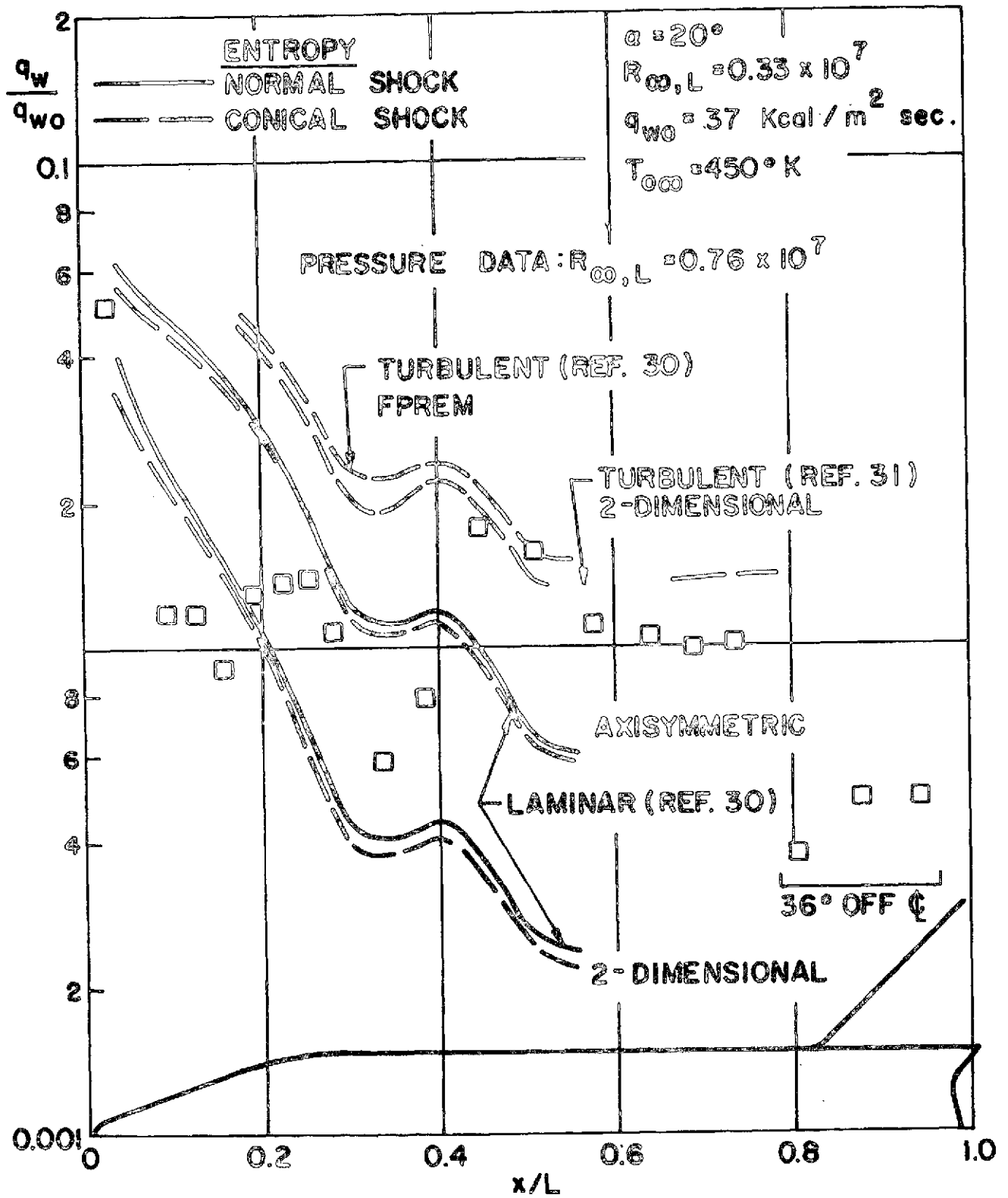


Fig. 24 Heat Transfer Distribution along Leeward Centerline ;
 $\alpha = 20^\circ, R_{\infty,L} = 0.33 \times 10^7$

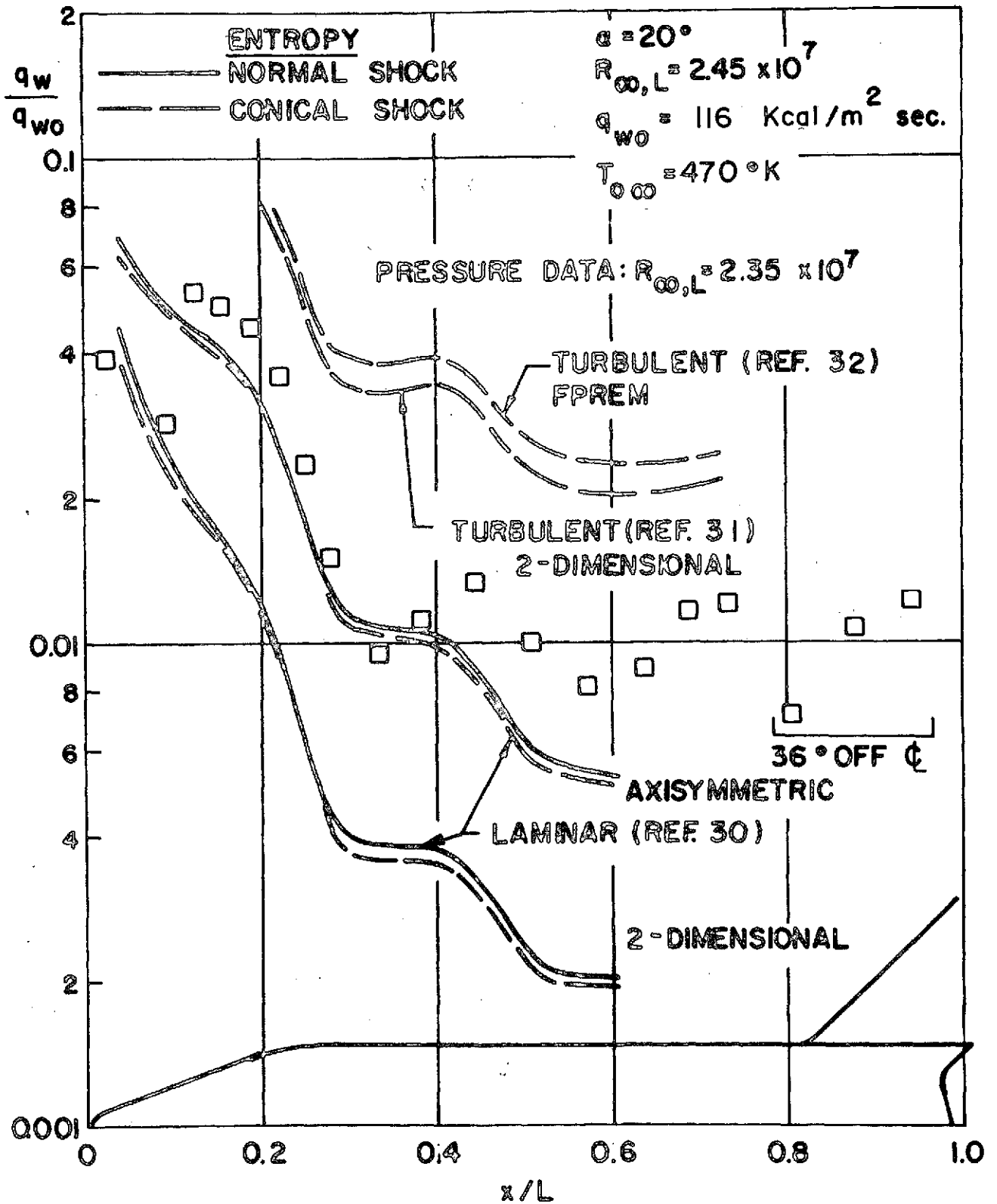


Fig. 25 Heat Transfer Distribution along Leeward Centerline ;
 $\alpha = 20^\circ, R_{\infty,L} = 2.45 \times 10^7$

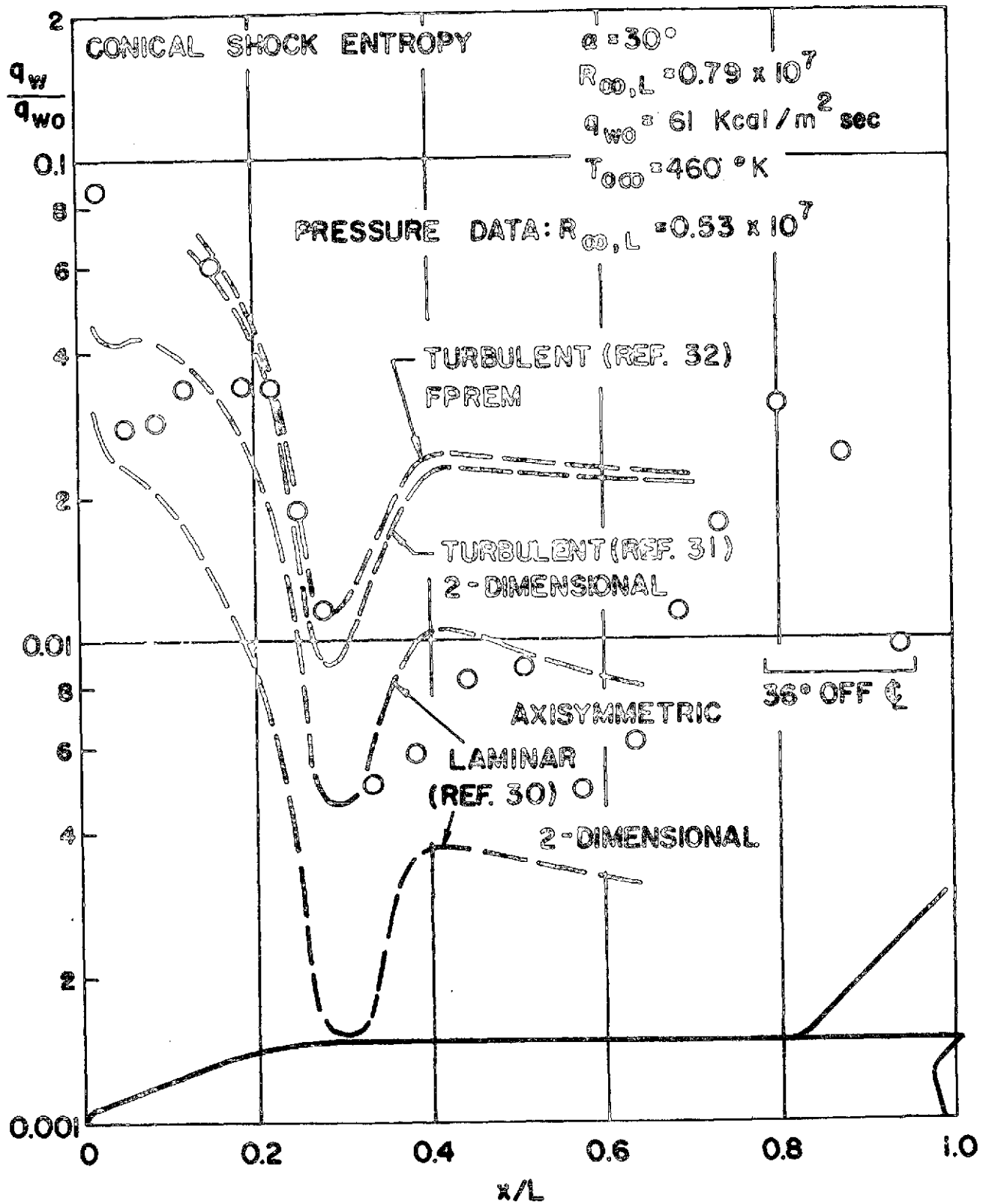


Fig. 26 Heat Transfer Distribution along Leeward Centerline ;
 $\alpha = 30^\circ$, $R_{\infty,L} = 0.79 \times 10^7$

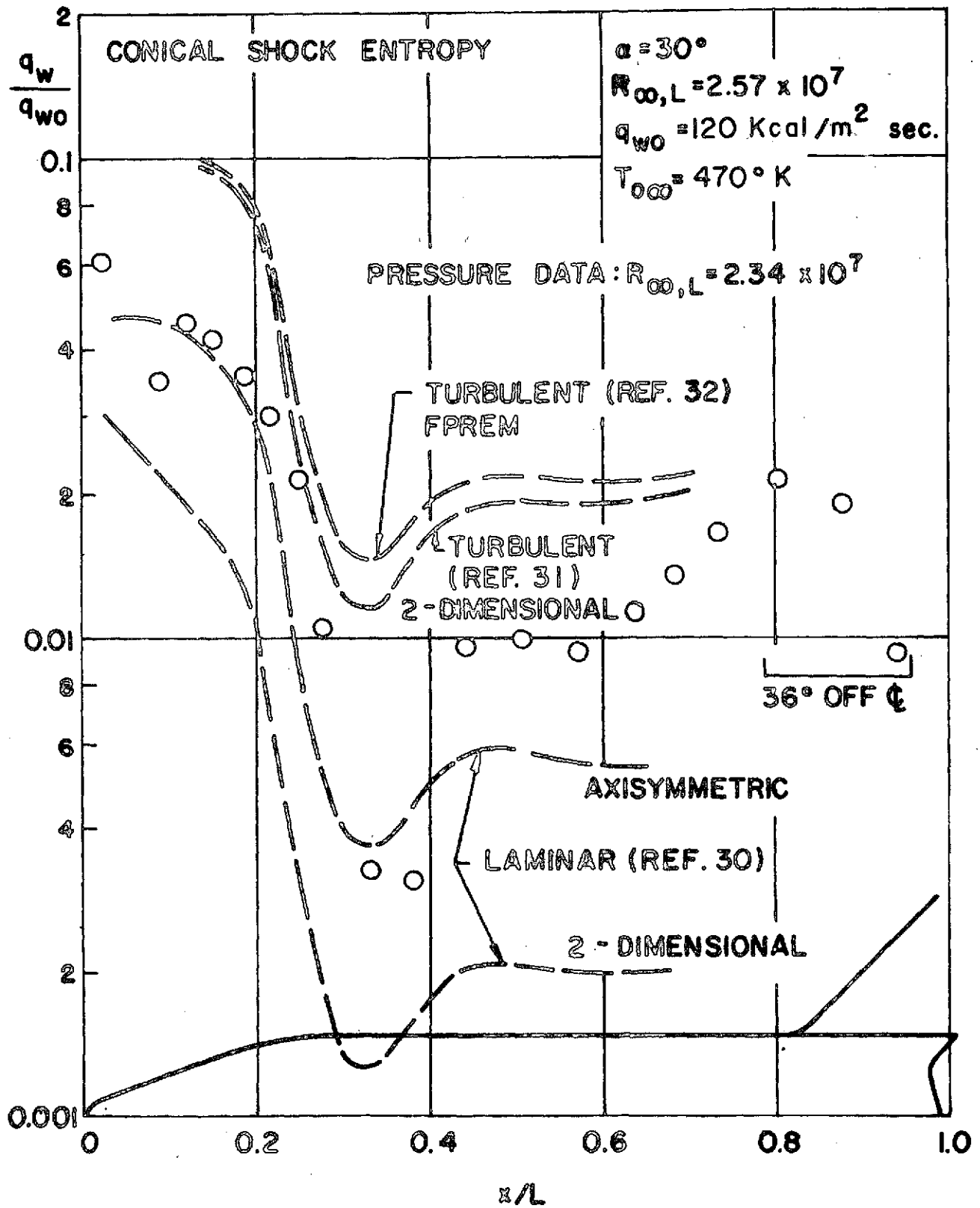


Fig. 27 Heat Transfer Distribution along Leeward Centerline ;
 $\alpha = 30^\circ, R_{\infty,L} = 2.57 \times 10^7$

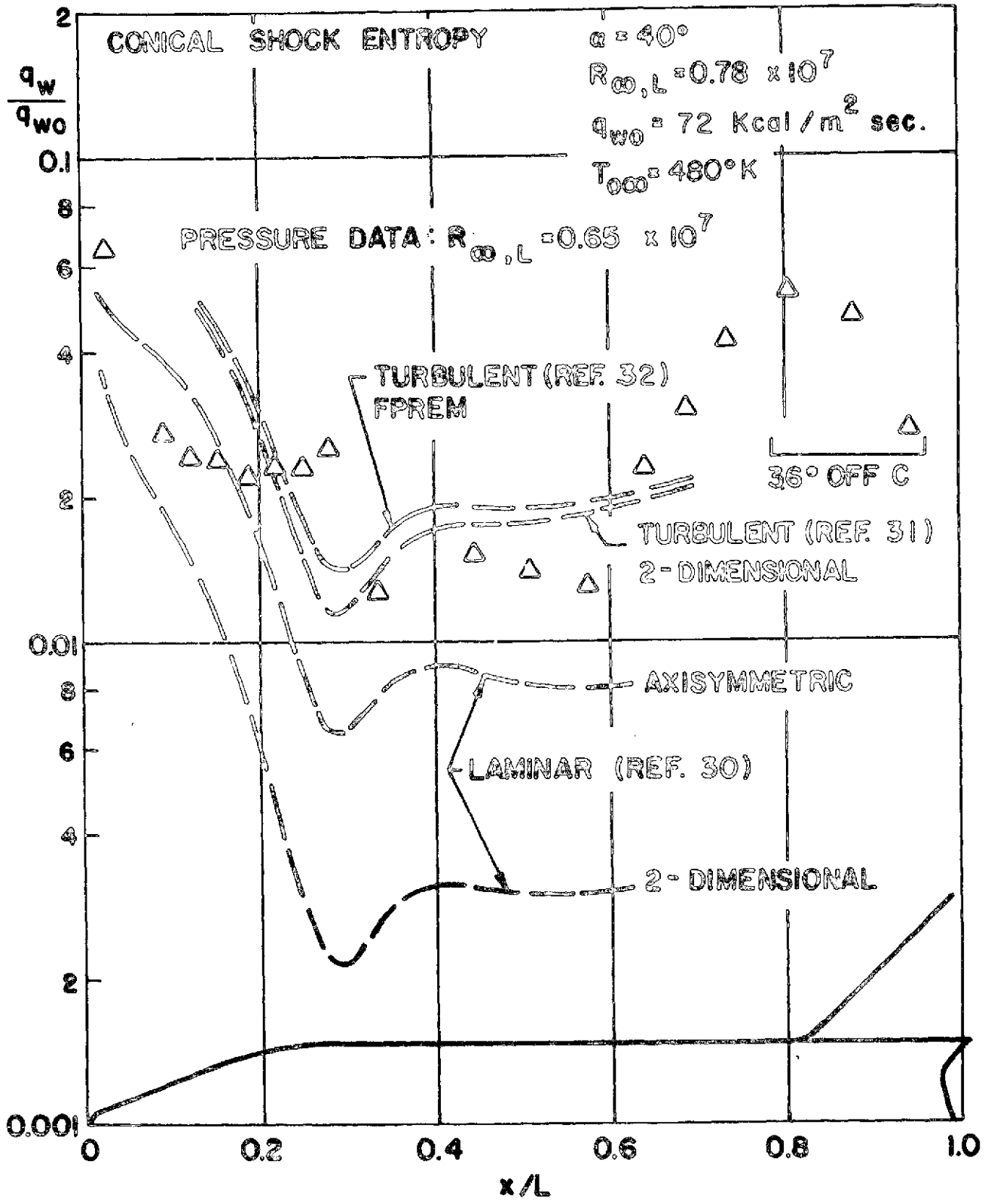


Fig. 20 Heat Transfer Distribution along Leeward Centerline ;
 $\alpha = 40^\circ, R_{\infty,L} = 0.78 \times 10^7$

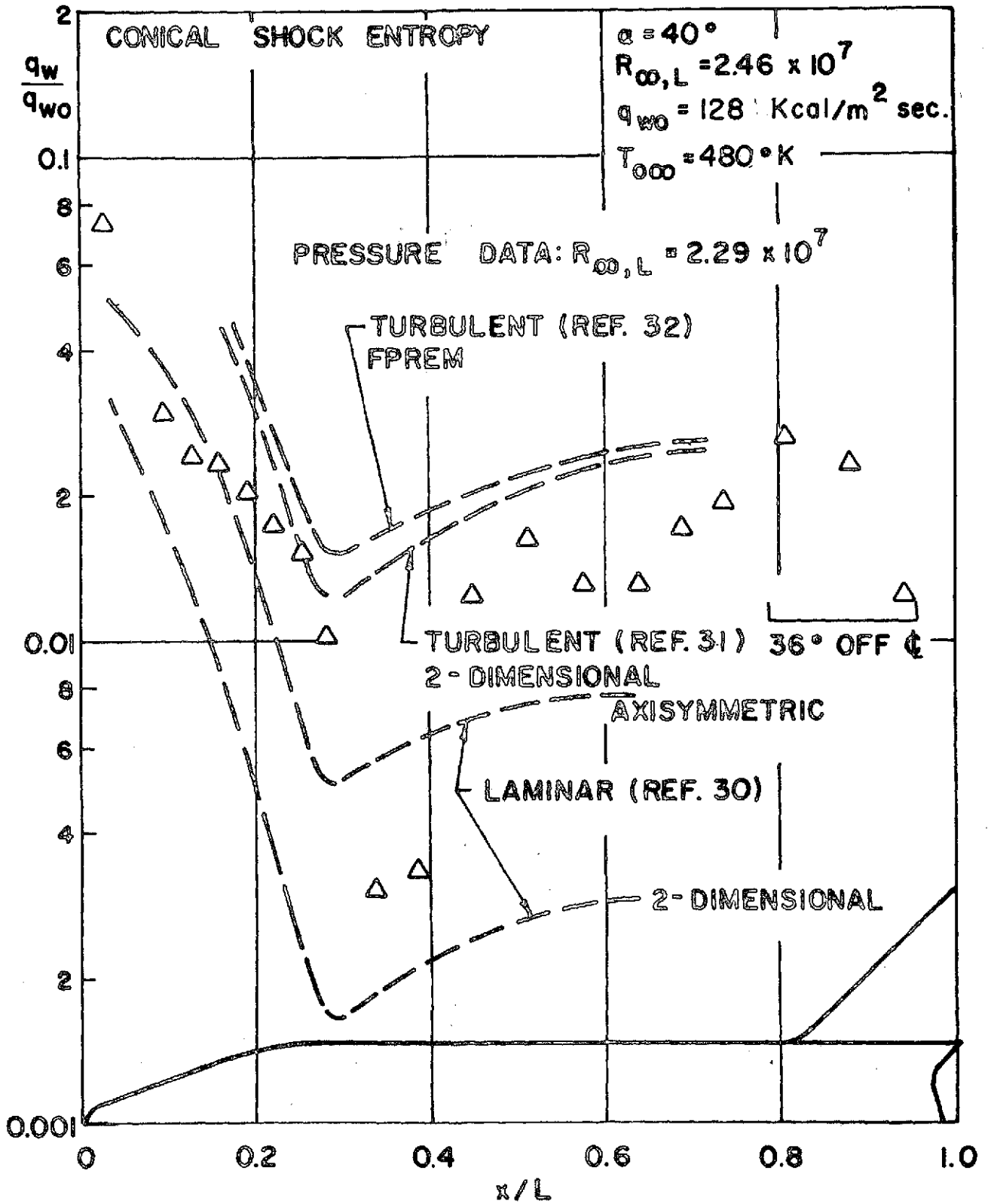


Fig. 29 Heat Transfer Distribution along Leeward Centerline ;
 $\alpha = 40^\circ, R_{\infty,L} = 2.46 \times 10^7$

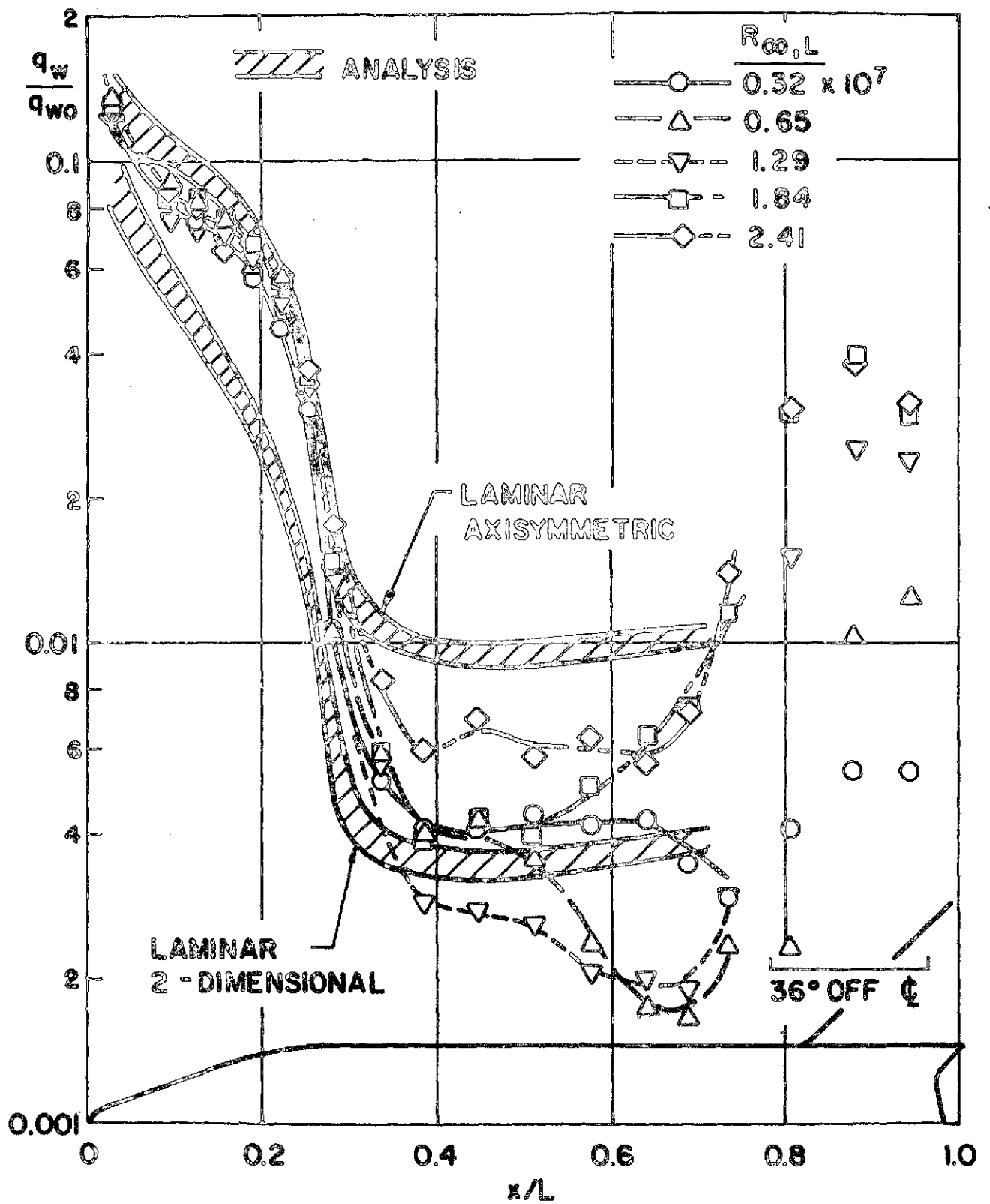


Fig. 30 Heat Transfer Distributions along Leeward Centerline ; $\alpha = 0^\circ$

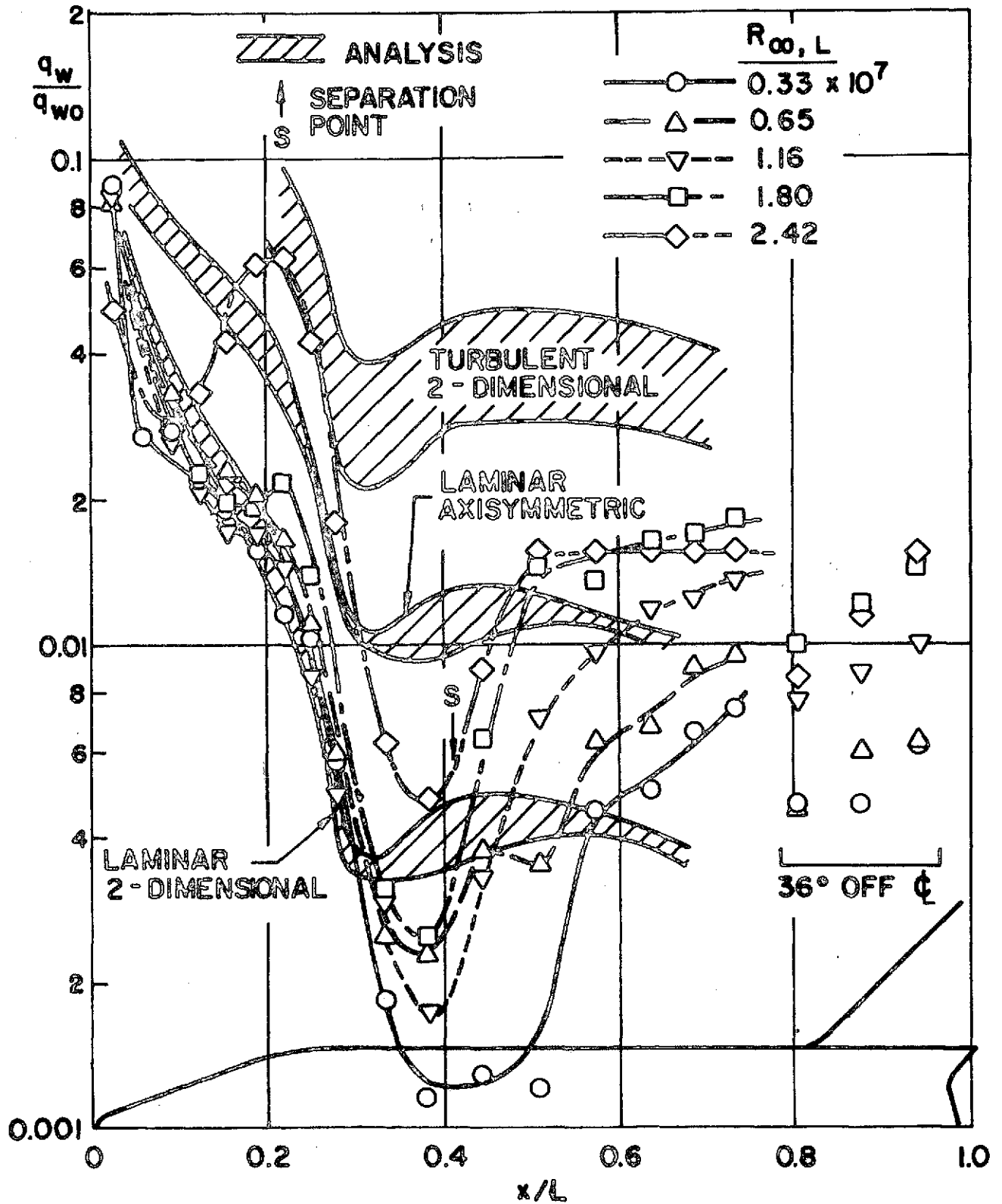


Fig. 31 Heat Transfer Distributions along Leeward Centerline ; $\alpha = 10^\circ$

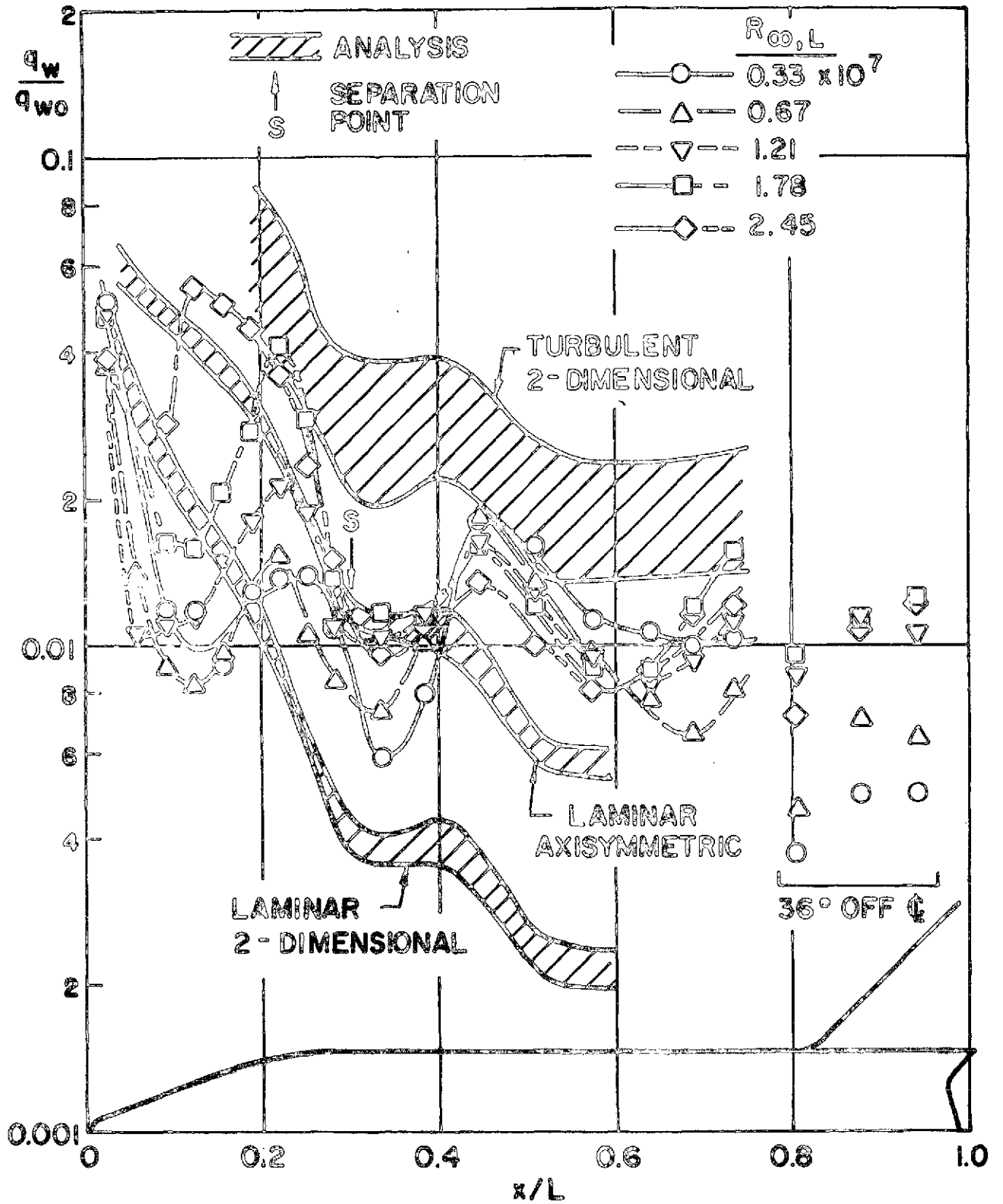


Fig. 32 Heat Transfer Distributions along Leeward Centerline ; $\alpha = 20^\circ$

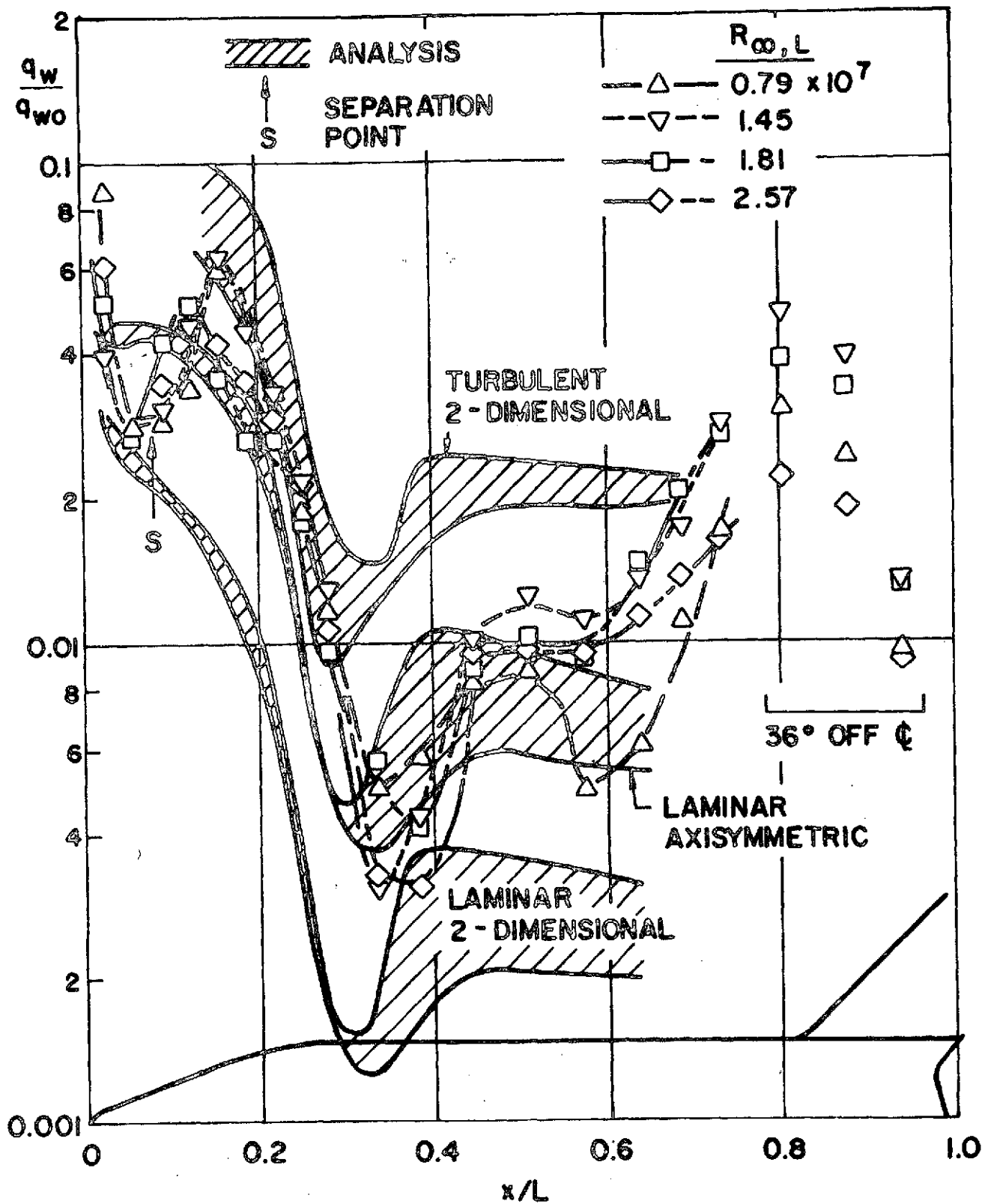


Fig. 33 Heat Transfer Distributions along Leeward Centerline ; $\alpha = 30^\circ$

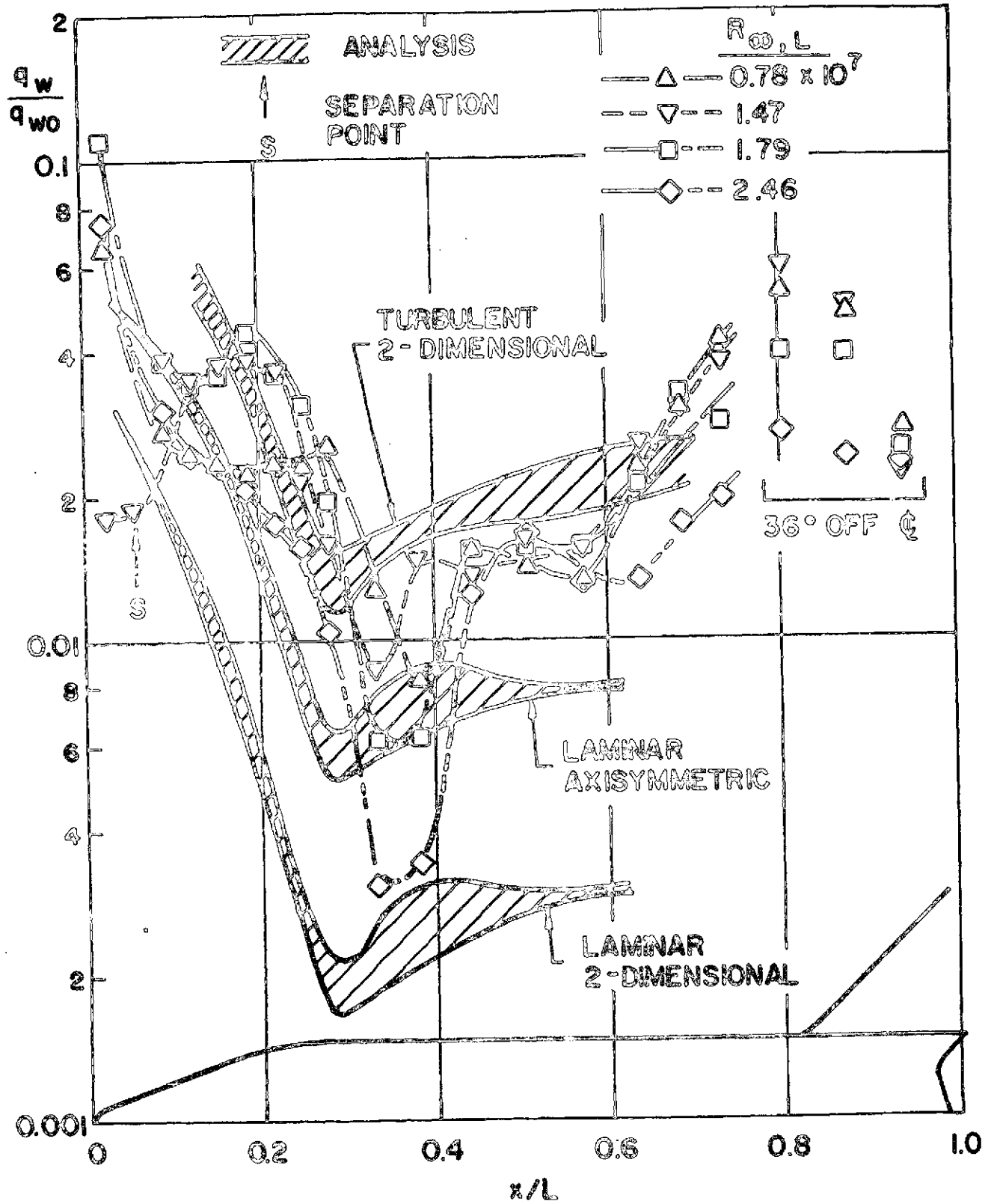


Fig. 30 Heat Transfer Distribution along Leeward Centerline ; $\alpha = 40^\circ$

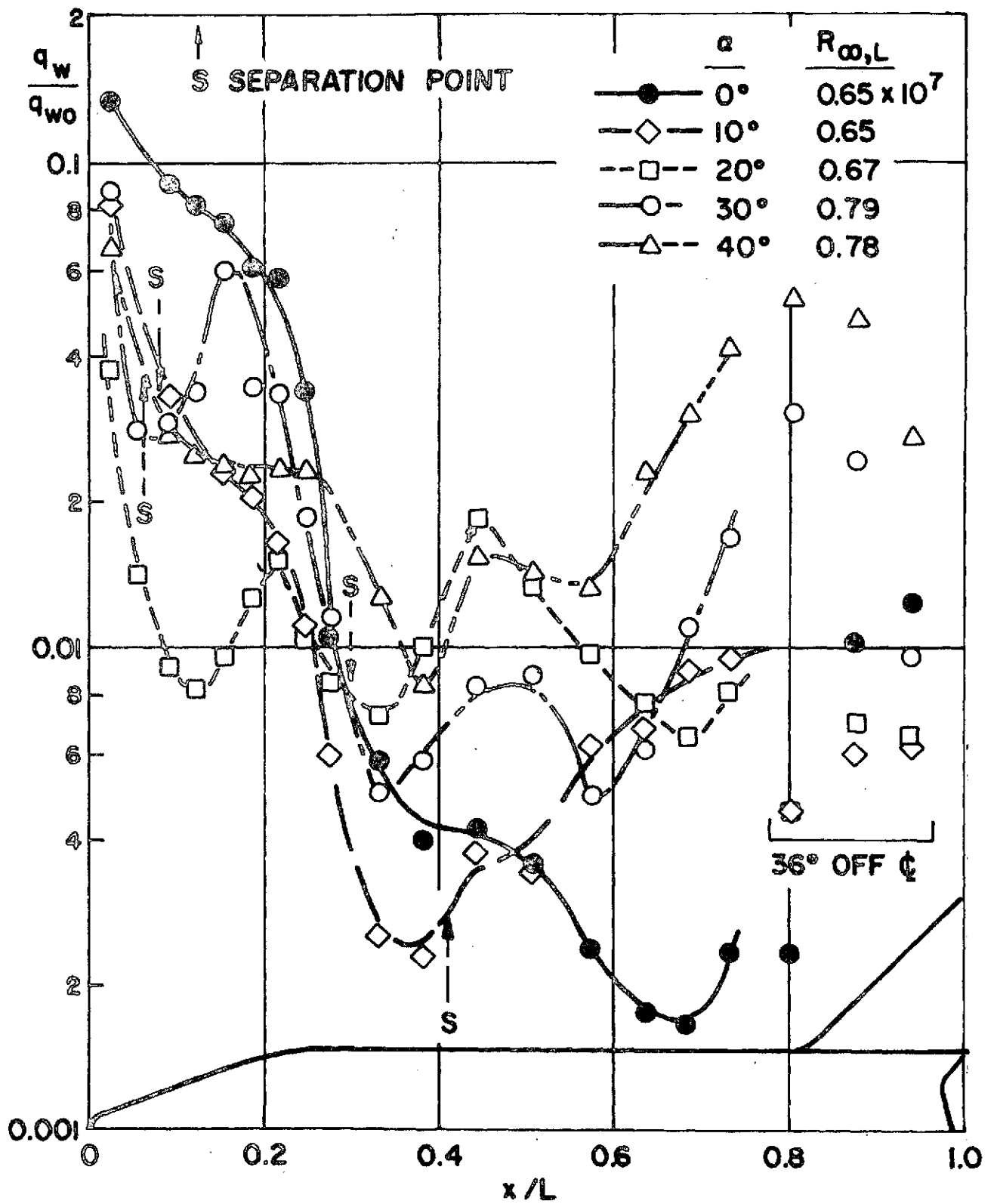


Fig. 35 Heat Transfer Distributions along Leeward Centerline ; $R_{\infty,L} \approx 0.7 \times 10^7$

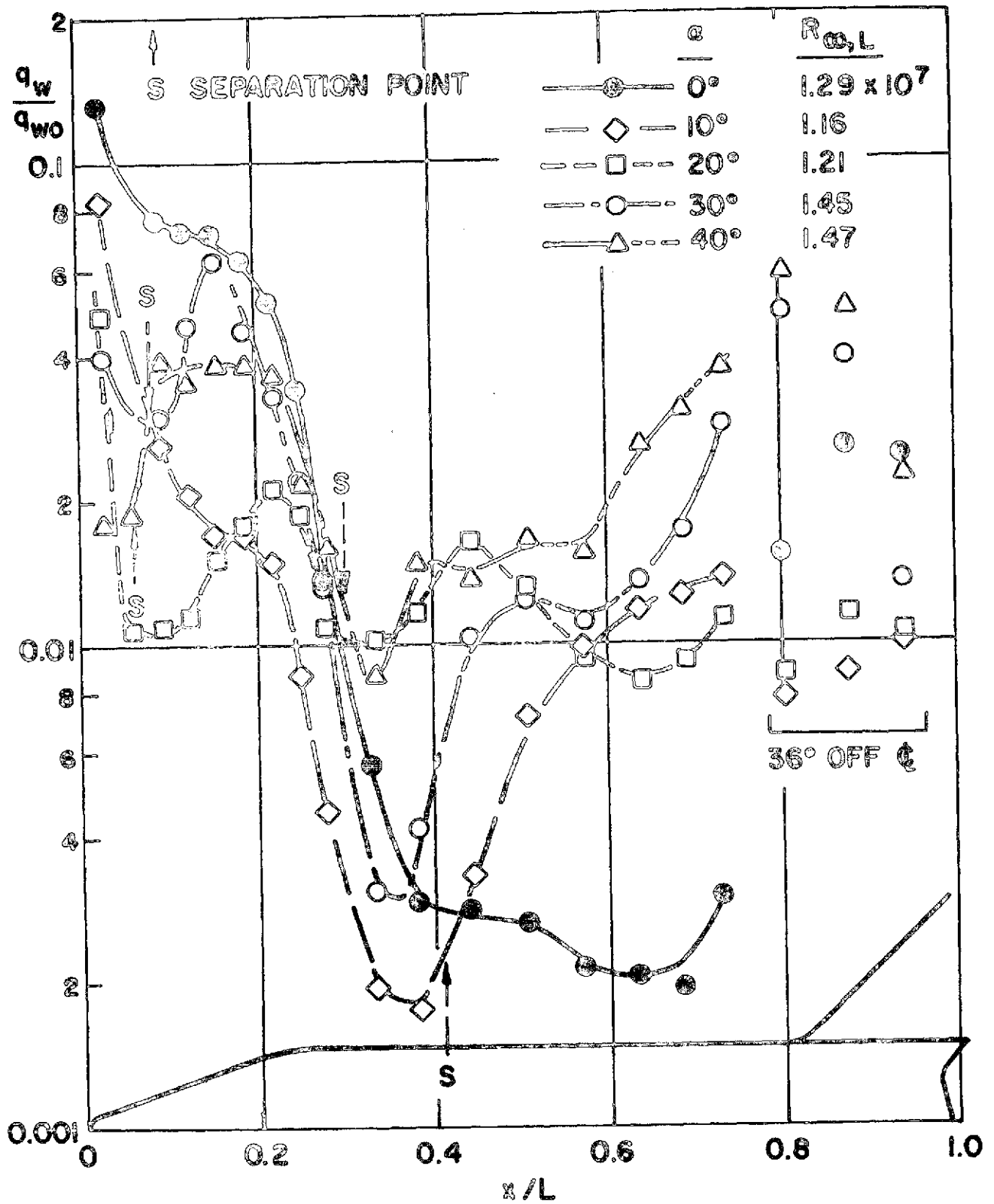


Fig. 36 Heat Transfer Distributions along Leeward Centerline ; $R_{\infty,L} = 1.3 \times 10^7$

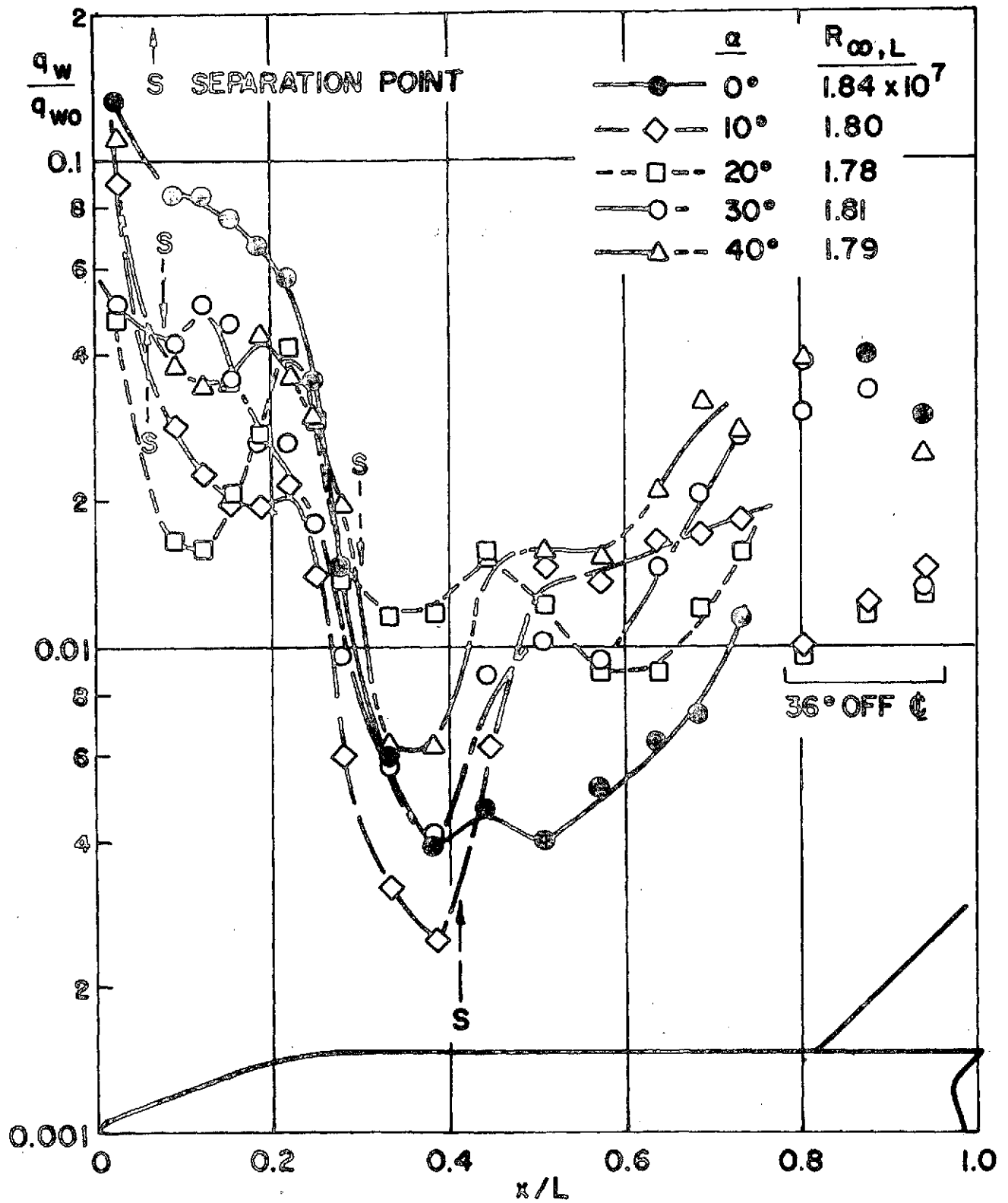


Fig. 37 Heat Transfer Distributions along Leeward Centerline ; $R_{\infty,L} \approx 1.8 \times 10^7$

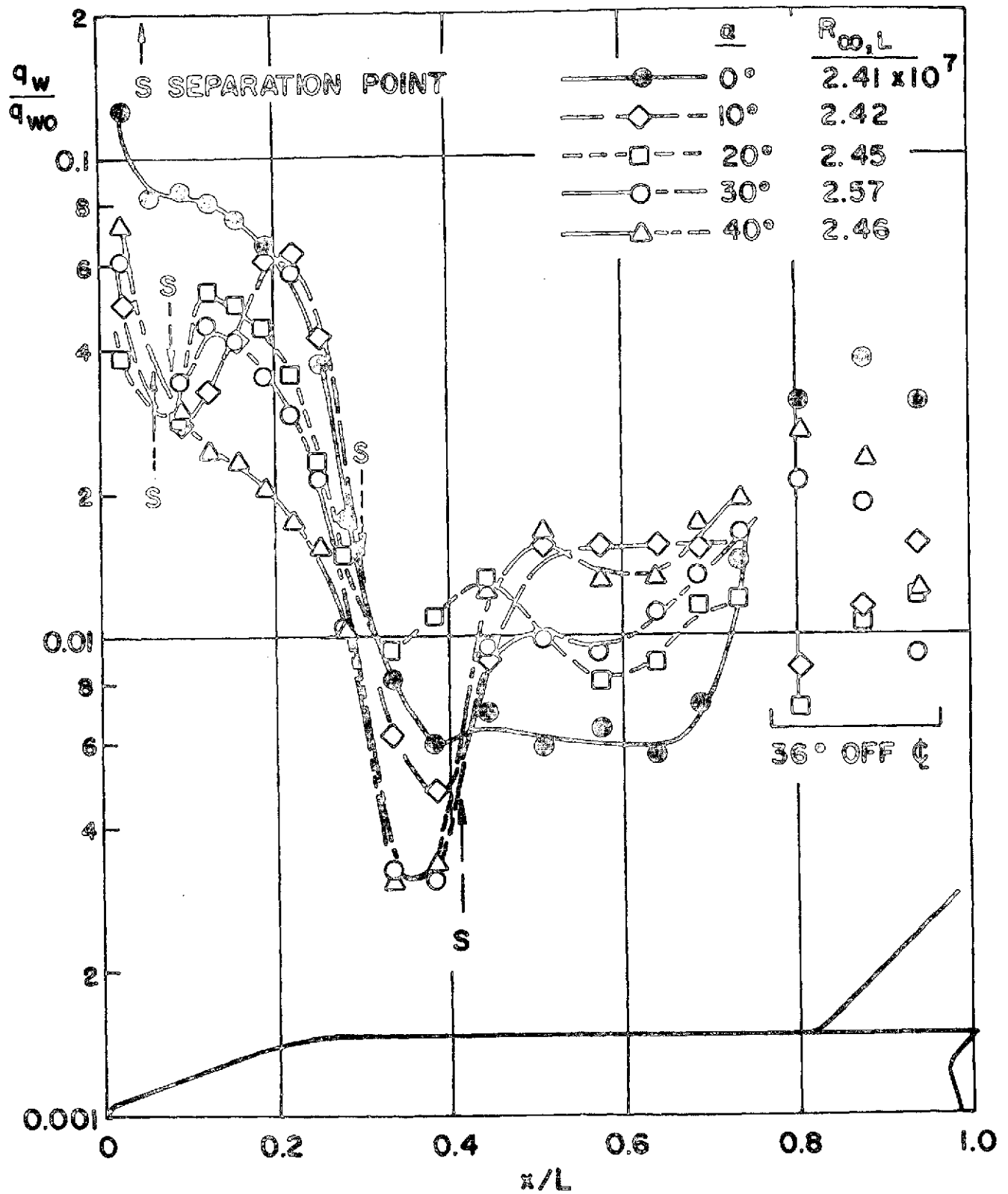


Fig. 38 Heat Transfer Distributions along Leeward Centerline ; $R_{\infty,L} \approx 2.4 \times 10^7$

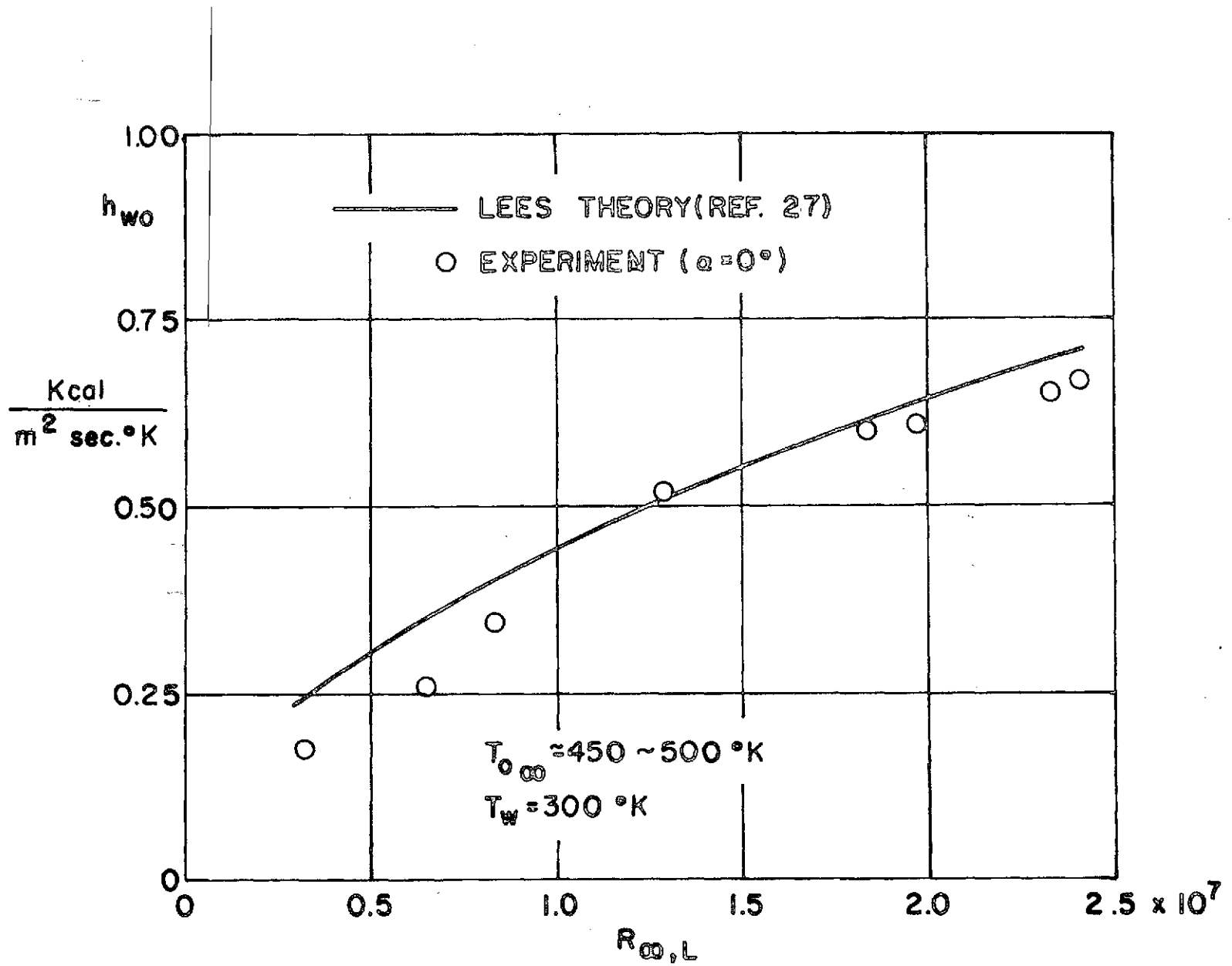


Fig. 39 Laminar Stagnation Heat Transfer Coefficient for an Axisymmetric Flow

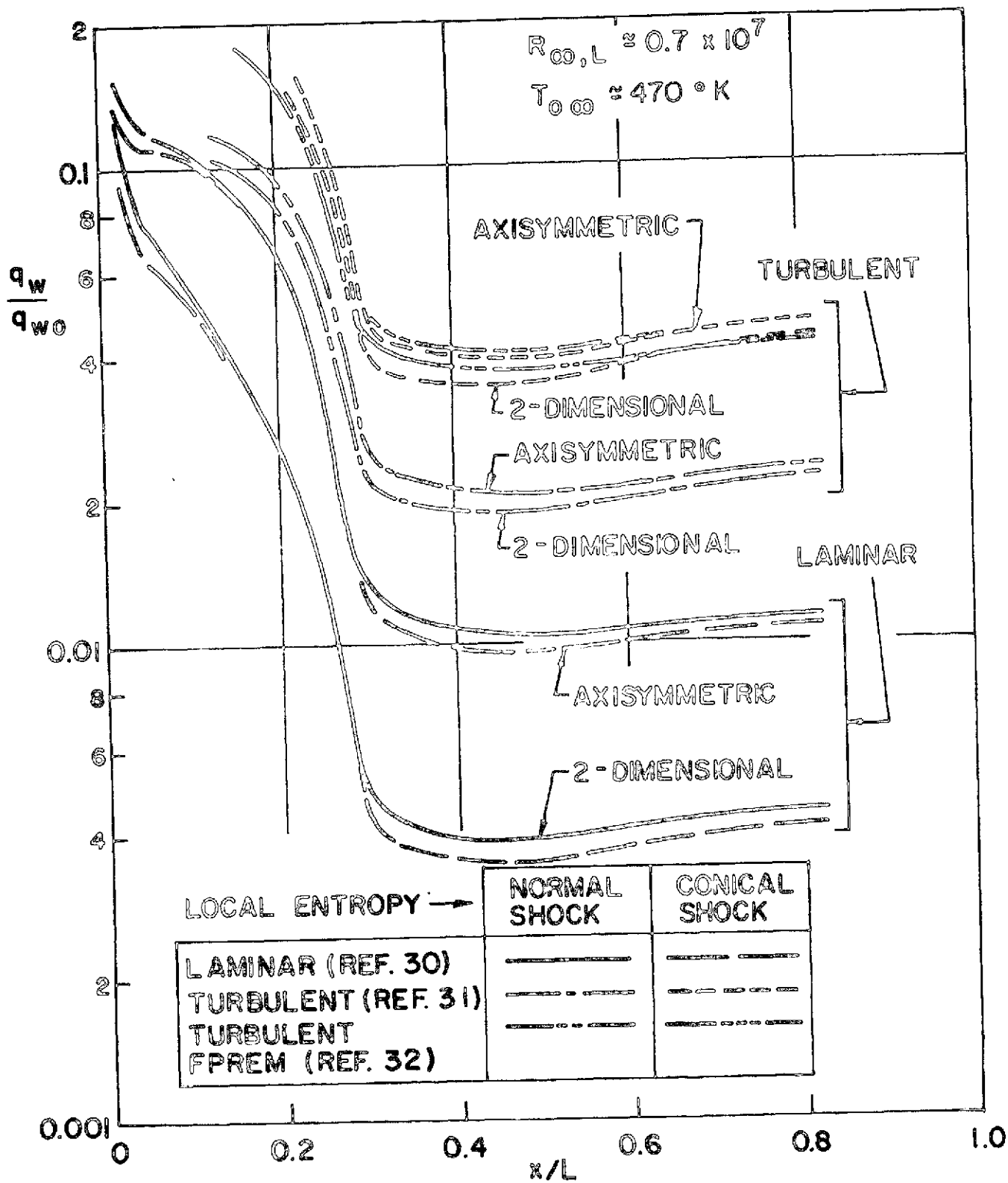


Fig. 40 Lee-Surface Heat Transfer Calculations Based on Measured Pressure Distribution ; $\alpha = 0^\circ$

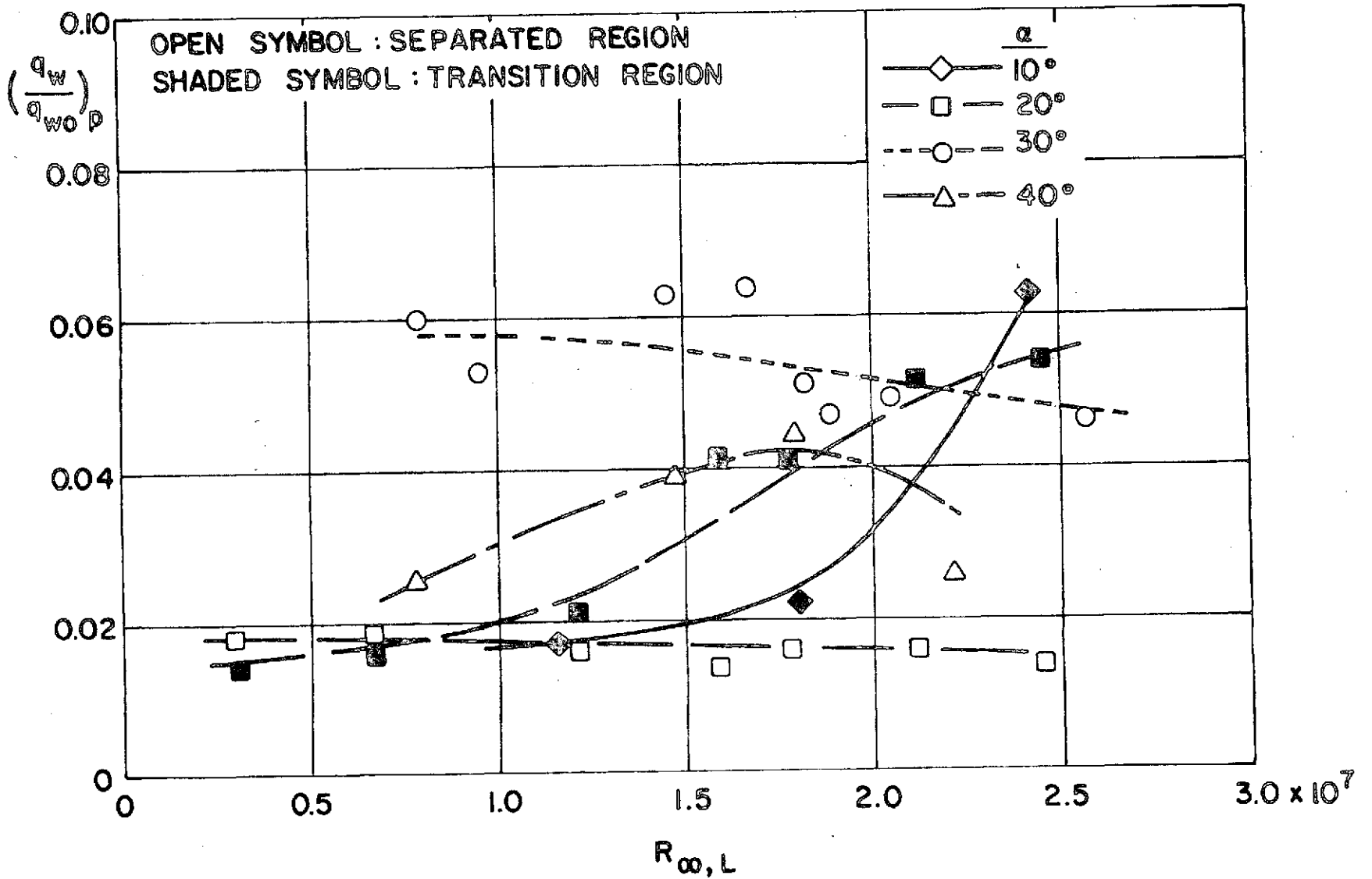


Fig. 41 Effect of Reynolds Number on Peak Heating

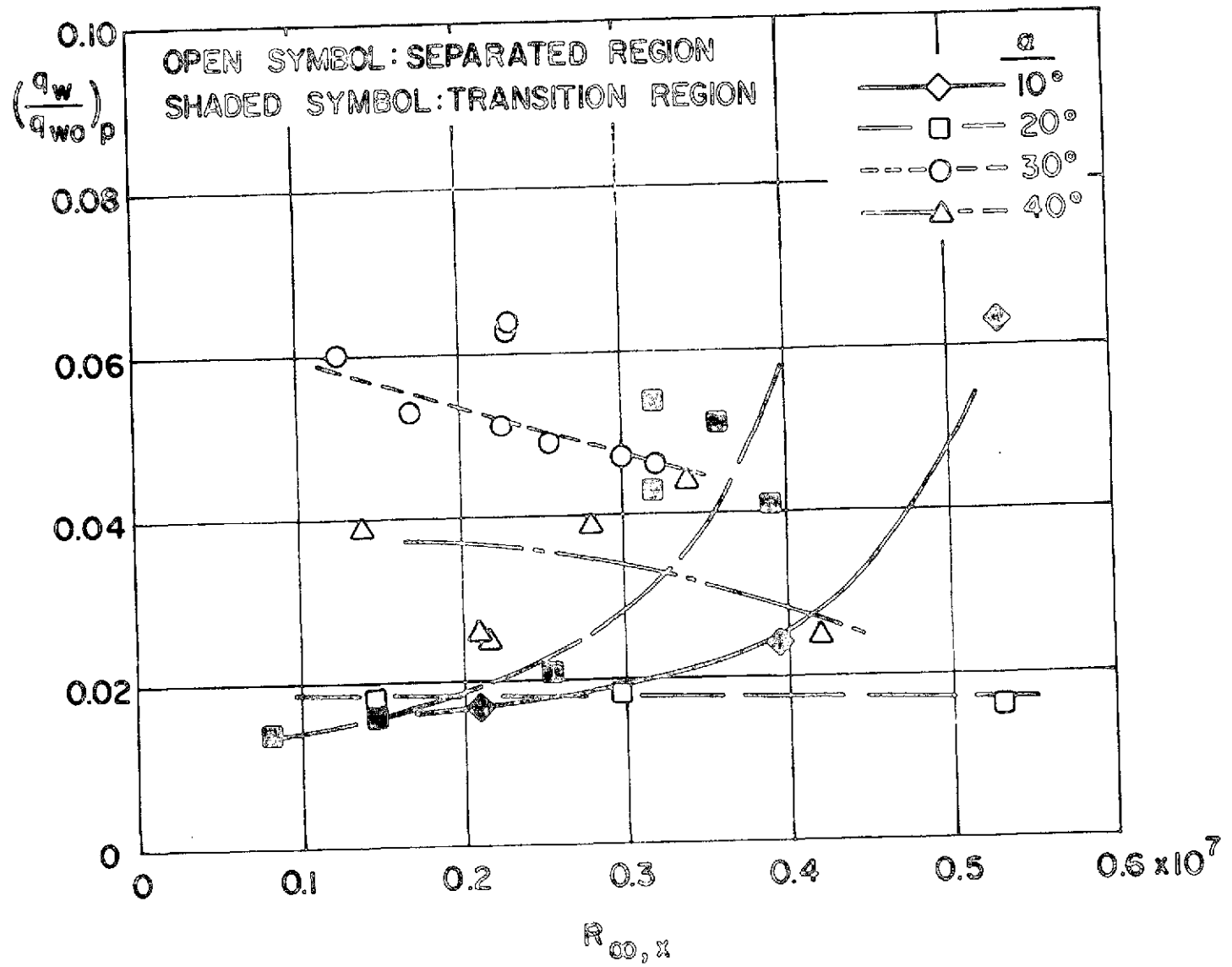


Fig. 42 Effect of Local Reynolds Number on Peak Heating

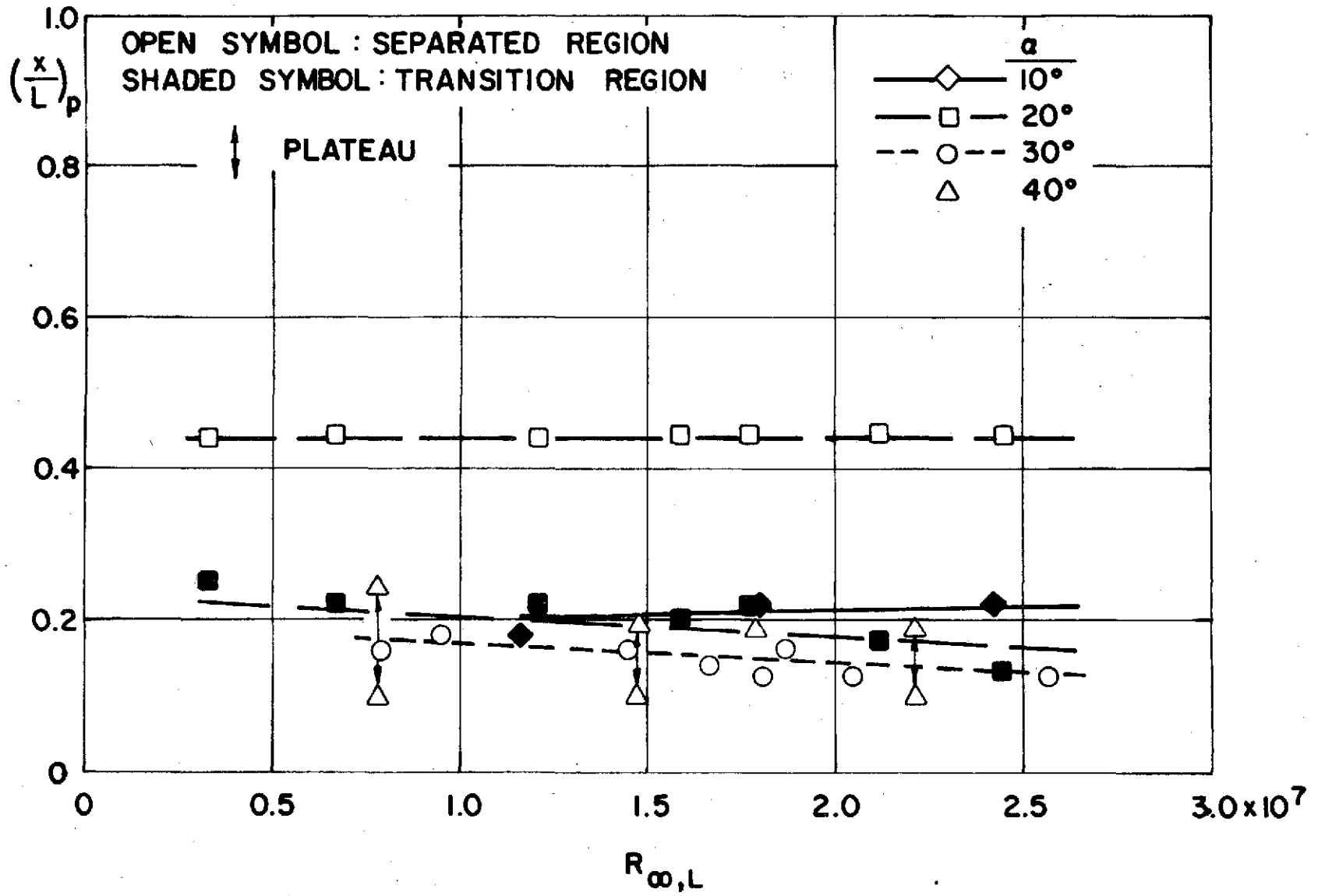


Fig. 43 Effect of Reynolds Number on Location of Peak Heating

NATIONAL BUREAU OF STANDARDS
 WASHINGTON, D. C. 20540

REPRODUCIBILITY OF THE
ORIGINAL PAGE IS POOR

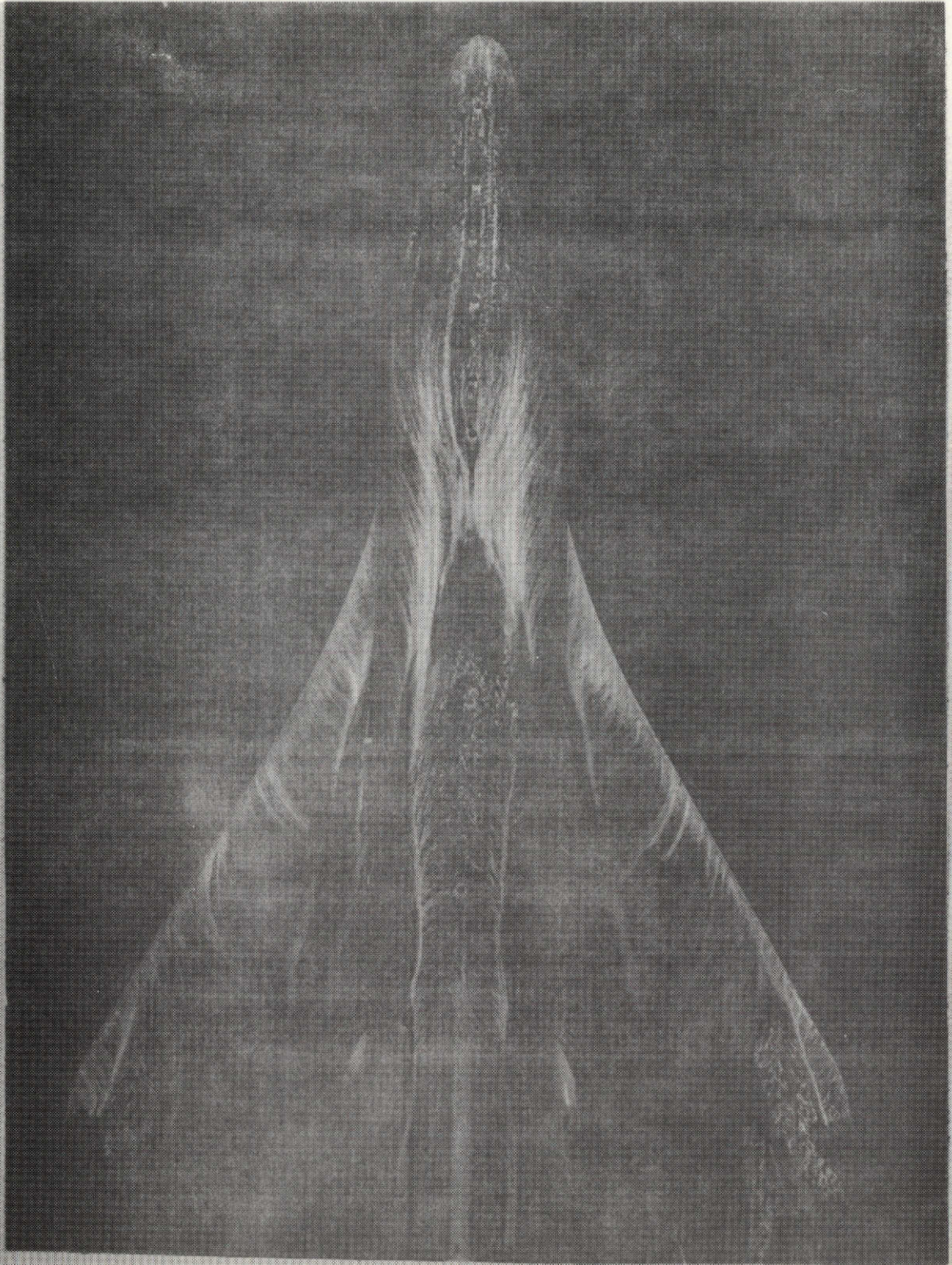


Fig. 44 Oil Flow Photograph of Space Shuttle Model; $\alpha = 10^\circ$, $R_{\infty,L} = 1.00 \times 10^7$



Fig. 45 Oil Flow Photograph of Space Shuttle Model, $\alpha = 10^\circ$, $R_{\alpha,L} = 2.27 \times 10^7$

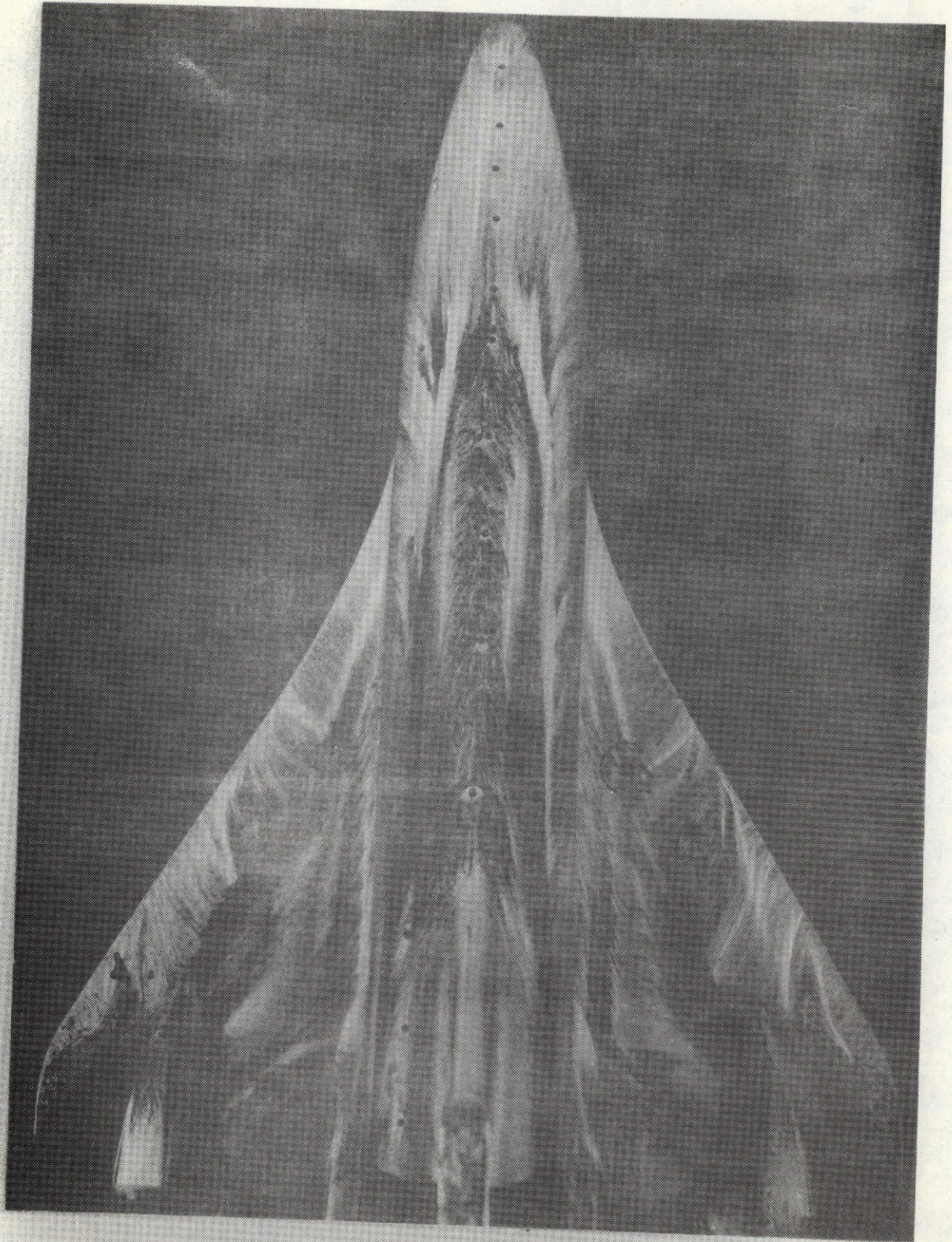


Fig. 46 Oil Flow Photograph of Space Shuttle Model, $\alpha = 20^\circ$, $R_{\infty,L} = 0.93 \times 10^7$

REPRODUCIBILITY OF THE ORIGINAL PAGE IS POOR.

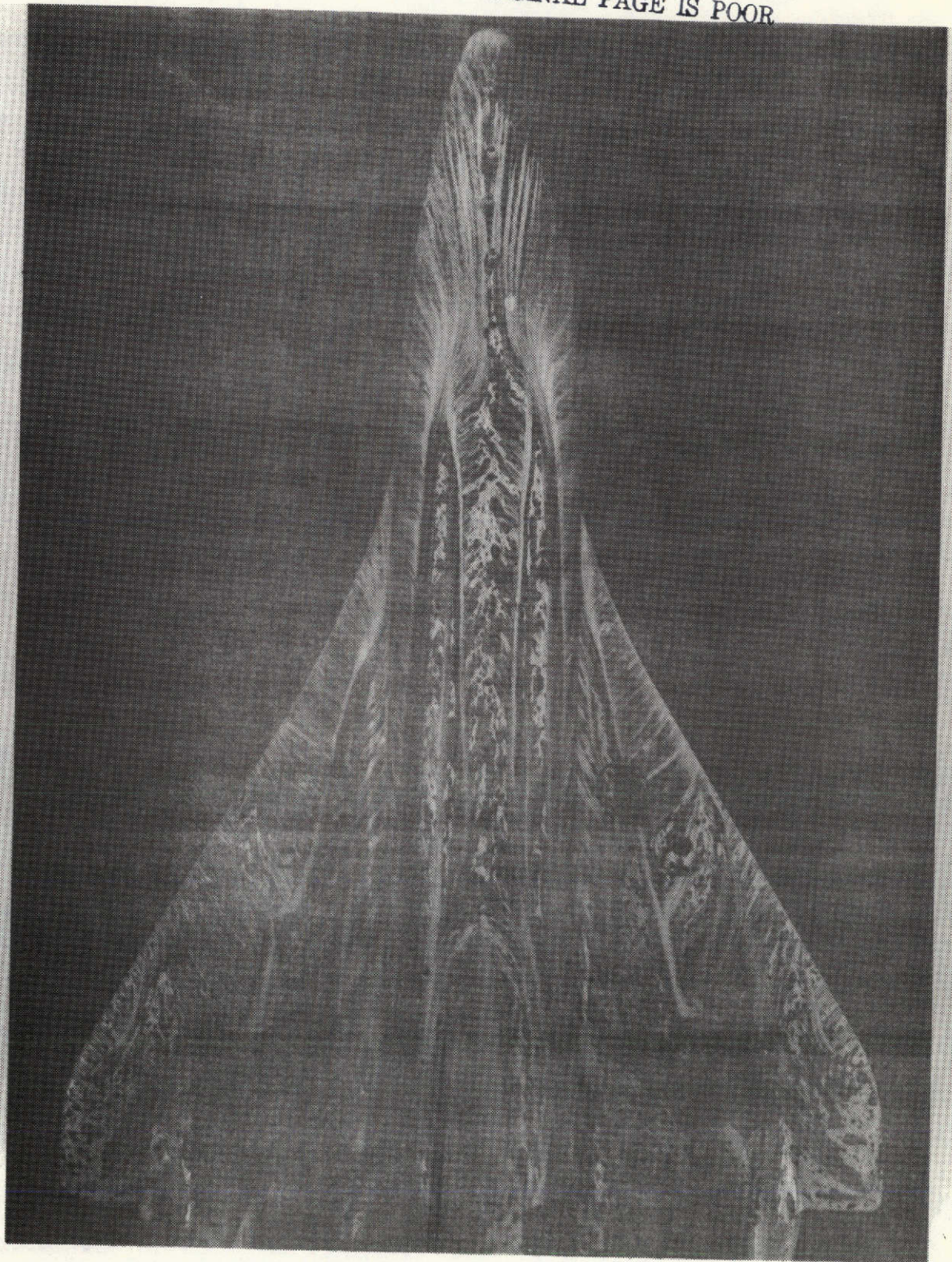


Fig. 17. (1) - (10) - $\alpha = 20^\circ$, $R_{v,1} = 2.21 \times 10^7$

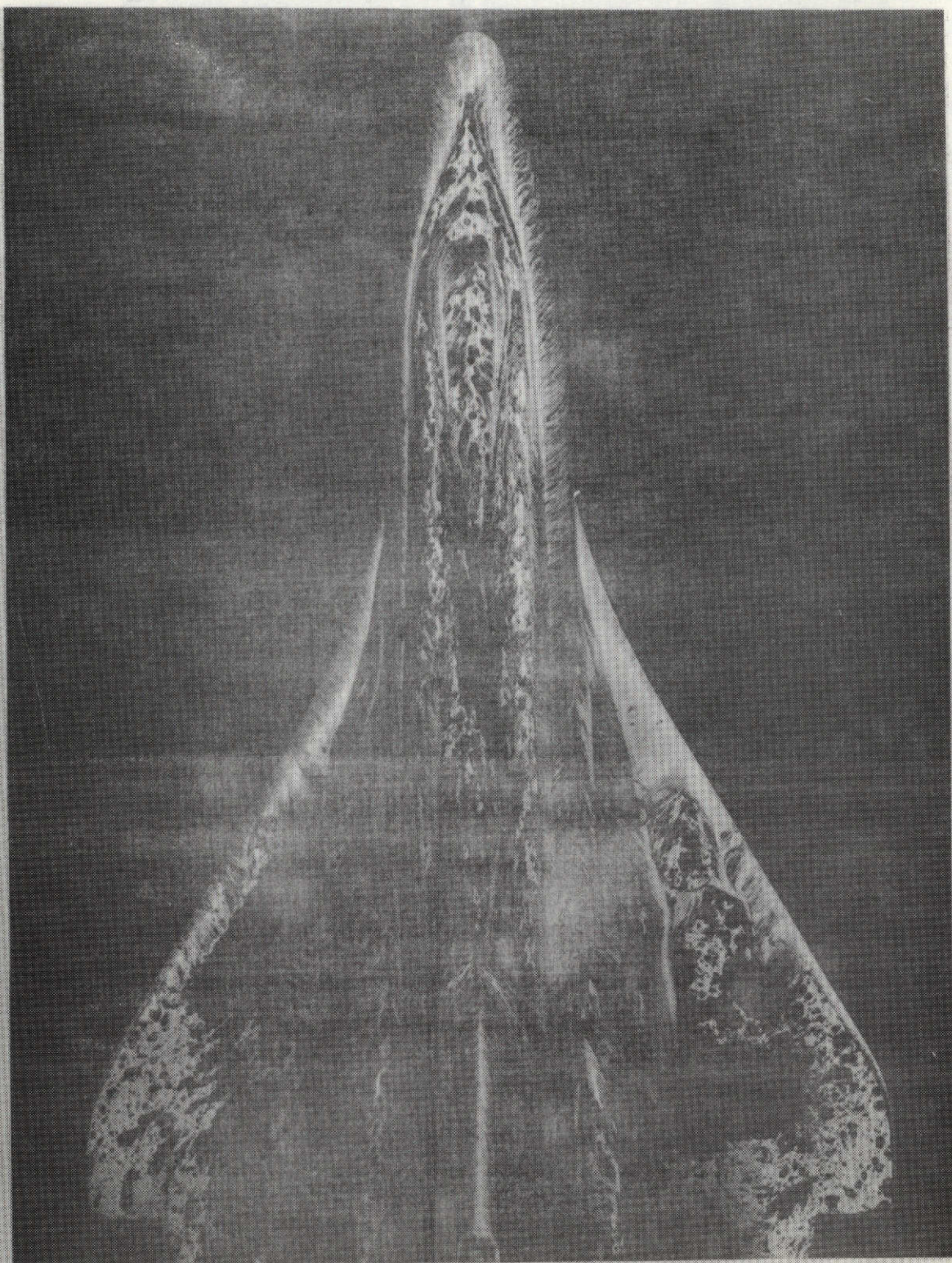


Fig. 48 Oil Flow Photograph of Space Shuttle Model; $\alpha = 30^\circ$, $R_{\infty,L} = 0.97 \times 10^7$

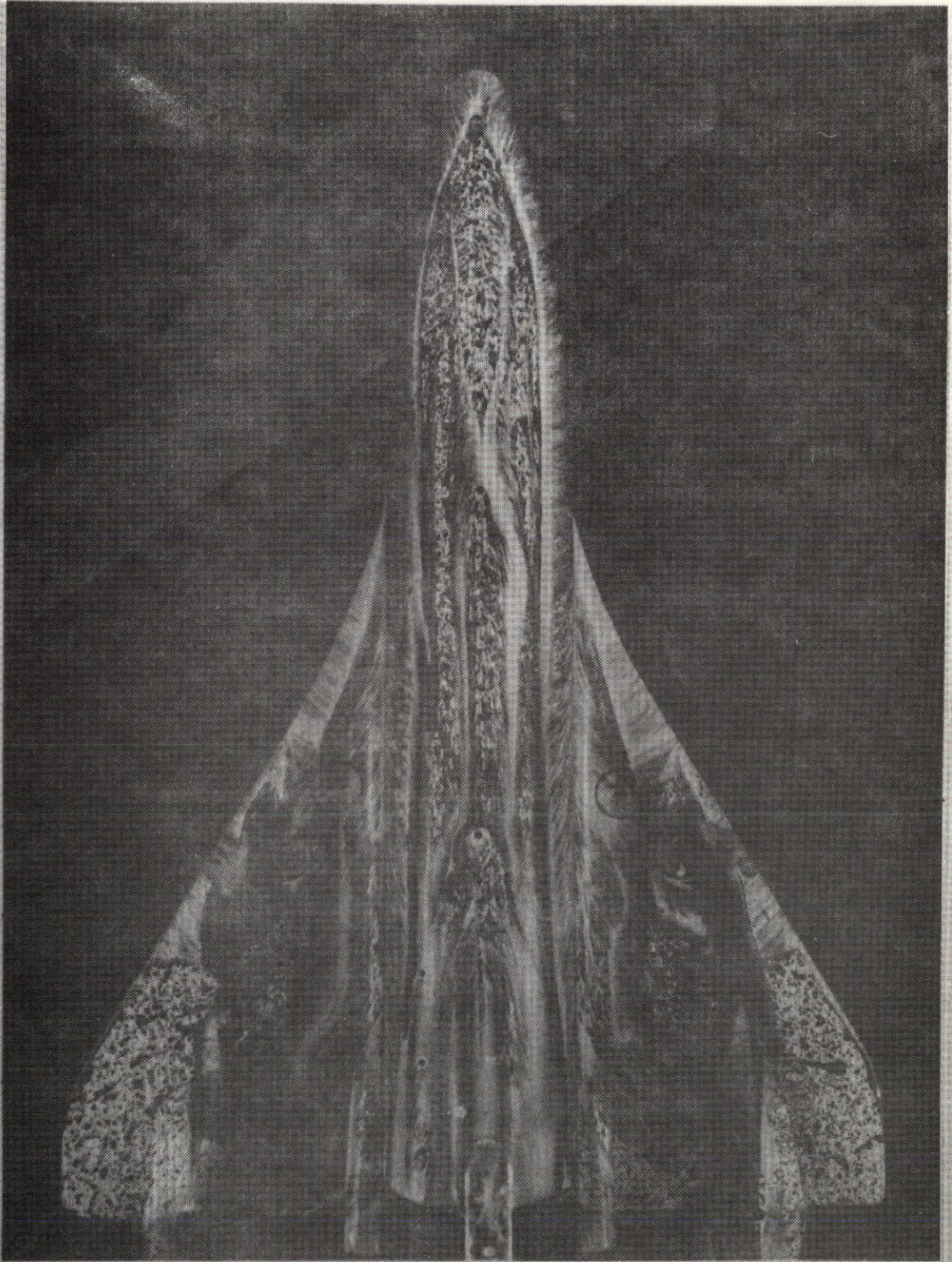


Fig. 49 Oil Flow Photograph of Space Shuttle Model; $\alpha = 30^\circ$, $R_{\infty,L} = 1.43 \times 10^7$

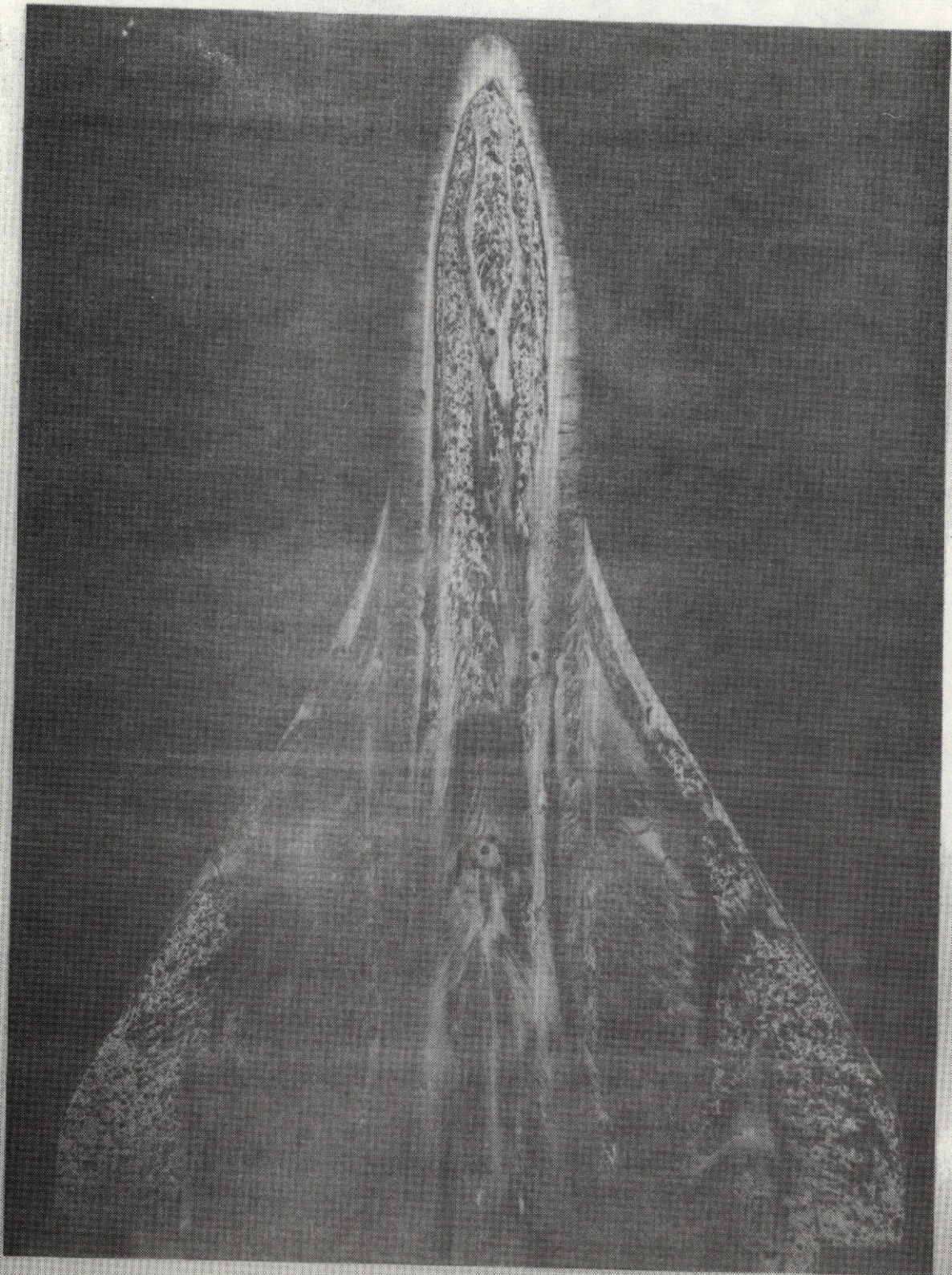


Fig. 50 Oil Flow Photograph of Space Shuttle Model; $\alpha = 40^\circ$, $R_{\infty, L} = 0.92 \times 10^7$

REPRODUCIBILITY OF THE
ORIGINAL PAGE IS POOR

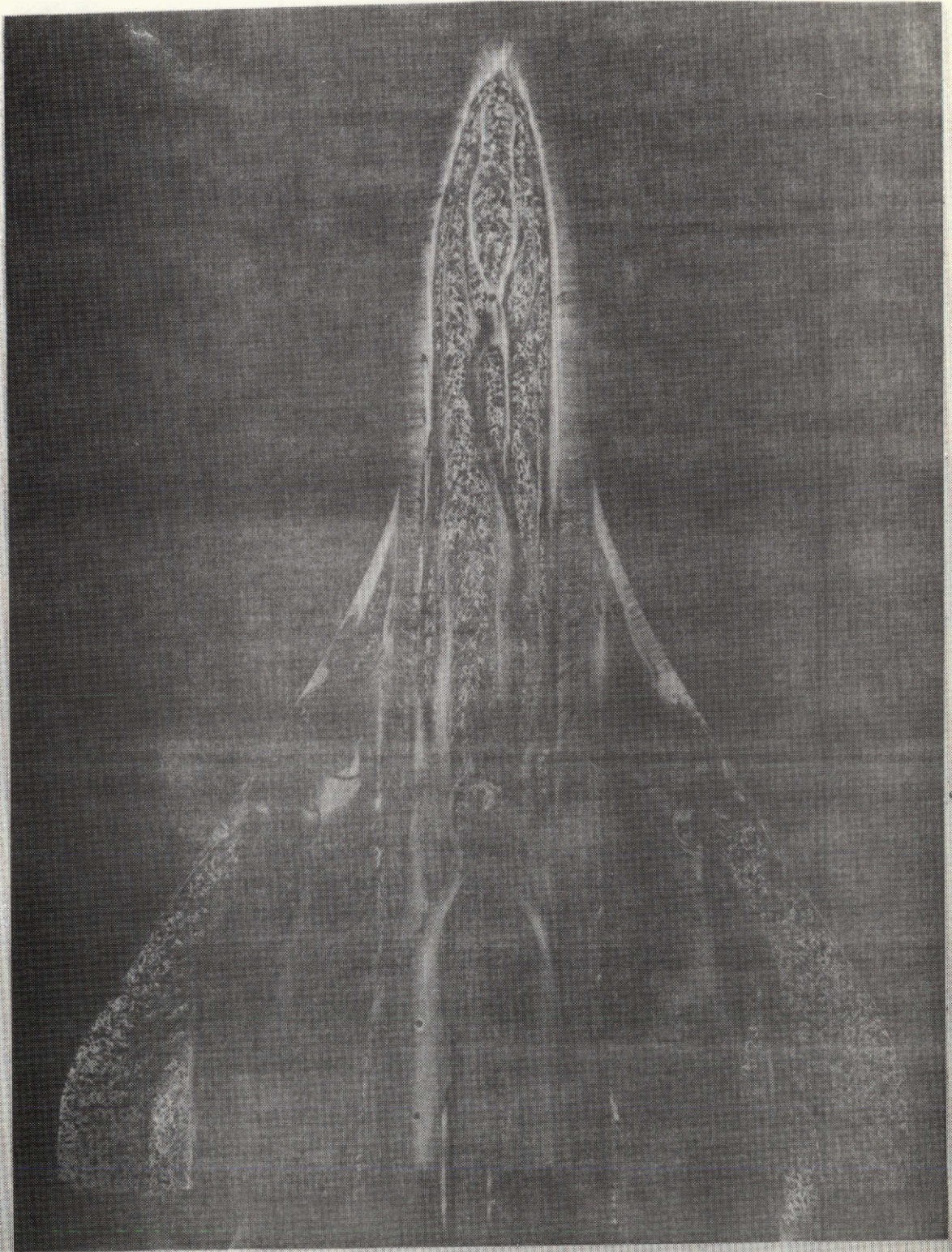
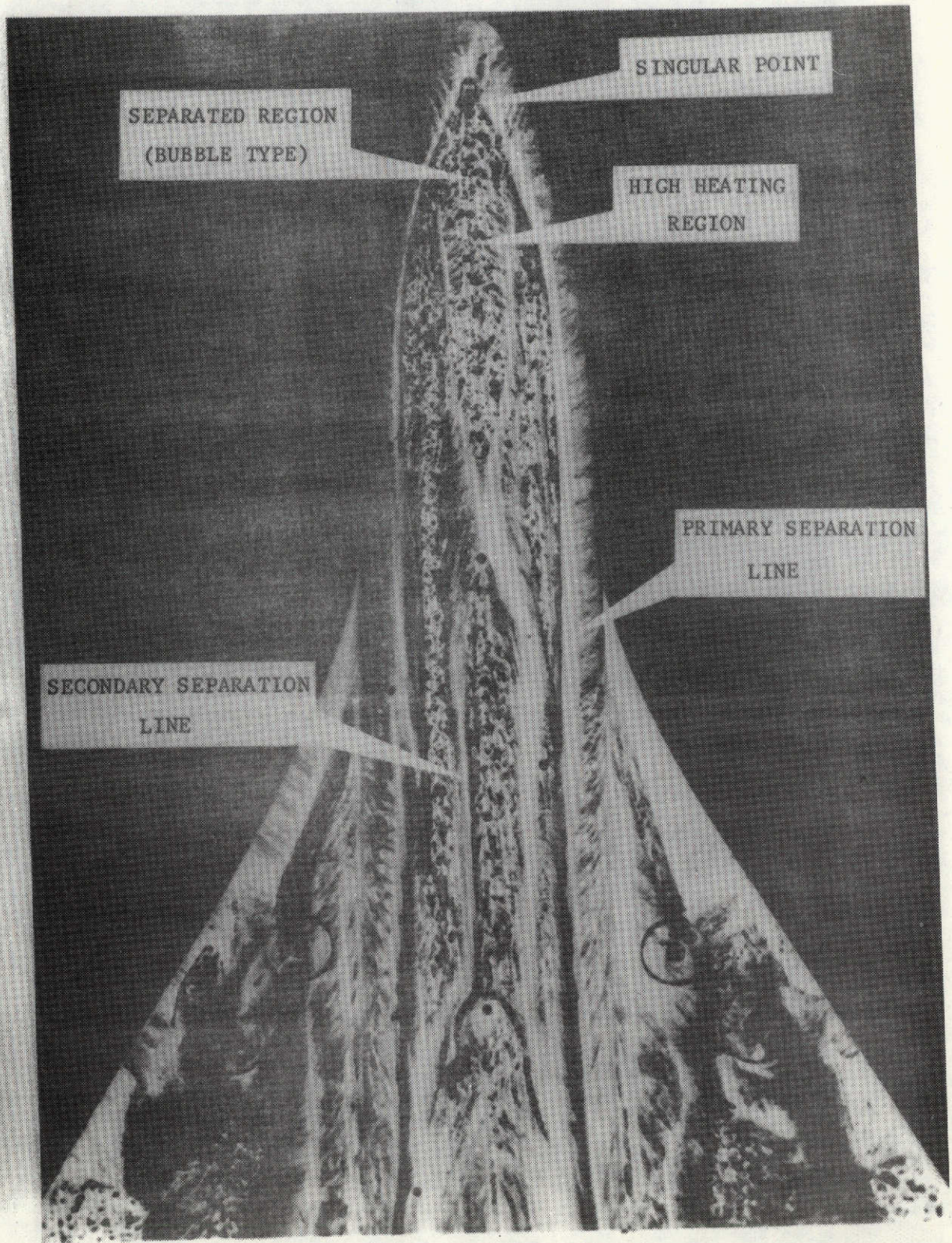


Fig. 51 Oil Flow Photograph of Space Shuttle Model; $\alpha = 40^\circ$, $R_{\infty, L} = 1.29 \times 10^7$

REPRODUCIBILITY OF THE ORIGINAL PAGE IS POOR



$$\alpha = 30^\circ, R_{\tau, \text{max}} = 1.43 \times 10^7$$

Fig. 52 Surface flow pattern near the nose of space shuttle model at large angle of attack.

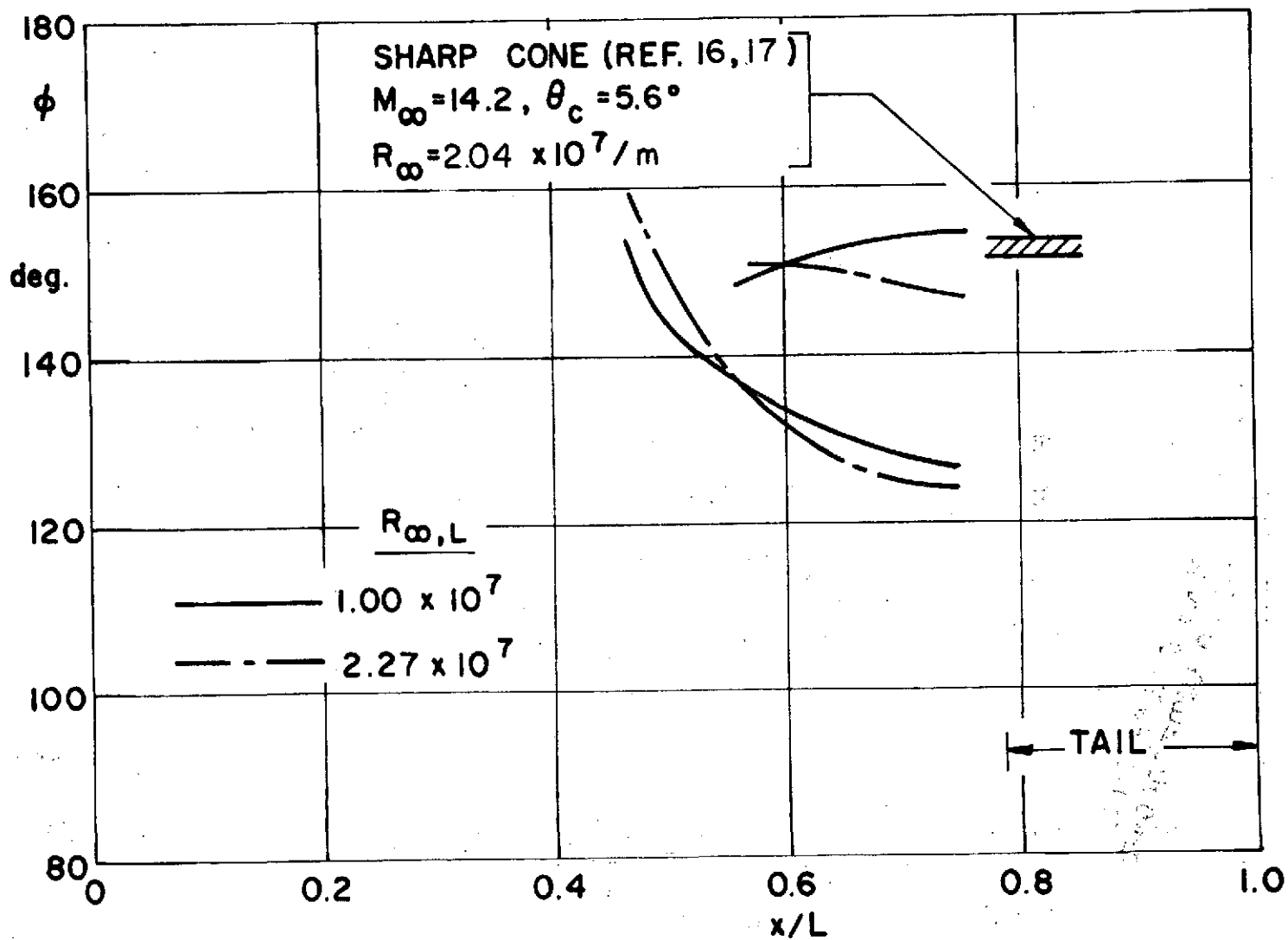


Fig. 53 Separation Lines on Space Shuttle Model ; $\alpha = 10^\circ$

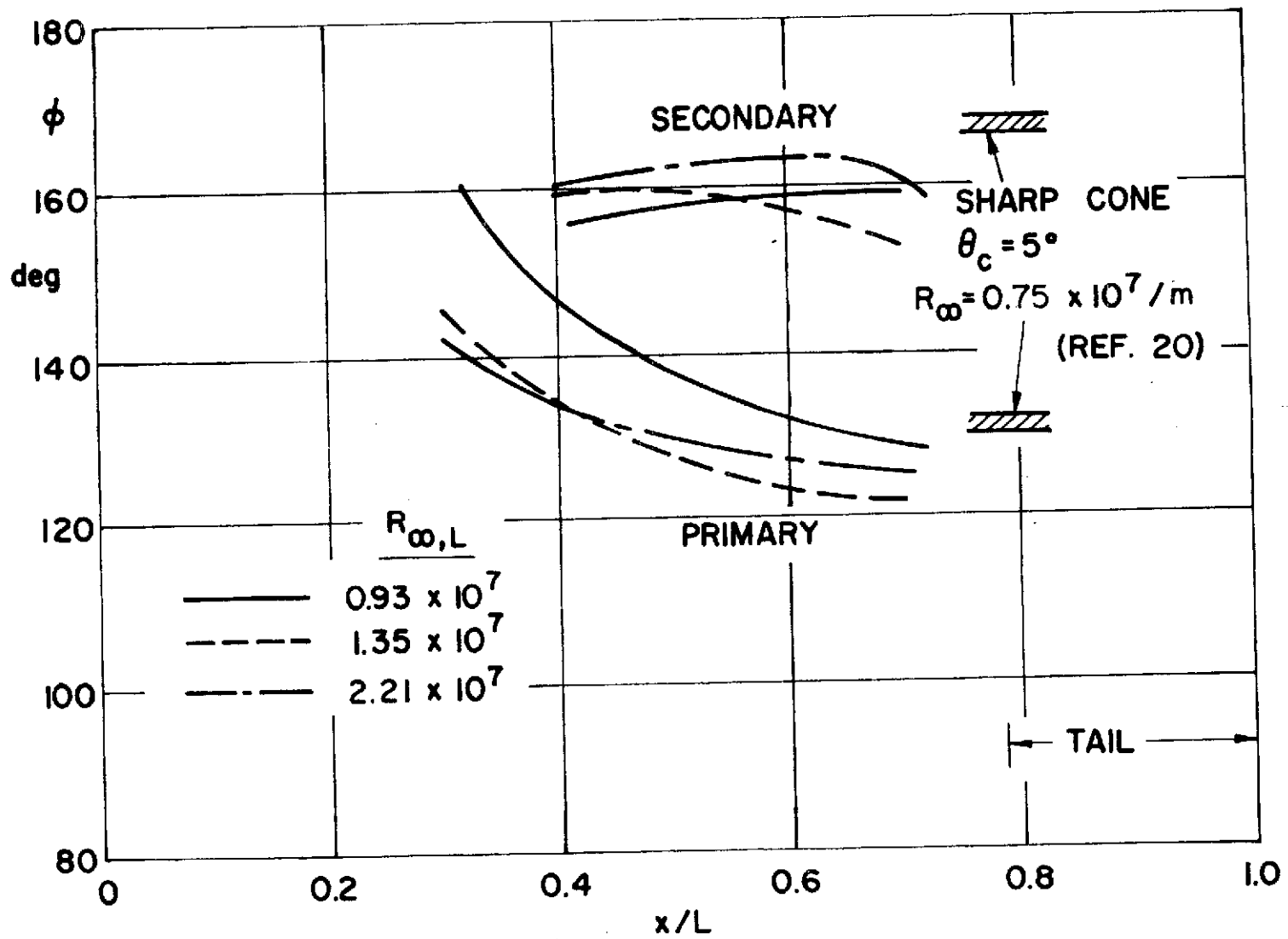


Fig. 54 Separation Lines on Space Shuttle Model ; $\alpha = 20^\circ$

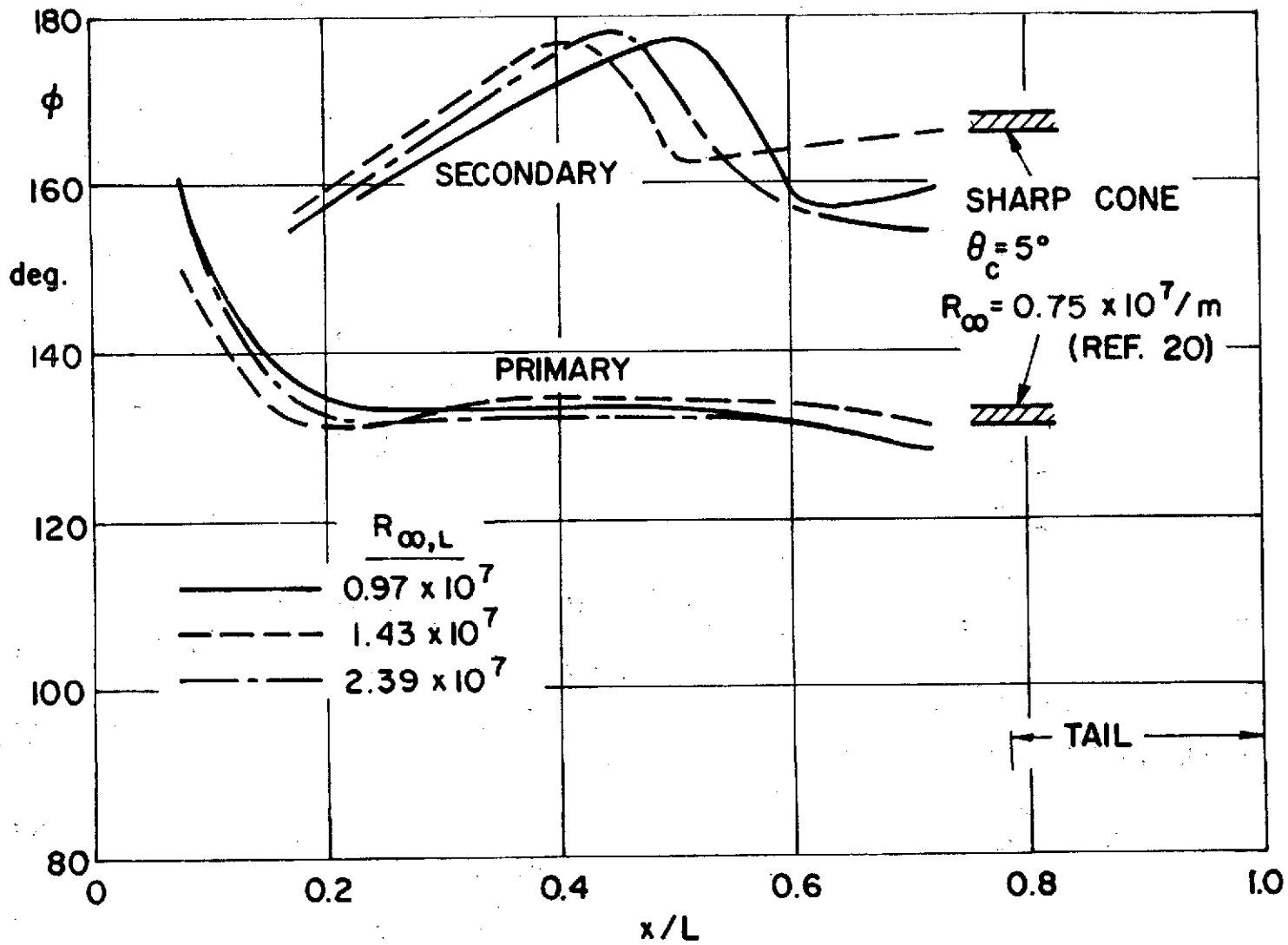


Fig. 55 Separation Lines on Space Shuttle Model ; $\alpha = 30^\circ$

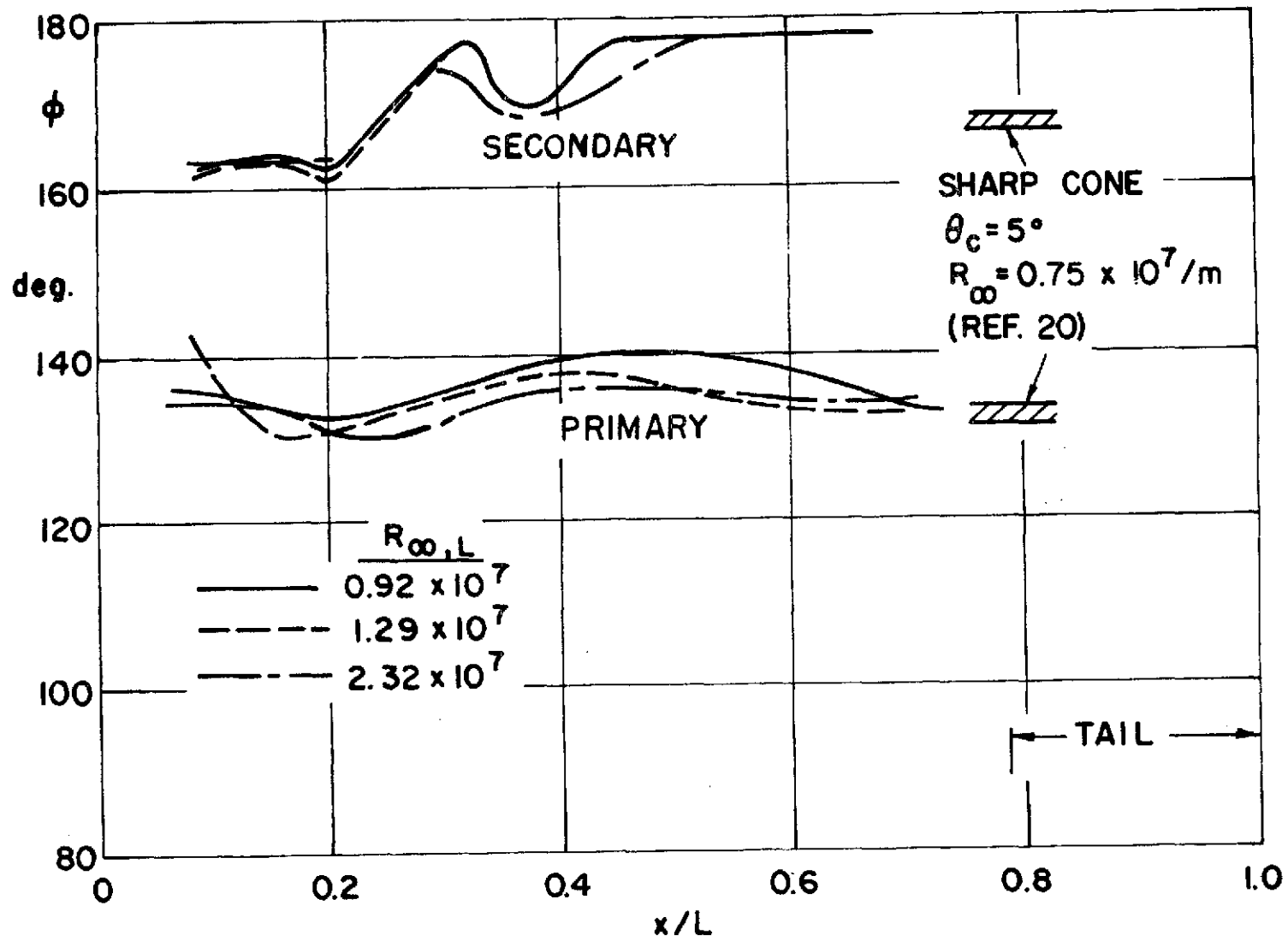


Fig. 56 Separation Lines on Space Shuttle Model ; $\alpha = 40^\circ$

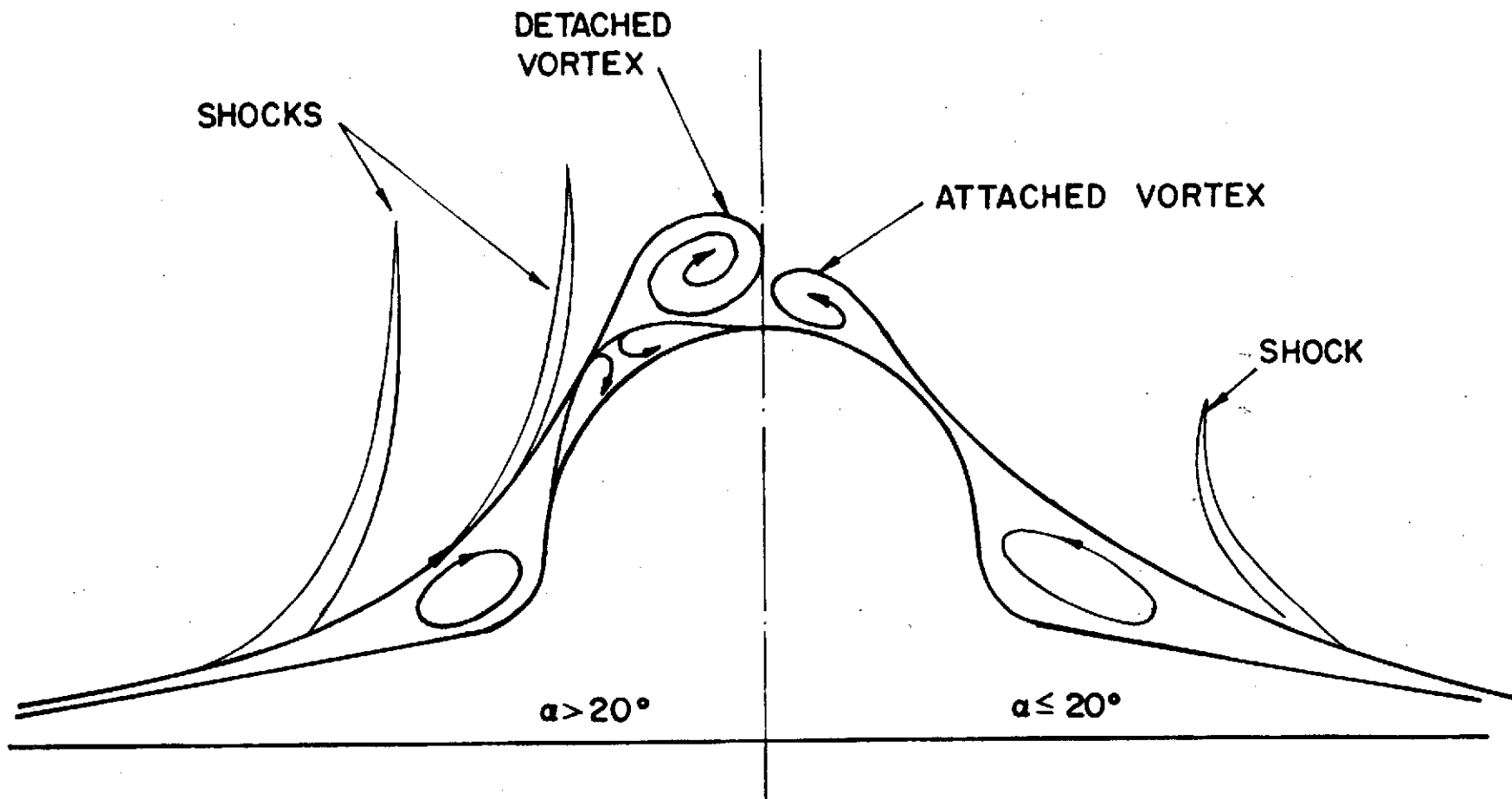


Fig. 57 Schematic of Interaction for Laminar and Turbulent Conditions

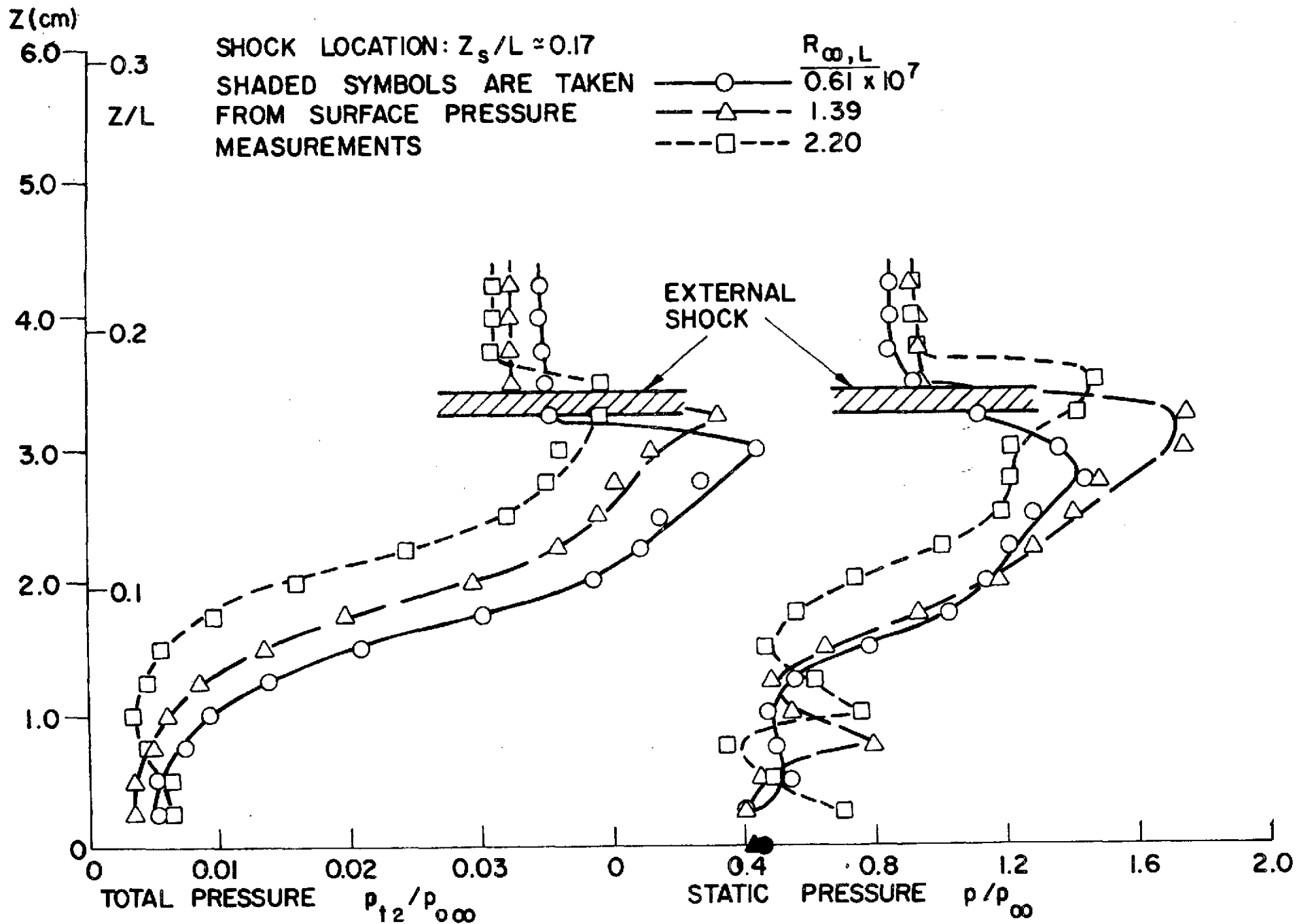


Fig. 58 Leeward Centerline Pressure Profiles ; $\alpha = 20^\circ$, $x/L = 0.326$

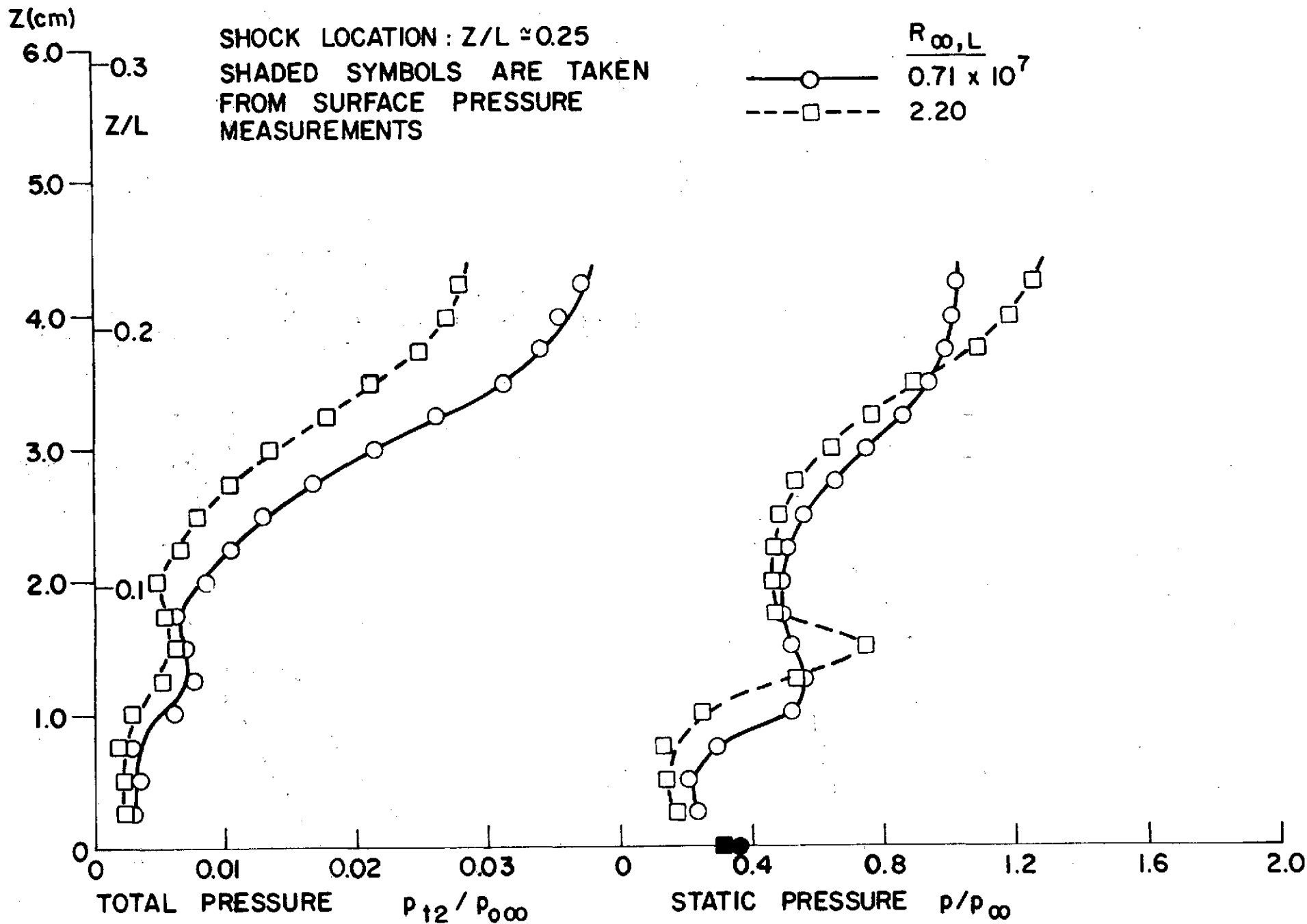


Fig. 59 Leeward Centerline Pressure Profiles ; $\alpha = 20^\circ$, $x/L = 0.457$

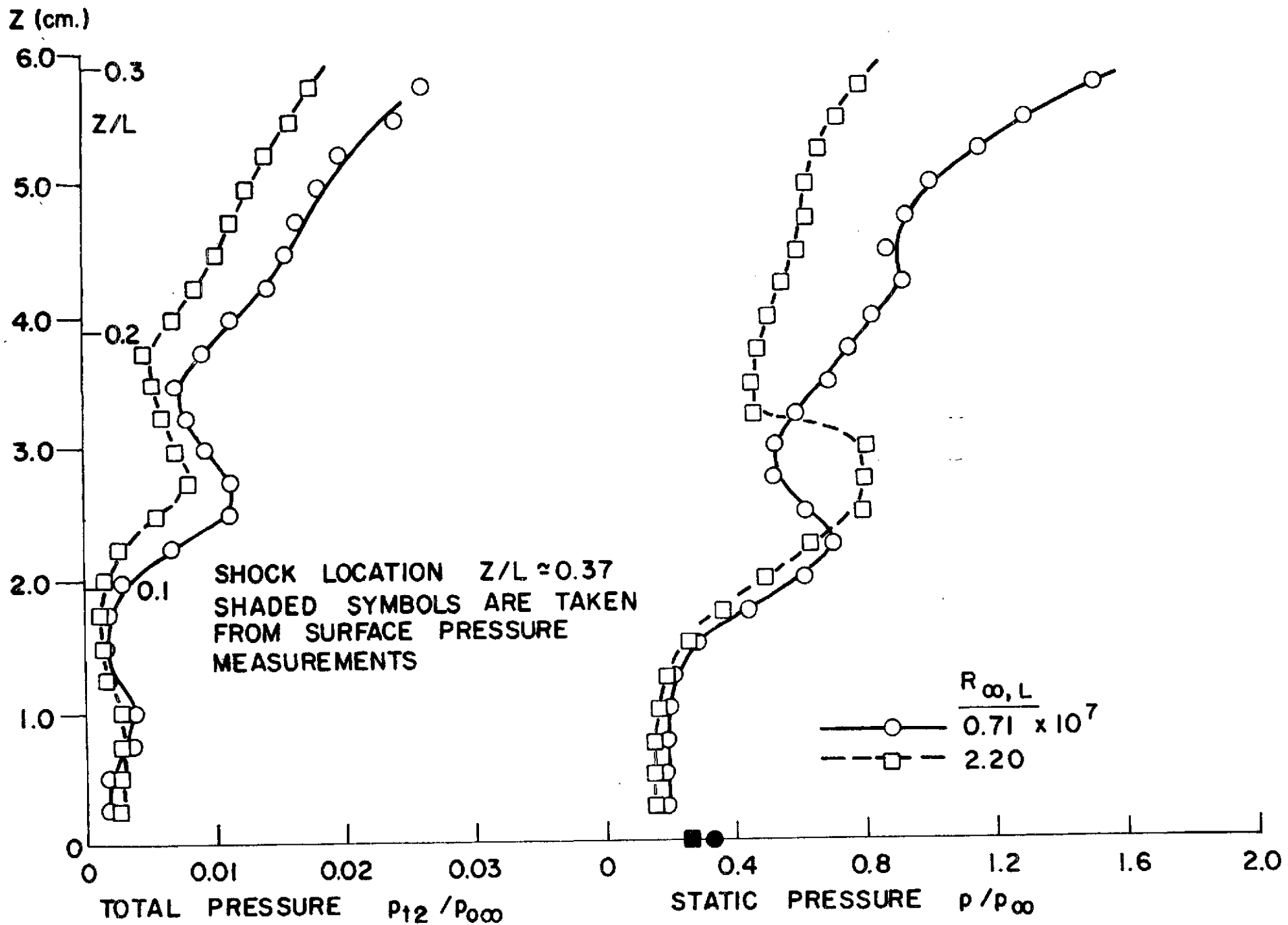


Fig. 60 Leeward Centerline Pressure Profiles ; $\alpha = 20^\circ$, $x/L = 0.654$

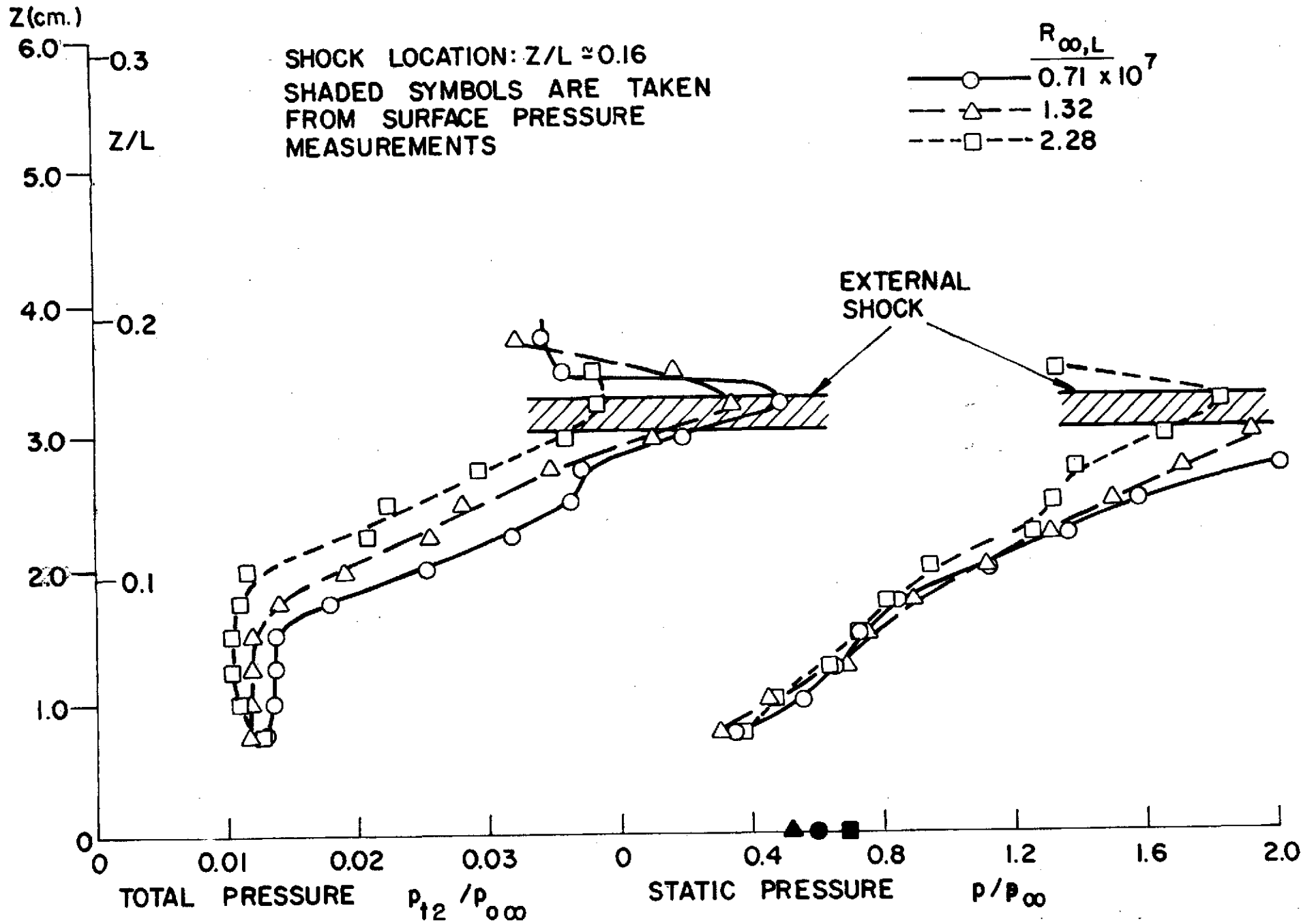


Fig. 61 Leeward Centerline Pressure Profiles ; $\alpha = 30^\circ$, $x/L = 0.203$

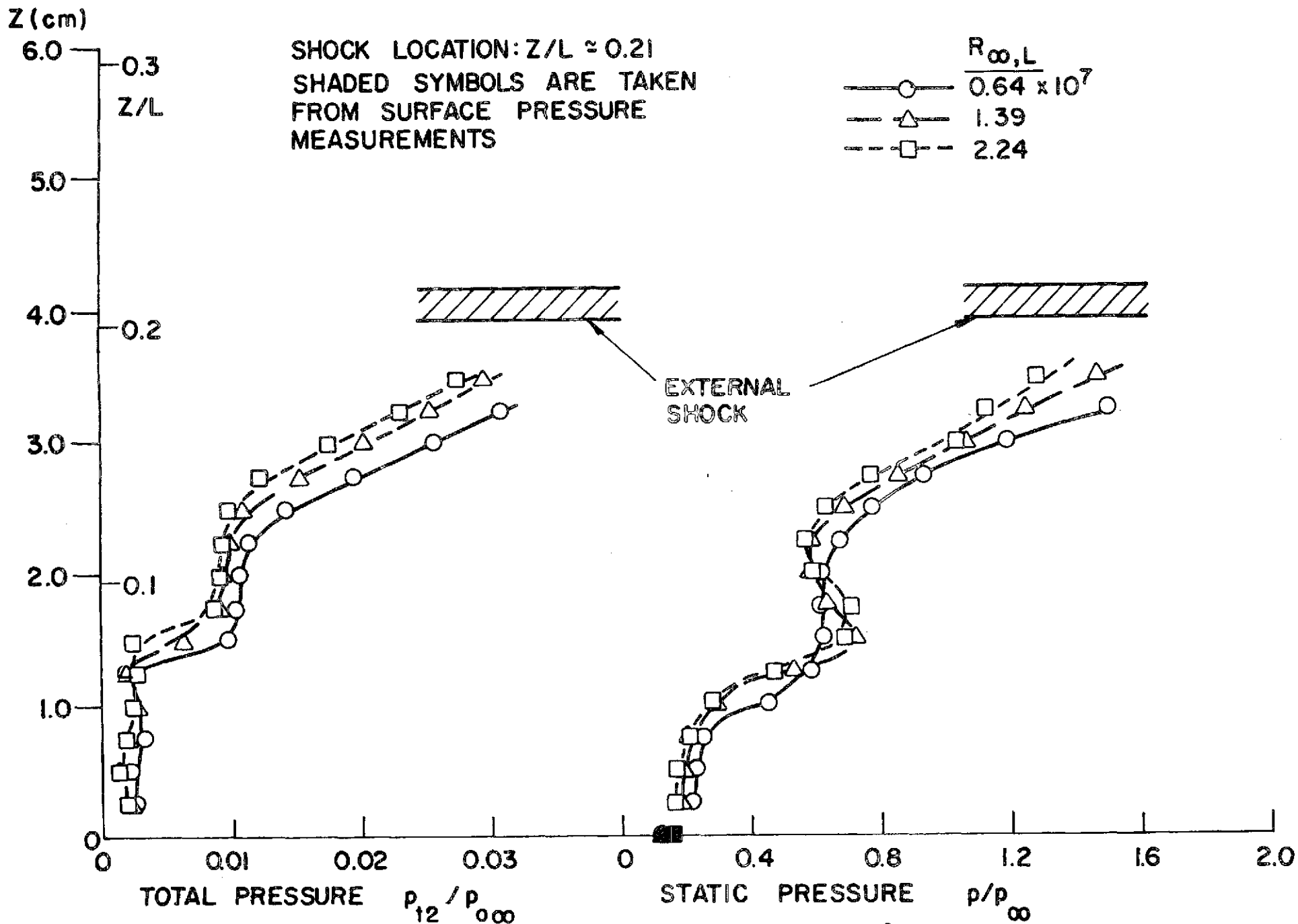


Fig. 62 Leeward Centerline Pressure Profiles ; $\alpha = 30^\circ$, $x/L = 0.282$

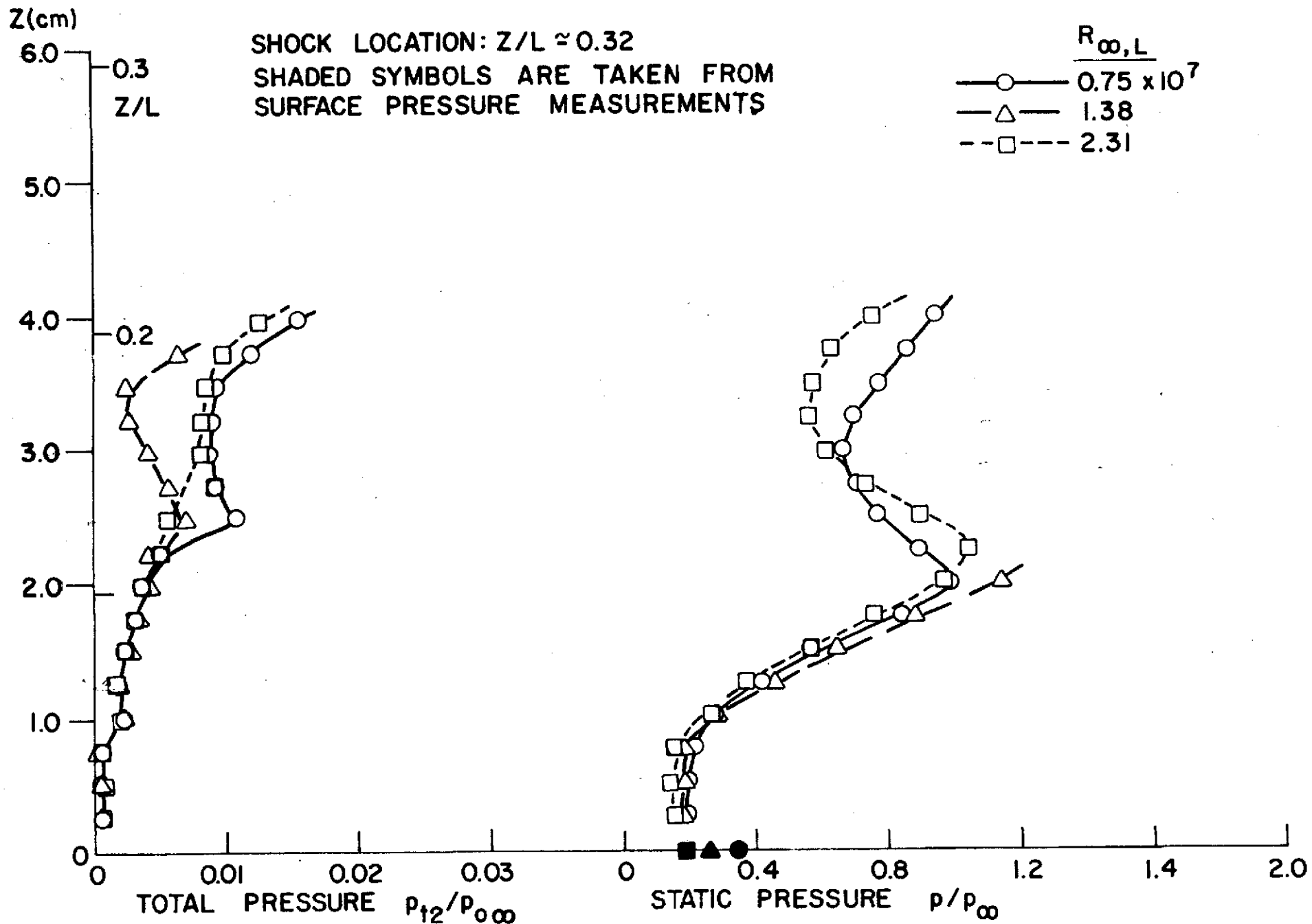


Fig. 63 Leeward Centerline Pressure Profiles ; $\alpha = 30^\circ$, $x/L = 0.407$

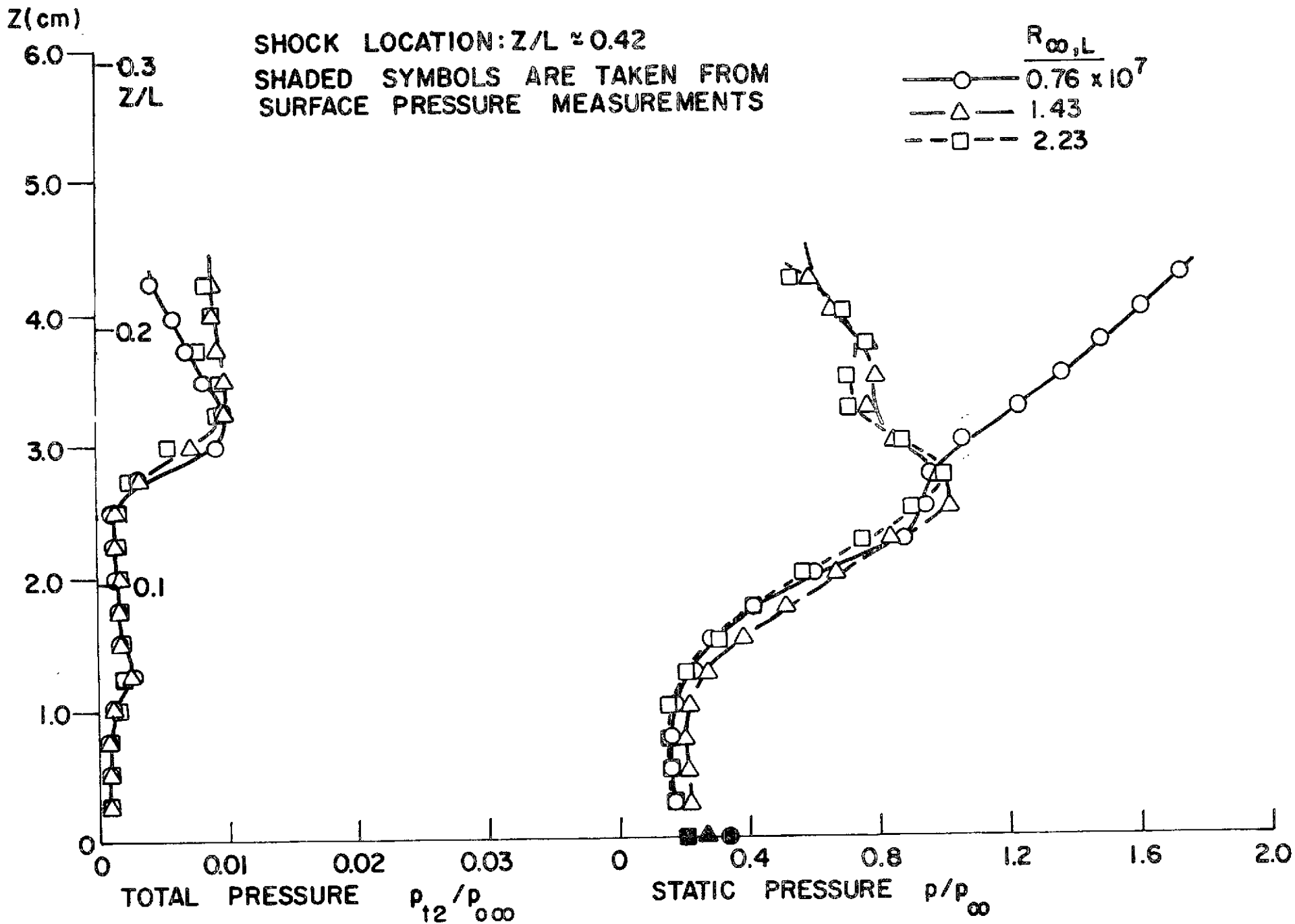


Fig. 64 Leeward Centerline Pressure Profiles ; $\alpha = 30^\circ$, $x/L = 0.520$

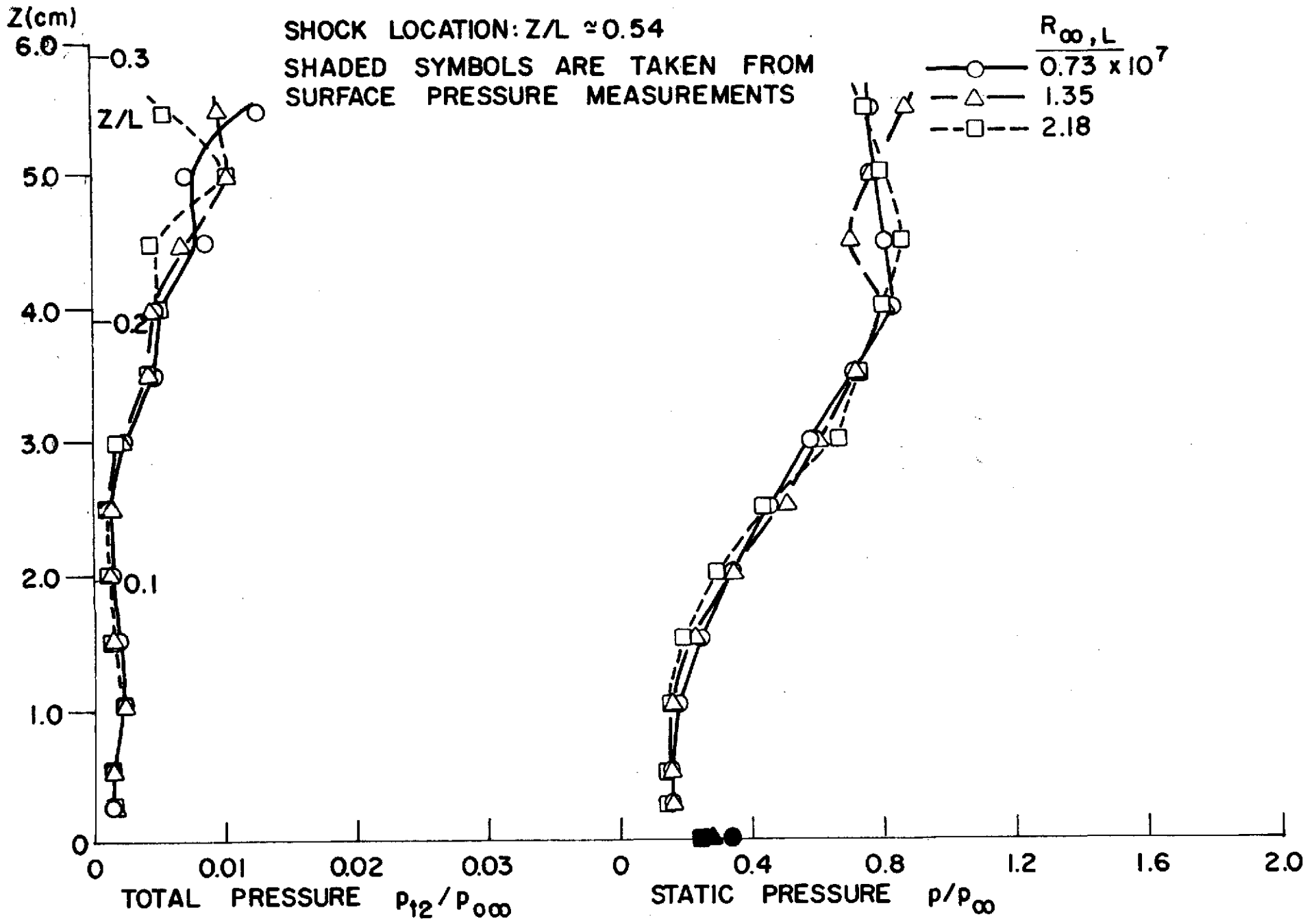


Fig. 65 Leeward Centerline Pressure Profiles ; $\alpha = 30^\circ$, $x/L = 0.654$

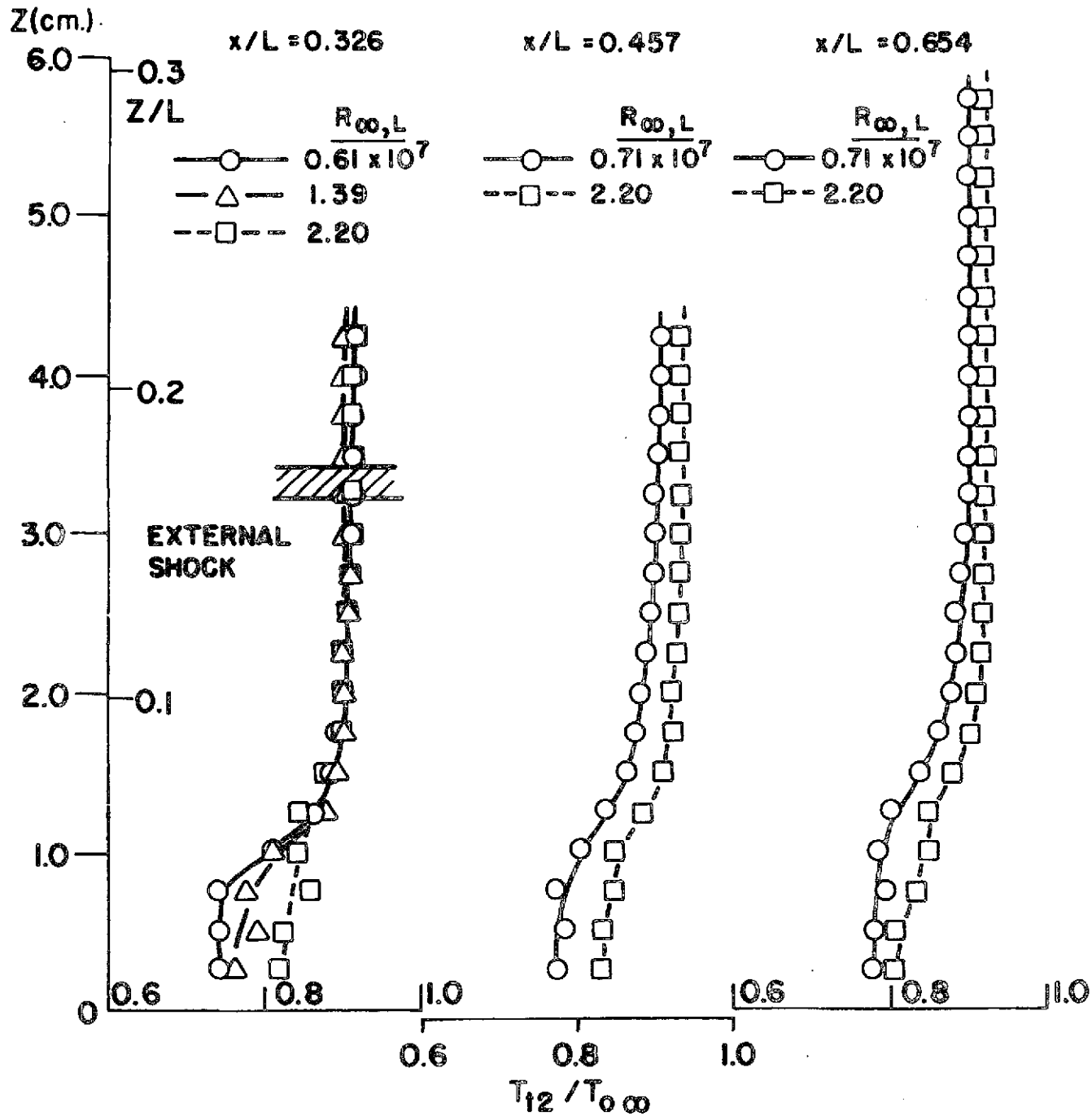


Fig. 66 Leeward Centerline Total Temperature Profiles ; $\alpha = 20^\circ$

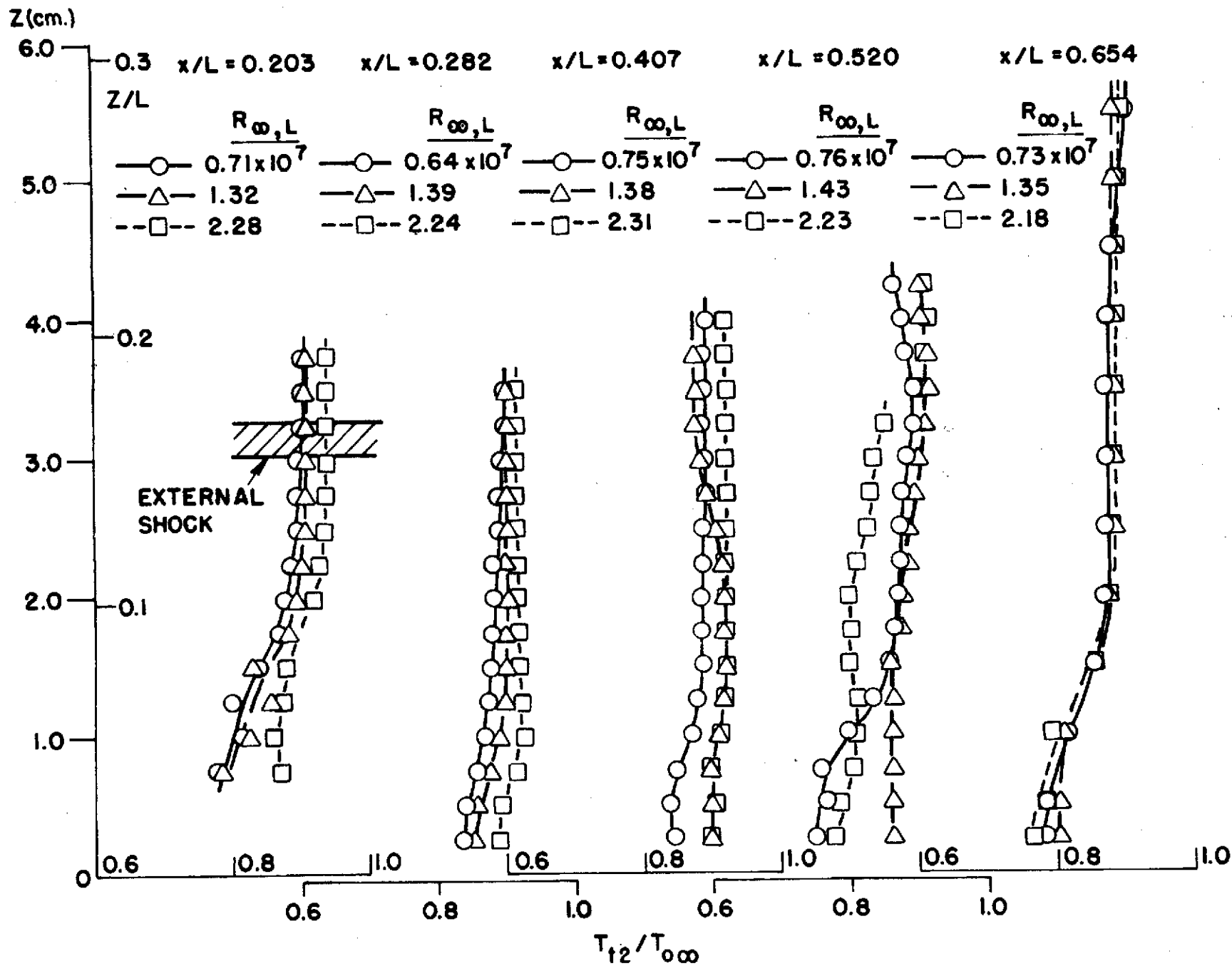


Fig. 67 Leeward Centerline Total Temperature Profiles ; $\alpha = 30^\circ$

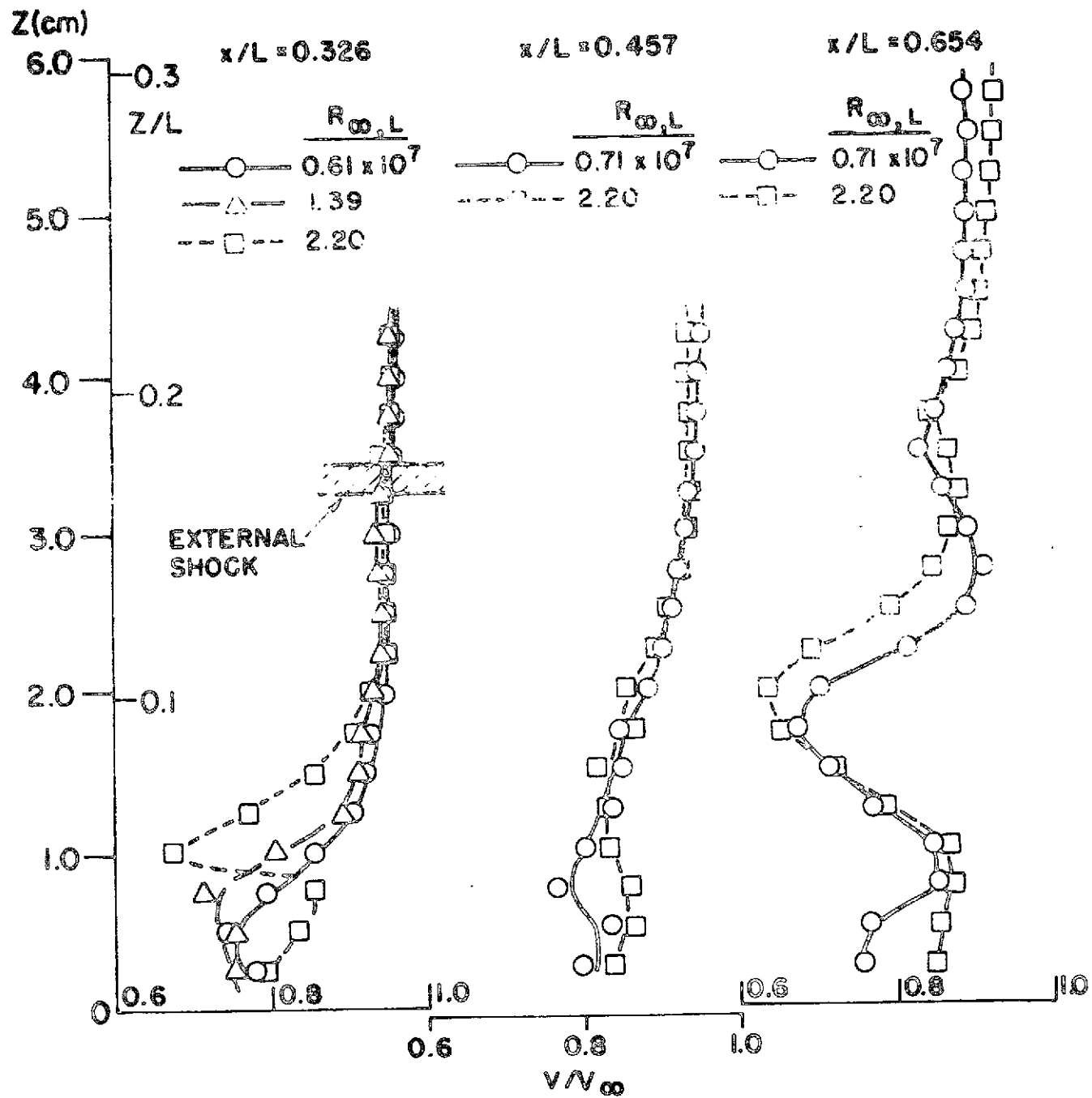


Fig. 68 Leeward Centerline Velocity Profiles : $\gamma = 20^\circ$

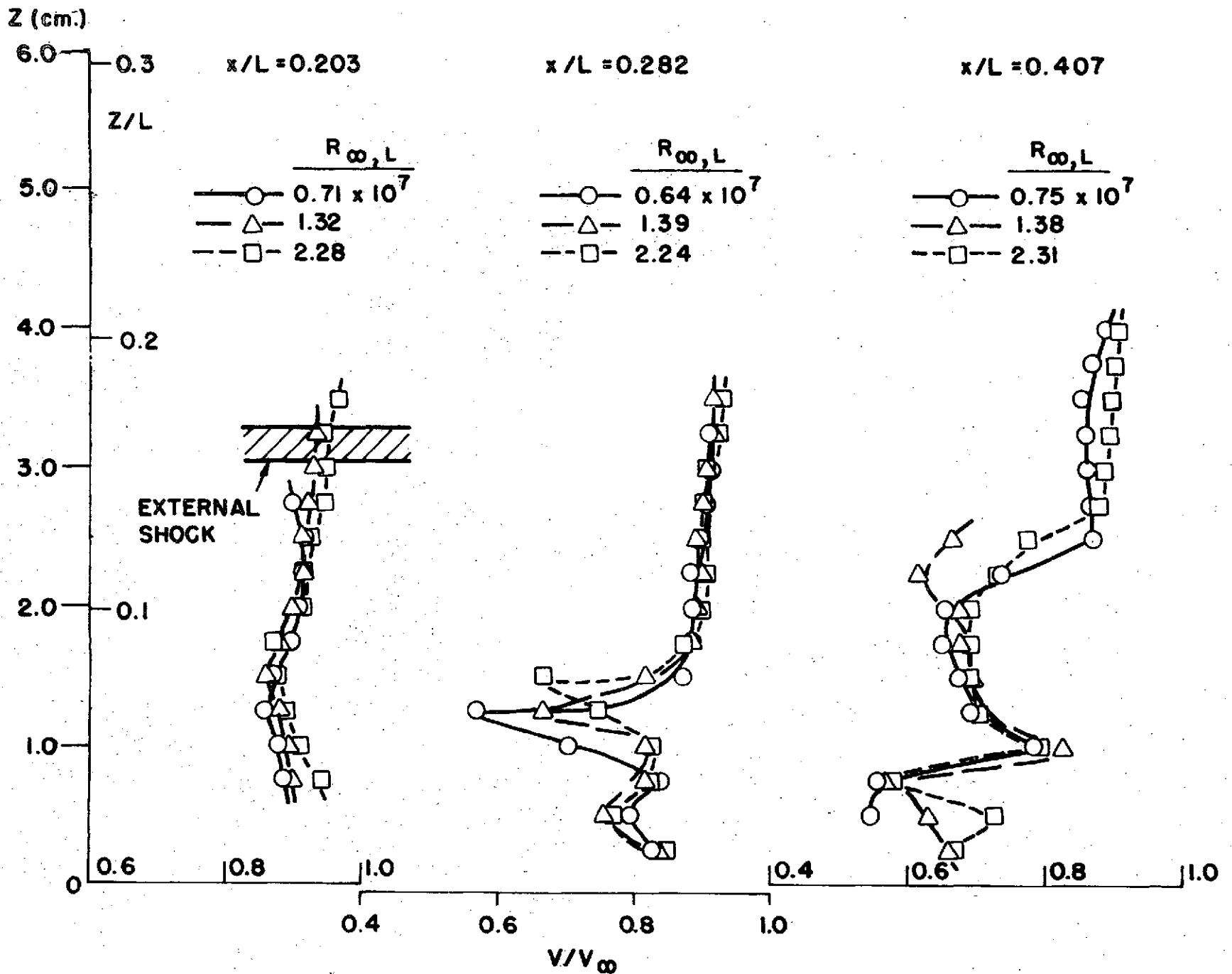


Fig. 69 Leeward Centerline Velocity Profiles ; $\alpha = 30^\circ$, $x/L = 0.203, 0.282, 0.407$

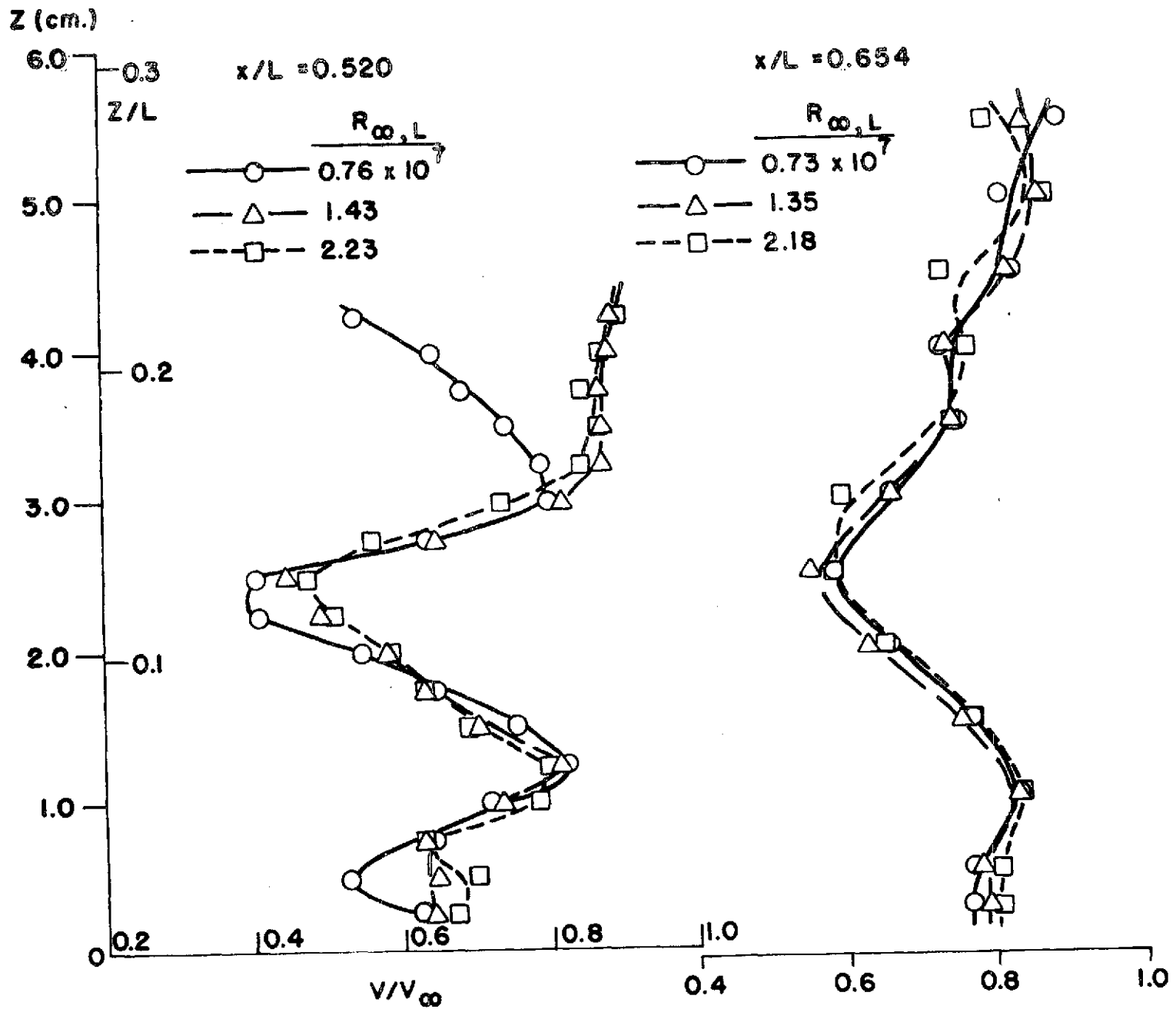
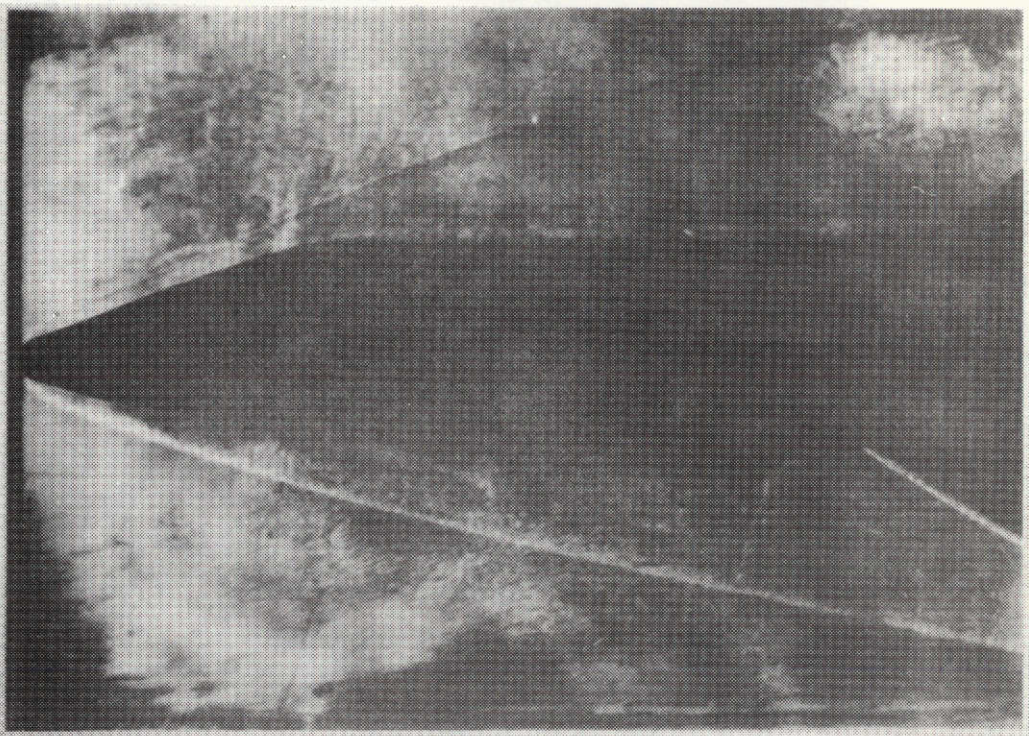


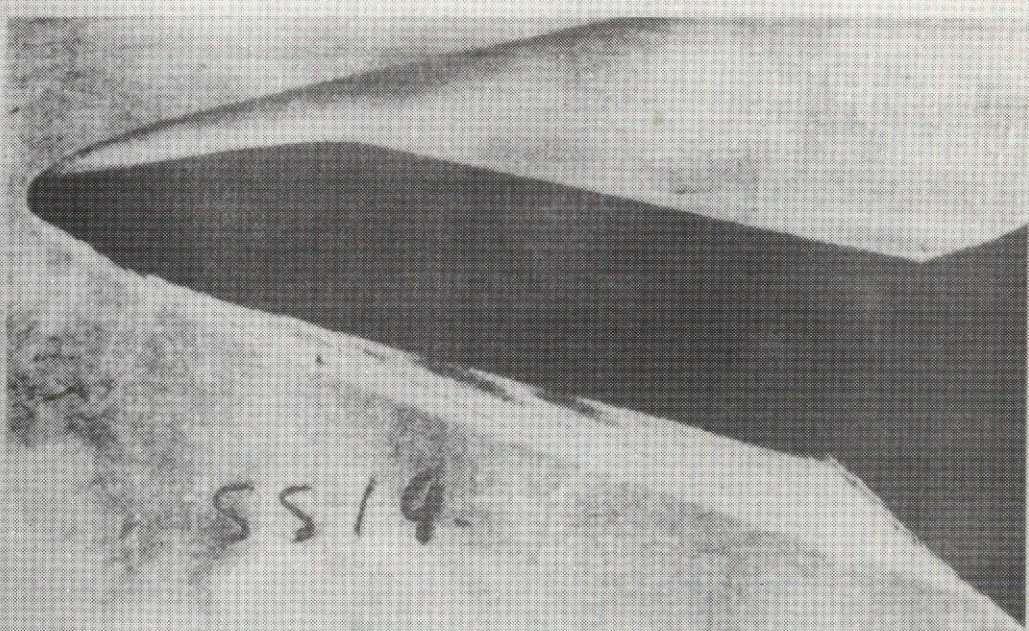
Fig. 70 Leeward Centerline Velocity Profiles ; $\alpha = 30^\circ$, $x/L = 0.520, 0.654$

REPRODUCIBILITY OF THE ORIGINAL PAGE IS POOR

REPRODUCIBILITY OF THE ORIGINAL PAGE IS POOR



a) $\alpha = 0^\circ$, $R_{\infty,L} = 0.32 \times 10^7$

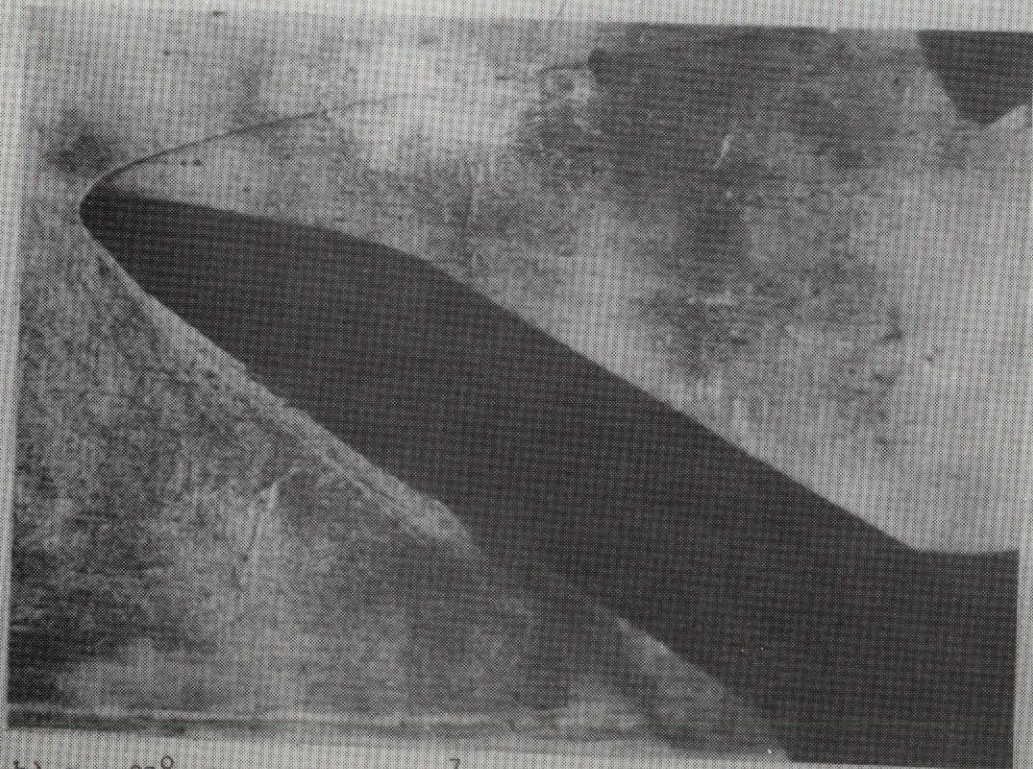


b) $\alpha = 10^\circ$, $R_{\infty,L} = 1.80 \times 10^7$

Fig. 71 Schlieren Photographs of Space Shuttle Model; $\alpha = 0^\circ, 10^\circ$



a) $\alpha = 20^\circ$, $R_{\infty,L} = 0.33 \times 10^7$



b) $\alpha = 30^\circ$, $R_{\infty,L} = 0.67 \times 10^7$

Fig. 72 Schlieren Photograph of Space Shuttle Model; $\alpha = 20^\circ, 30^\circ$

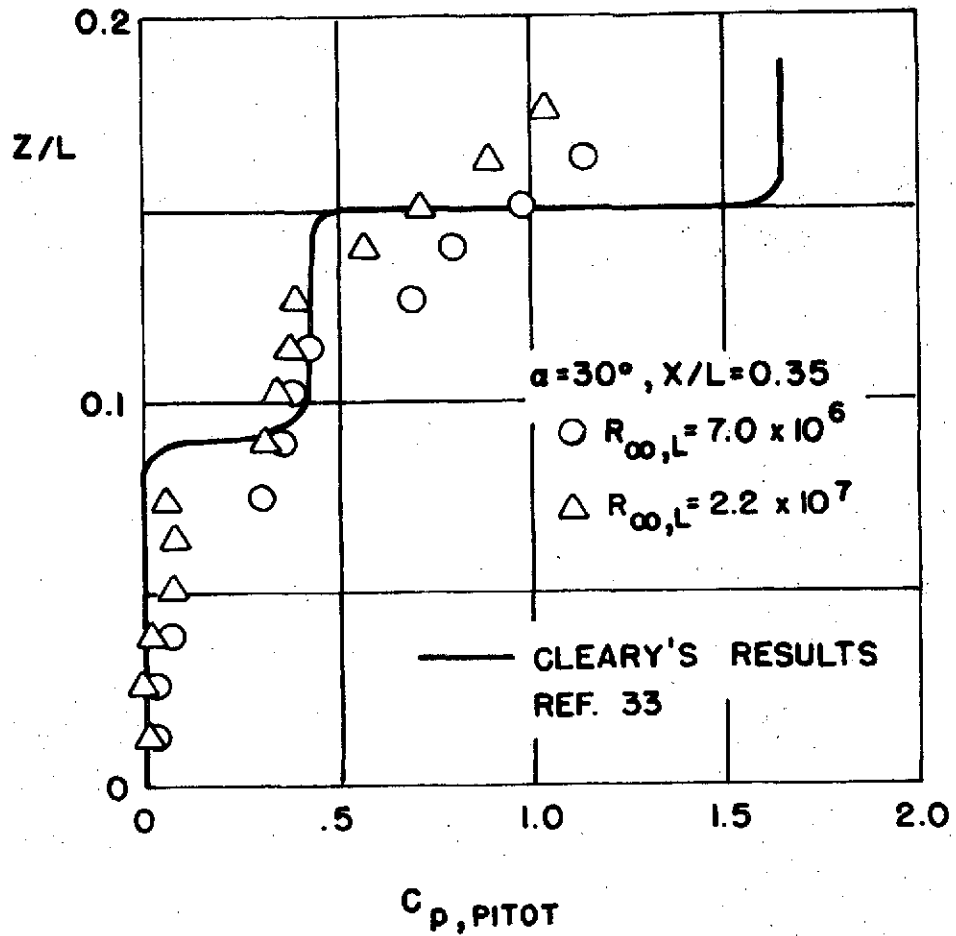


Fig. 73 Lee-Side Centerline Pitot Pressure Distribution, $x/L = 0.35$
 $\alpha = 30^\circ$

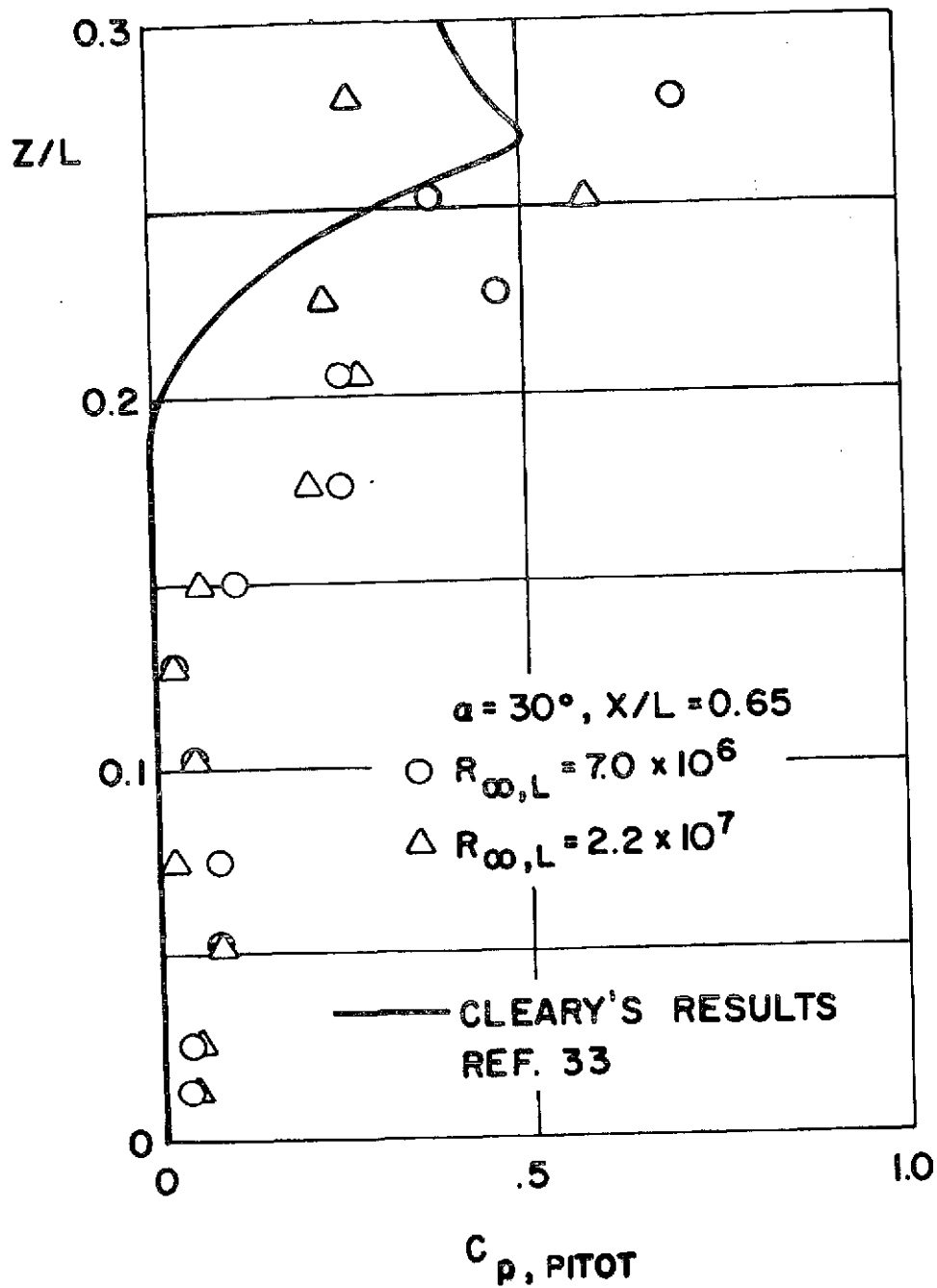


Fig. 74 Lee-Side Centerline Pitot Pressure Distribution, $x/L = 0.65$
 $\alpha = 30^\circ$

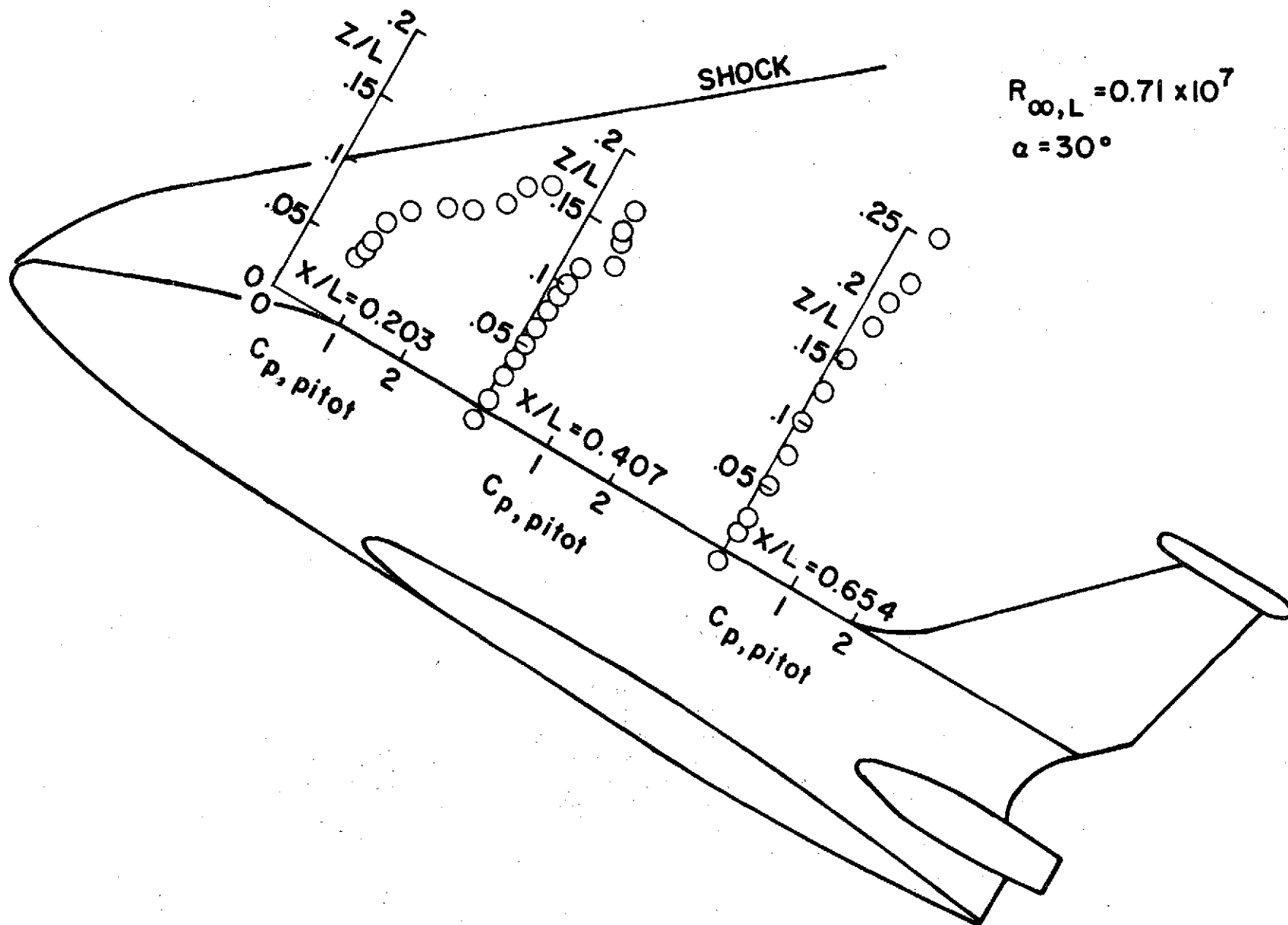


Fig. 75 Lee-Side Centerline Pitot Pressure Distributions, $\alpha = 30^\circ$

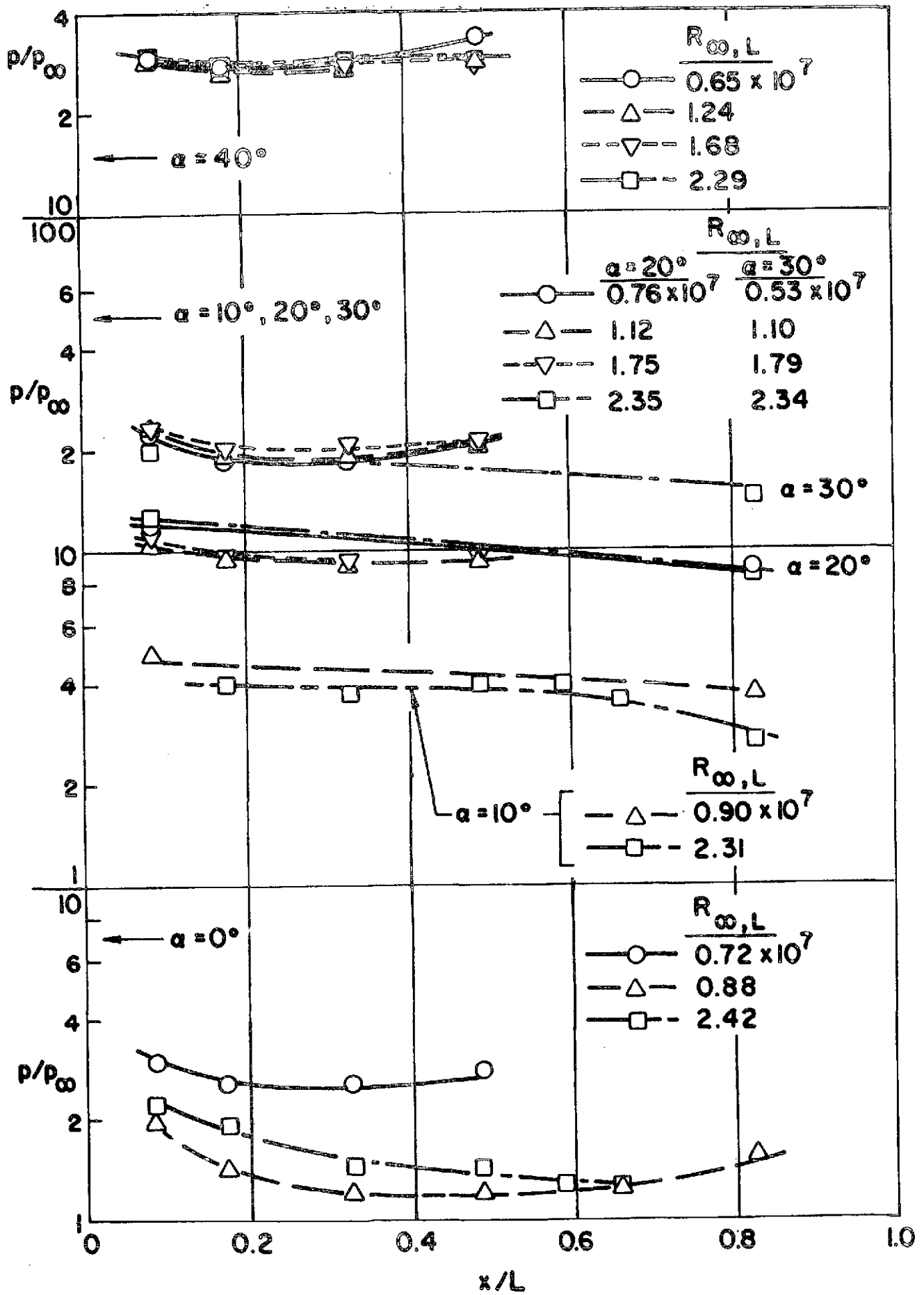


Fig. 76 Surface Pressure Distributions along Windward Centerline

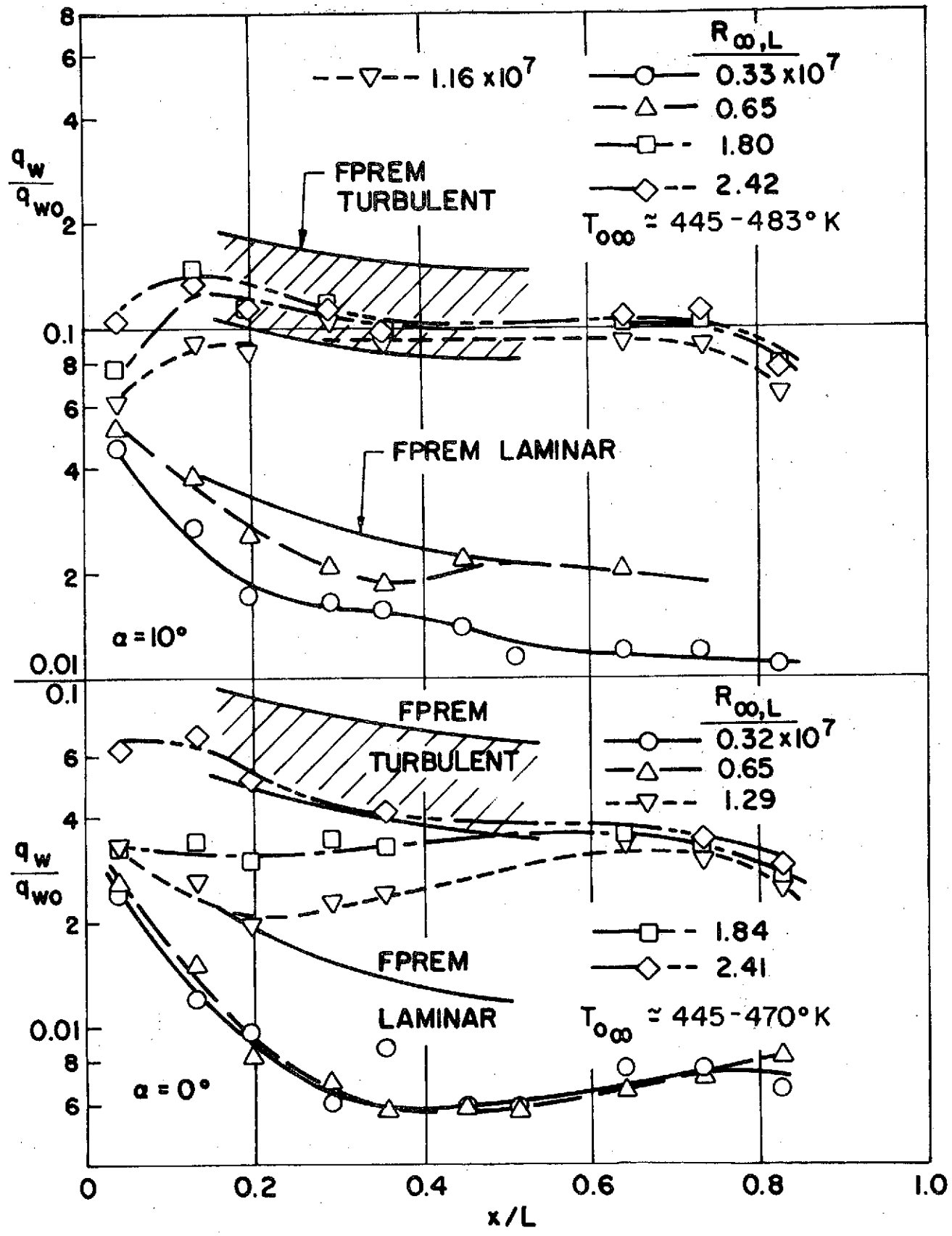


Fig. 77 Heat Transfer Distributions along Windward Centerline ; $\alpha = 0^\circ, 10^\circ$

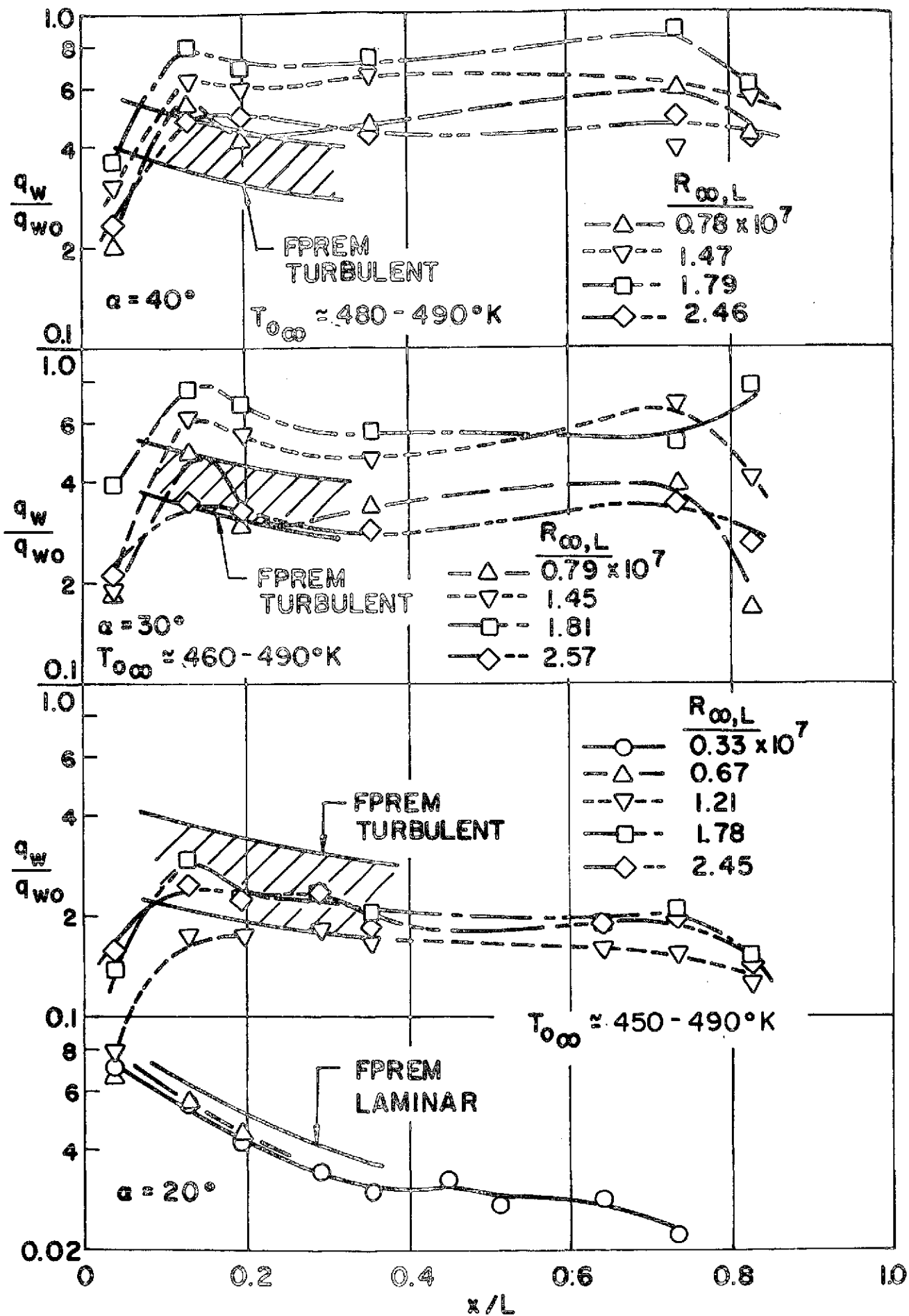


Fig. 78 Heat Transfer Distributions along Windward Centerline ; $\alpha = 20^\circ, 30^\circ, 40^\circ$

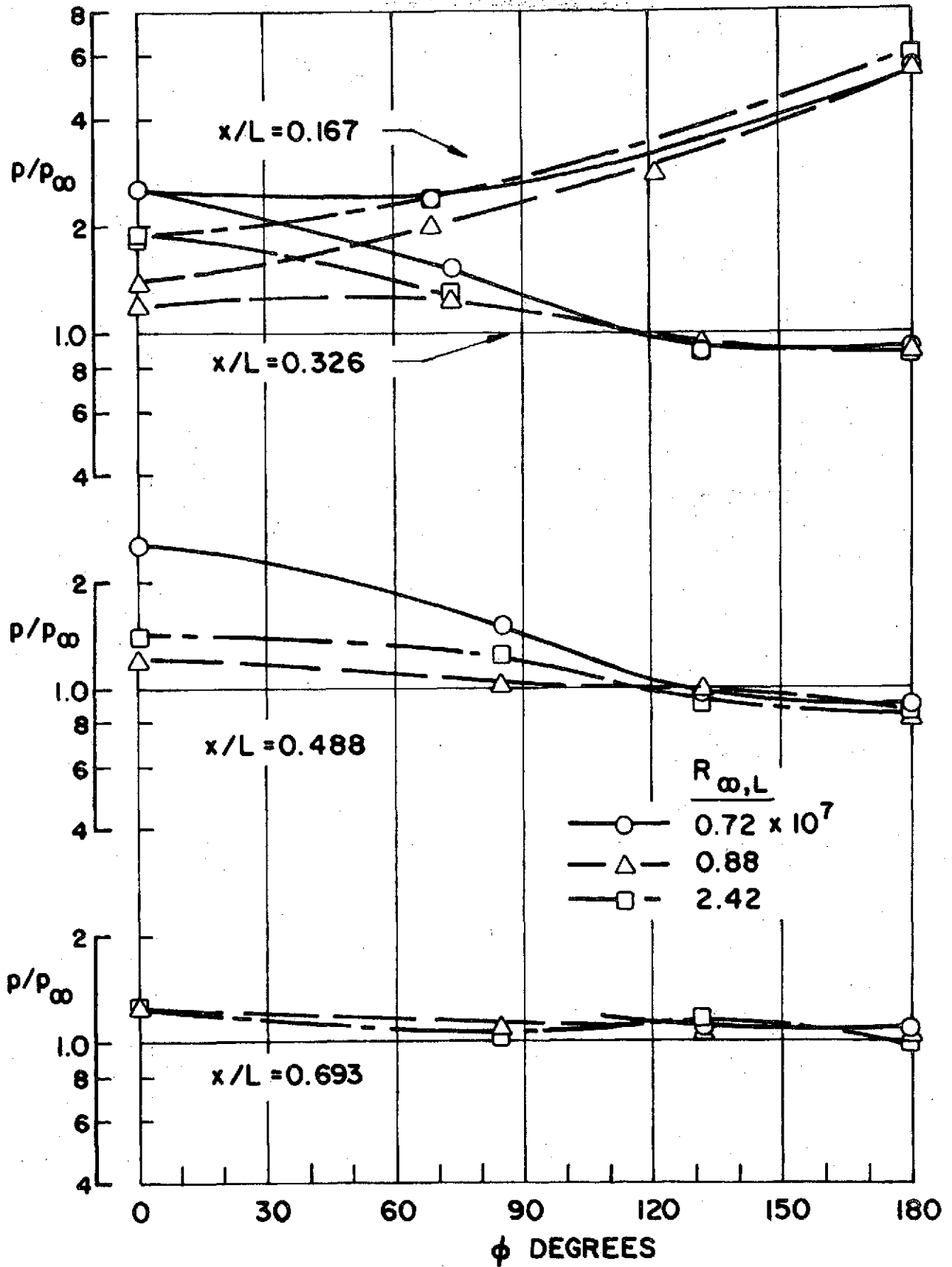


Fig. 79 Circumferential Surface Pressure Distributions ; $\alpha = 0^\circ$

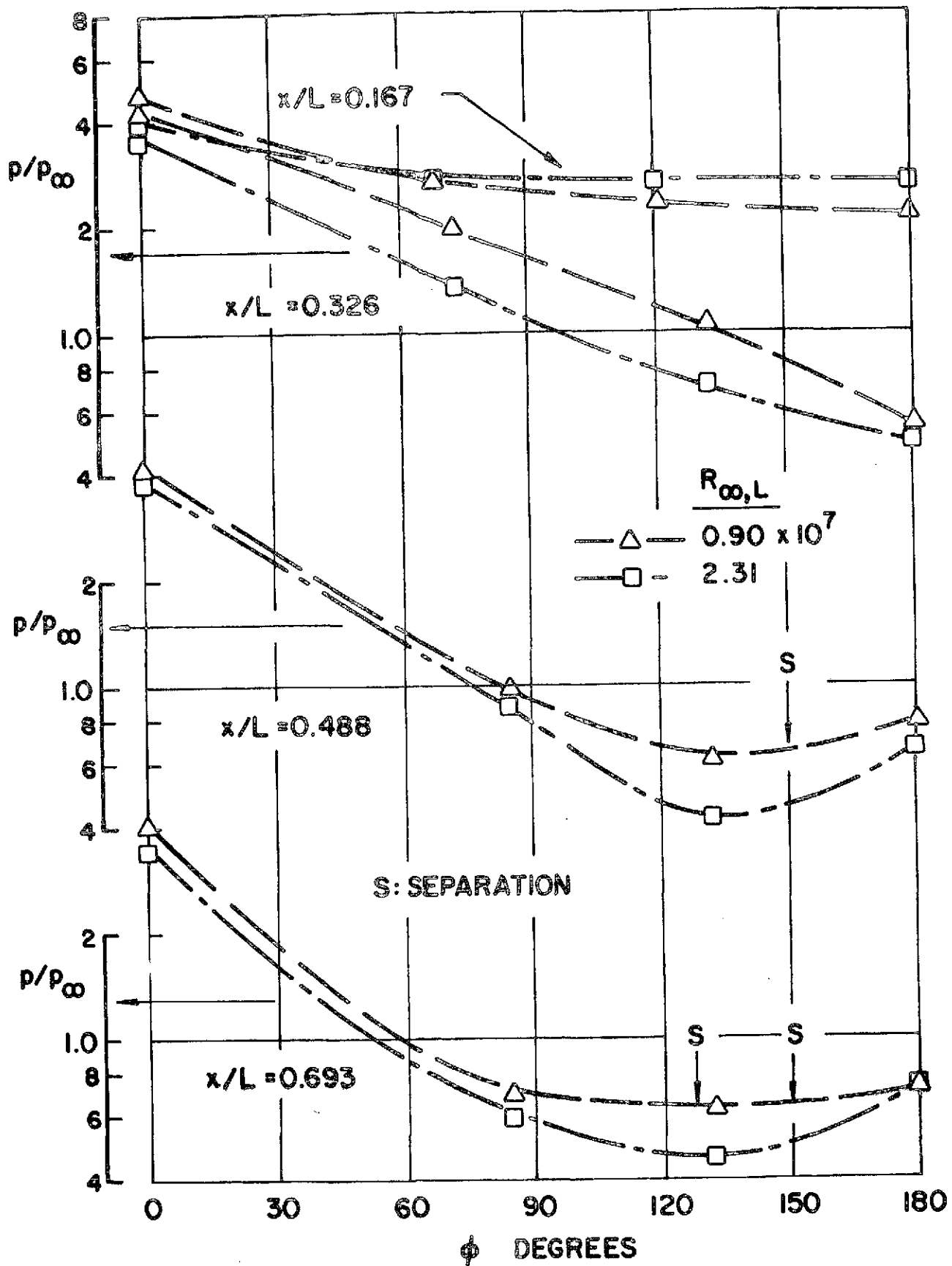


Fig. 80 Circumferential Surface Pressure Distributions ; $\alpha = 10^\circ$

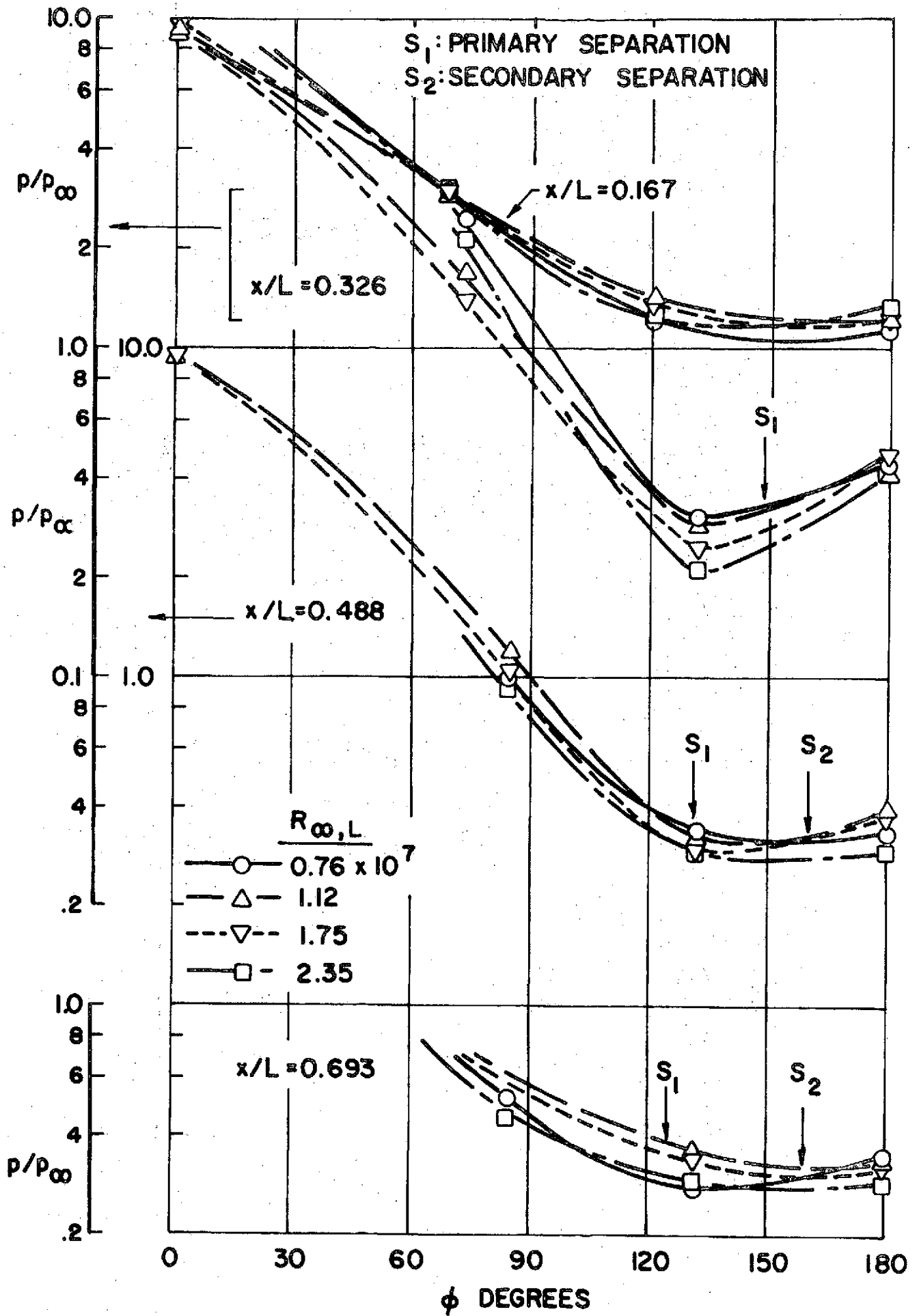


Fig. 81 Circumferential Surface Pressure Distributions ; $\alpha = 20^\circ$

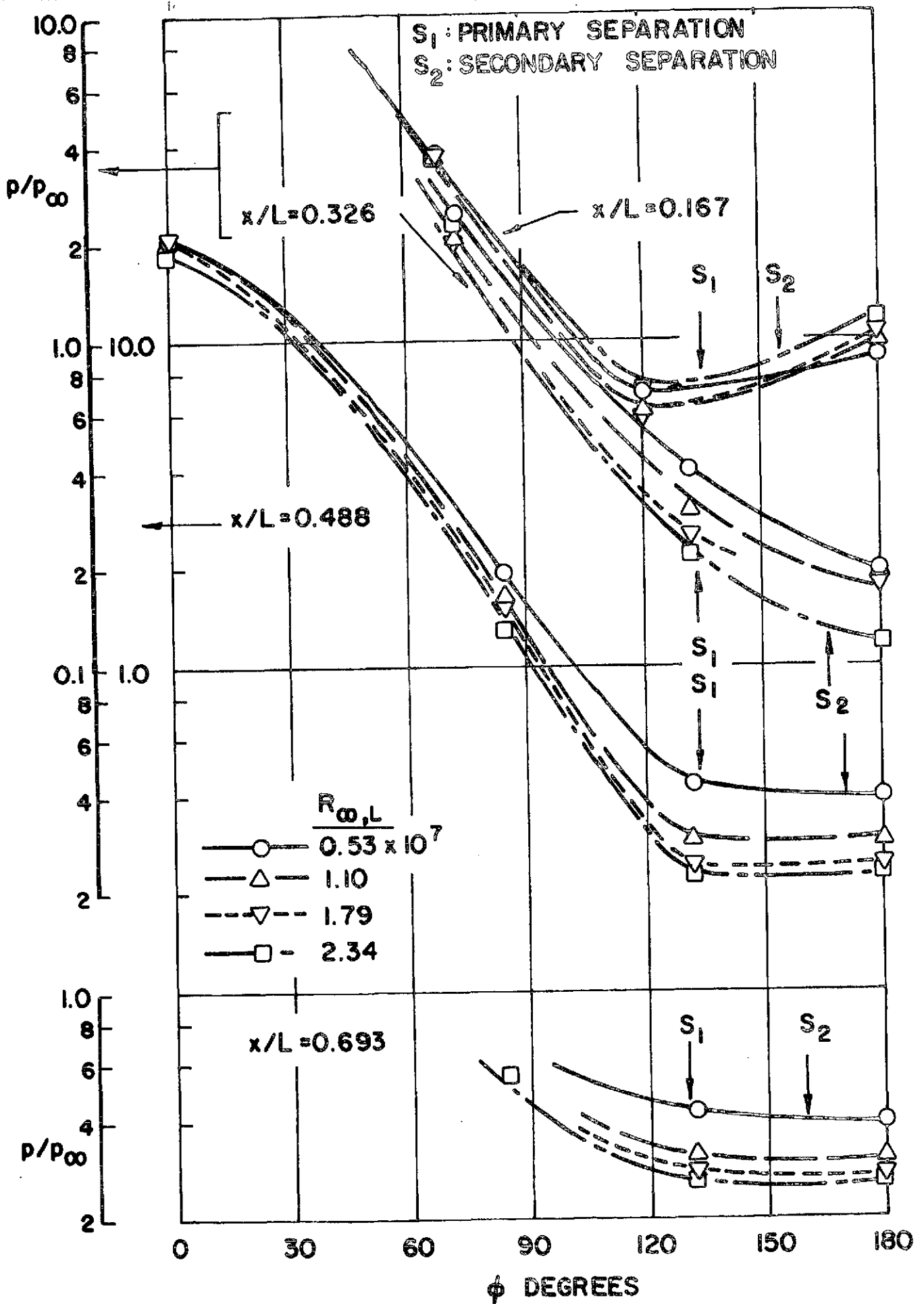


Fig. 82 Circumferential Surface Pressure Distributions ; $\alpha = 30^\circ$

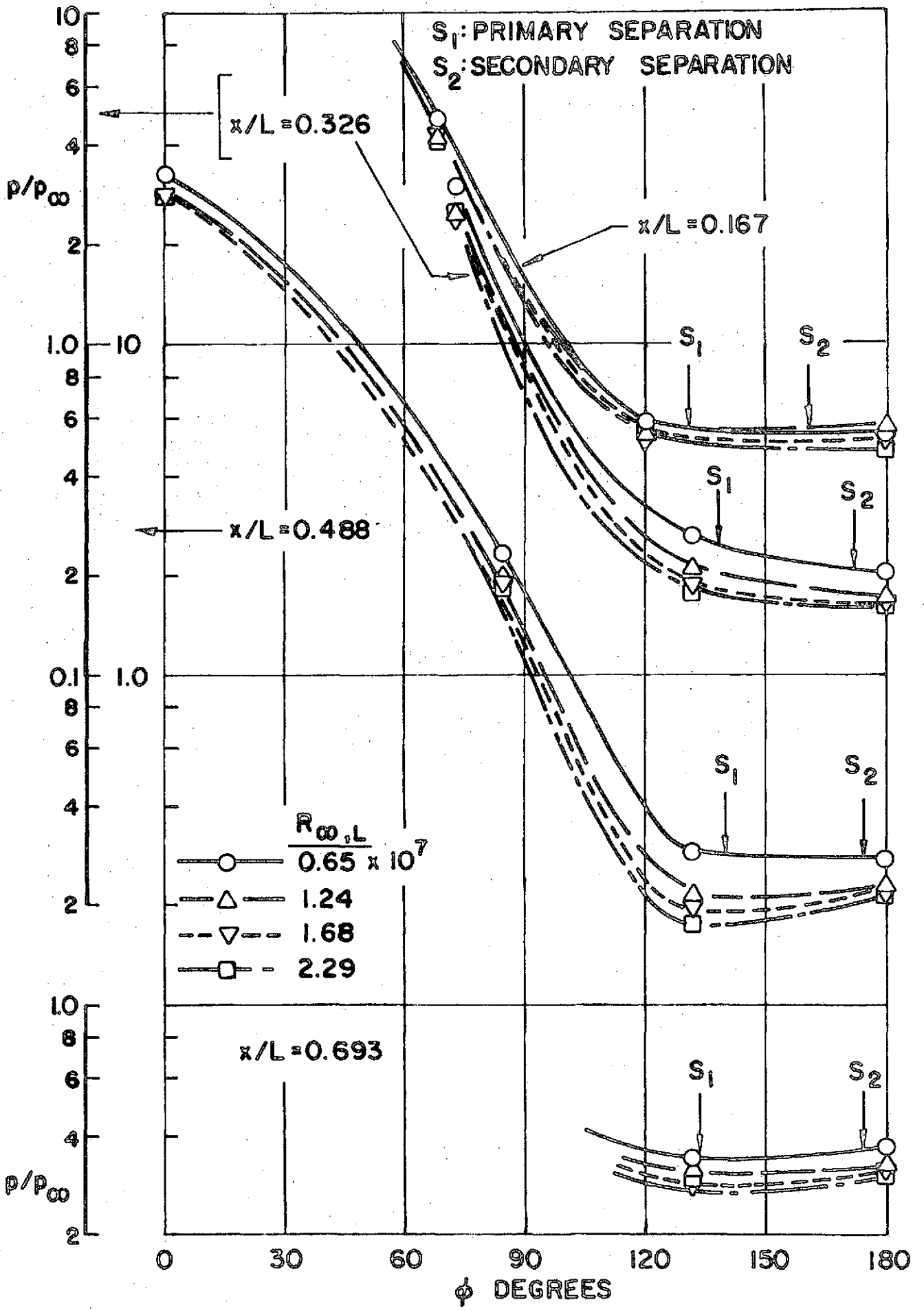


Fig. 83 Circumferential Surface Pressure Distributions ; $\alpha = 40^\circ$

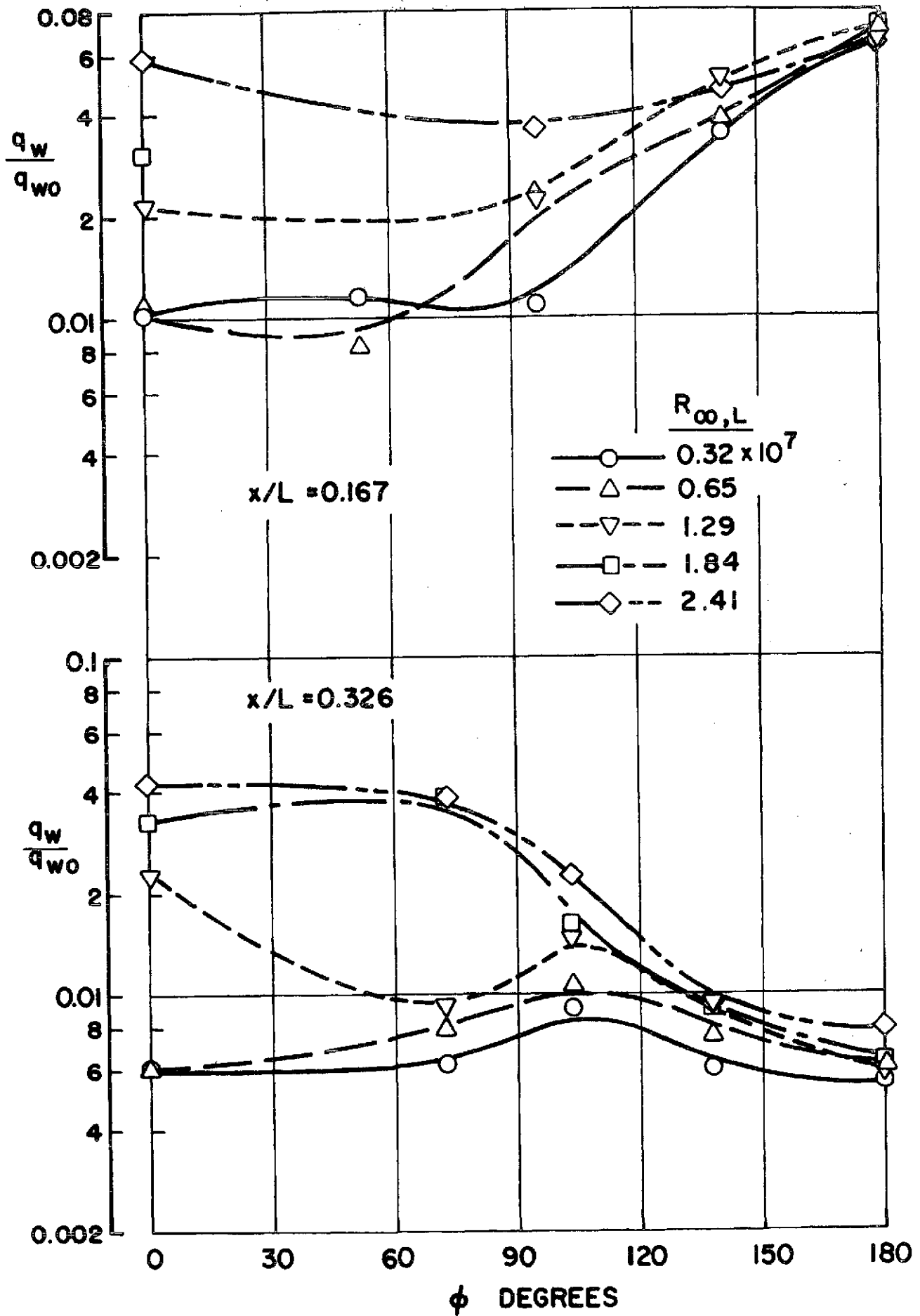


Fig. 84 Circumferential Heat Transfer Distributions ; $\alpha = 0^\circ$, $x/L = 0.167$, 0.326

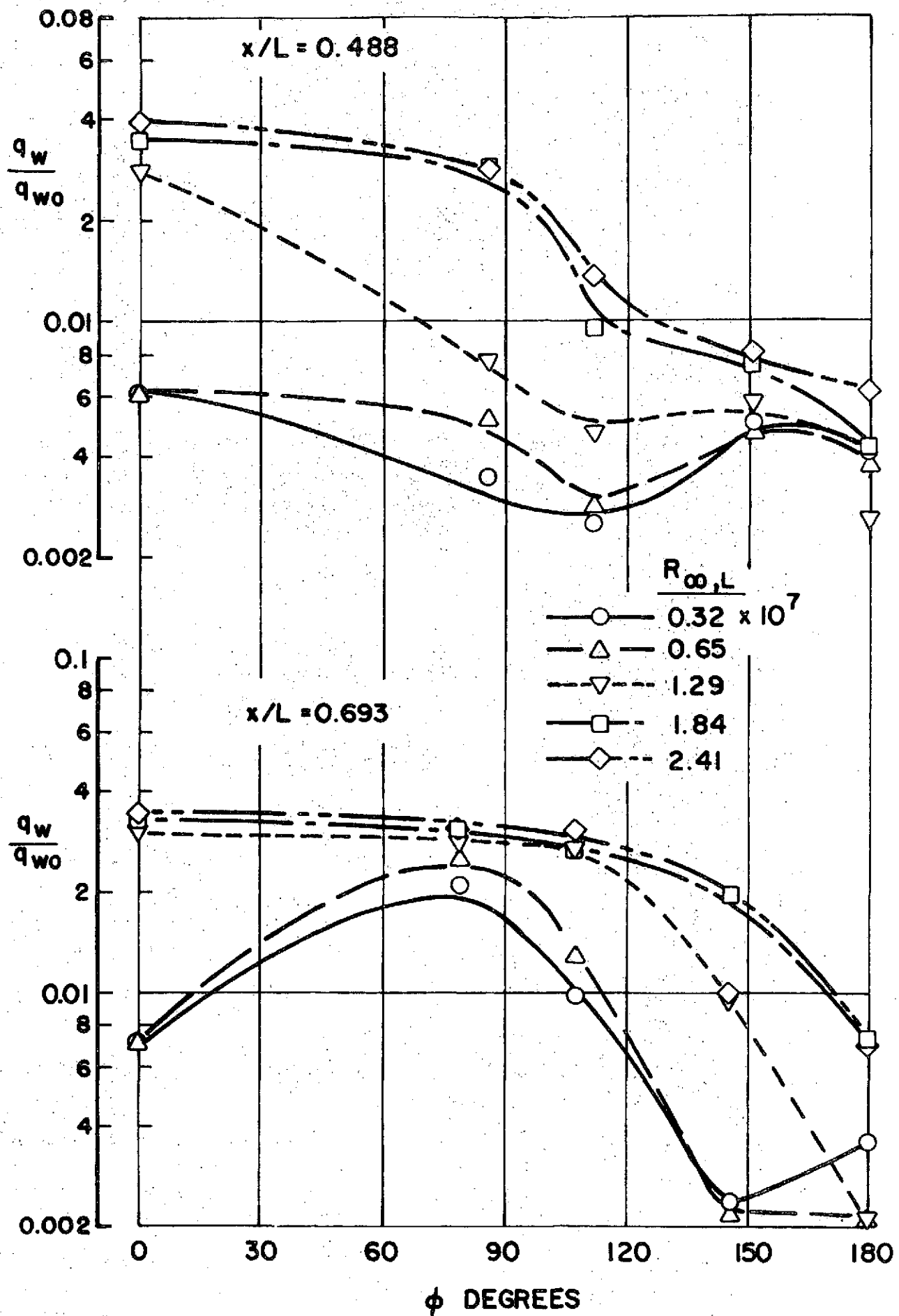


Fig. 85 Circumferential Heat Transfer Distributions ; $\alpha = 0^\circ$, $x/L = 0.488$, 0.693

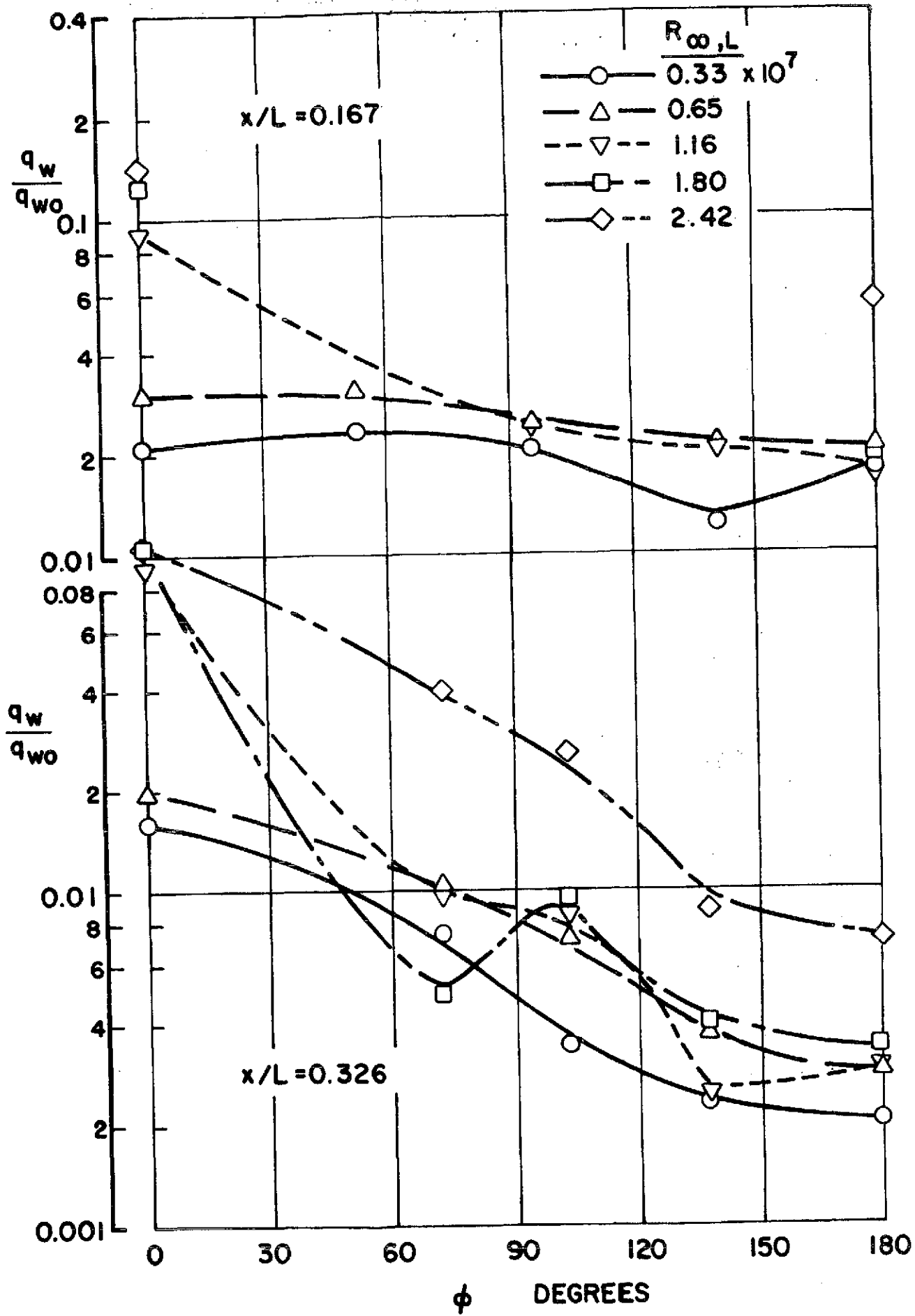


Fig. 86 Circumferential Heat Transfer Distributions ; $\alpha = 10^\circ$, $x/L = 0.167$, 0.326

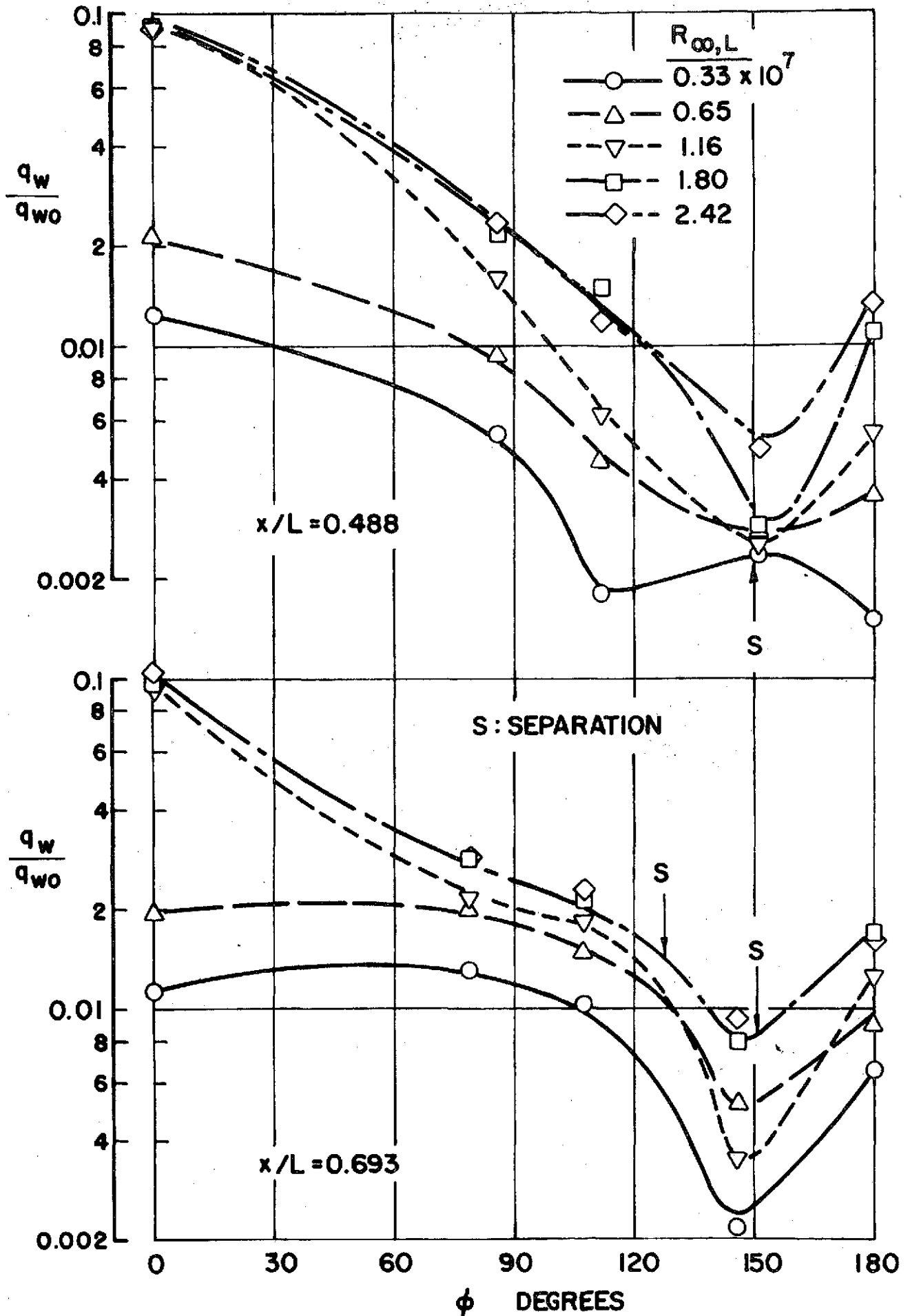


Fig. 87 Circumferential Heat Transfer Distributions ; $\alpha = 10^\circ$, $x/L = 0.488$, 0.693

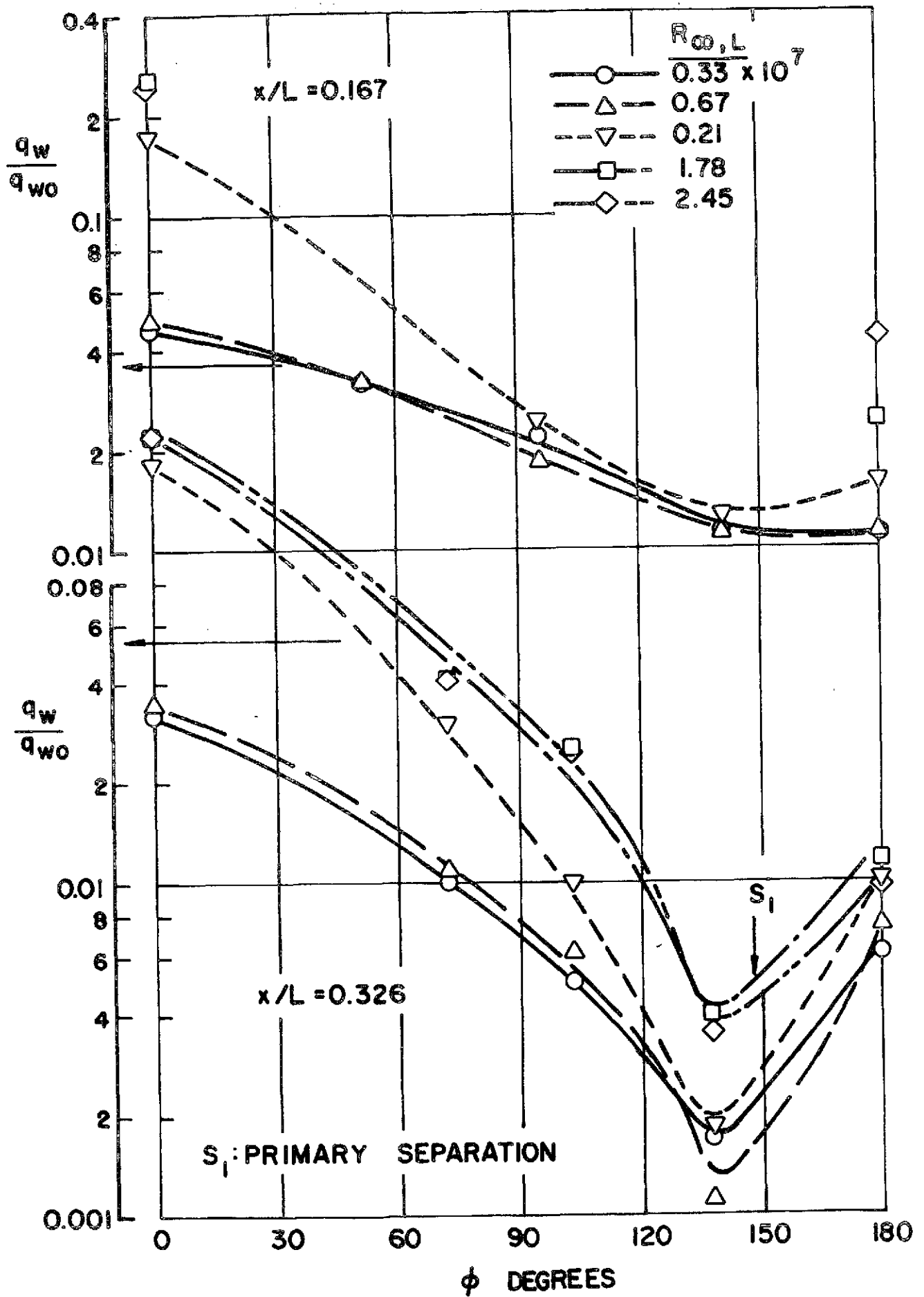


Fig. 88 Circumferential Heat Transfer Distributions ; $\alpha = 20^\circ$, $x/L = 0.167, 0.326$

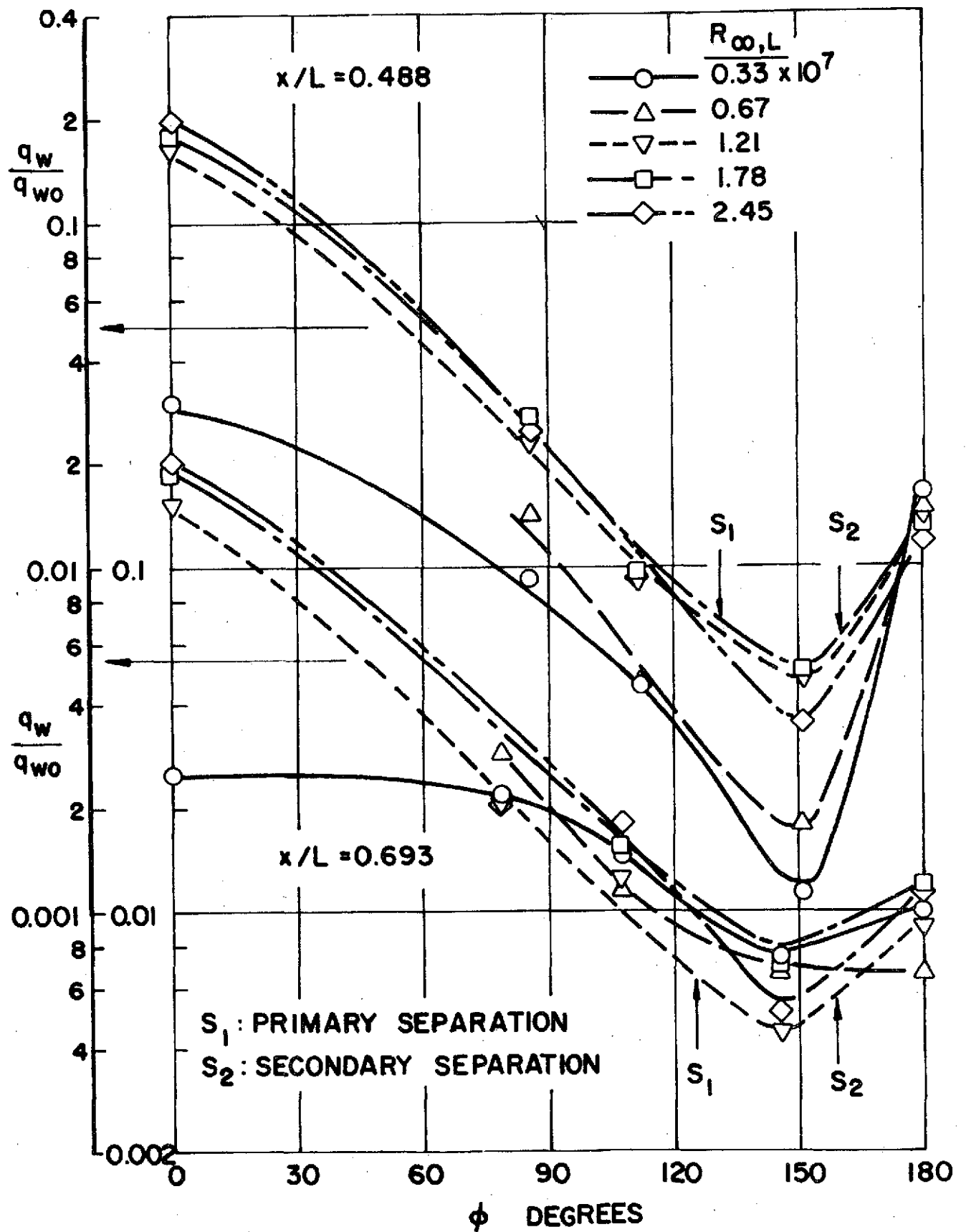


Fig. 89 Circumferential Heat Transfer Distributions ; $\alpha = 20^\circ$, $x/L = 0.488, 0.693$

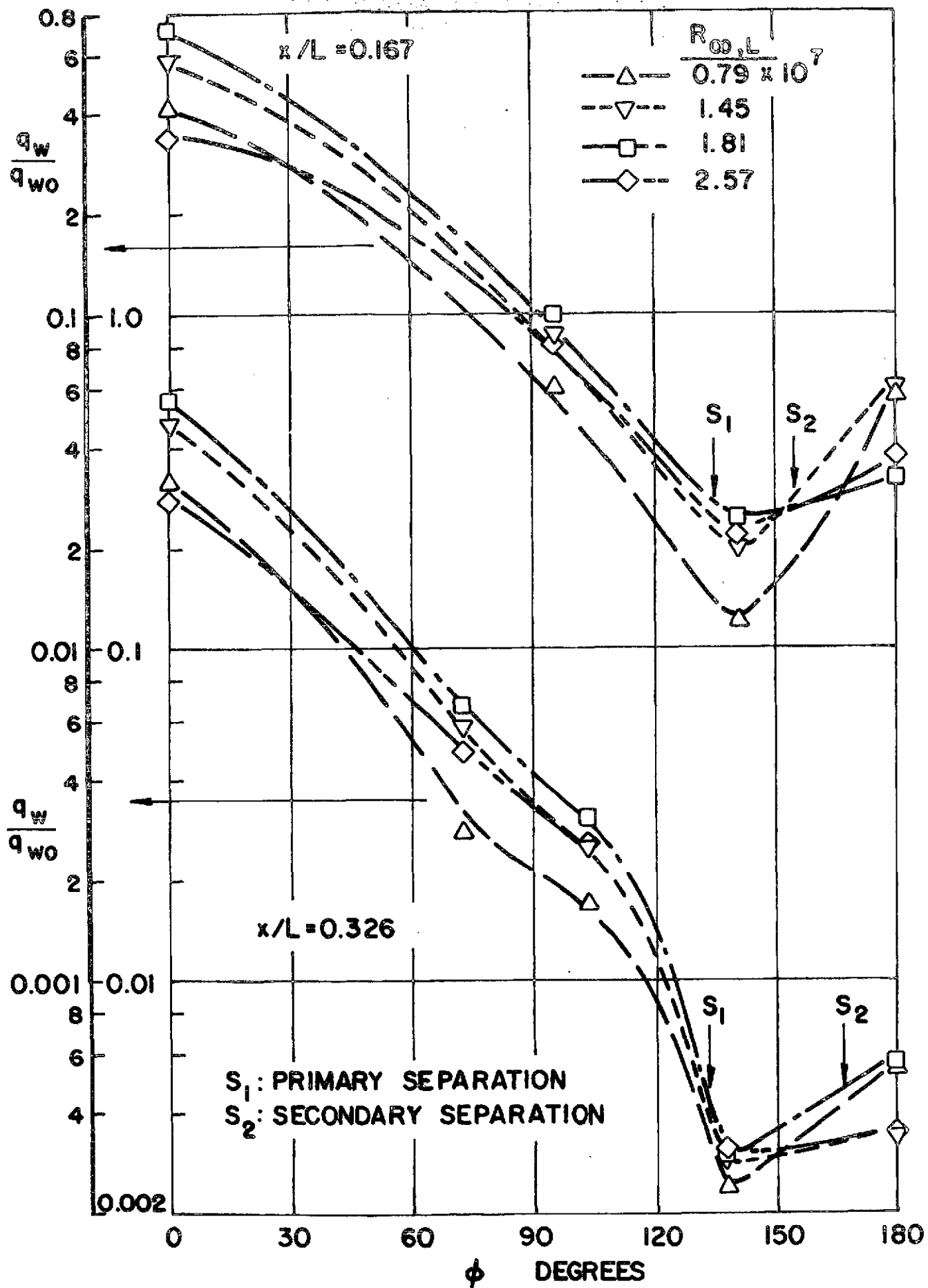


Fig. 90 Circumferential Heat Transfer Distributions ; $\alpha = 30^\circ$, $x/L = 0.167, 0.326$

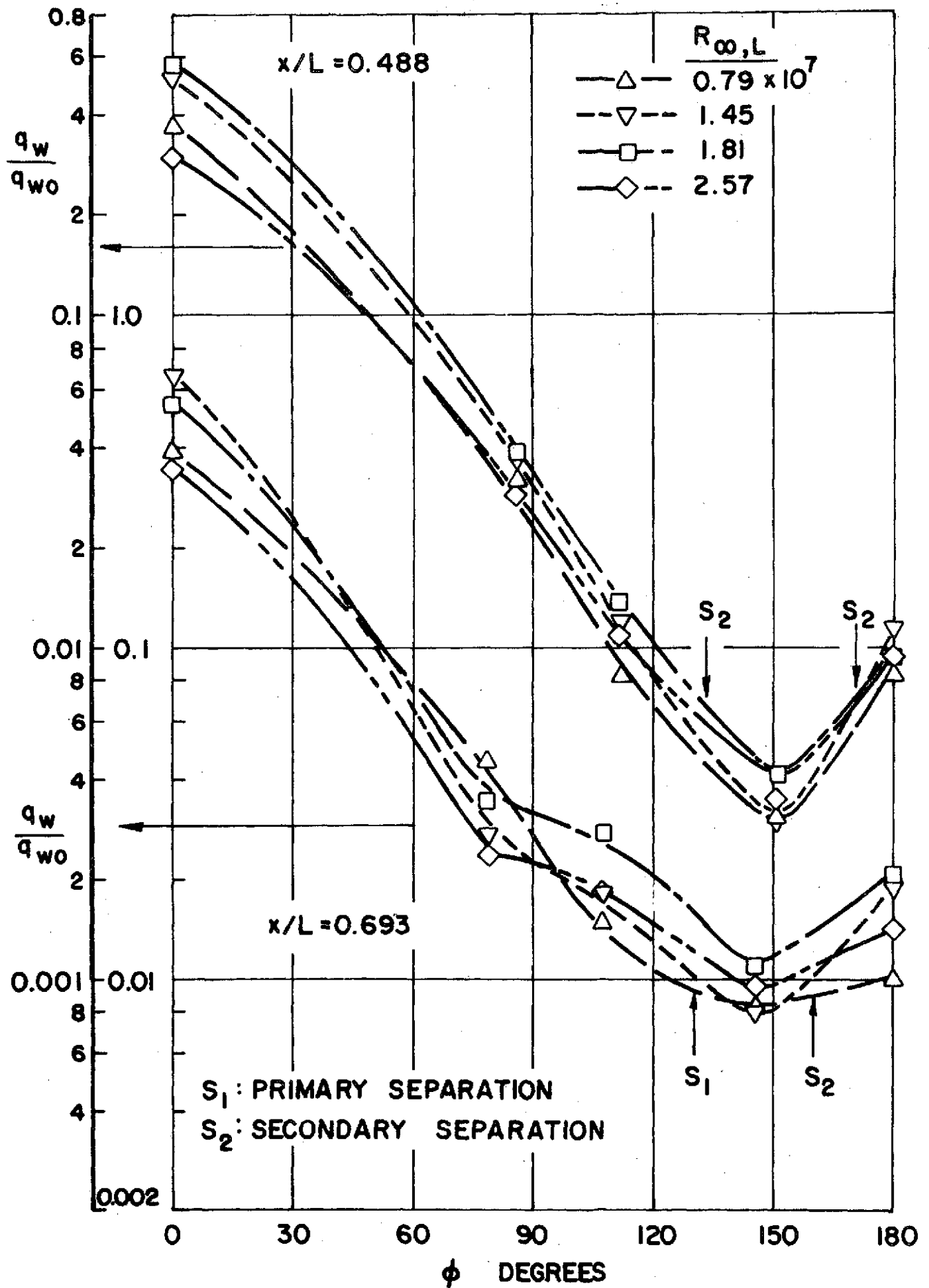


Fig. 91 Circumferential Heat Transfer Distributions ; $\alpha = 30^\circ$, $x/L = 0.488$, 0.693

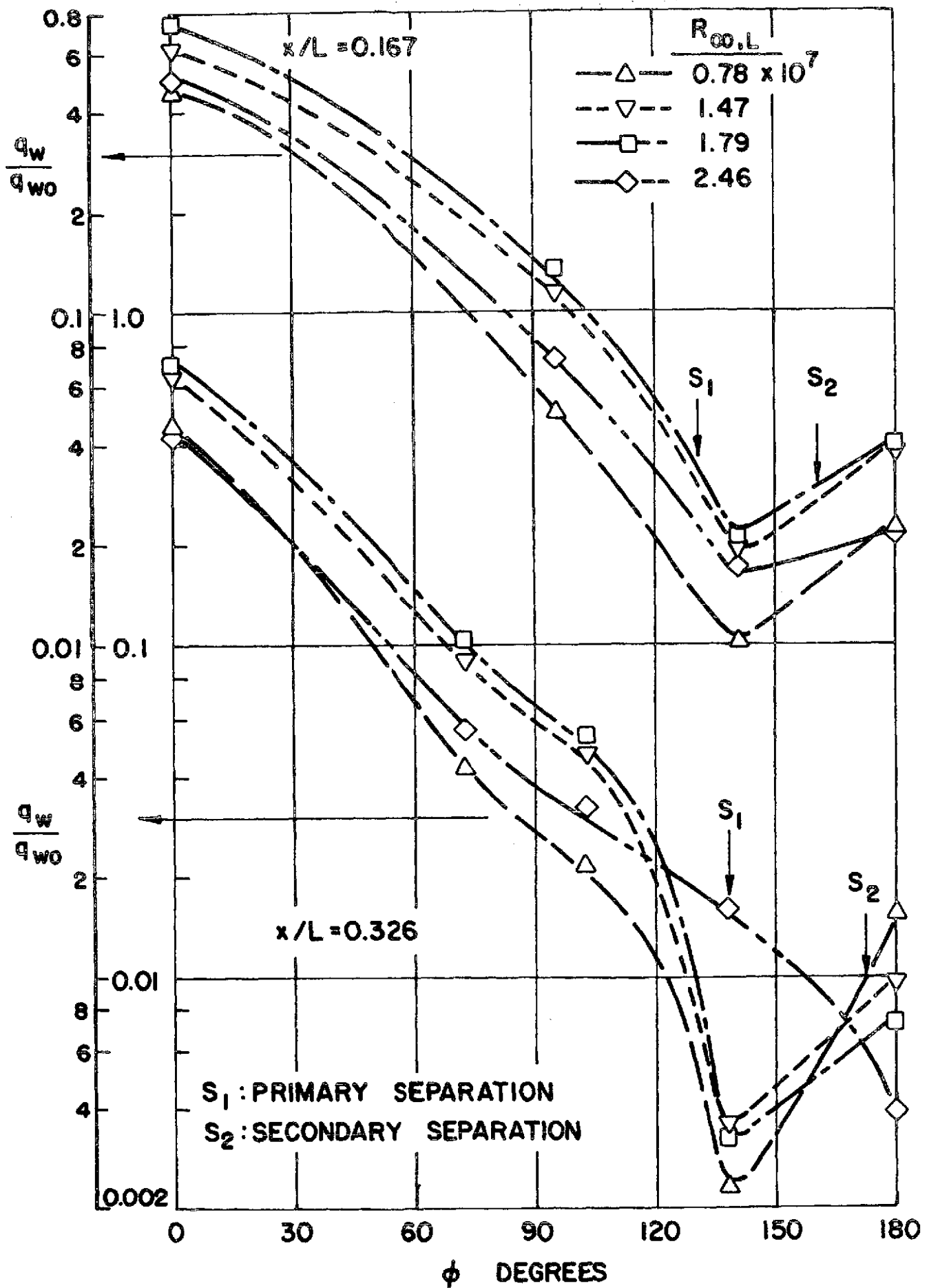


Fig. 92 Circumferential Heat Transfer Distributions ; $\alpha = 40^\circ$, $x/L = 0.167$, 0.326

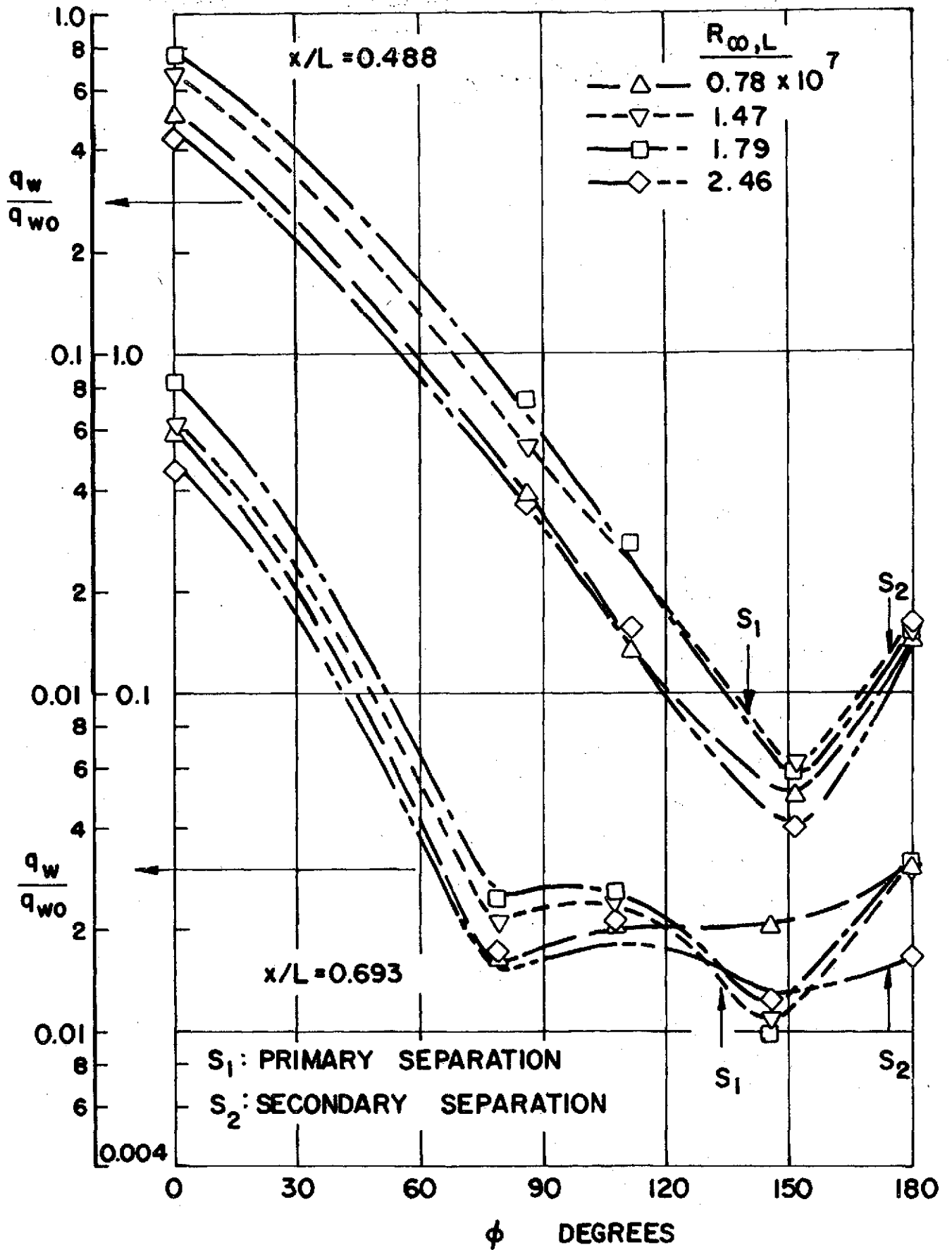


Fig. 93 Circumferential Heat Transfer Distributions ; $\alpha = 40^\circ$, $x/L = 0.488$, 0.693

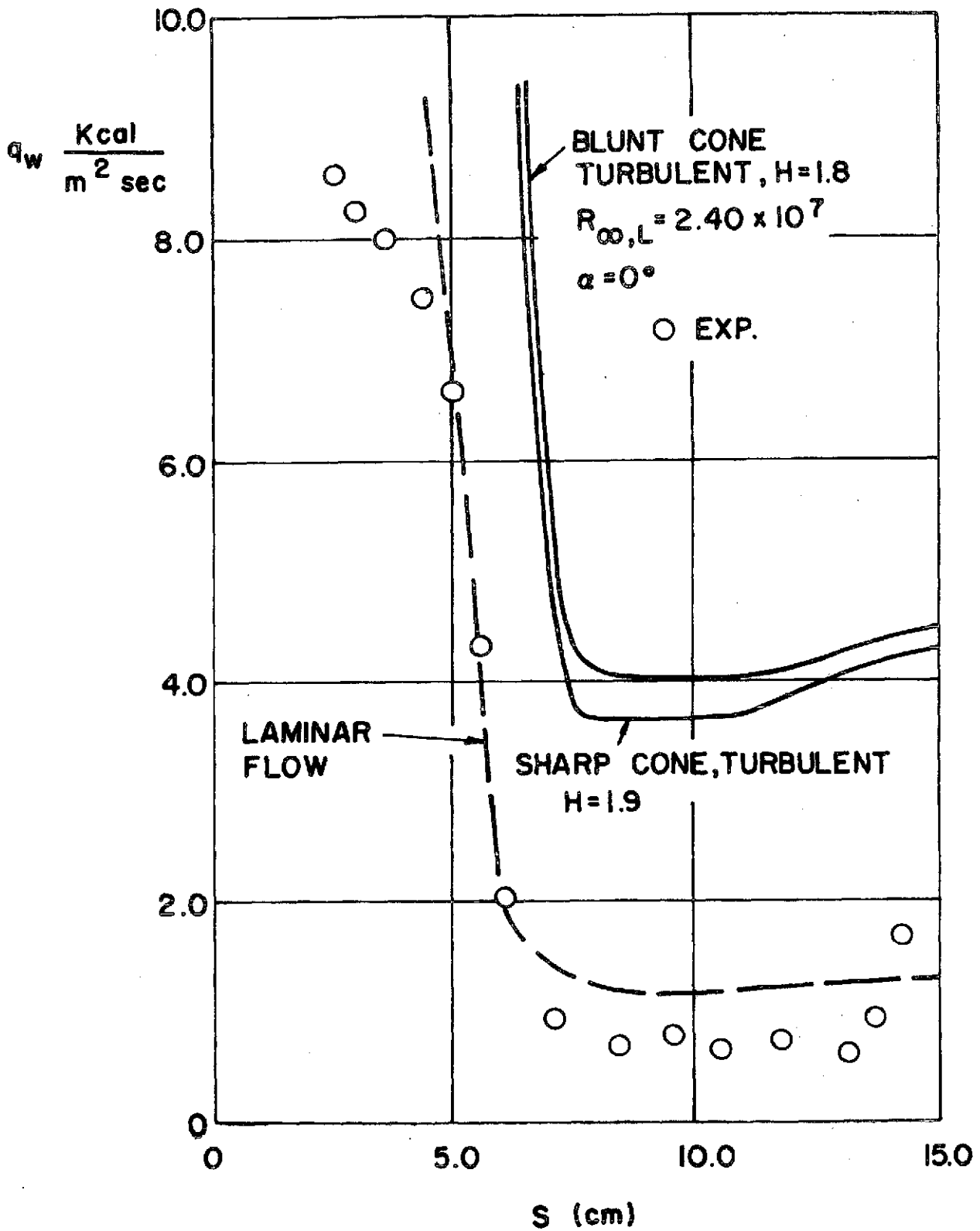


Fig. 94 Comparison of Leeward Centerline Heat Transfer Rates Between Turbulent Boundary Layer Theory and Experiments, $\alpha = 0^\circ$

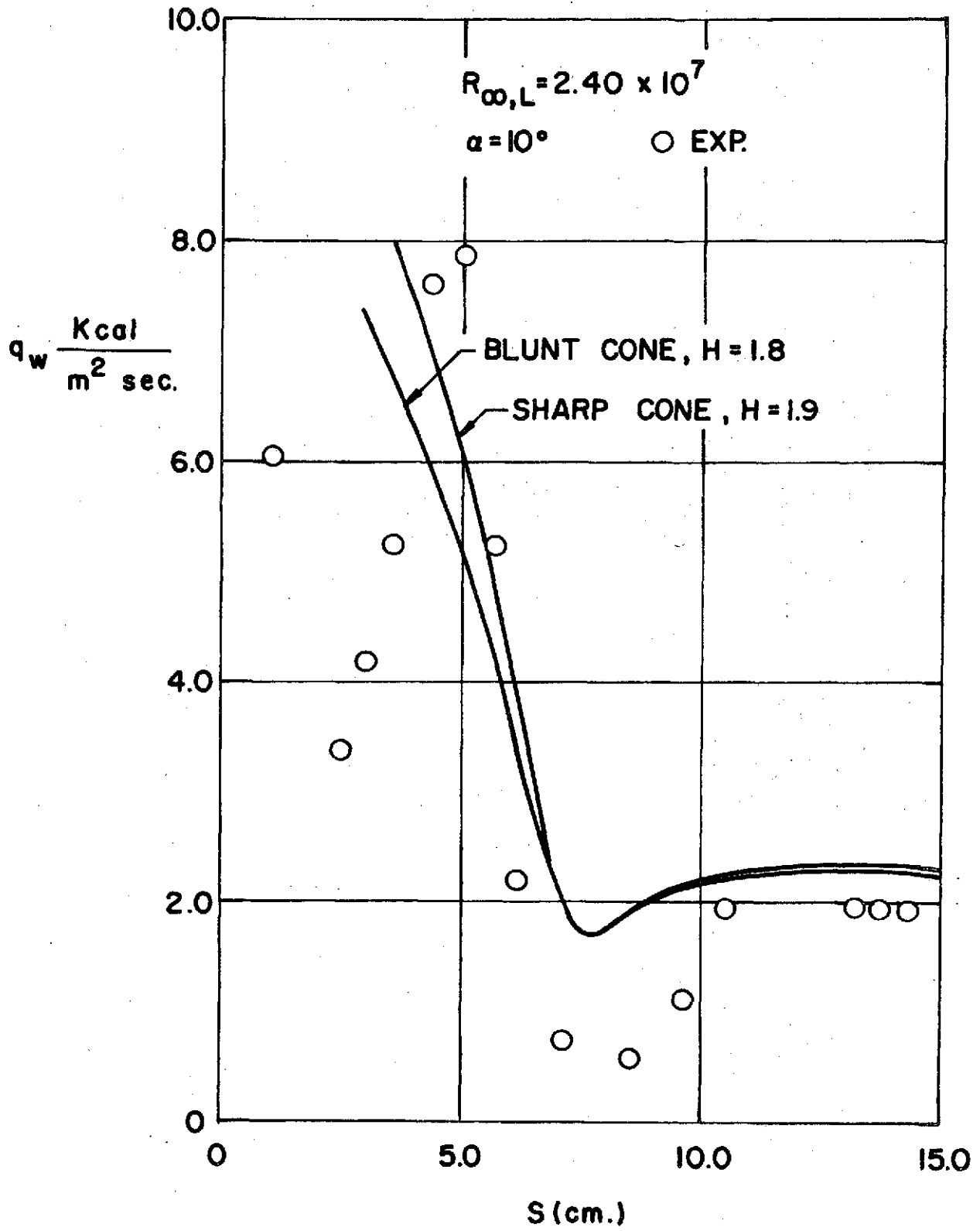


Fig. 95 Comparison of Leeward Centerline Heat Transfer Rates Between Turbulent Boundary Layer Theory and Experiments, $\alpha = 10^\circ$

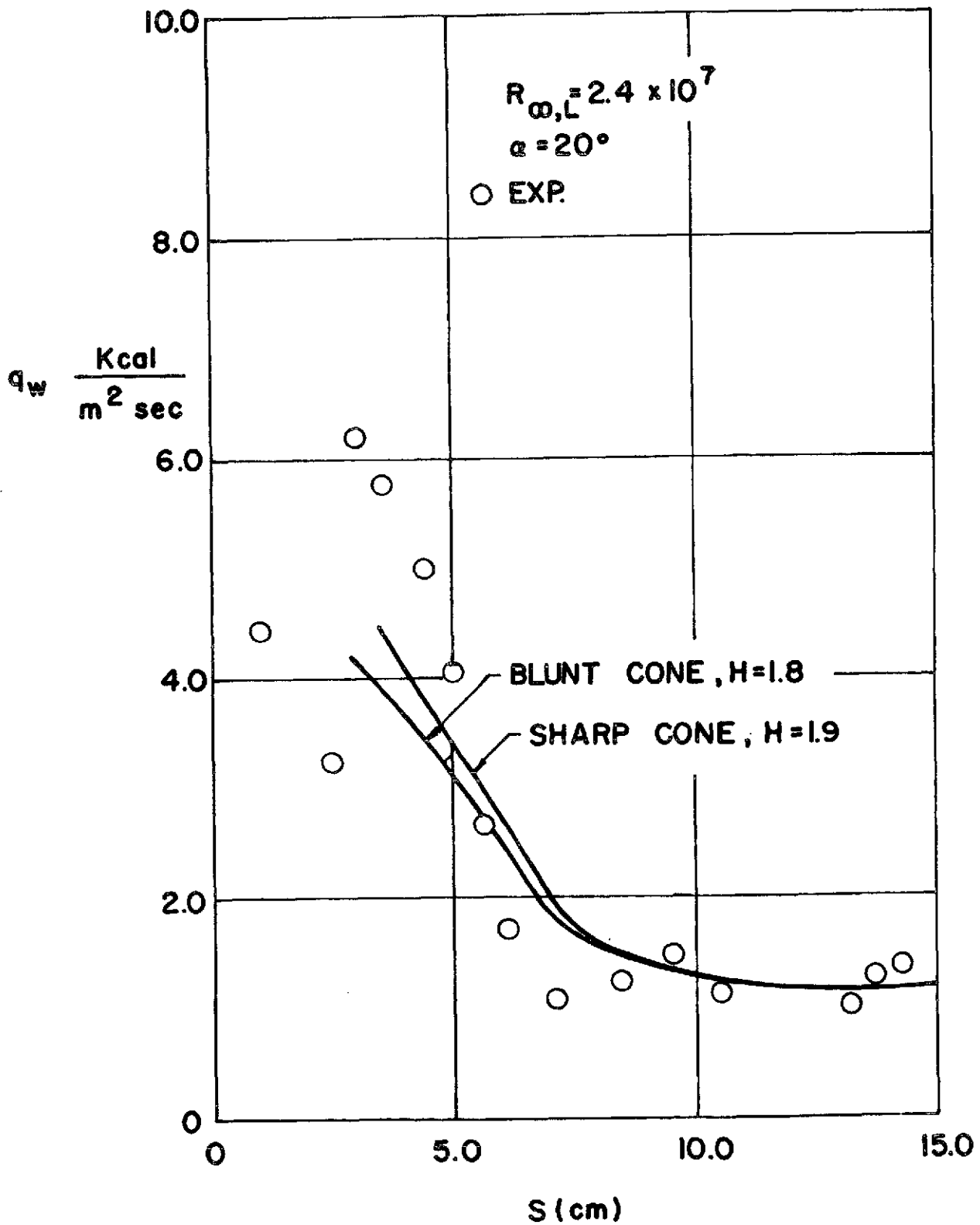


Fig. 96 Comparison of Leeward Centerline Heat Transfer Rates Between Turbulent Boundary Layer Theory and Experiments, $\alpha = 20^\circ$

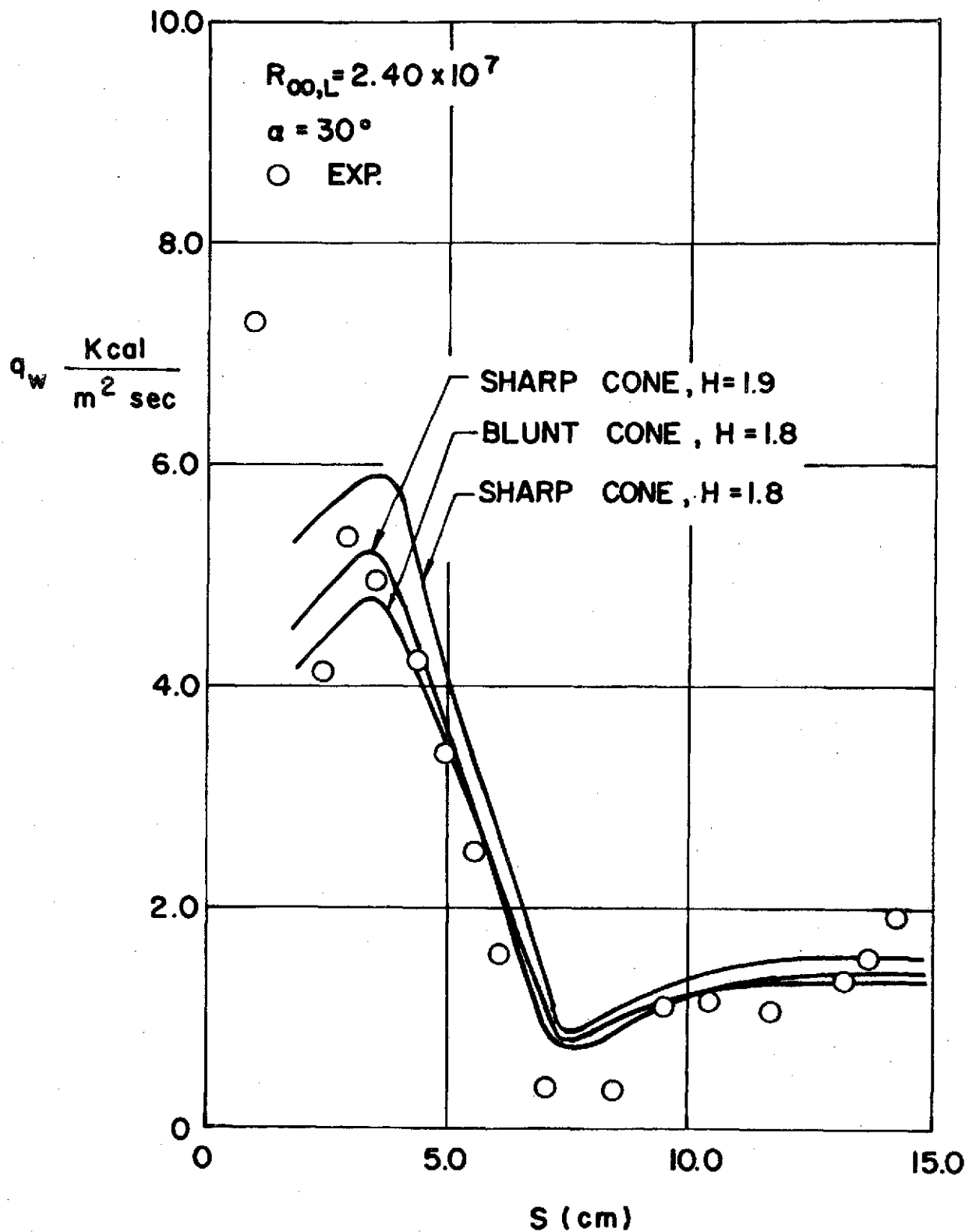


Fig. 97 Comparison of Leeward Centerline Heat Transfer Rates
 Between Turbulent Boundary Layer Theory and Experiments, $\alpha = 30^\circ$

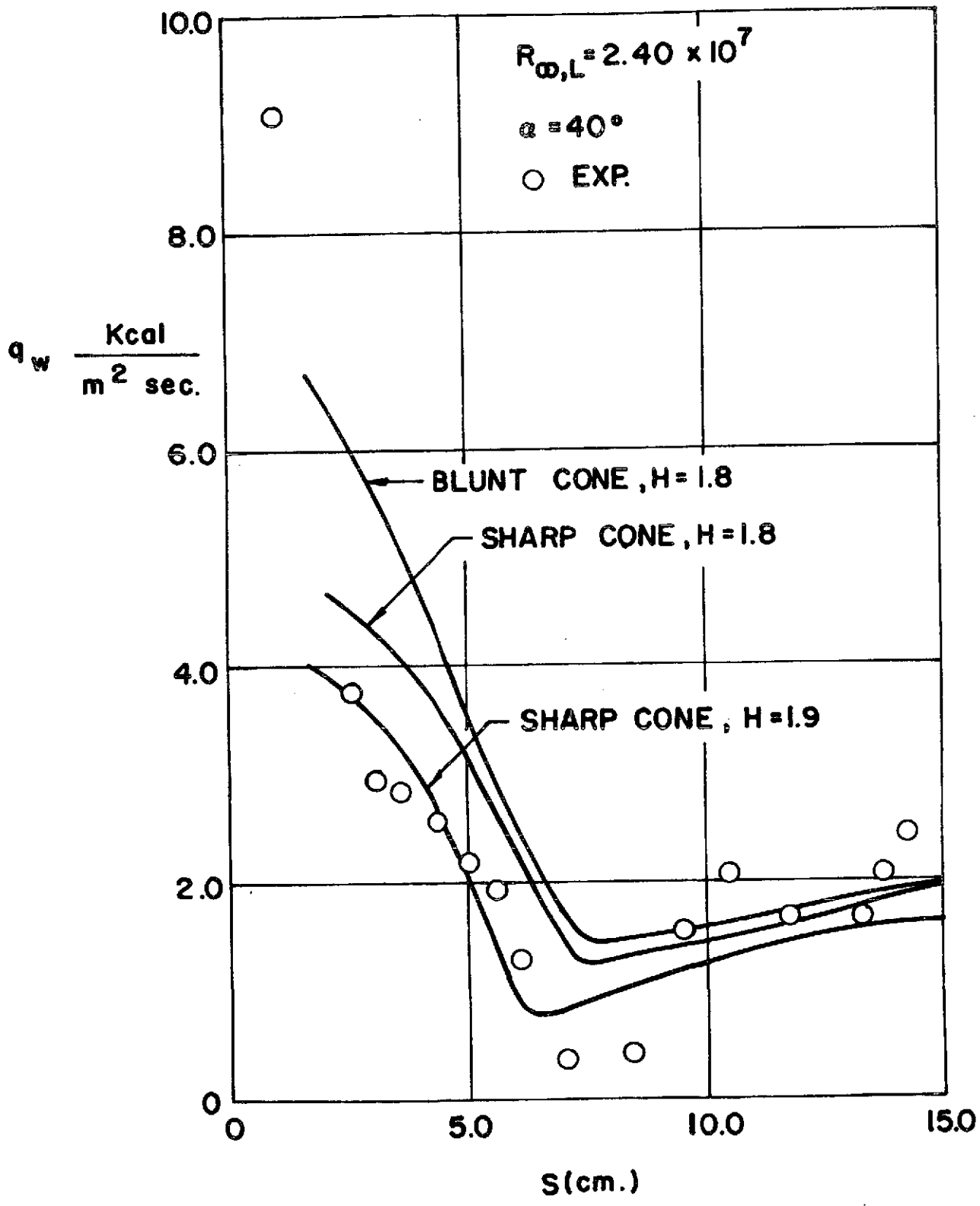


Fig. 98 Comparisons of Leeward Centerline Heat Transfer Rates Between Turbulent Boundary Layer Theory and Experiments, $\alpha = 40^\circ$

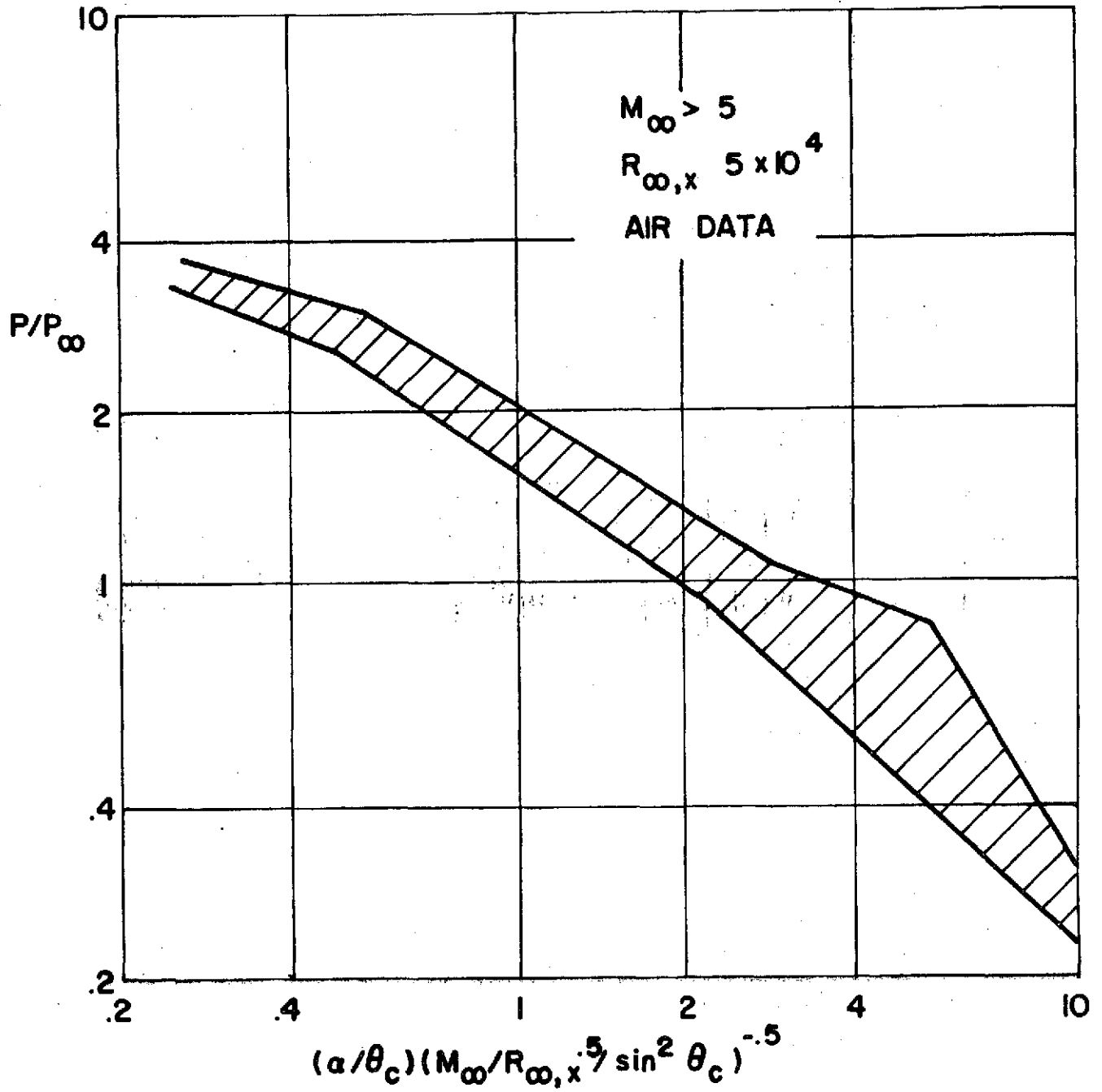


Fig. 99 Correlation of the Leeward Surface Pressure over Conical Body

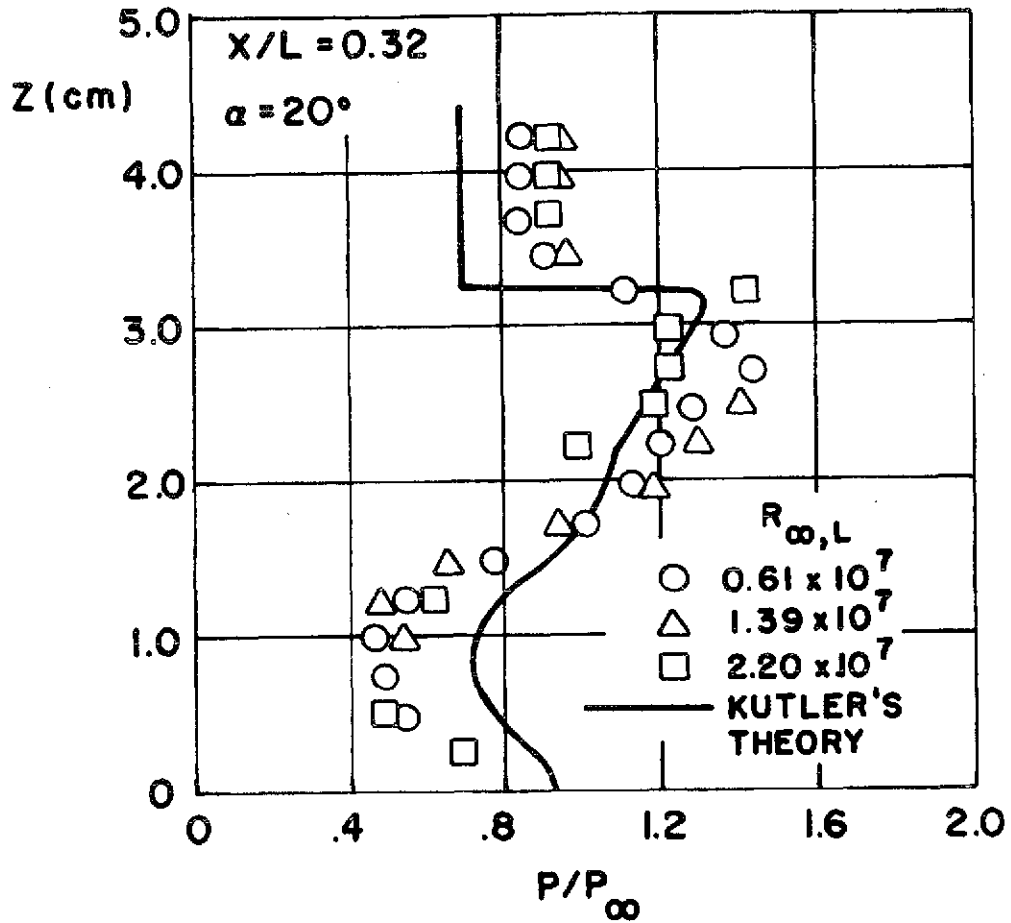


Fig. 100 Comparison of the Static Pressure Profiles Between Experiments and Inviscid Flow Theory, $\alpha = 20^\circ$

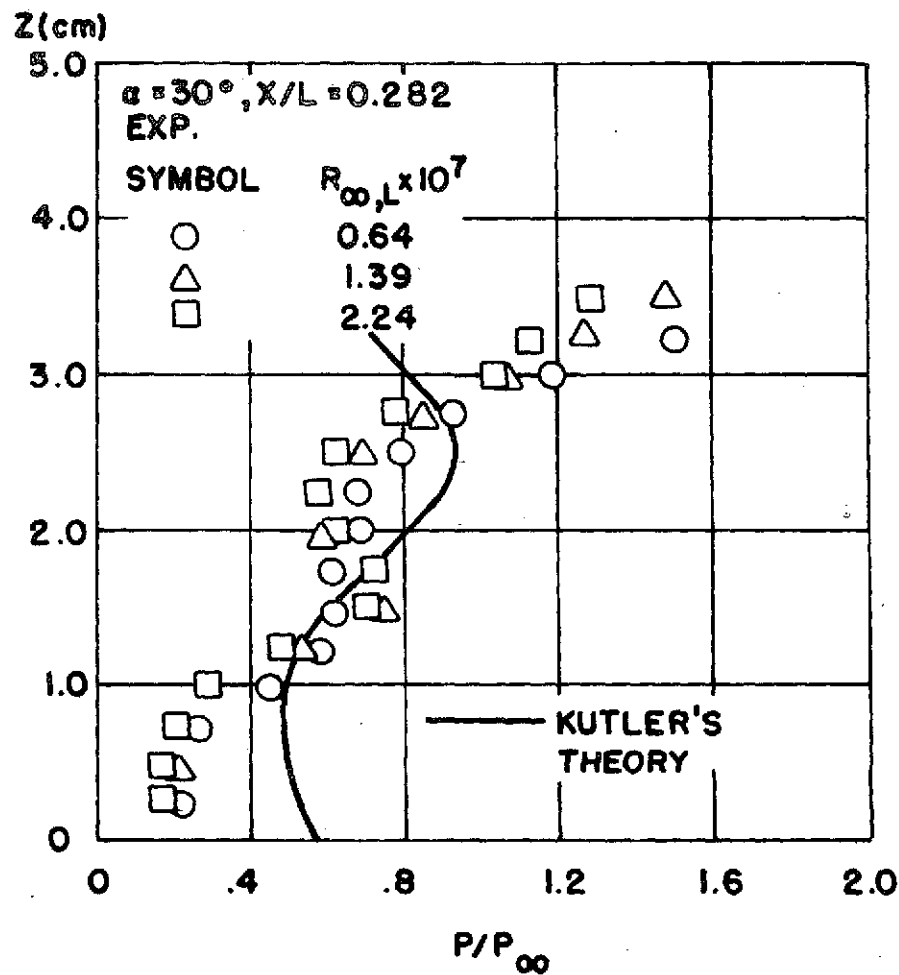
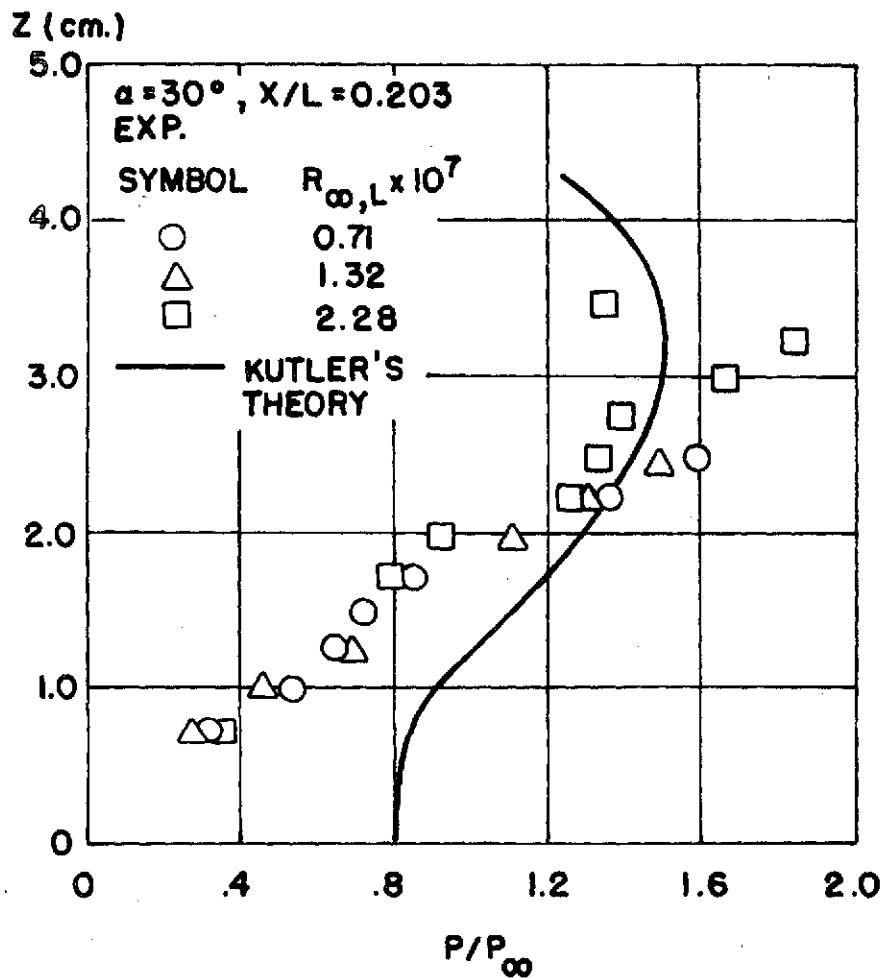
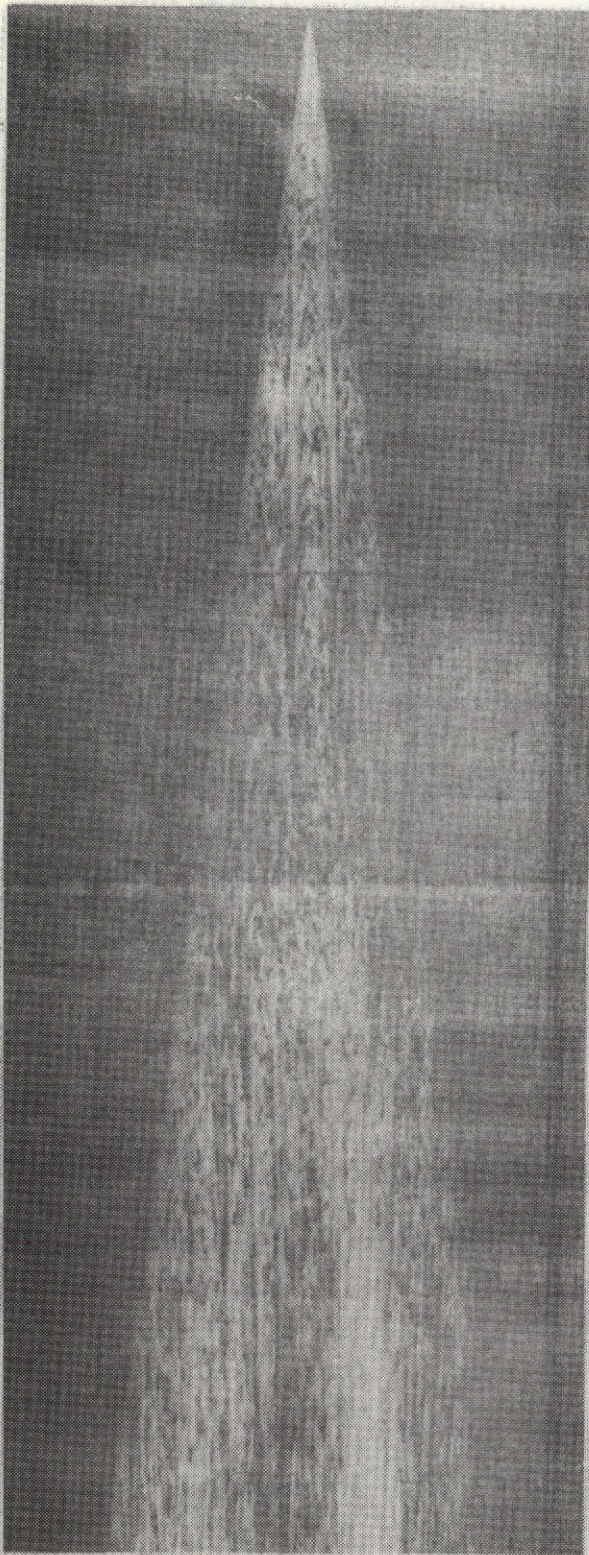
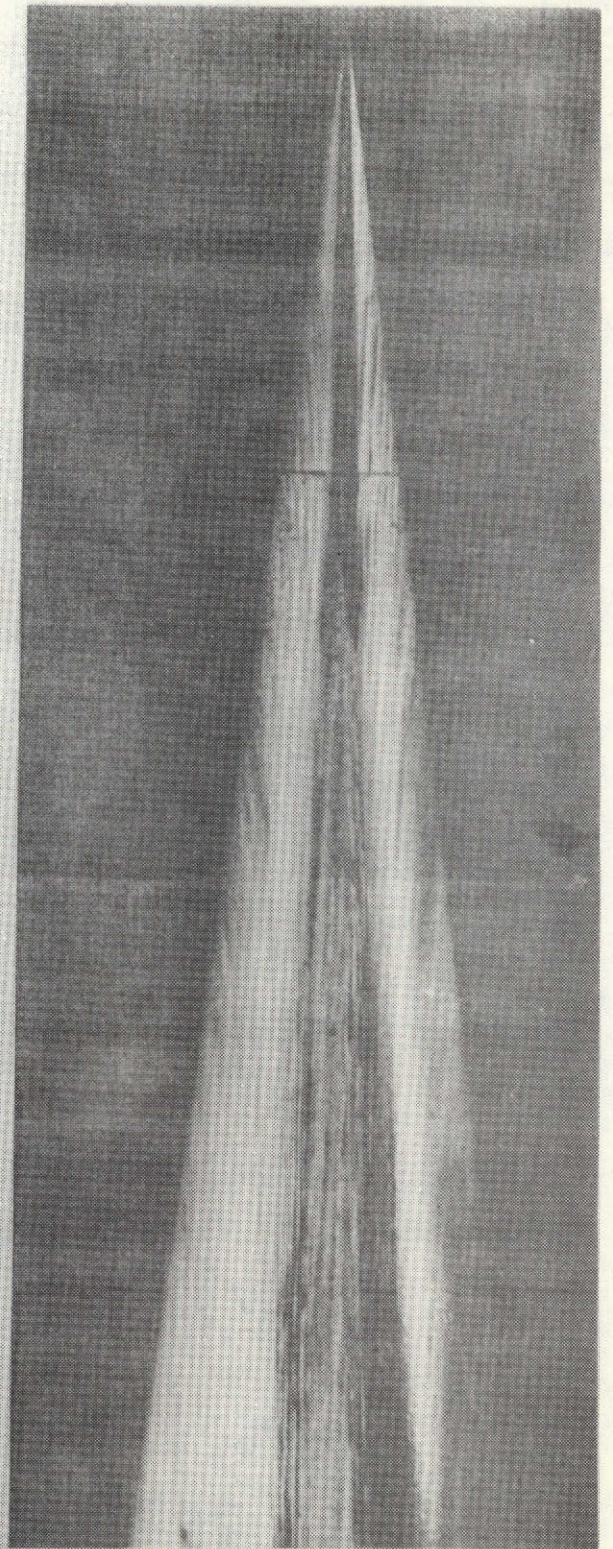


Fig. 101 Comparison of the Static Pressure Profiles Between Experiments and Inviscid Flow Theory, $\alpha = 30^\circ$

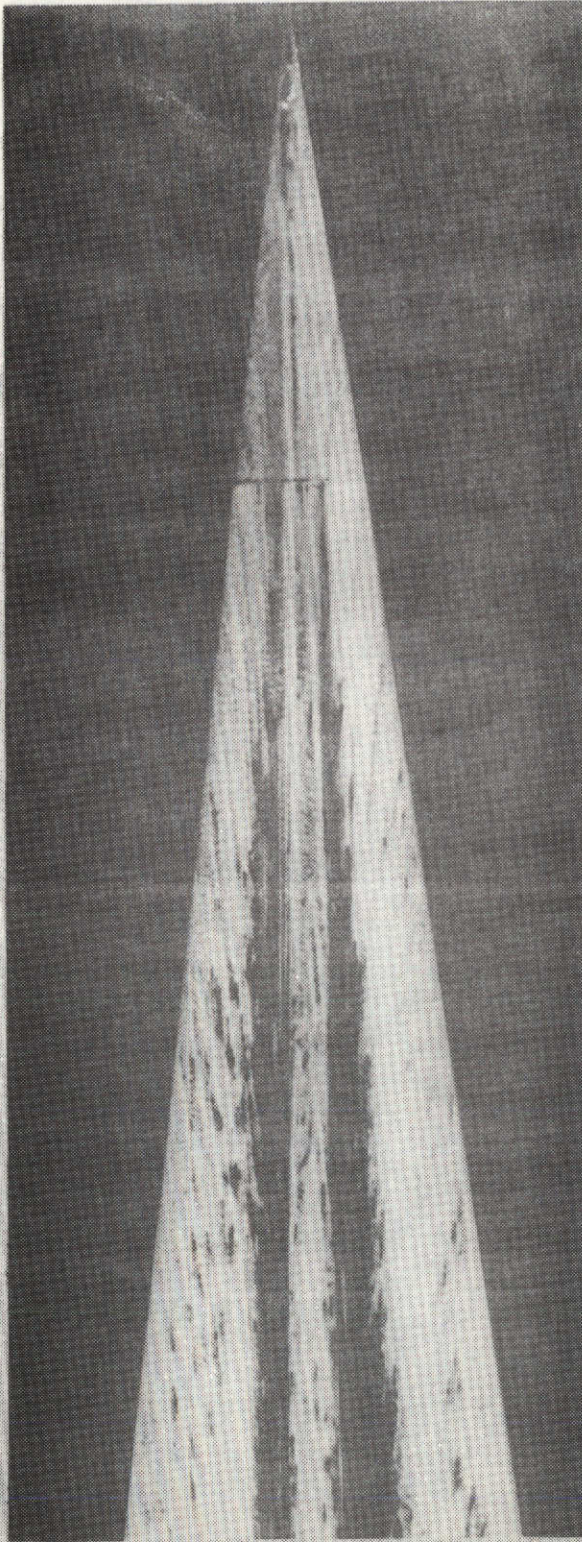


a) $\alpha = 7.5^\circ$, $\alpha/\theta_c = 1.0$
 $R_\infty = 1.61 \times 10^7/m$

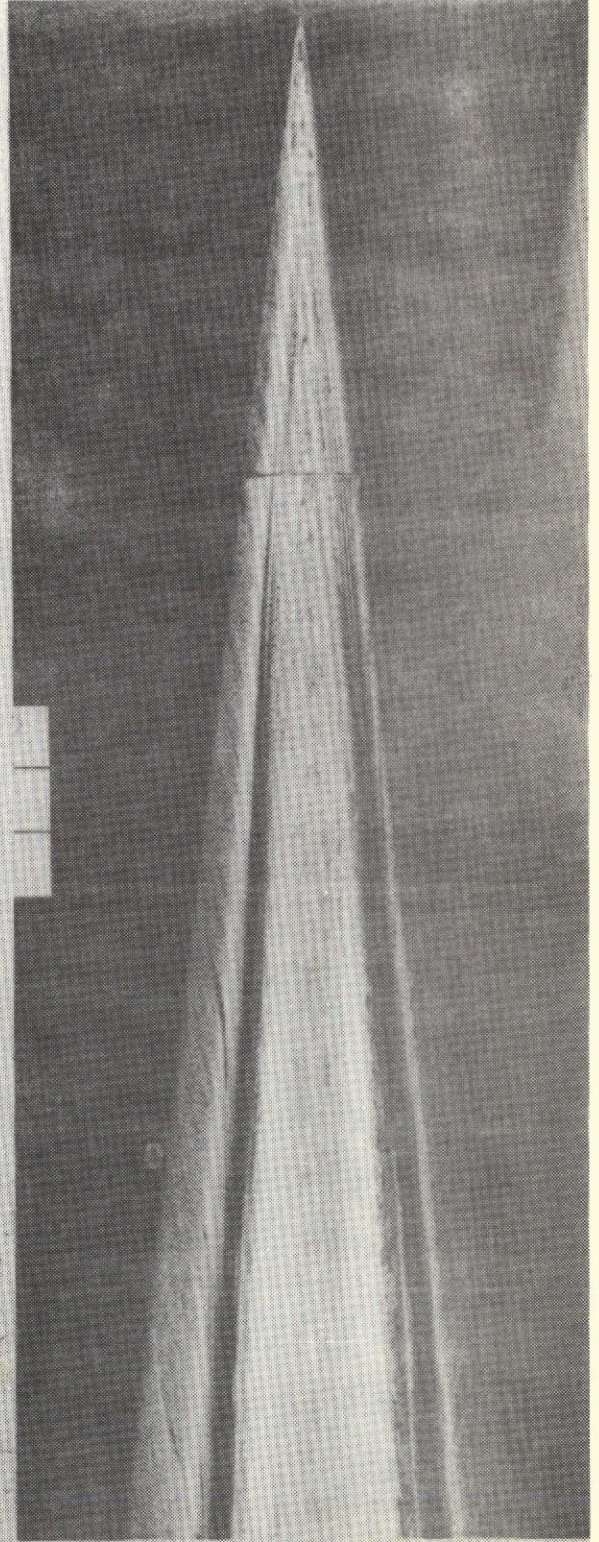


b) $\alpha = 7.5^\circ$, $\alpha/\theta_c = 1.0$
 $R_\infty = 3.12 \times 10^7/m$

Fig. 102 Oil Flow Photographs of a Sharp Cone, $\alpha = 7.5^\circ$

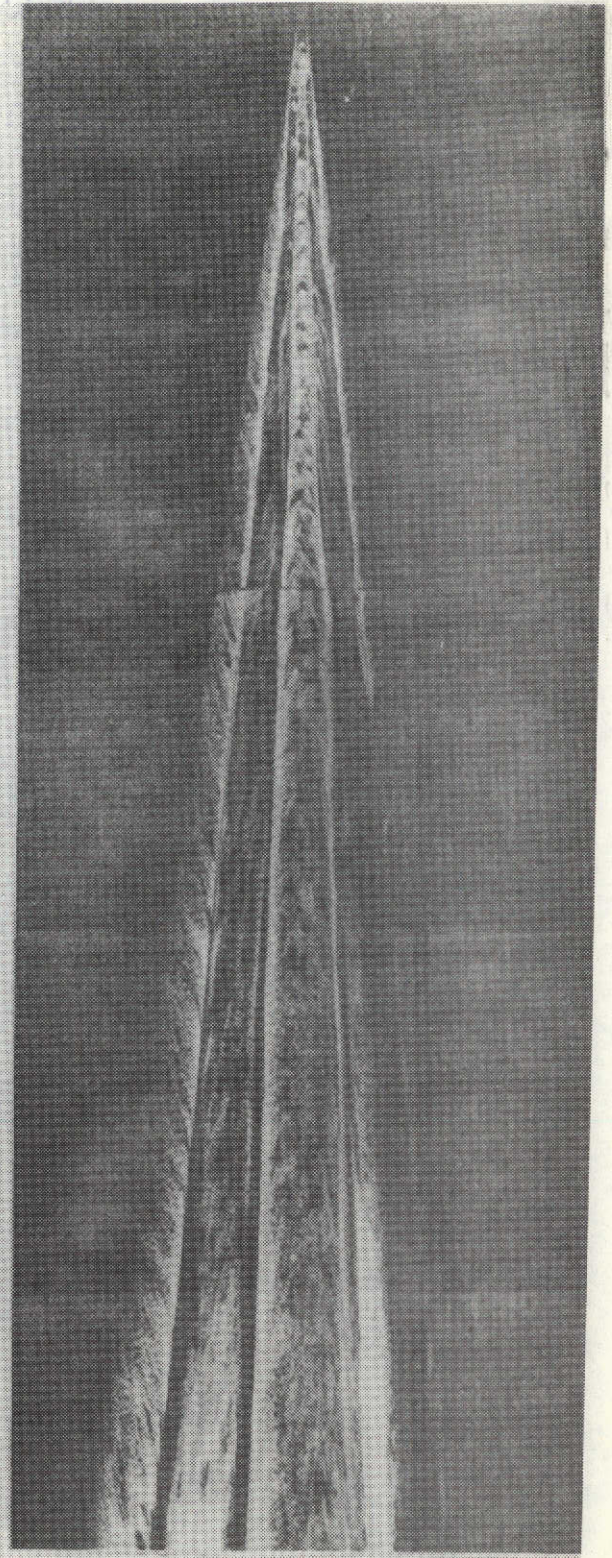
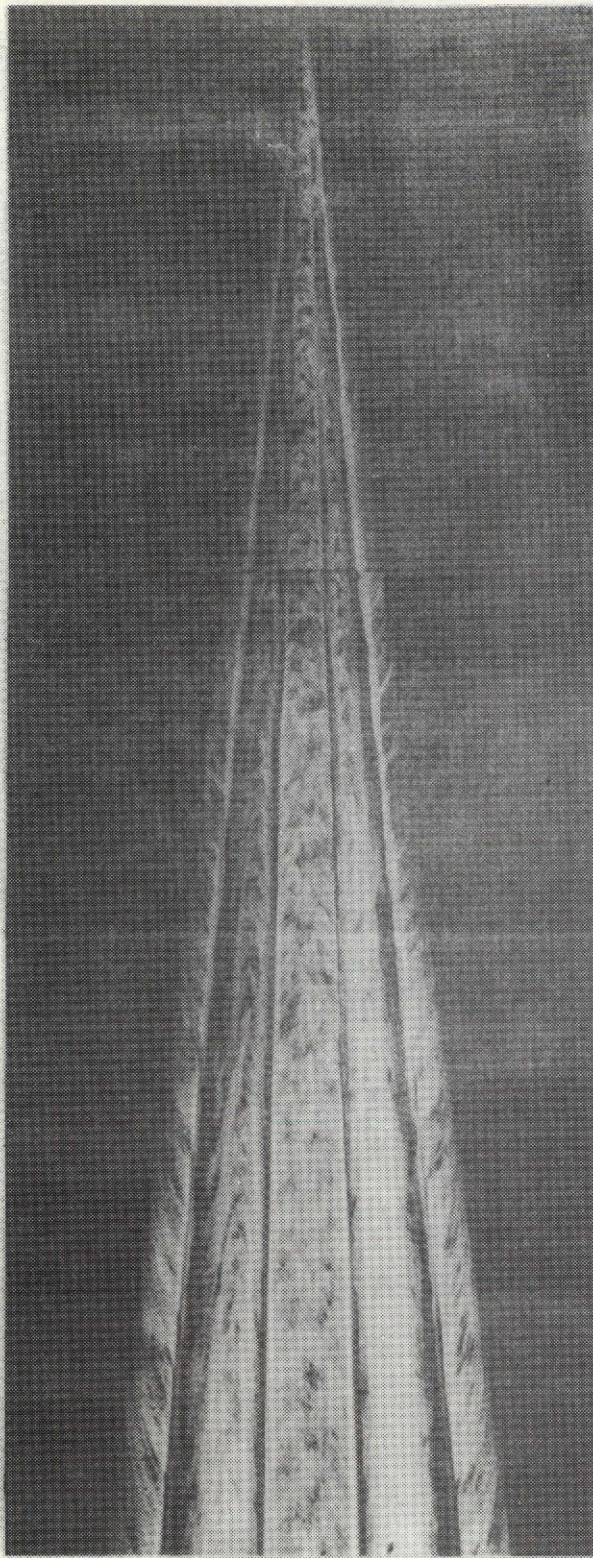


a) $\alpha = 7.5^\circ$, $\alpha/\theta_c = 1.0$
 $R_\infty = 11.8 \times 10^7/\text{m}$



b) $\alpha = 10^\circ$, $\alpha/\theta_c = 1.33$
 $R_\infty = 11.6 \times 10^7/\text{m}$

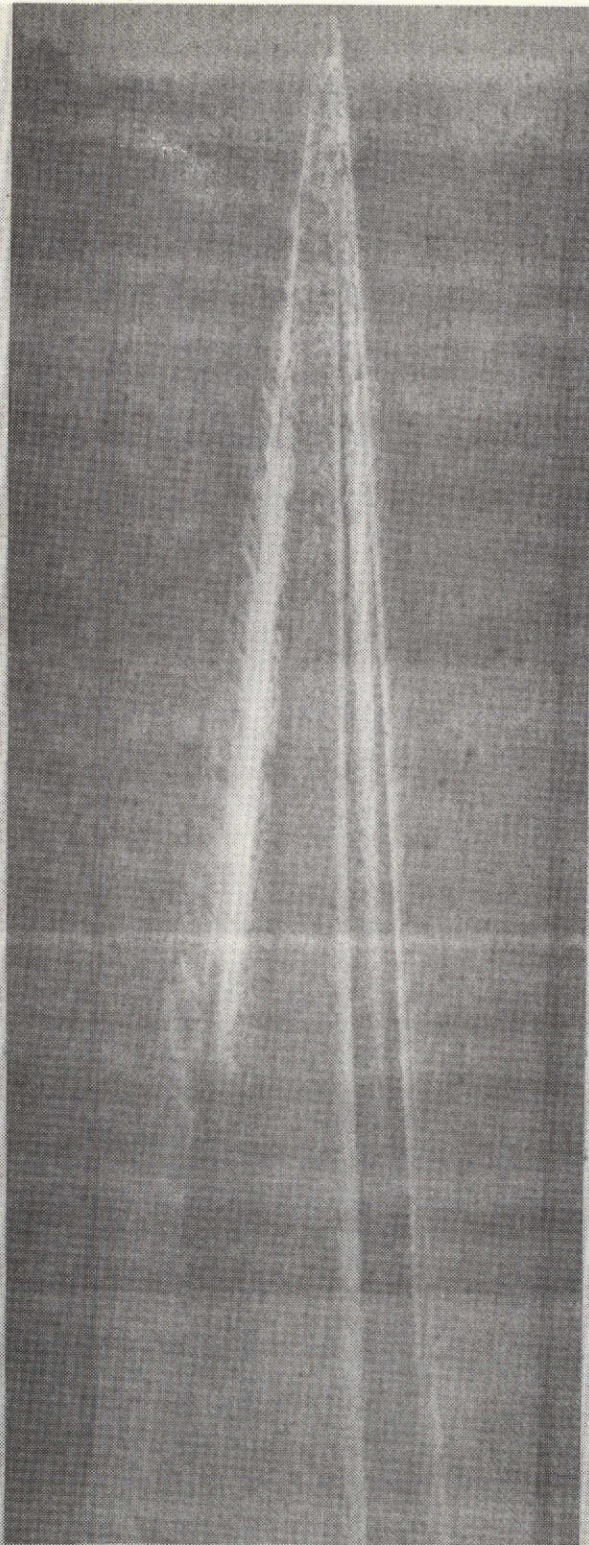
Fig. 103 Oil Flow Photographs of a Sharp Cone; $\alpha = 7.5^\circ, 10^\circ$



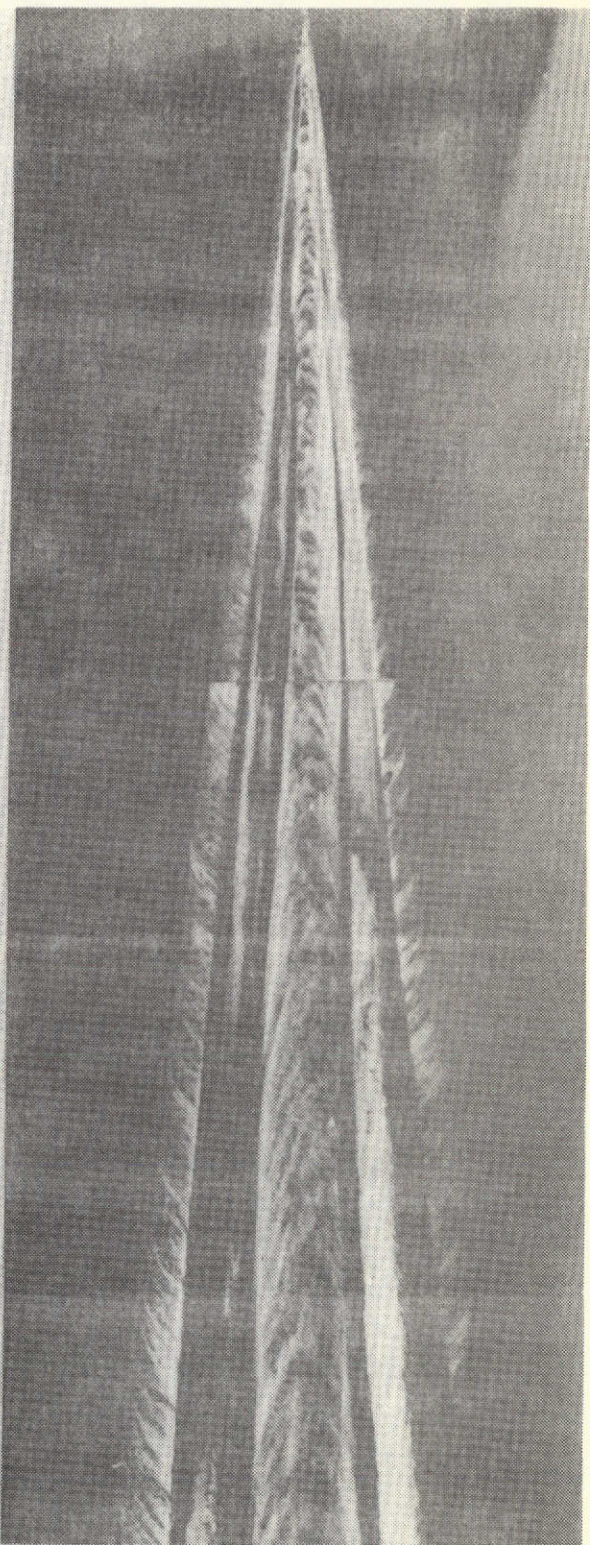
a) $\alpha = 11.5^\circ$, $\alpha/\theta_c = 1.53$
 $R_\infty = 12.3 \times 10^7/m$

b) $\alpha = 11.5^\circ$, $\alpha/\theta_c = 1.53$
 $R_\infty = 12.3 \times 10^7/m$

Fig. 104. (a) Flow photographs of a Sharp Cone; $\alpha = 11.5^\circ$



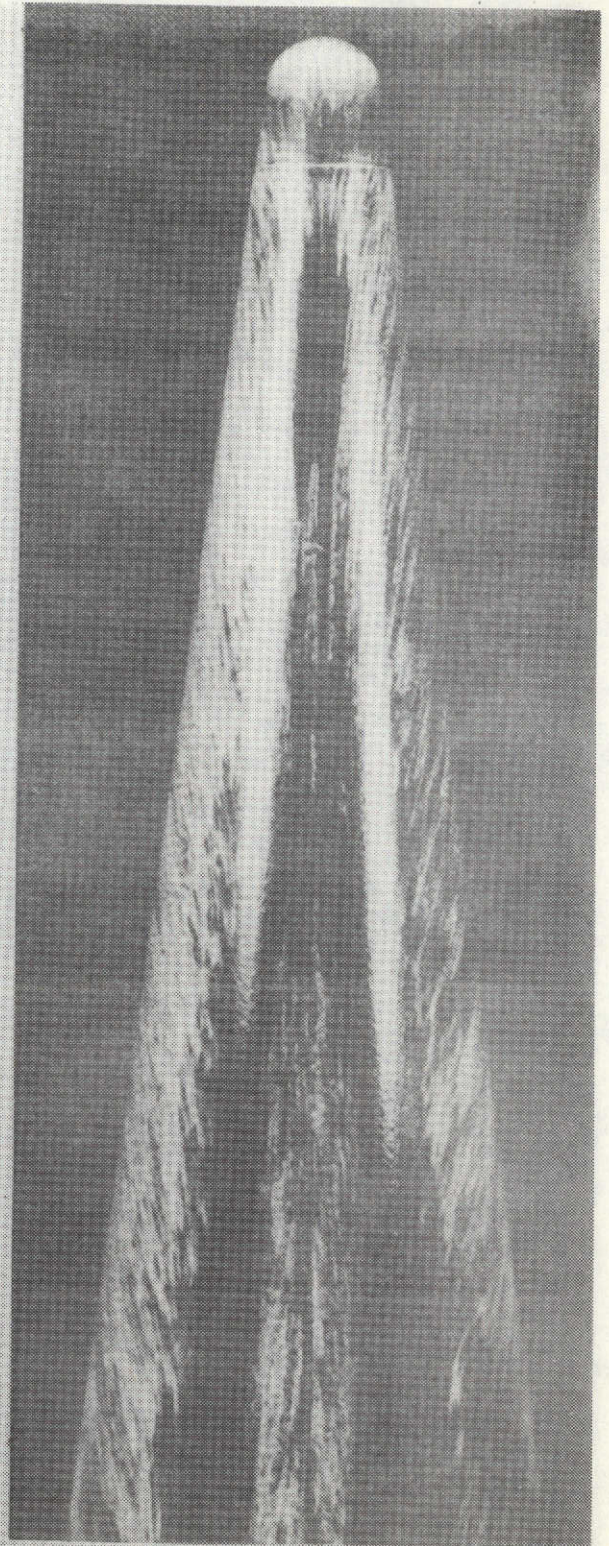
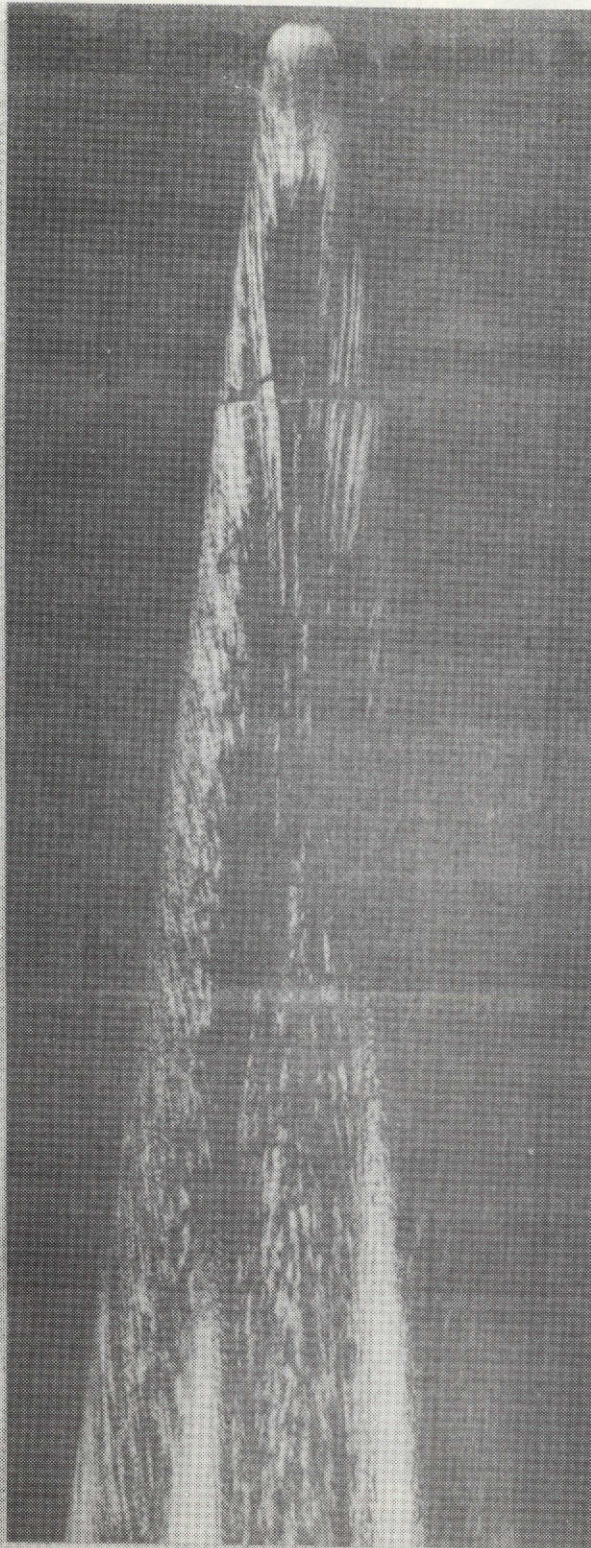
a) $\alpha = 20^\circ$, $\alpha/\beta_c = 2.67$
 $R_\infty = 11.8 \times 10^7/\text{m}$



b) $\alpha = 22.5^\circ$, $\alpha/\beta_c = 3.0$
 $R_\infty = 12.7 \times 10^7/\text{m}$

Fig. 105 Oil Flow Photographs of a Sharp Cone $\alpha = 20^\circ, 22.5^\circ$

**REPRODUCIBILITY OF THE
ORIGINAL PAGE IS POOR**

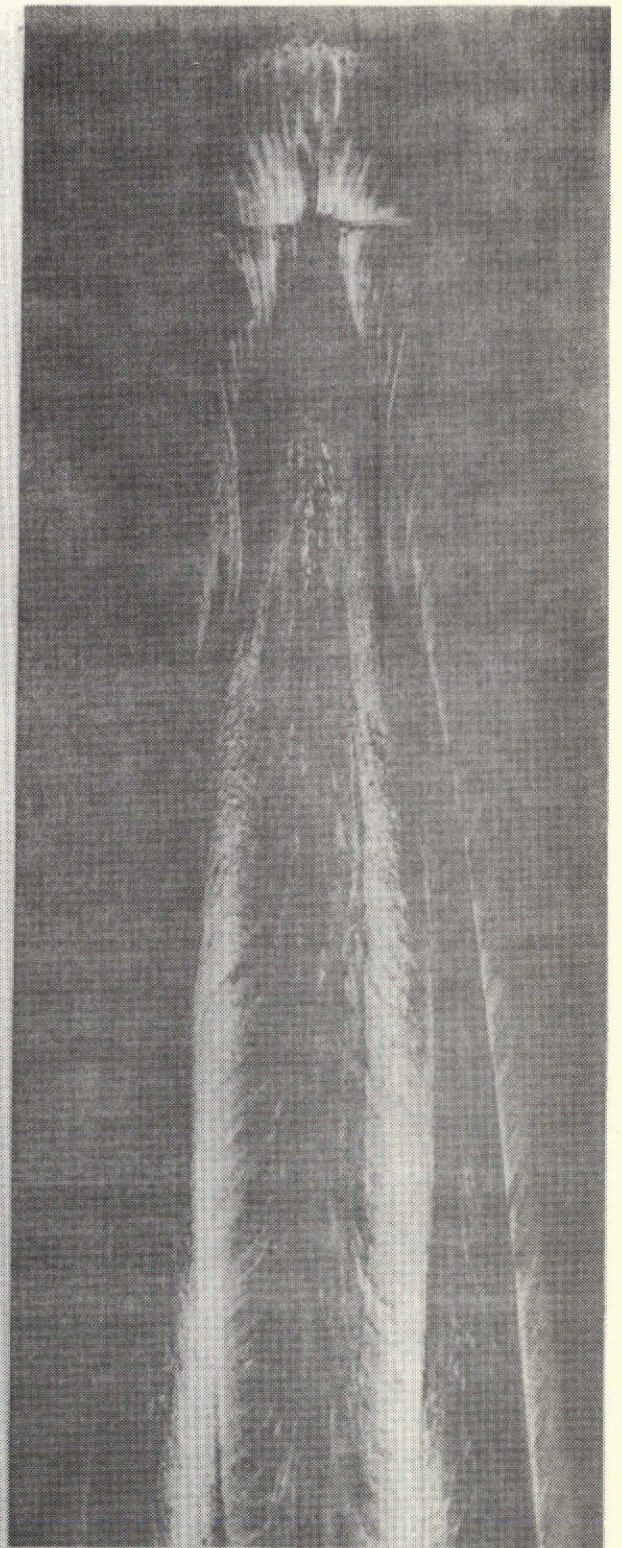
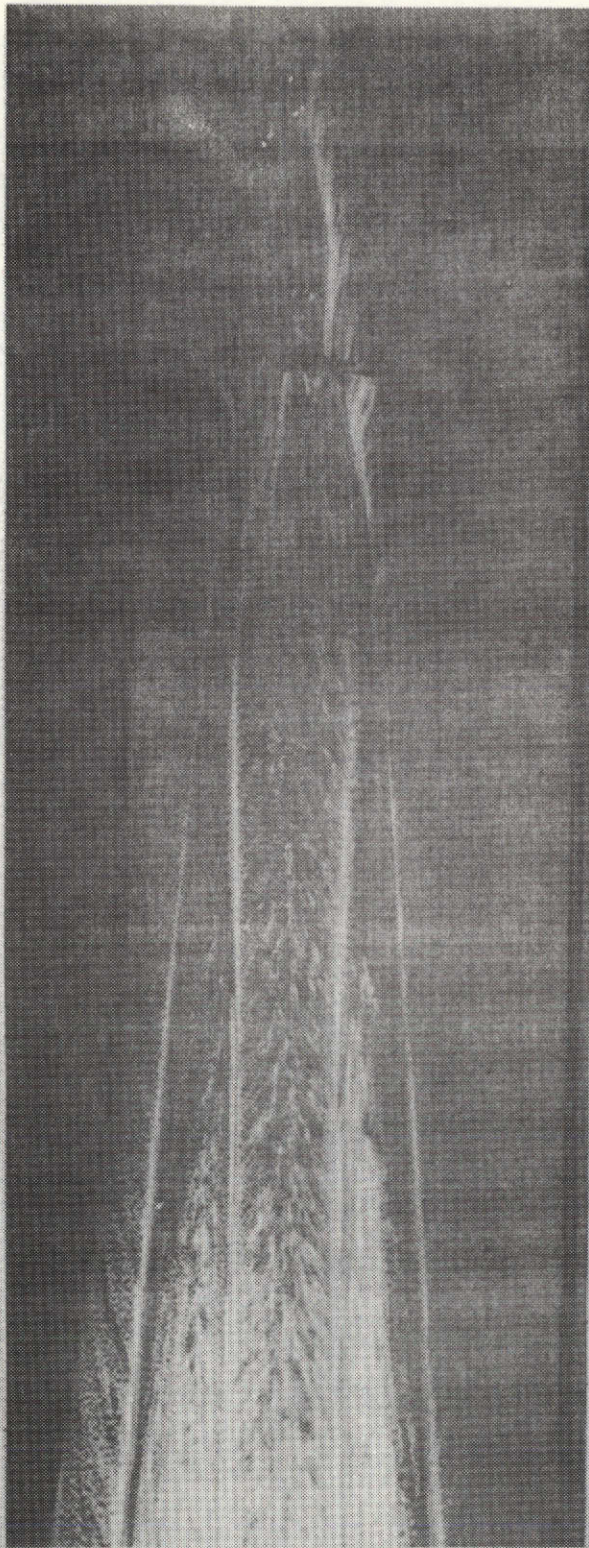


a) $\alpha = 7.5^\circ$, $\alpha/\theta_c = 1.0$, $R_N/R_B = 0.12$
 $R_\infty = 13.0 \times 10^7/\text{m}$

b) $\alpha = 10^\circ$, $\alpha/\theta_c = 1.33$, $R_N/R_B = 0.24$
 $R_\infty = 12.5 \times 10^7/\text{m}$

Fig. 106 Oil Flow Photographs of Blunt Cones; $\alpha = 7.5^\circ, 10^\circ$

LIBRARY OF THE
 NATIONAL BUREAU OF STANDARDS

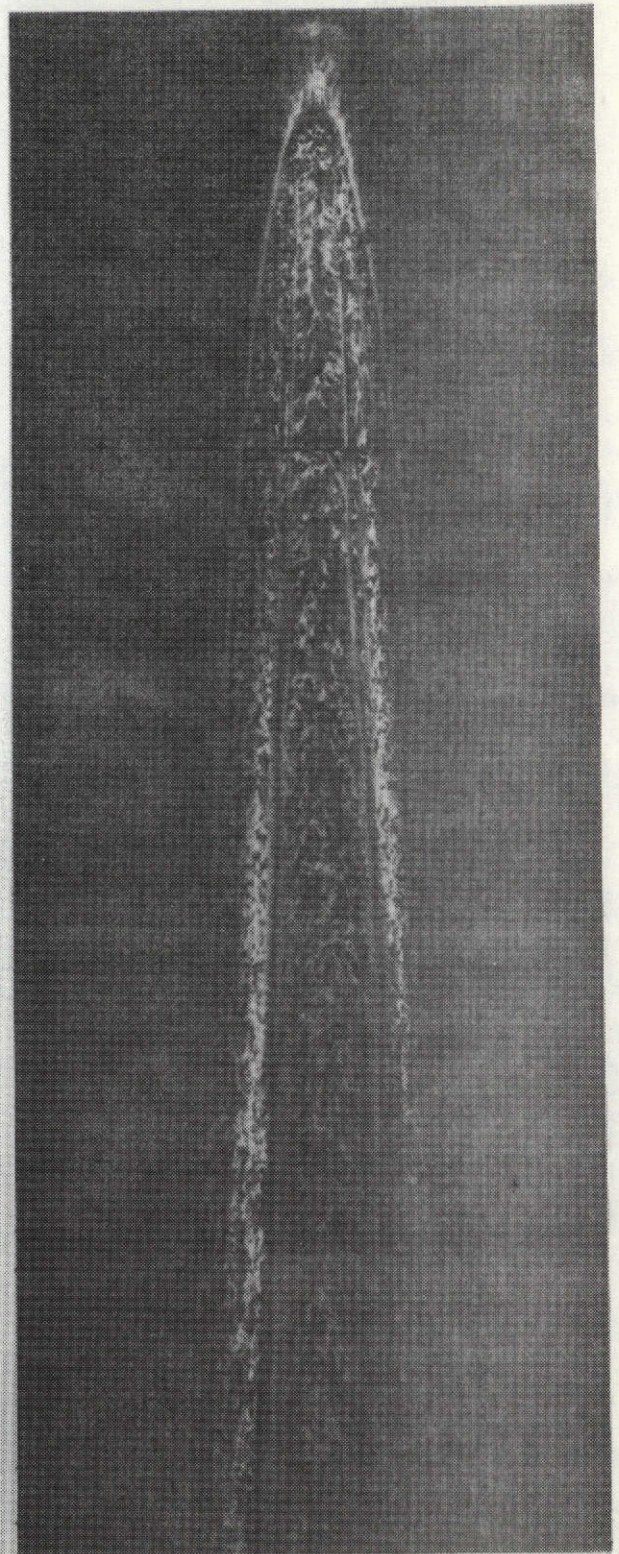
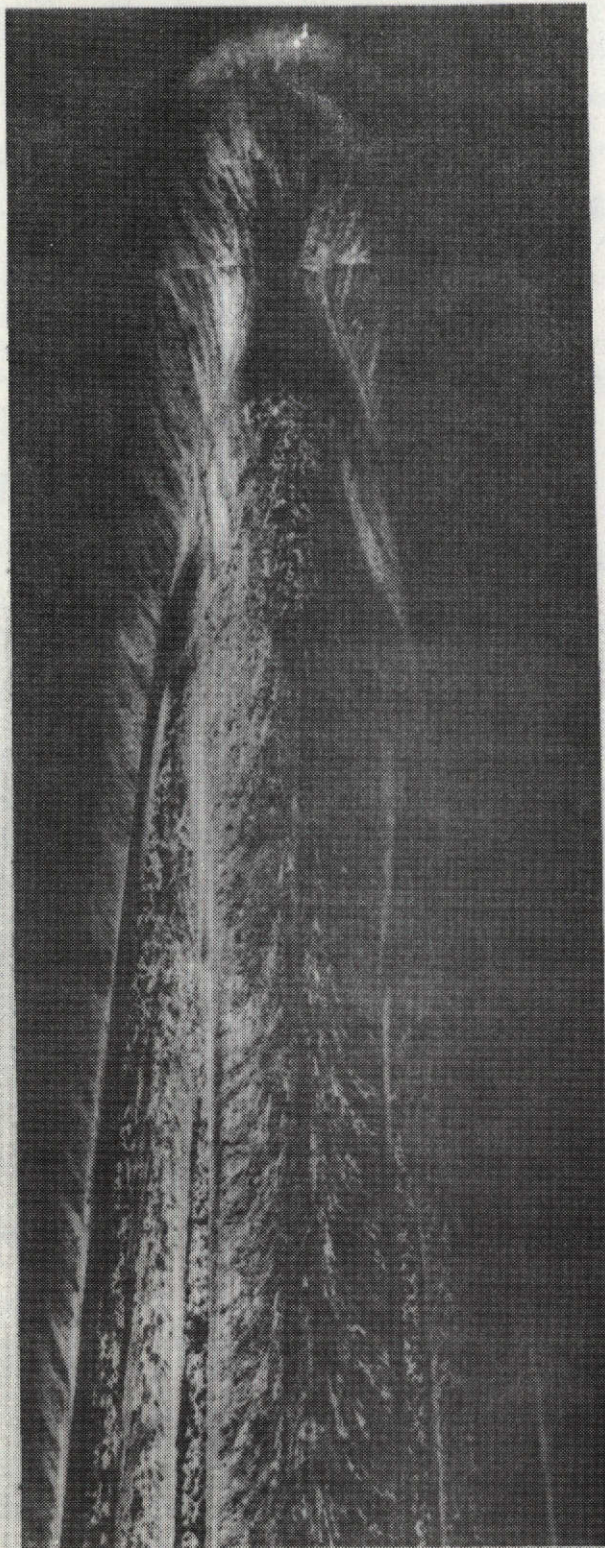


a) $\alpha = 11.5^\circ$, $\alpha/\theta_c = 1.53$, $R_N/R_B = 0.12$
 $R_\infty = 11.9 \times 10^7/\text{m}$

b) $\alpha = 15^\circ$, $\alpha/\theta_c = 2.0$, $R_N/R_B = 0.24$
 $R_\infty = 11.7 \times 10^7/\text{m}$

Fig. 107 Oil Flow Photographs of Blunt Cones; $\alpha = 11.5^\circ$, 15°

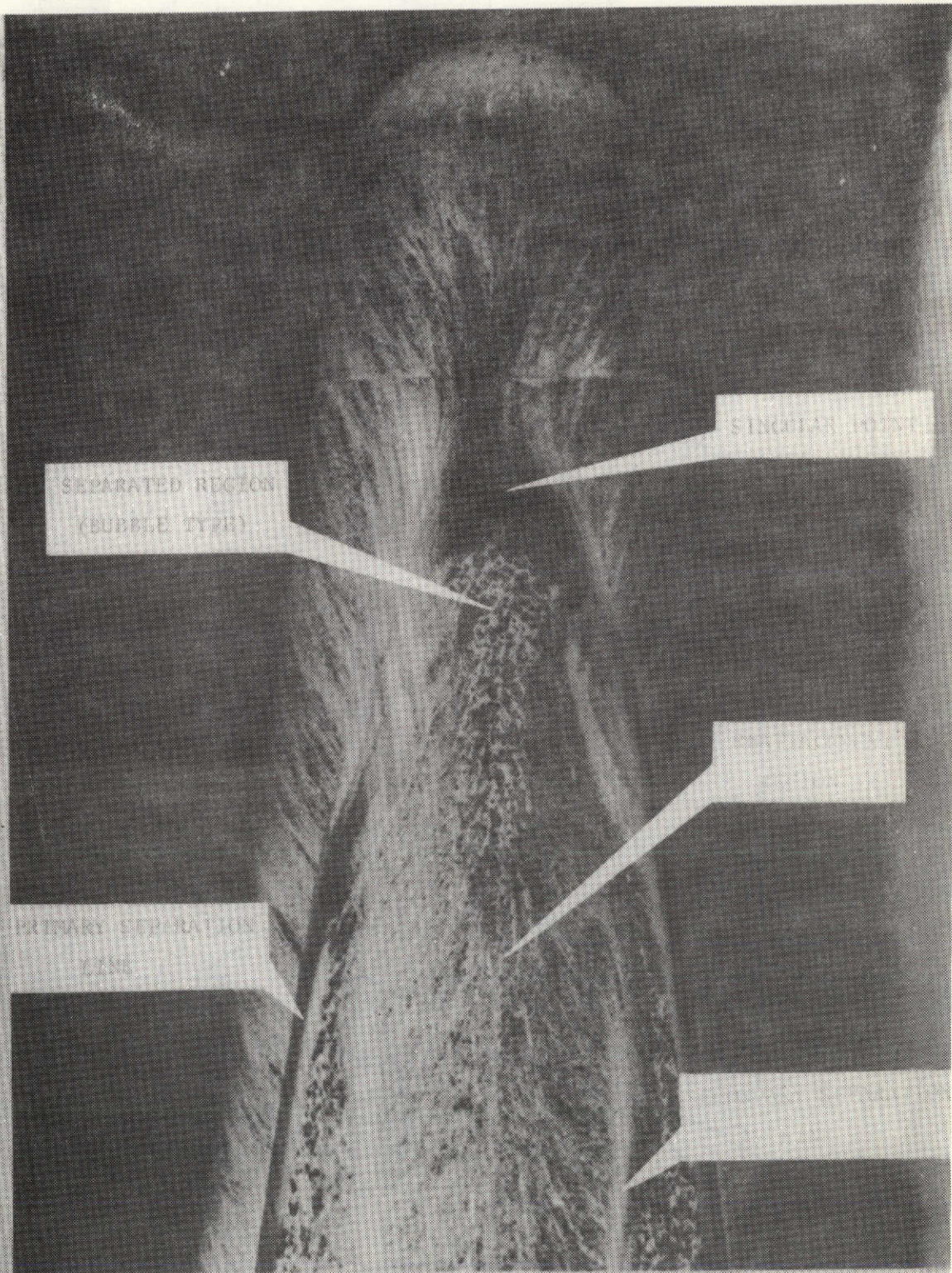
**REPRODUCIBILITY OF THE
 ORIGINAL PAGE IS POOR**



a) $\alpha = 20^\circ$, $\alpha/\theta_c = 2.67$, $R_N/R_B = 0.24$
 $R_\infty = 11.6 \times 10^7/m$

b) $\alpha = 22.5^\circ$, $\alpha/\theta_c = 3.0$, $R_N/R_B = 0.12$
 $R_\infty = 11.5 \times 10^7/m$

Fig. 108 Oil Flow Photographs of Blunt Cones; $\alpha = 20^\circ, 22.5^\circ$



$$\alpha = 20^\circ, \alpha/\theta_c = 2.67, R_N/R_B = 0.24, R_\infty = 11.6 \times 10^7 / \text{m}$$

Fig. 109 Surface Flow Pattern Near the Nose of a Blunt Cone

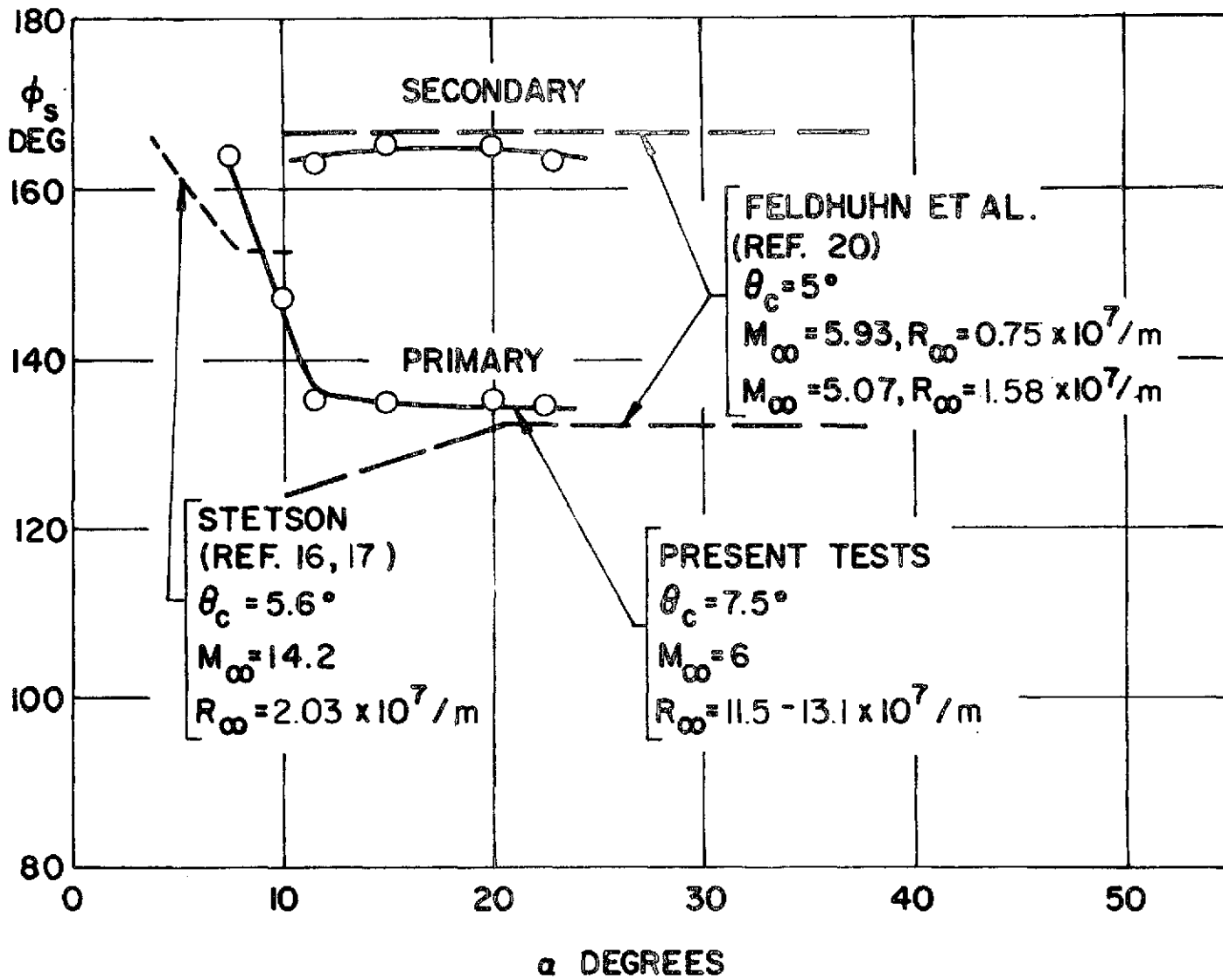


Fig. 110 Separation Lines on a Sharp Cone (ϕ_s vs. α)

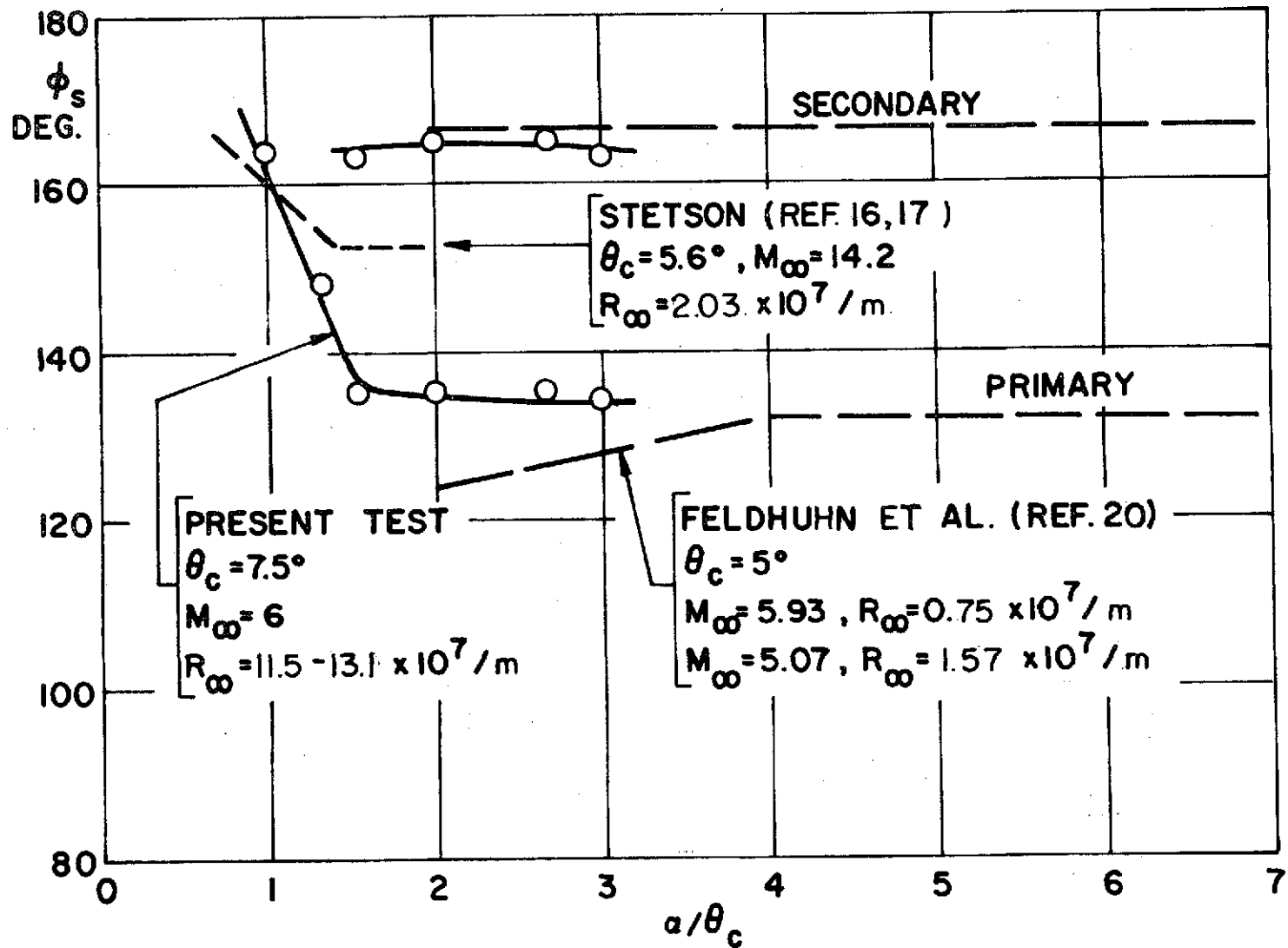


Fig. 111 Separation Lines on a Sharp Cone (ϕ_s vs. α/θ_c)

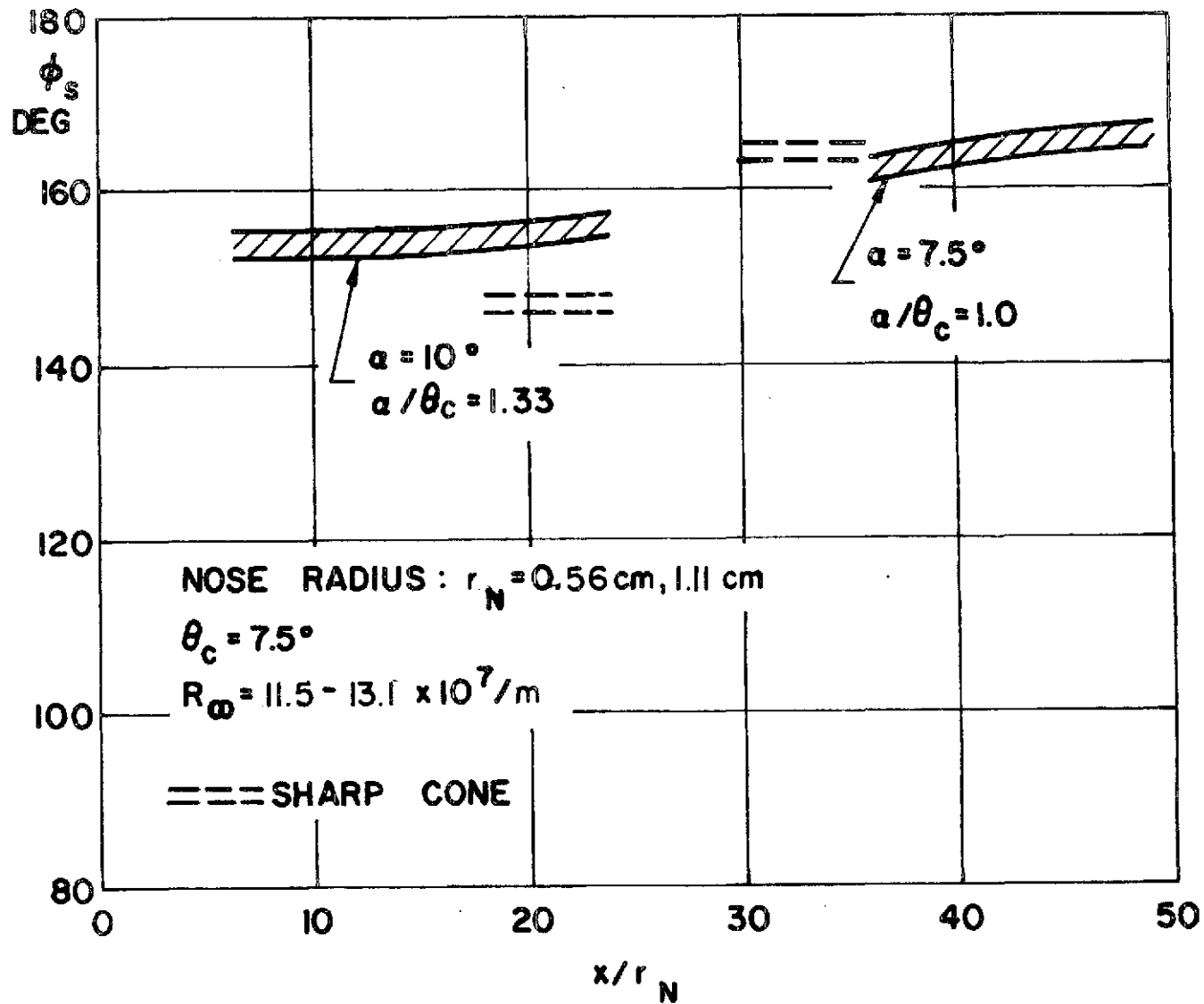


Fig. 112 Separation Lines on Blunt Cones ; $\alpha = 7.5^\circ, 10^\circ$

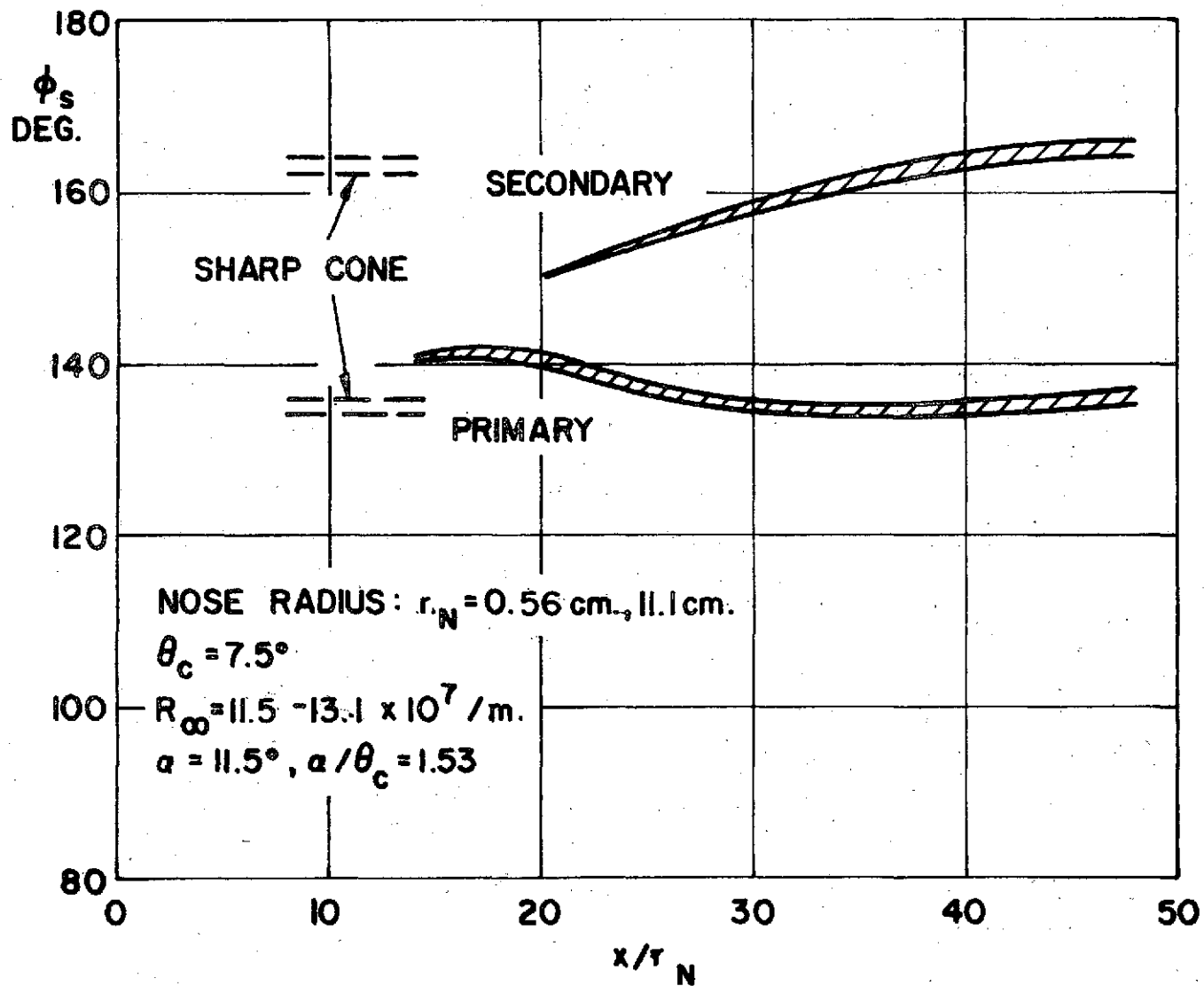


Fig. 113 Separation Lines on Blunt Cones ; $\alpha = 11.5^\circ$

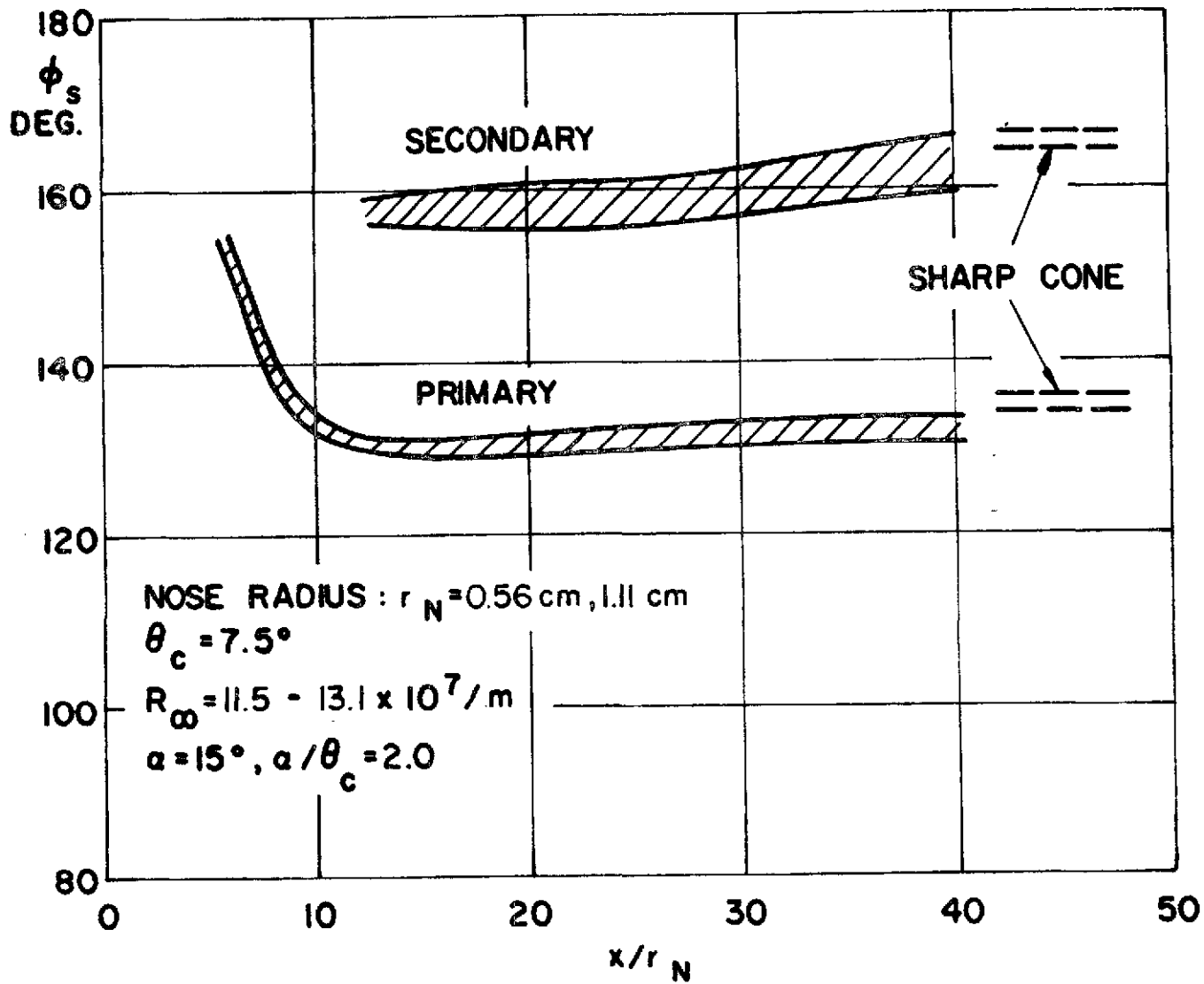


Fig. 114 Separation Lines on Blunt Cones ; $\alpha = 15^\circ$

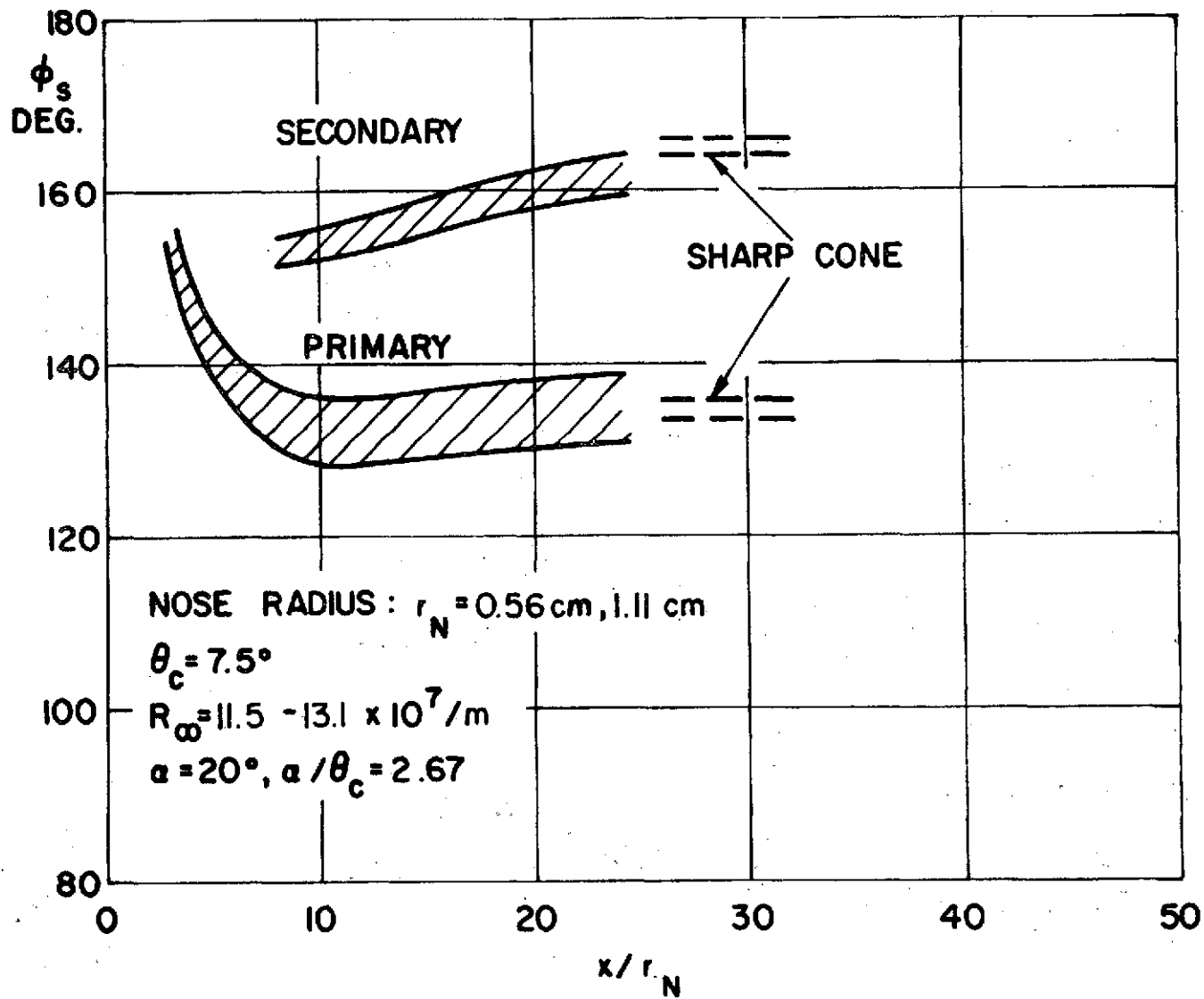


Fig. 115 Separation Lines on Blunt Cones ; $\alpha = 20^\circ$

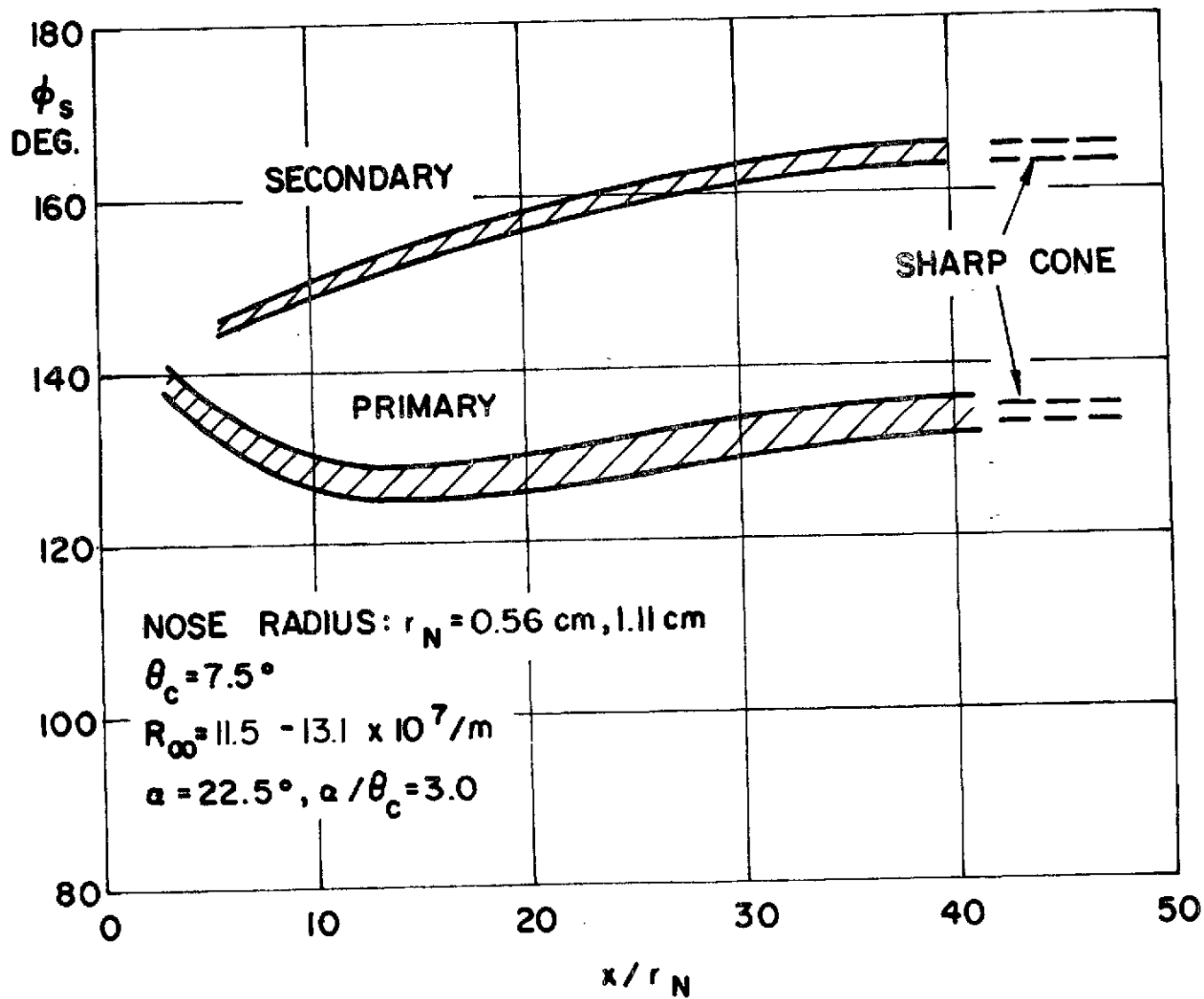


Fig. 116 Separation Lines on Blunt Cones ; $\alpha = 22.5^\circ$

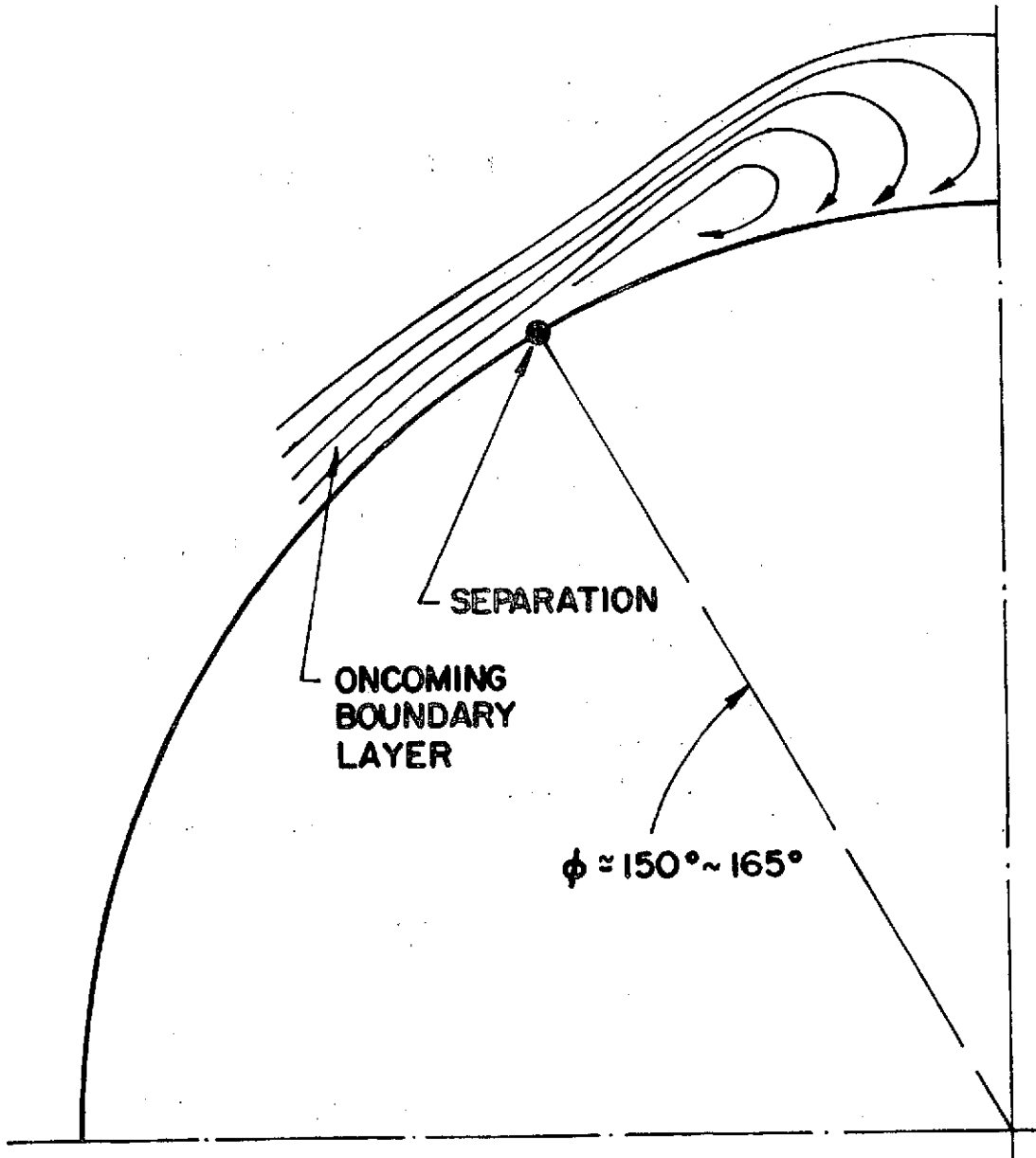


Fig. 117 Flow Model at Moderate Angle of Attack

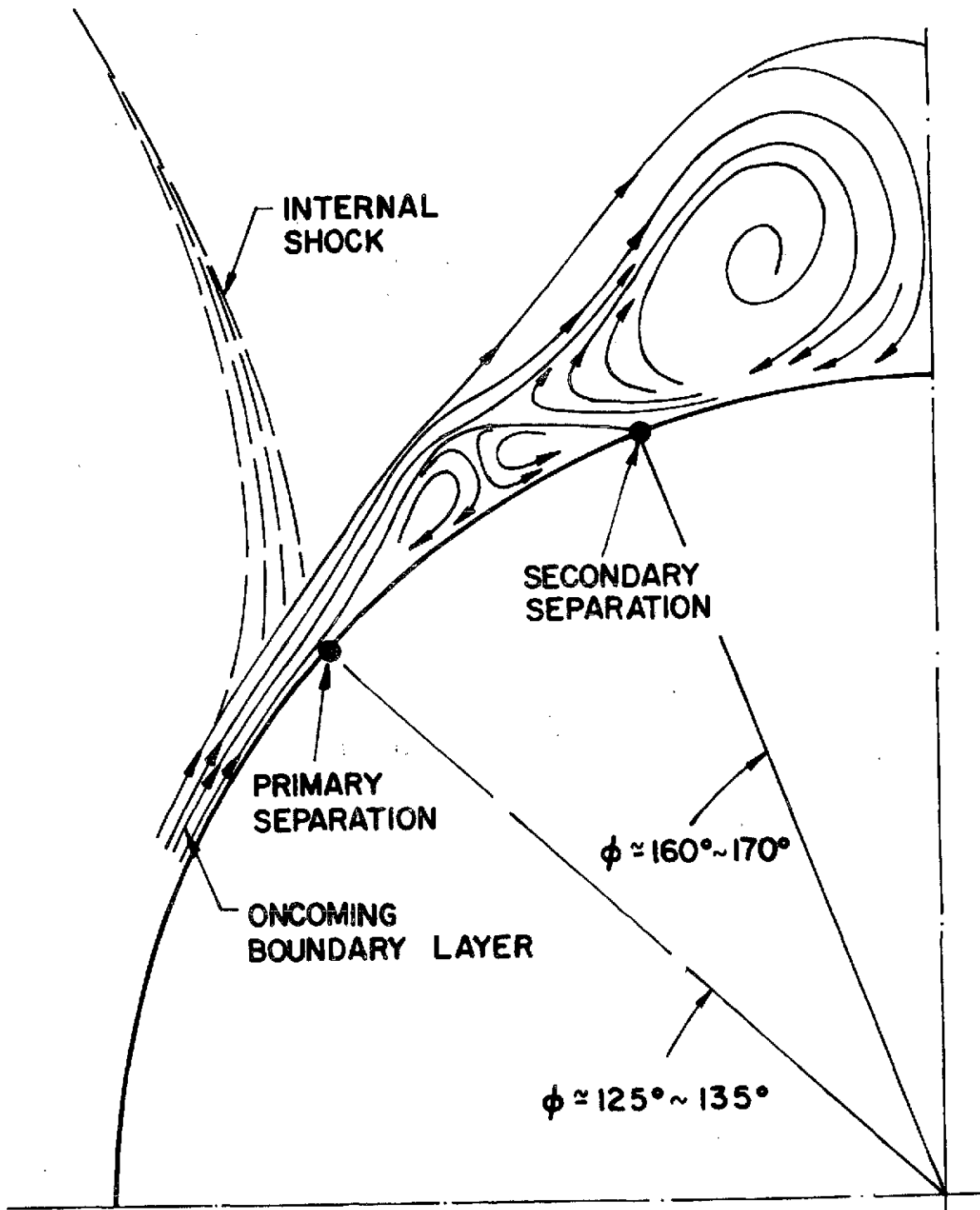


Fig. 118 Flow Model at Large Angle of Attack

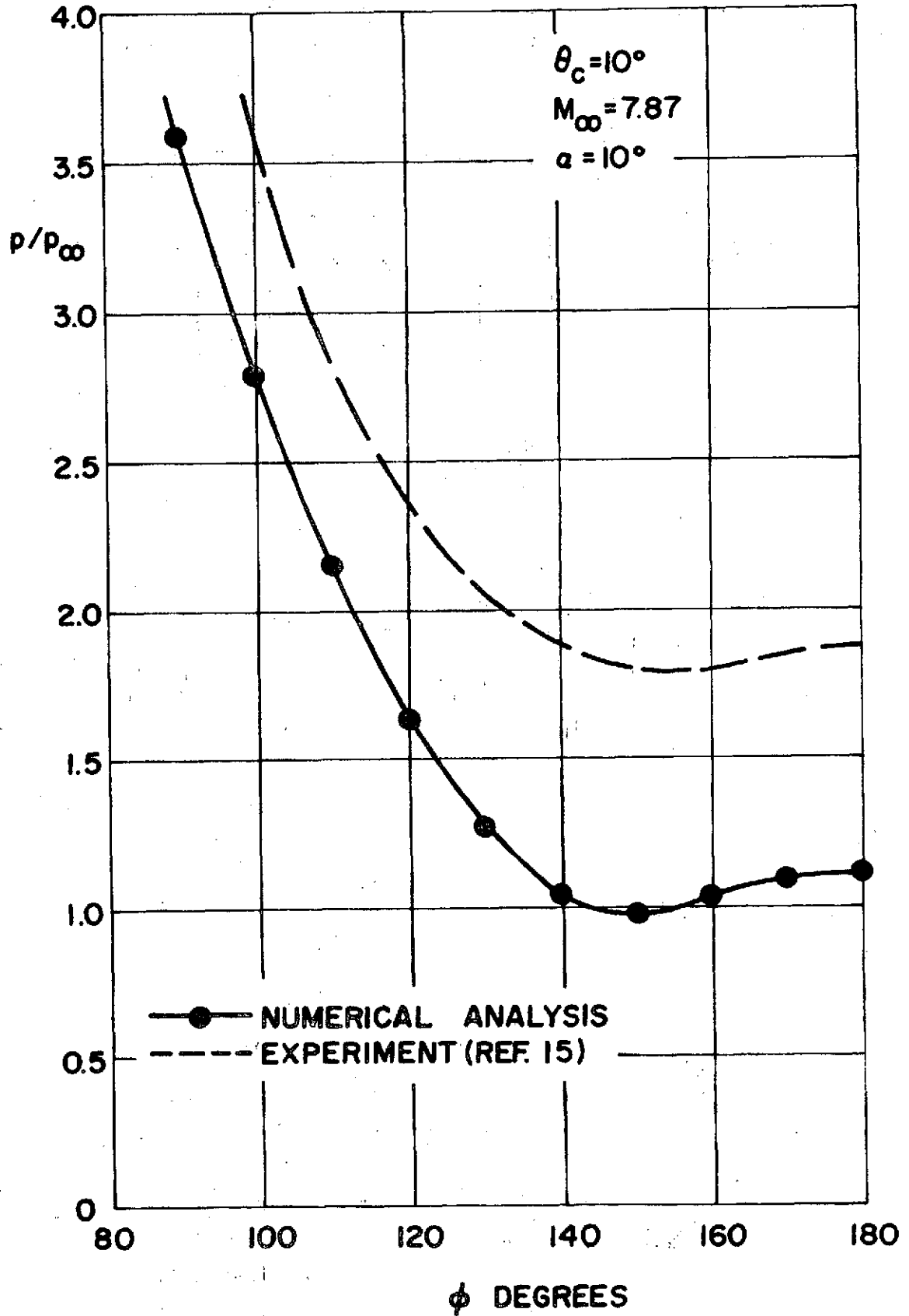


Fig. 119 Surface Pressure Distribution over a Circular Cone ;
 $\theta_c = 10^\circ$, $M_\infty = 7.87$, $\alpha = 10^\circ$

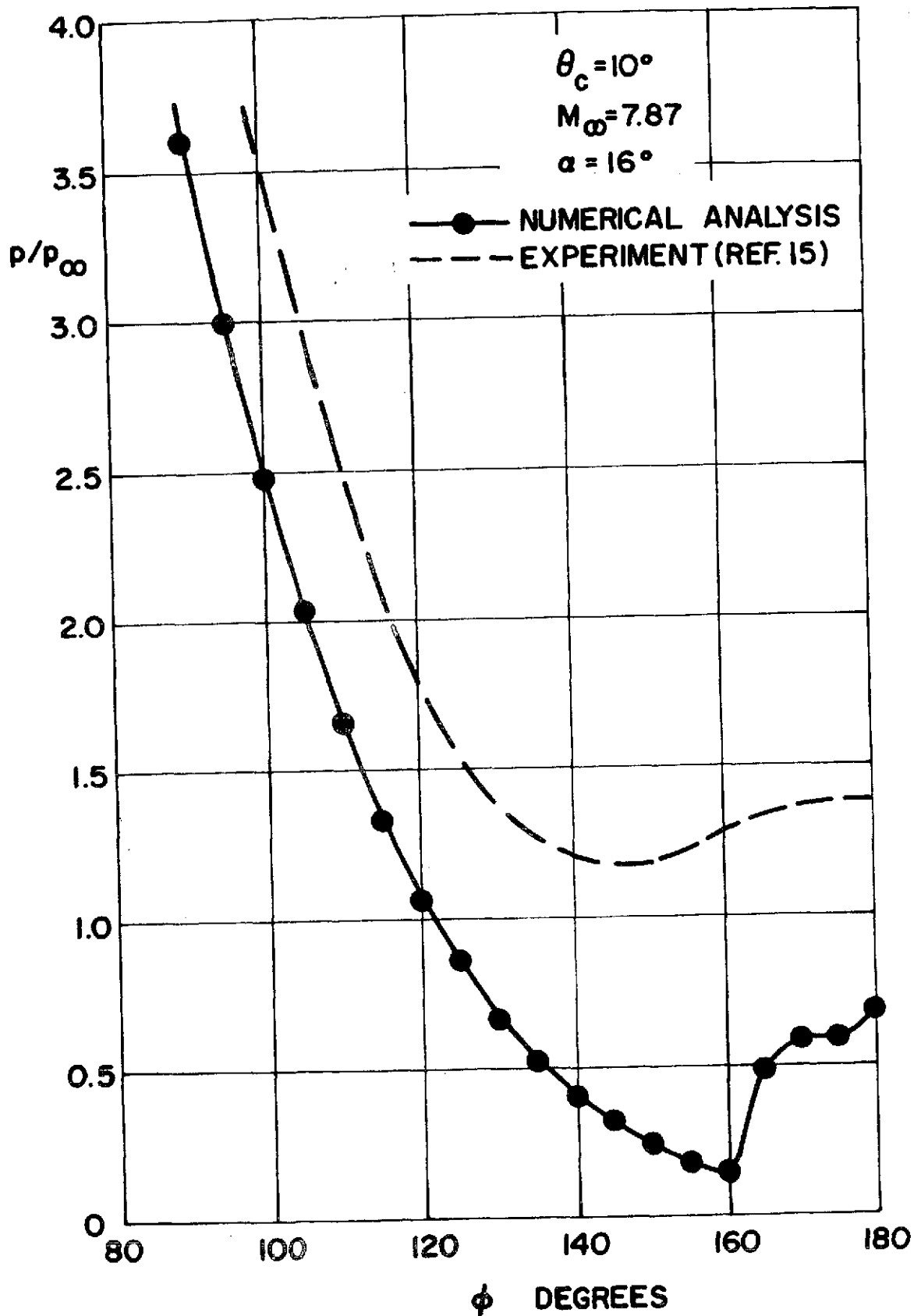


Fig. 120 Surface Pressure Distribution over a Circular Cone;
 $\theta_c = 10^\circ$, $M_\infty = 7.87$, $\alpha = 16^\circ$

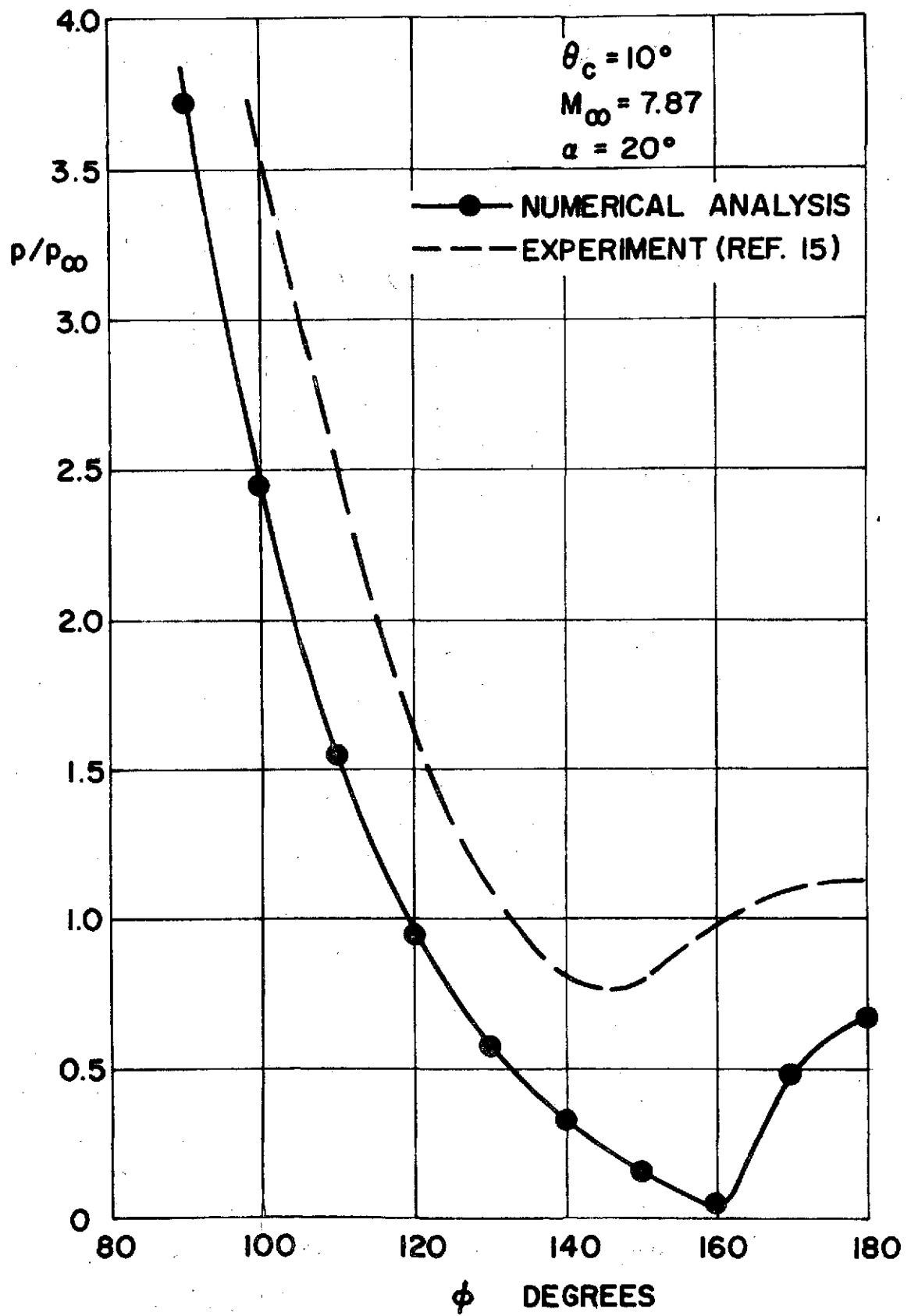


Fig. 121 Surface Pressure Distribution over a Circular Cone ;
 $\theta_c = 10^\circ$, $M_\infty = 7.87$, $\alpha = 20^\circ$

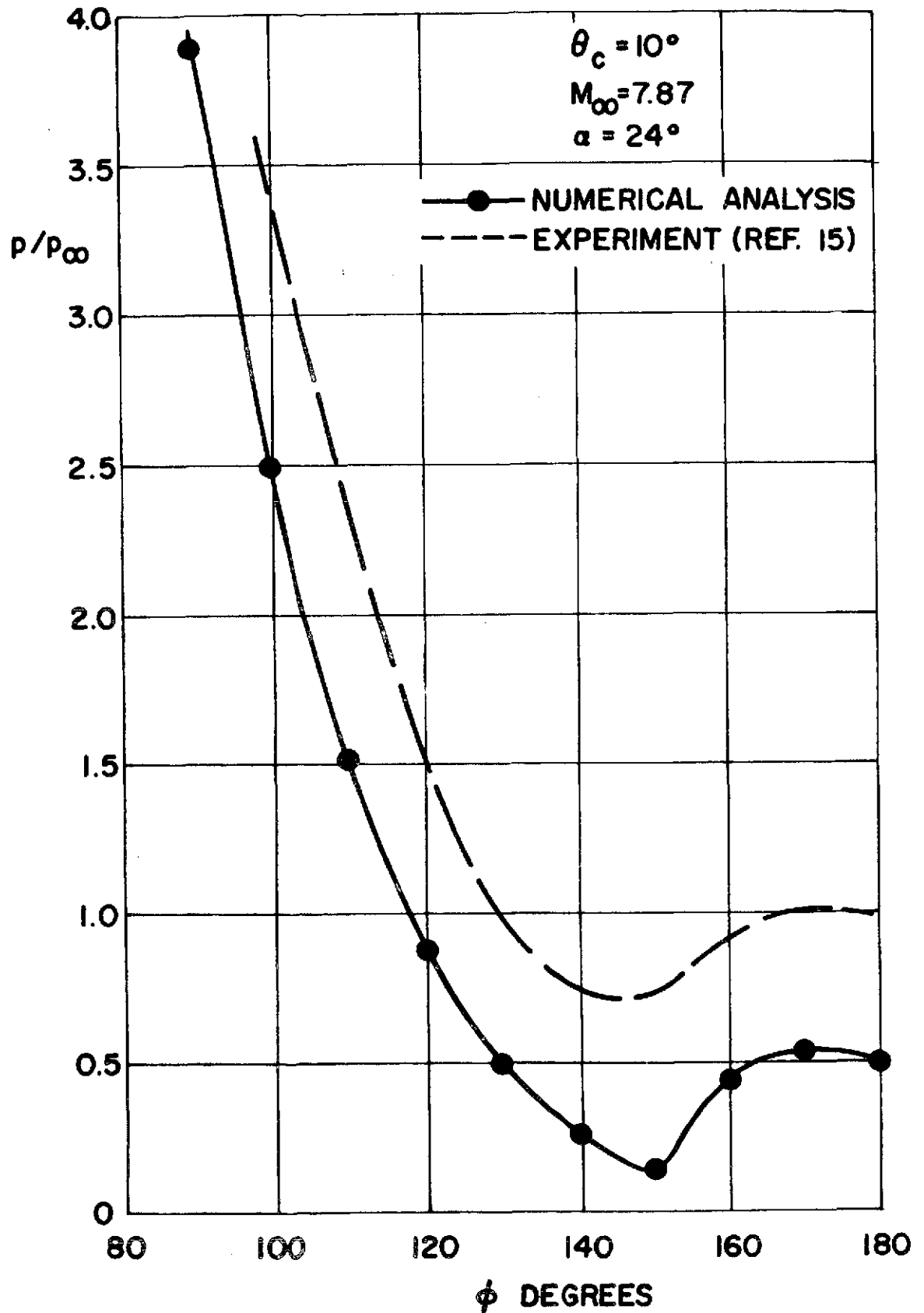


Fig. 122 Surface Pressure Distribution over a Circular Cone ;
 $\theta_c = 10^\circ$, $M_\infty = 7.87$, $\alpha = 24^\circ$

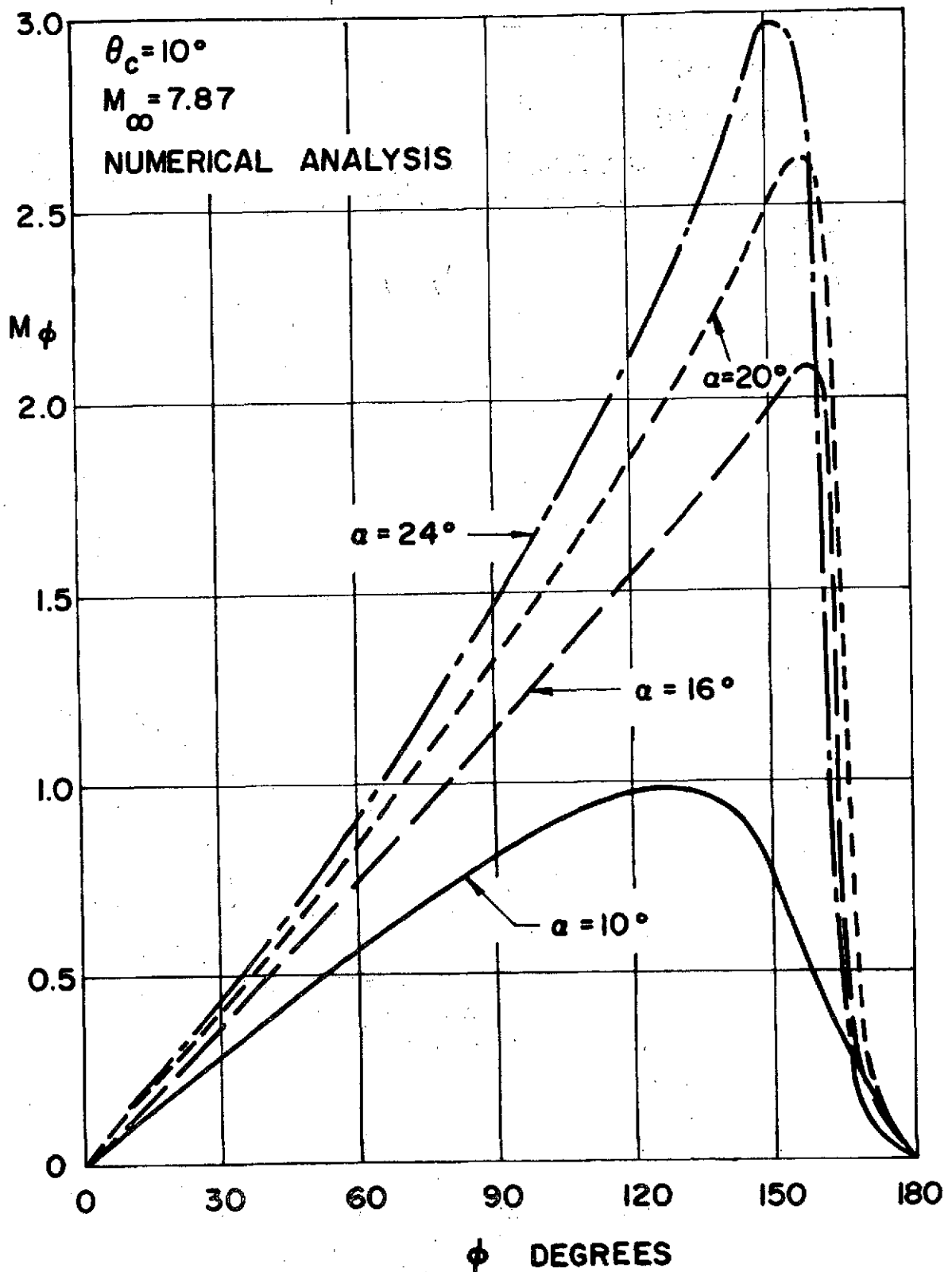


Fig. 123 Cross-Flow Mach Number Distributions on the Surface of a Circular Cone ; $\theta_c = 10^\circ$, $M_\infty = 7.87$

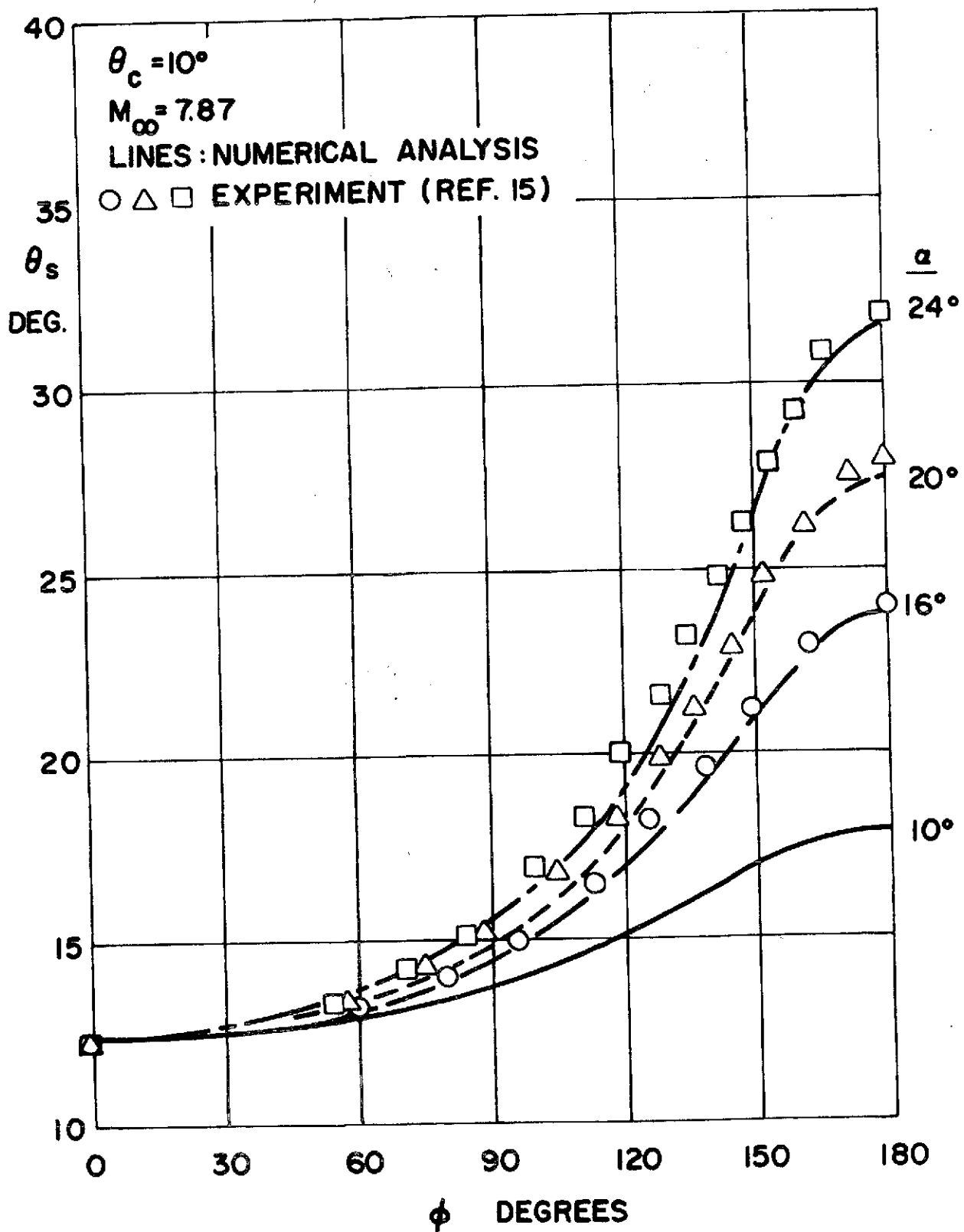


Fig. 124 External Shock Locations for a Circular Cone ;
 $\theta_c = 10^\circ$, $M_\infty = 7.87$

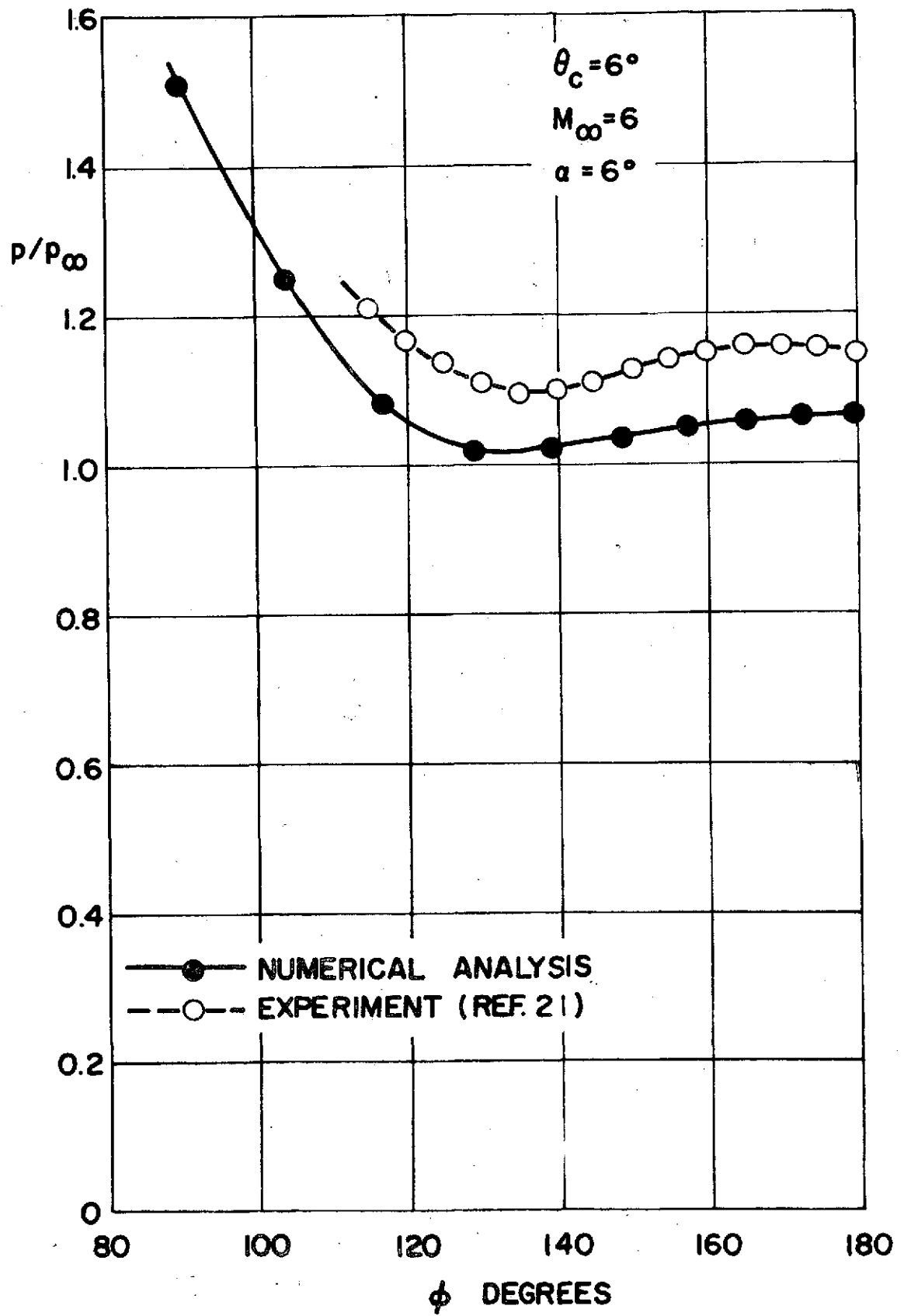


Fig. 125 Surface Pressure Distribution over a Circular Cone ;
 $\theta_c = 6^\circ, M_\infty = 6, \alpha = 6^\circ$

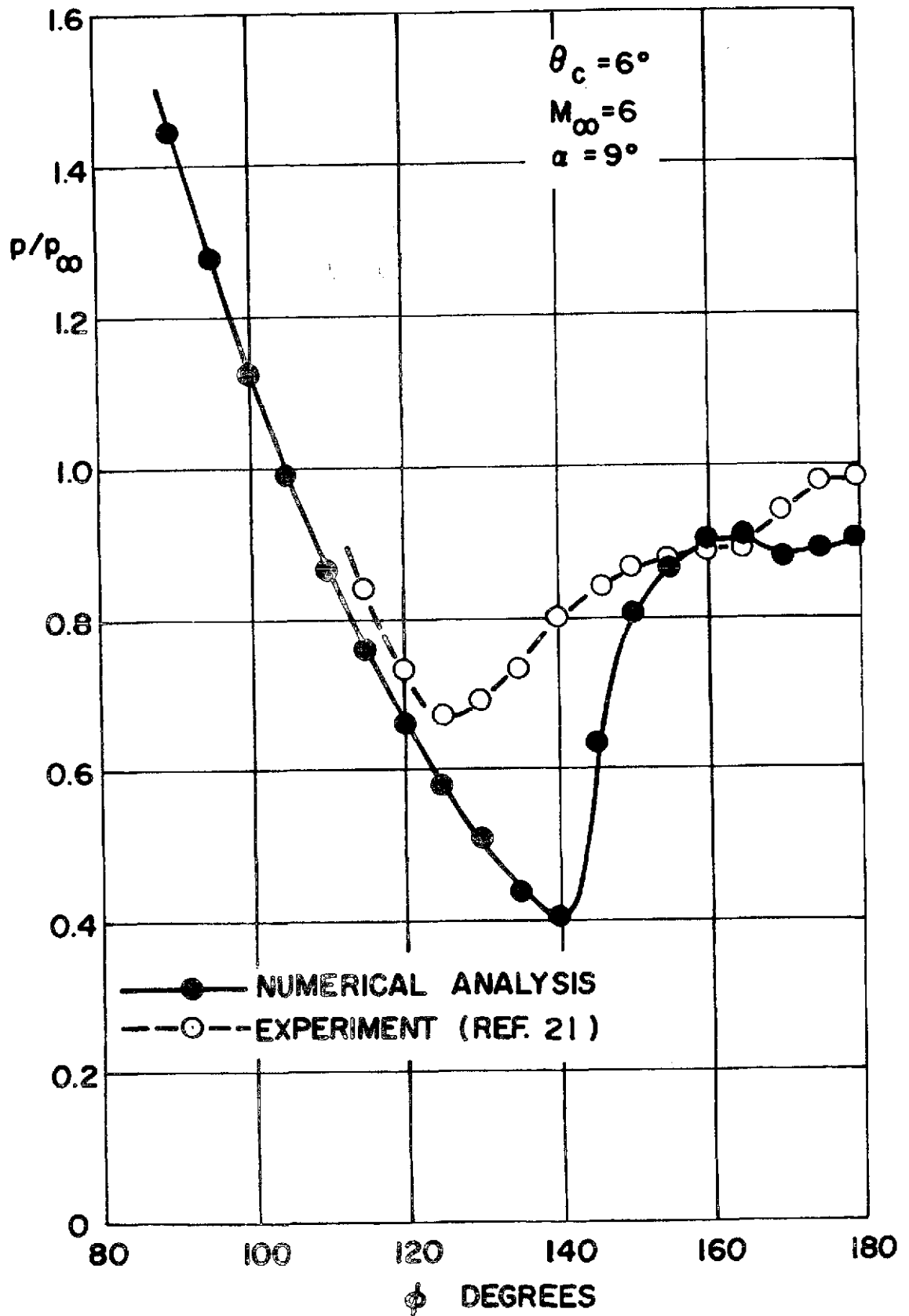


Fig. 126 Surface Pressure Distribution over a Circular Cone ;
 $\theta_c = 6^\circ, M_\infty = 6, \alpha = 9^\circ$

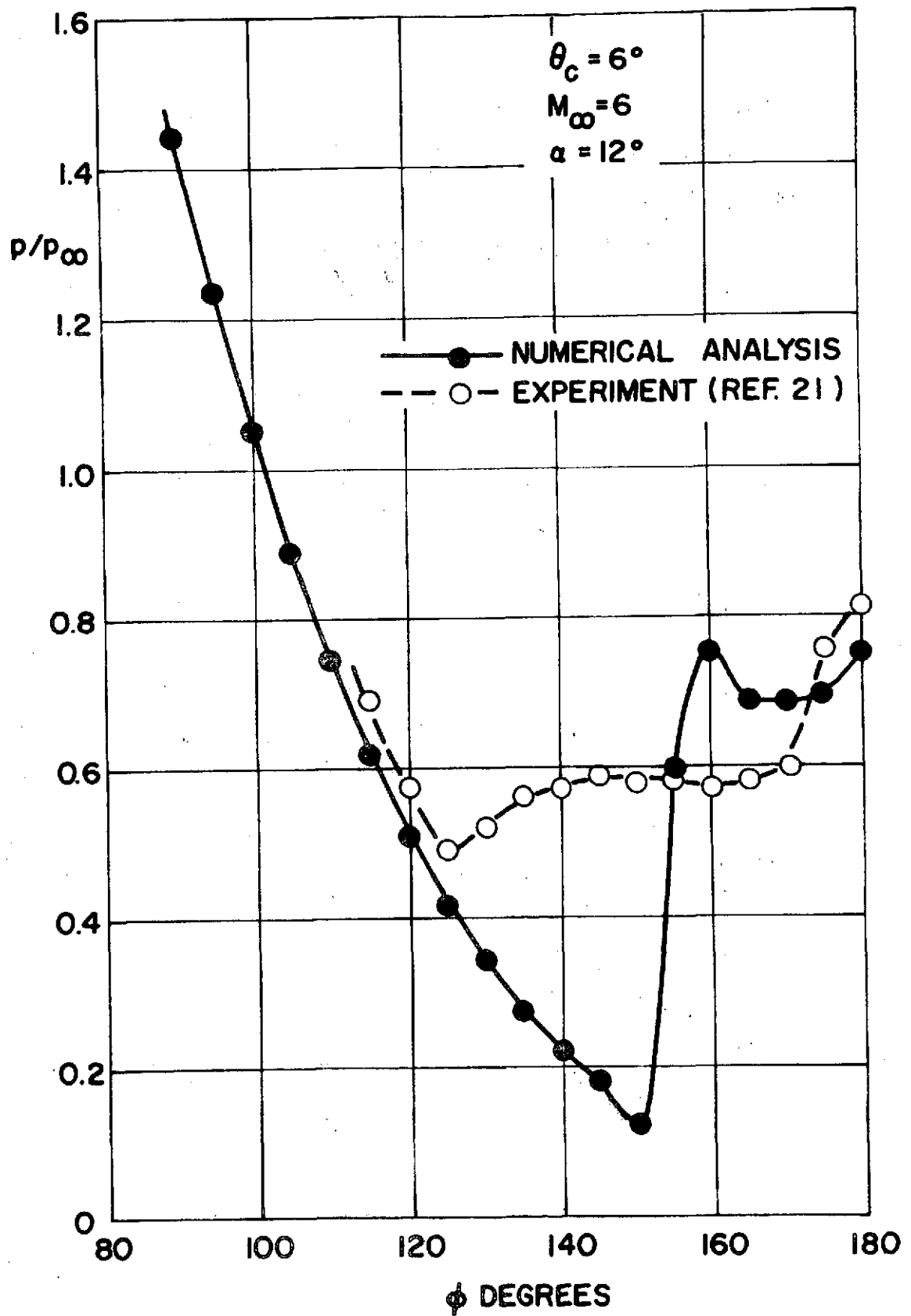


Fig. 127 Surface Pressure Distribution over a Circular Cone ;
 $\theta_c = 6^\circ$, $M_\infty = 6$, $\alpha = 12^\circ$

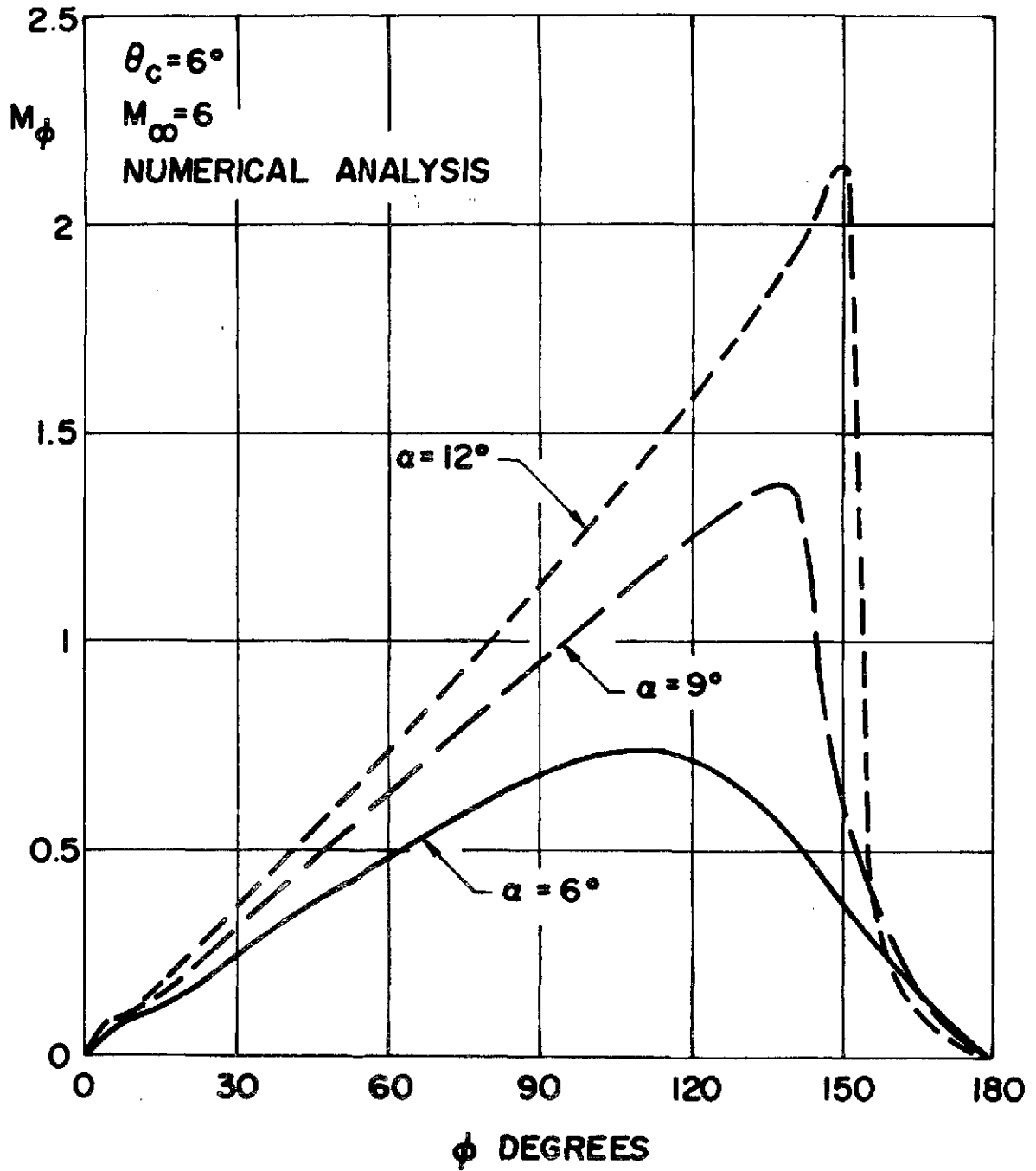


Fig. 128 Cross-Flow Mach Number Distributions on the Surface of a Circular Cone ; $\theta_c = 6^\circ$, $M_\infty = 6$

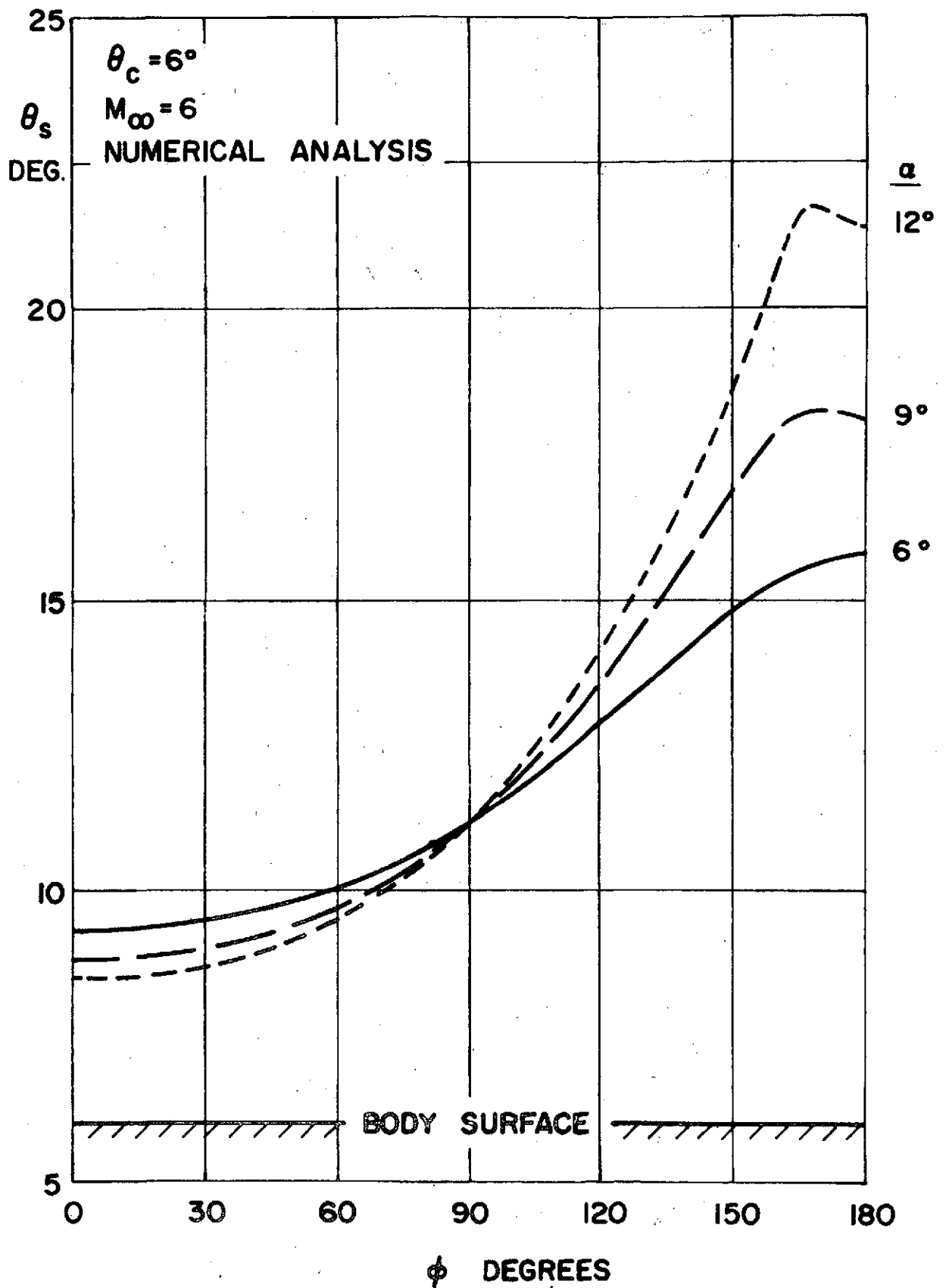


Fig. 129 External Shock Locations for a Circular Cone ;
 $\theta_c = 6^\circ, M_\infty = 6$

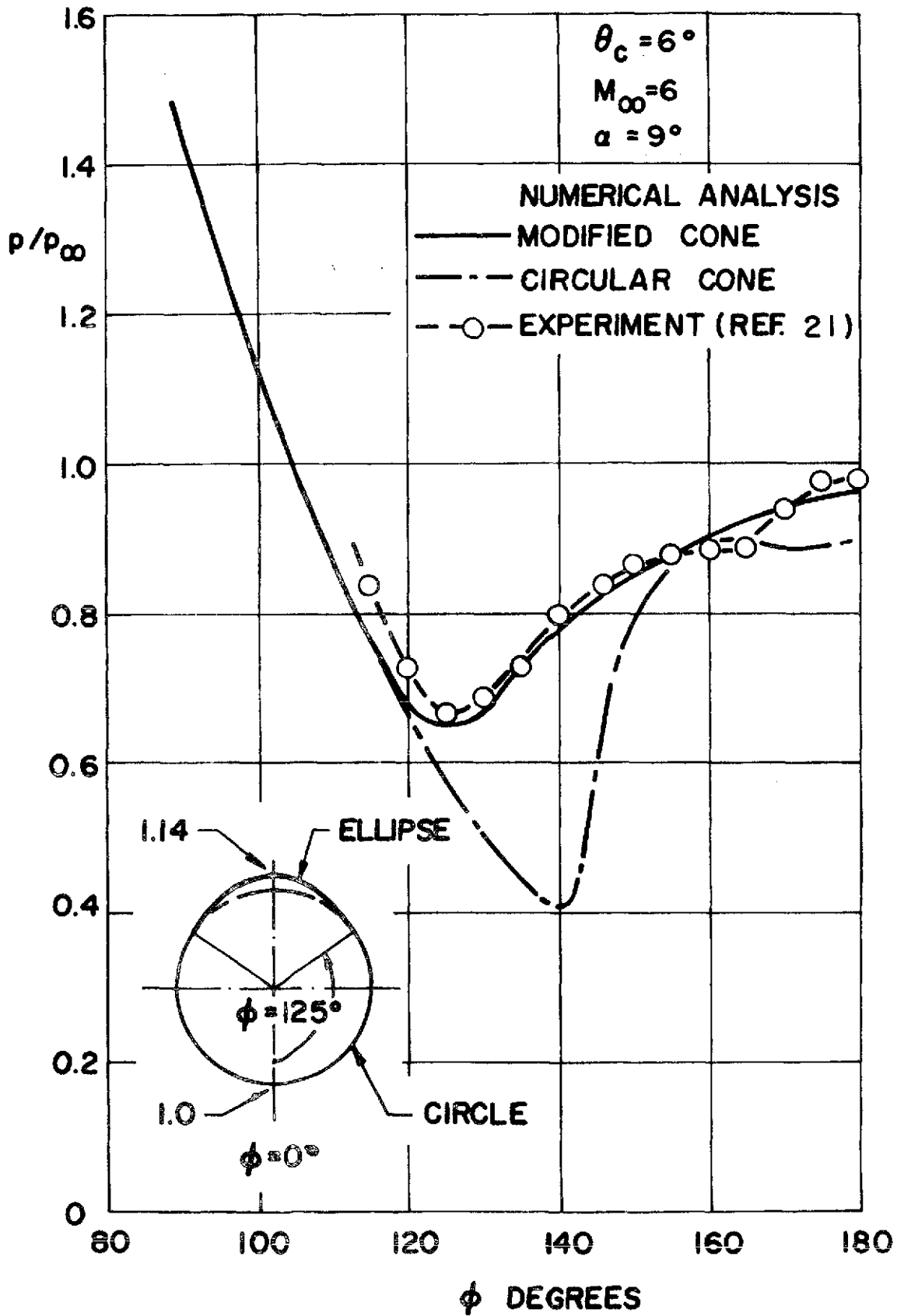


Fig. 130 Surface Pressure Distributions over Modified and Circular Cones ; $\theta_c = 6^\circ$, $M_\infty = 6$, $\alpha = 9^\circ$

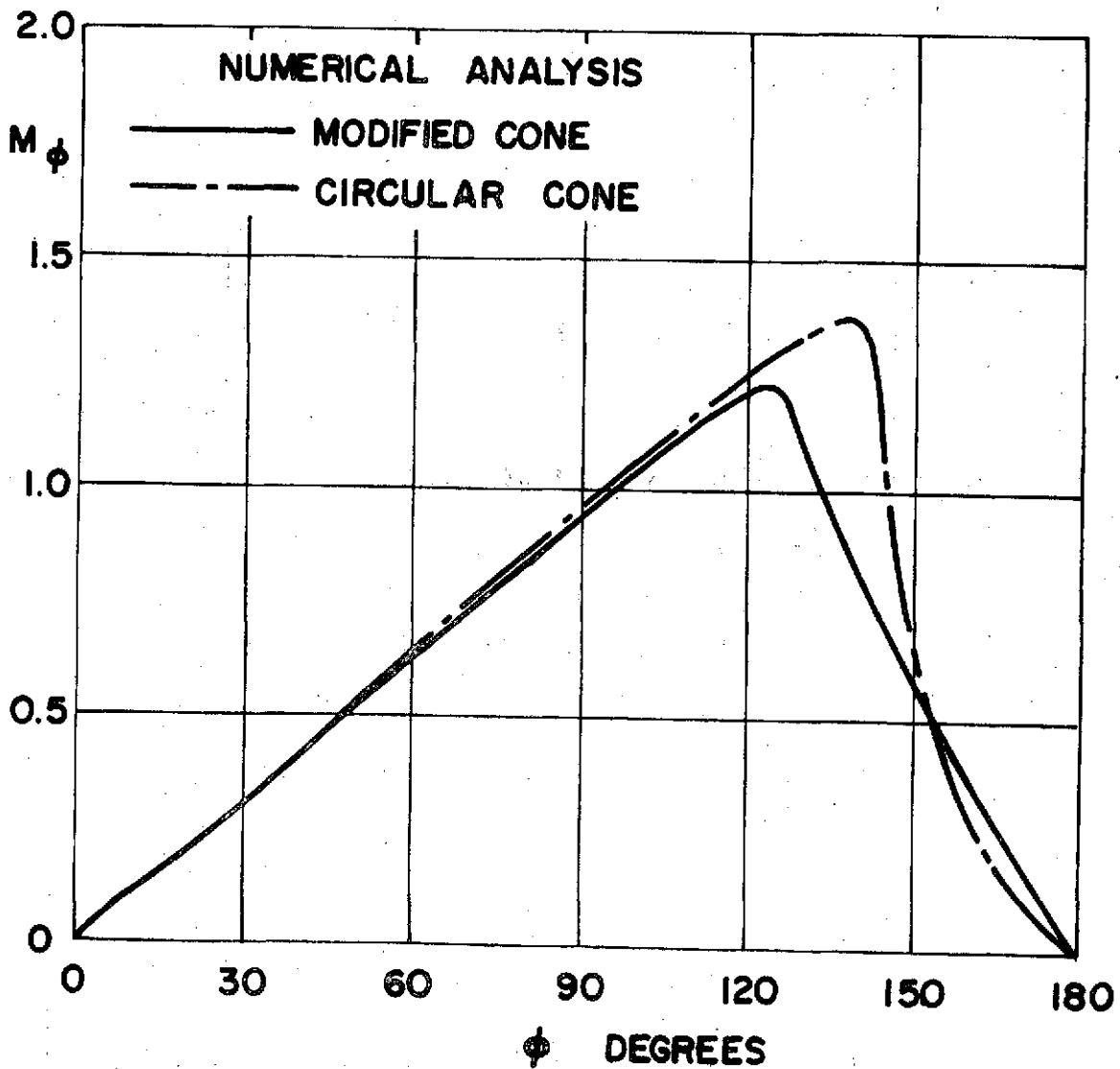
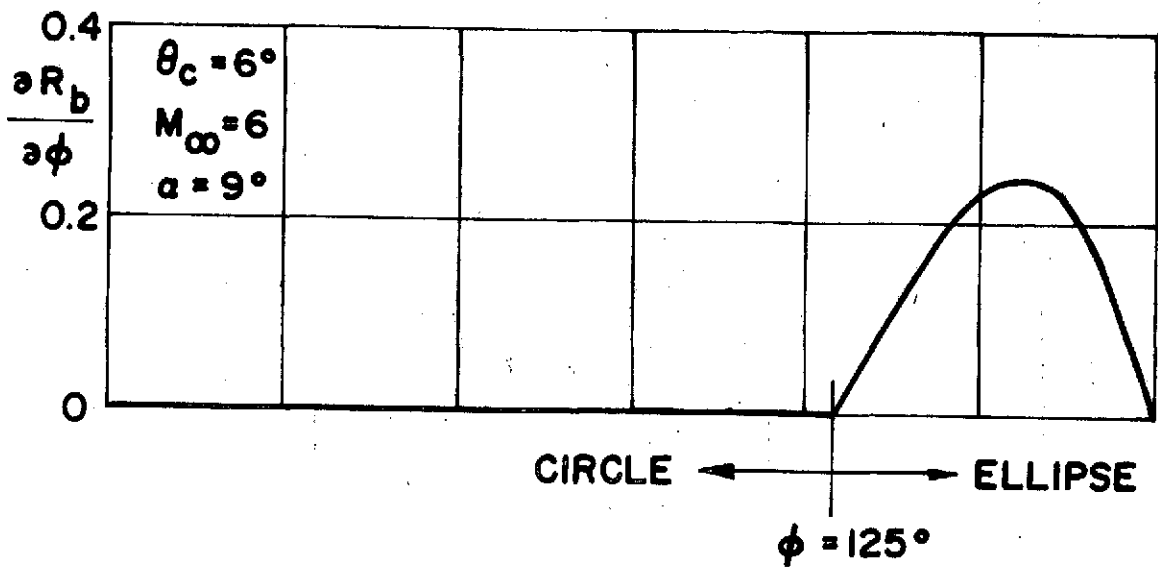


Fig. 131 Cross-Flow Mach Number Distributions on the Surface of Modified and Circular Cones ; $\theta_c = 6^\circ$, $M_\infty = 6$, $\alpha = 9^\circ$